Journal of Nanomaterials

Hybrid Nanofluids for Heat Transfer and Energy Applications

Lead Guest Editor: Zafar Said
Guest Editors: Hafiz Muhammad Ali and Arun Kumar Tiwari

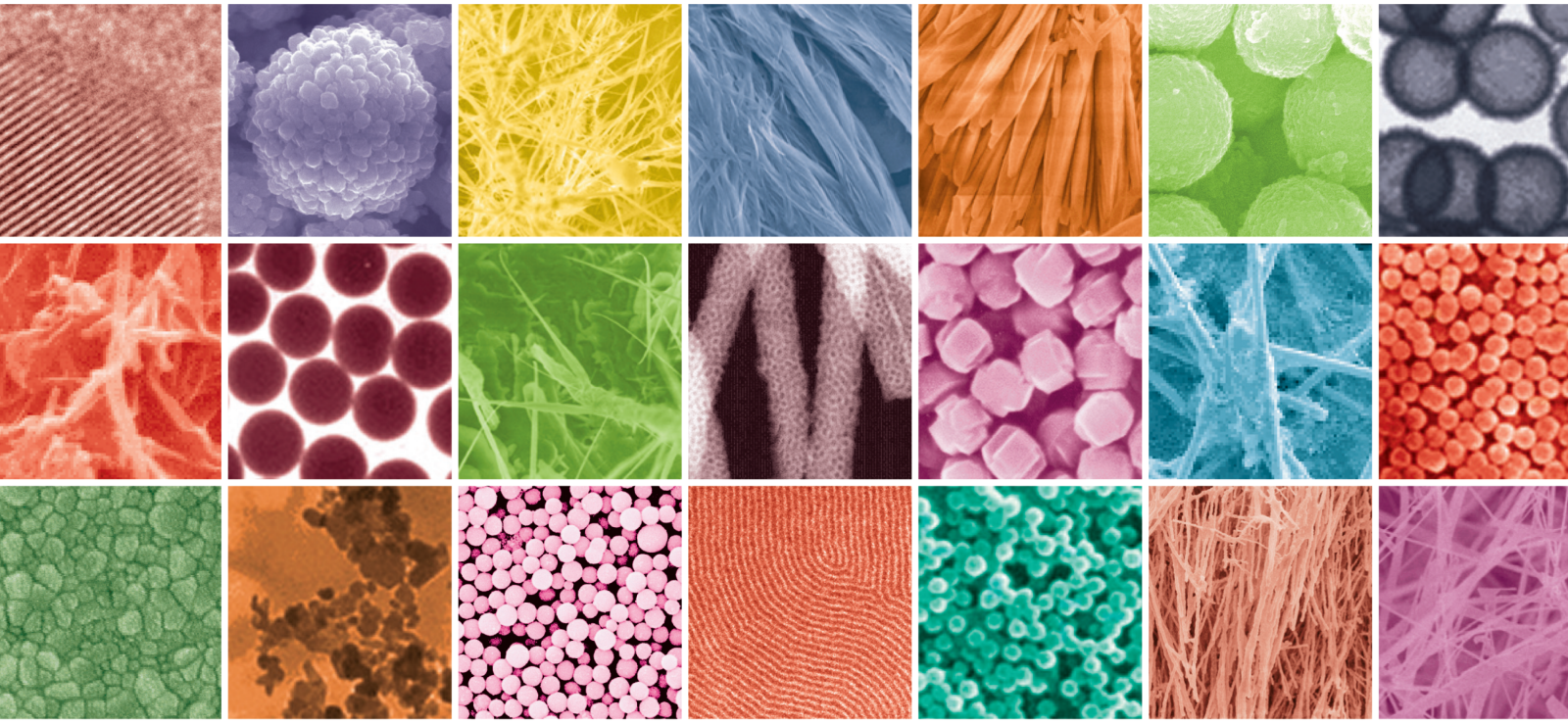

Hybrid Nanofluids for Heat Transfer and Energy Applications

Journal of Nanomaterials

Hybrid Nanofluids for Heat Transfer and Energy Applications

Lead Guest Editor: Zafar Said
Guest Editors: Hafiz Muhammad Ali and Arun Kumar Tiwari

Contents

Hindawi
Journal of Nanomaterials
Volume 2023, Article ID 9208703, 13 pages
https://doi.org/10.1155/2023/9208703

Research Article

Coupled Dufour and Soret Effects on Hybrid Nanofluid Flow through Gyrating Channel Subject to Chemically Reactive Arrhenius Activation Energy

Zehba Raizah,[1] **Arshad Khan**,[2] **Taza Gul**,[3] **Anwar Saeed**,[4] **Ebenezer Bonyah**,[5] **and Ahmed M. Galal**[6,7]

[1]*Department of Mathematics, College of Science, King Khalid University, Abha, Saudi Arabia*
[2]*College of Aeronautical Engineering, National University of Sciences and Technology (NUST), Sector H-12, Islamabad 44000, Pakistan*
[3]*Cambridge Graphene Centre, Electrical Engineering Division, Cambridge University Engineering Department, 9 JJ Thomson Avenue, Cambridge CB3 0FA, UK*
[4]*Center of Excellence in Theoretical and Computational Science (TaCS-CoE), Faculty of Science, King Mongkut's University of Technology Thonburi (KMUTT), 126 Pracha Uthit Road, Bang Mod, Thung Khru, Bangkok 10140, Thailand*
[5]*Department of Mathematics Education, Akenten Appiah Menka University of Skills Training and Entrepreneurial Development, Kumasi, Ghana*
[6]*Department of Mechanical Engineering, College of Engineering, Prince Sattam Bin Abdulaziz University, Wadi Alddawasir 11991, Saudi Arabia*
[7]*Production Engineering and Mechanical Design Department, Faculty of Engineering, Mansoura University, P.O. Box 35516, Mansoura, Egypt*

Correspondence should be addressed to Ebenezer Bonyah; ebbonya@gmail.com

Received 20 August 2022; Accepted 29 September 2022; Published 24 April 2023

Academic Editor: Zafar Said

This study explores the magnetohydrodynamic fluid flow through two rotating plates subjected to the impact of microorganisms. The nanoparticles of copper and alumina are mixed with water for formulating hybrid nanofluid with new combination $(Cu + Al_2O_3 + H_2O)$. This new combination augments the thermal conductivity of pure fluid. The flow is influenced by the coupled effects of Dufour and Soret diffusions. The joined effects of chemically reactive activation energy have been incorporated in the mass transportation equation. A constant magnetic field has been employed to the flow field with strength B_0 in normal direction to the plates. The equations that controlled fluid flow have been transferred to dimension-free form by implementing suitable set of variables. The influence of the different factors has been examined theoretically by employing the graphical view of different flow profiles. It has been concluded in this work that, linear velocity has declined by augmentation in magnetic factor and rotational parameter whereas these factors have enhanced microrotational profiles of fluid. Higher values of radiation parameter, Dufour number, and volumetric fractions have augmented fluid's thermal profiles. The concentration of fluid has been retarded with upsurge in Soret number and chemical reaction parameter whereas growth in activation energy parameter has supported the upsurge in concentration. The rate of motile microorganisms has retarded by upsurge in the values of Lewis and Peclet numbers. It has been noticed that when K_r, M, and Re varies from 0.2 to 0.6 then in case of nanofluid, skin friction changes from 0.288 to 0.633 at $\phi_1 = 0.01$ and from 0.292 to 0.646 at $\phi_1 = 0.02$ and in case of hybrid nanofluid the variations in skin friction are from 0.328 to 0.646 at $\phi_1, \phi_2 = 0.01$ and from 0.335 to 0.703 at $\phi_1, \phi_2 = 0.02$.

1. Introduction

In the earlier times, the transfer of mass and heat has appealed the interest of research community with more significance for its important applications at industrial level. Some of these applications are electronic devices in the field of engineering, compact thermal exchangers, nuclear reactors, etc. In the combined mass and heat transfer progressions, the fluid flow is occurred due to variations in density resulted from gradient in concentration, temperature, and composition of material. The transmission of mass is caused by variation in the thermal behavior of fluid particles which is termed as Soret effect. The energy's flux occurred due to variations in concentration and termed as Dufour effect. It is worth mentioning that these effects are of more importance for transmission of mass and heat in different engineering processes. Both Dufour and Soret effects become more significant whenever some species are acquainted at the surface of fluid with density smaller than that of surrounding fluid. Numerous applications of Soret and Dufour effects can be seen in the field of combustion flames, safety reactor, solar collectors, and building energy conservations. Chamkha and Ben-Nakhi [1] investigated MHD fluid flow upon a porous semi-infinite isothermal sheet with Soret and Dufour effects. Rasool et al. [2] revealed the impact of Soret and Dufour effect upon nanofluid flow with Darcy–Forchheimer terms in the mathematical model. It has concluded that the flow of nanoparticles has declined with higher values of porosity parameter. Khan et al. [3] have introduced the Soret and Dufour effects with significant characteristics to viscous MHD fluid flow through a rotary cone by discussing its generation of entropy as well. Vafai et al. [4] have inspected about the MHD and Dufour, Sorret effects for fluid flow upon a stretching surface and have established that thermal flow rate has declined with upsurge in radiation and viscous dissipation effects. Khan et al. [5] have concluded about the flow of viscous fluid with combined influence of Soret and Dufour. The authors in this study have focused mainly upon the flow of heat mechanism and established that magnetic effects have upsurge the thermal flow rate. The thermal fluid flow for Casson fluid with ethylene glycol as pure fluid has inspected with impacts of Soret and Dufour effects by Hafeez et al. [6]. Layek et al. [7] deliberated the collective influence of Soret and Dufour on time-dependent mass and heat transfer over permeable surface. Kotnurkar and Katagi [8] have discussed the characteristics of nanofluid flow with Soret and Dufour effects.

The combination of small-sized particles in a base fluid for enhancement of its thermal flow characteristics is termed as nanofluid. The nanoparticles flow analysis has been the topic of widespread research for various investigators, as it has upgraded the thermal characteristics of thermal flow phenomena. The nanoparticles are composed of various metal oxides such as (CuO, Al_2O_3), metals such as (Cu, Au, Ag), semiconductors such as (TiO_2, SiC), nitride ceramics such as (AlN, SiN), and carbide ceramics such as (SiC, TiC). The idea of suspending nanoparticles into a base fluid was first drifted by Choi and Eastman [9]. This work has provided a new base in the field of fluid mechanics. For its significant applications in the field of engineering and at industrial level various studies have been carried out with main focus upon thermal diffusivity among the nanoparticles. Sheikholeslami et al. [10] inspected the nanofluid flow with thermal transmission through a gyrating channel by implementing the magnetic effects. It has concluded in this inspection that there has been a direct relationship between nanoparticles volume fraction and Nusselt number for both injection and suction cases. Said et al. [11] have analyzed experimentally the novel ionic nanofluid's energy storage characteristics. Sharma et al. [12] have explored contemporary advancements in the machine learning for nanofluid-based thermal transmission in the system of renewable energy. Ahmad and Khan [13] have simulated numerically the MHD Sisko nanofluid flow past a curved movable surface.

With the passage of time researchers have realized that the dispersion of two dissimilar kinds of nanoparticles in a pure fluid, results in a fluid that has higher thermal diffusion. This new class of fluid is termed as hybrid nanofluid. Islam et al. [14] deliberated the effects of Hall current for radiated hybrid nanofluid flow through a channel and have concluded that hybrid nanofluid has superior thermal flow characteristics than traditional fluid. Said et al. [15] have explored the thermal capacity for hybrid nanofluid flow for solar energy applications. Li et al. [16] deliberated the creation of entropy for hybrid nanofluid between two plates by considering the effects of Marangoni convection in the flow model with other flow conditions. It has been concluded in this work that, rate of flow transmission is at peak for greater values of exponential and thermal source sink. Said et al. [17] have used hybrid nanofluid to discuss the applications of innovative frameworks based upon the collective enhanced regressions for modeling of heat performance small-scale Rankin cycles.

In a rotating system, the flow of fluid is a natural phenomenon. Actually, these effects of rotation occur internally among a fluid's particles that augment when the fluid gets into motion. Hence in the fluid motion the natural rotation exists up to a specific range. The concept of rotating system in viscous fluid flow was floated by Taylor [18]. The investigation of rotational motion for different flow system has been conducted in detail by Greenspan [19]. The idea of rotational motion has also extended to moving disks [20]. Forbes [21] has investigated the axisymmetric flow of fluid between two plates with lower plate as static and the upper plate as rotational. Dogonchi et al. [22] inspected the influence of stretching surface upon nanofluid flow and heat conduction in rotary channel. Muhammad et al. [23] have inspected the squeezing fluid flow between rotational plates. In this work, the effects of MHD have also taken into account for flow system. Salahuddin et al. [24] have picked second-grade fluid motion through rotary plates by considering variable fluid characteristics. It has been proved in this study that diffusivity and concentration of fluid particles are related directly with thermal conductivity and thermal transmission.

The least energy required by molecules for commencement of a chemical reaction is termed as activation energy introduced by Arrhenius. Activation energy has many applications in processing of food, and emulsions of different suspensions. First result in the paper format with combine impact of activation energy was established by Bestman [25]. Khan et al. [26] have inspected the influence of Arrhenius activation energy upon MHD second-grade fluid flow in a permeable surface. The term has been also used by Bhatti and Michaelides [27] by considering its impact upon thermos-bioconvective nanofluid flow over a Riga plate and has concluded that flow profiles have been weakened by expanding values of Rayleigh number. Khan et al. [28] have deliberated a wonderful work upon hybrid nanofluid flow by considering the influence of Arrhenius activation energy upon flow system. The authors have concluded in their investigation that mass diffusivity has jumped up for expansion in activation energy parameter. More established work can be studied in previous studies [29–33].

The effects of magnetic field have a considerable part in fluid mechanics. It has numerous engineering and industrial applications for instance MHD generators and pumps, etc. Various investigations have been conducted with main emphasis upon transportation of heat with MHD effects. Shehzad et al. [34] have inspected the influence of MHD upon three-dimensional flow of Jeffery fluid with Newtonian heating effects and have revealed that fluid's motion has opposed while the thermal flow rate and skin friction have supported with augmentation in magnetic parameter. Ahmad et al. [35] have investigated unsteady MHD nanofluid flow over a cylindrical disk placed vertically. Usman et al. [36] have investigated the EMHD impact upon couple stress film flow of nanofluid over spinning disk and have calculated the percentage augmentation in thermal flow rate for single and double nanoparticles fluid flow. Ahmad and Khan [37] have inspected the significance of activation energy in the advancement of covalent bonding using Sisko MHD nanofluid flow past a moveable curved sheet. Ahmad et al. [38] have investigated thermally radiated Sisko fluid flow subject to Joule heating and MHD effects and have concluded that thermal flow has augmented with corresponding growth in radiation and magnetic factors.

From the aforementioned investigations, it has been discovered that no study has yet been steered to deliberate the thermal flow rate for hybrid nanofluid flow through rotating plates by employing the combined Dufour, Soret effects and the impact of microorganisms. The following points support the novelty of the work:

(i) Coupled Dufour and Soret effects are taken in mathematical model of flow problem.

(ii) Chemically reactive Arrhenius activation energy is also incorporated in concentration equation.

(iii) The plates at the boundaries are considered as rotating, where the spinning effects of plates are coupled in the flow equations.

(iv) The effects of microorganism has used in the modeled equations.

(v) Magnetic effect is applied to the flow system and is incorporated mathematically in momentum equations.

(vi) HAM is worked out for solution of model problem.

2. Problem Formulation

Take an incompressible viscous hybrid nanofluid fluid flow between two plates. The system of coordinates is selected so that plates along fluid are rotating with angular velocity Ω about y-axis. h is the distance between the plates such that Cu, Al_2O_3—nanoparticles are mixed with water for formulating hybrid nanofluid with combination$(Cu + Al_2O_3 + H_2O)$. The flow is influenced by the coupled effects of Dufour and Soret diffusions. The collective impact of chemically reactive Arrhenius activation energy has been incorporated in mathematical model of problem. Magnetic field has also been employed to the flow system with strength B_0 in normal direction to the plates, as shown in Figure 1. It is supposed that the existence of nanoparticles will not affect the microorganisms' direction, swimming, and their velocity.

With the help of above assumptions, one has following set of equations [14, 39, 40]:

$$\frac{\partial u}{\partial x} + \frac{\partial w}{\partial z} + \frac{\partial v}{\partial y} = 0, \tag{1}$$

$$v\frac{\partial u}{\partial y} + u\frac{\partial u}{\partial x} + 2\omega w + \frac{1}{\rho_{\mathrm{hnf}}}\frac{\partial p}{\partial x} = \frac{\mu_{\mathrm{hnf}}}{\rho_{\mathrm{hnf}}}\left(\frac{\partial^2 u}{\partial x^2} + \frac{\partial^2 u}{\partial y^2}\right) - \frac{\sigma {B_0}^2}{\rho_{\mathrm{hnf}}}u, \tag{2}$$

$$v\frac{\partial v}{\partial y} + u\frac{\partial v}{\partial x} + \frac{1}{\rho}\frac{\partial p}{\partial y} = +\frac{\mu_{\mathrm{hnf}}}{\rho_{\mathrm{hnf}}}\left(\frac{\partial^2 v}{\partial y^2} + \frac{\partial^2 v}{\partial x^2}\right), \tag{3}$$

$$u\frac{\partial w}{\partial x} + v\frac{\partial w}{\partial y} - 2\omega u = \frac{\mu_{\mathrm{hnf}}}{\rho_{\mathrm{hnf}}}\left(\frac{\partial^2 w}{\partial x^2} + \frac{\partial^2 w}{\partial y^2}\right) - \frac{\sigma {B_0}^2}{\rho_{\mathrm{hnf}}}w, \tag{4}$$

$$u\frac{\partial T}{\partial x} + v\frac{\partial T}{\partial y} + w\frac{\partial T}{\partial z} = \alpha^*\left(\frac{\partial^2 T}{\partial x^2} + \frac{\partial^2 T}{\partial y^2} + \frac{\partial^2 T}{\partial z^2}\right) - \frac{1}{\left(\rho c_{\mathrm{p}}\right)_{\mathrm{hnf}}}\frac{\partial q_r}{\partial y} + \frac{D_{\mathrm{M}}k_{\mathrm{T}}}{c_{\mathrm{s}}c_{\mathrm{p}}}\left(\frac{\partial^2 C}{\partial x^2} + \frac{\partial^2 C}{\partial y^2} + \frac{\partial^2 C}{\partial z^2}\right), \tag{5}$$

$$u\frac{\partial C}{\partial x} + v\frac{\partial C}{\partial y} + z\frac{\partial C}{\partial z} = D\left(\frac{\partial^2 C}{\partial x^2} + \frac{\partial^2 C}{\partial y^2} + \frac{\partial^2 C}{\partial z^2}\right) + \frac{D_{\mathrm{M}}k_{\mathrm{T}}}{T_{\mathrm{m}}}\left(\frac{\partial^2 T}{\partial x^2} + \frac{\partial^2 T}{\partial y^2} + \frac{\partial^2 T}{\partial z^2}\right) - {k_{\mathrm{r}}}^2(C - C_h)\left(\frac{T}{T_h}\right)^n \exp\left(-\frac{E_a}{k_{\mathrm{B}}T}\right), \tag{6}$$

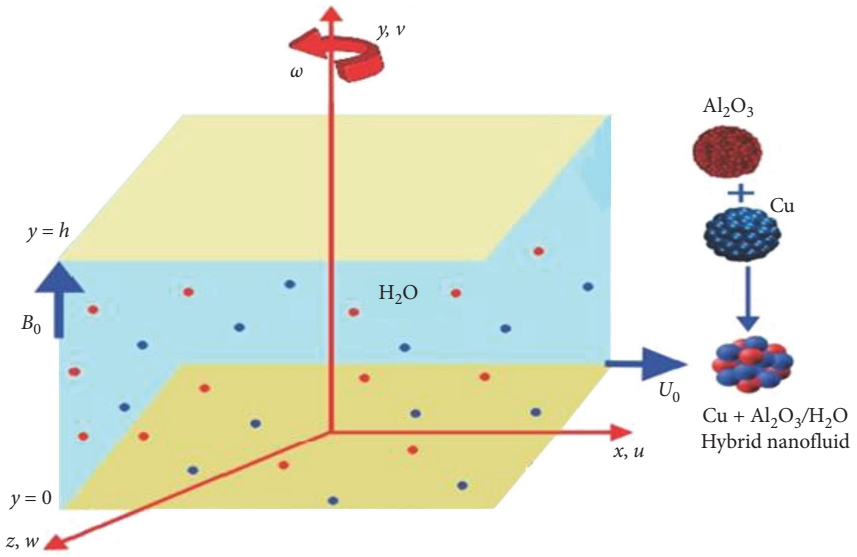

FIGURE 1: Physical view of flow problem.

$$u\frac{\partial n}{\partial x}+v\frac{\partial n}{\partial y}+w\frac{\partial n}{\partial z}+\left(\frac{bW_c}{C_b-C_t}\right)\frac{\partial}{\partial y}\left(n\frac{\partial C}{\partial y}\right)=D_m\left(\frac{\partial^2 n}{\partial x^2}+\frac{\partial^2 n}{\partial y^2}+\frac{\partial^2 n}{\partial z^2}\right). \tag{7}$$

Above, the flow components u, v, w are, respectively, along coordinate axes; μ_{hnf}, ρ_{hnf} are the dynamic viscosity and density of hybrid nanofluid, ω is the angular velocity, q_r is the heat flux due to radiation, $(\rho c_p)_{hnf}$ is heat capacitance, $\alpha^* = k_{hnf}/(\rho C_p)_{hnf}$ is the thermal diffusion in which k_{hnf} is thermal conductance of nanofluid, D_M is mass diffusivity, k_T is ratio of thermal diffusion, D_m is diffusion of microorganism, C_0 and T_0 are the concentration and temperature at lower plate of channel while C_h and T_h are the corresponding quantities at the upper plate. Moreover, $(T/T_t)^n e^{(-E_a/k_B T)}$ is modified Arrhenius function, W_c is speed of microorganism cells, E_a is activation energy, and $k_r{}^2$ is the rate of reaction.

Conditions at boundaries are:

$$\begin{aligned} &u = ax,\ w = 0,\ v = 0,\ C = C_0,\ T = T_0,\ n = n_0,\ \text{at } y = 0\\ &u = 0,\ w = 0,\ v = 0,\ C = C_h,\ T = T_h,\ n = n_h,\ \text{at } y = h. \end{aligned} \tag{8}$$

Use the following set of suitable transformations [41, 42]:

$$\begin{aligned} &u = axf'(\eta);\quad v = -ahf(\eta);\quad w = axg(\eta);\quad \chi(\eta) = \frac{n-n_h}{n_0-n_h};\\ &\theta(\eta) = \frac{T-T_h}{T_0-T_h};\quad \phi(\eta) = \frac{C-C_h}{C_0-C_h};\quad \text{with } \eta = \frac{y}{h}. \end{aligned} \tag{9}$$

For simplification of q_r use the Rosseland approximation as given in Equation (10) [43, 44]:

$$q_r = -\frac{4}{3}\left(\frac{\sigma^* \partial T^4}{\kappa^* \partial \hat{y}}\right). \tag{10}$$

In Equation (10), σ^*, κ^* are termed as Stefan Boltzmann constant and coefficient of Rosseland mean absorption such that $\sigma^* = 5.6697 \times 10^{-8}\ \text{Wm}^{-2}\ \text{K}^{-4}$. If the thermal gradient is sufficiently small within the flow of fluid then T^4 can be simplified by using Taylor's expansion as [44]:

$$T^4 \cong 4TT_h{}^3 - T_h{}^4. \tag{11}$$

In light of Equations (10) and (11), we have from Equation (5) as:

$$\begin{aligned} u\frac{\partial T}{\partial x}+v\frac{\partial T}{\partial y}+w\frac{\partial T}{\partial z} &= \alpha^*\left(\frac{\partial^2 T}{\partial x^2}+\frac{\partial^2 T}{\partial y^2}+\frac{\partial^2 T}{\partial z^2}\right)\\ &+\frac{1}{(\rho c_p)_{hnf}}\left(\frac{16\sigma^*}{3k^*}T_h{}^3\frac{\partial^2 T}{\partial y^z}\right)\\ &+\frac{Dk_T}{c_s c_p}\left(\frac{\partial^2 C}{\partial x^2}+\frac{\partial^2 C}{\partial y^2}+\frac{\partial^2 C}{\partial z^2}\right). \end{aligned} \tag{12}$$

In light of Equation (9), we have from Equations (1–4, 6, 7 and 12) in dimensionless form as follows:

$$\begin{aligned} &\{(1-\phi_1)(1-\phi_2)\}^{-2.5} f^{(iv)}\\ &+\left\{(1-\phi_2)\left((1-\phi_1)+\phi_1\frac{\rho_{s1}}{\rho_f}\right)+\phi_2\frac{\rho_{s2}}{\rho_f}\right\}\\ &(\text{Re}(ff''' - f'f'')) - 2K_r g' - Mf'' = 0 \end{aligned} \tag{13}$$

Table 1: Numerical values of base fluid and nanoparticles for thermophysical characteristics.

Properties	Cu-nanoparticles	Al_2O_3-nanoparticles	H_2O-base fluid
$\rho\ (\mathrm{kg\cdot m^{-3}})$	8,933.00	3,970.00	997.10
$C_p\ (\mathrm{J\cdot kg^{-1}\cdot K^{-1}})$	385.00	765.00	4,179.00
$\kappa\ (\mathrm{W\cdot m^{-1}K^{-1}})$	400.00	40.00	0.613.00

$$\begin{aligned}&\{(1-\phi_1)(1-\phi_2)\}^{-2.5}g''\\&-\left\{(1-\phi_2)\left((1-\phi_1)+\phi_1\frac{\rho_{s1}}{\rho_f}\right)+\phi_2\frac{\rho_{s2}}{\rho_f}\right\}\\&(\mathrm{Re}(f'g-fg')-2K_rf')-\mathrm{Mg}=0\end{aligned} \tag{14}$$

$$\begin{aligned}&\frac{k_{nf}}{k_f}\left(1+\frac{4}{3}\mathrm{Rd}\right)\theta''+\left\{(1-\phi_2)\left((1-\phi_1)+\phi_1\frac{\rho_{s1}}{\rho_f}\right)+\phi_2\frac{\rho_{s2}}{\rho_f}\right\}\\&\mathrm{Pr}(\mathrm{Re}\,\theta'f'+\mathrm{Du}\,\phi'')=0\end{aligned} \tag{15}$$

$$\phi''-\mathrm{Sc}\phi'+\mathrm{ScSr}\,\theta''-\mathrm{Sc}\,\Gamma(1+\tau\theta)^n\ \exp\left(\frac{-E}{1+\tau\theta}\right)\phi=0 \tag{16}$$

$$\chi''-\mathrm{Re}Lbf\chi'+\mathrm{Pe}[\chi'\phi'+(\delta+\chi)\phi'']=0. \tag{17}$$

Above, Re is Reynolds number, K_r is rotation parameter, M is magnetic parameter, Pr is Prandtl number, Rd is radiation parameter, Du is Dufour number, E is activation energy parameter, τ is temperature parameter, Sr is Soret number, Γ is chemical reaction parameter, Sc is Schmidt number Lb,Pe are bioconvection Lewis and Peclet numbers. These parameters are mathematically described as:

$$\begin{aligned}&\mathrm{Re}=\frac{ah^2}{\upsilon_f},\ \ K_r=\frac{\omega h^2}{\upsilon_f},\ \ M=\frac{h^2\sigma_f{B_0}^2}{\mu_f},\ \mathrm{Pr}=\frac{\mu_f(C_p)_f}{k_f},\\&\mathrm{Rd}=4\frac{\sigma^*}{k^*k_{\mathrm{hnf}}}{T_h}^3,\ \ \Gamma=\frac{{K_r}^2h^2}{\upsilon_f},\ \ \mathrm{Lb}=\frac{\upsilon_f}{D_M},\\&\mathrm{Du}=\frac{D_Mk_T}{C_sC_p}\frac{(C_0-C_h)}{(T_0-T_h)},\ \ E=\frac{E_a}{k_BT_h},\ \ \tau=\frac{T_0-T_h}{T_h},\\&\mathrm{Sr}=\frac{D_Mk_T}{T_M\upsilon_f}\frac{(T_0-T_h)}{(C_0-C_h)},\ \ \mathrm{Sc}=\frac{\upsilon_f}{D_M},\ \ \mathrm{Pe}=\frac{bW_c}{D_M}.\end{aligned} \tag{18}$$

The thermos-physical characteristics of solid nanoparticles are defined as follows with its numerical values are depicted in Table 1:

$$\begin{aligned}\mu_{\mathrm{hnf}}&=\frac{\mu_f}{\{(1-\phi_1)(1-\phi_2)\}^{2.5}},\\\rho_{\mathrm{hnf}}&=\left\{(1-\phi_2)\left((1-\phi_1)+\phi_1\frac{\rho_{s1}}{\rho_f}\right)+\phi_2\frac{\rho_{s2}}{\rho_f}\right\}\rho_f,\\(\rho C_p)_{\mathrm{hnf}}&=\left\{(1-\phi_2)\left((1-\phi_1)+\phi_1\frac{(\rho C_p)_{s1}}{(\rho C_p)_f}\right)\right.\\&\quad\left.+\phi_2\frac{(\rho C_p)_{s2}}{(\rho C_p)_f}\right\}(\rho C_p)_f,\\\kappa_{\mathrm{hnf}}&=\frac{\kappa_{s2}+2\kappa_f-2\phi_2(\kappa_f-\kappa_{s2})}{\kappa_{s2}+2\kappa_f+\phi_2(\kappa_f-\kappa_{s2})}\kappa_{\mathrm{nf}}.\end{aligned} \tag{19}$$

The related conditions at the boundaries are:

$$\begin{aligned}&f(0)=0,g(0)=0,f'(0)=1,\theta(0)=1,\phi(0)=1,n(0)=1\ \text{at}\ \eta=0,\\&f(1)=0,g(1)=0,f'(1)=0,\theta(1)=0,\phi(1)=0,n(1)=0\ \text{at}\ \eta=h.\end{aligned} \tag{20}$$

2.1. Physical Quantities. In the problems related to thermodynamics, the engineers and scientists are normally interested to determine the thermal and mass flow rates for fluid flow system. In this regard, some quantities of interest are depicted in Equation (21):

$$\begin{aligned}C_f&=\frac{h\mu_{\mathrm{nf}}}{\rho_fu}.\frac{\partial u}{\partial y}\Big|_{\,y=0},\\\mathrm{Nu}&=\frac{h}{k_f(T_0-T_h)}\left(k_{\mathrm{hnf}}+\frac{16\sigma^*{T_h}^3}{3k^*}\right)\frac{\partial T}{\partial y}\Big|_{\,y=0},\\\mathrm{Sh}&=-\frac{h}{(C_0-C_h)}\frac{\partial C}{\partial y}\Big|_{\,y=0},\\\mathrm{Nn}&=\frac{x}{D_m(n_b-n_t)}\left\{-D_m\frac{\partial n}{\partial y}\Big|_{\,y=0}\right\}.\end{aligned} \tag{21}$$

Incorporating Equation (9) in Equation (21), the resultant equation in refined form is expressed as:

$$\begin{aligned}&C_f=(1-\phi_1-\phi_2)^{2.5}f''(0),\ \ \mathrm{Nu}=\frac{k_{\mathrm{hnf}}}{k_f}\left(1+\frac{4}{3}\mathrm{Rd}\right)\theta'(0),\\&\mathrm{Sh}=-\phi'(0),\ \ \mathrm{Nn}=-\chi'(0).\end{aligned} \tag{22}$$

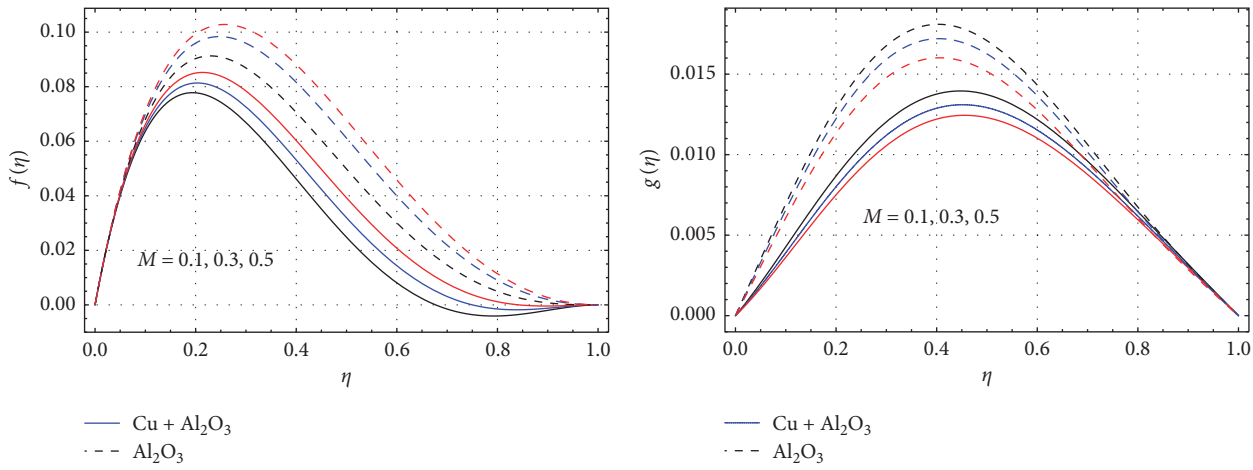

FIGURE 2: Linear and microrotation velocities vs. variations in M.

3. Problem Solution

For solution of modeled equations, the semianalytical technique HAM [45, 46] will be incorporated. This technique describes the solution in the form of functions and is most suitable for solving nonlinear equations. To solve Equations (13–17) by considering boundary conditions in Equation (20), we shall start with the following initial guesses:

$$\widehat{f}_0(\eta) = (\gamma + 2\lambda - 2\alpha + \beta)\eta^3 + (3\alpha - \beta - 2\lambda - 2\gamma)\eta^2 + \lambda\eta - \alpha$$

$$\widehat{\Theta}_0(\eta) = 1 - \eta, \quad \widehat{\Phi}_0(\eta) = 1 - \eta, \quad \widehat{\chi}_0(\eta) = 1 - \eta, \tag{23}$$

whereas the linear operators are described as:

$$L_f(f) = f''' - f', \quad L_\Theta(\Theta) = \theta'' - \theta,$$
$$L_\Phi(\Phi) = \phi'' - \phi, \quad L_\chi(\chi) = \chi'' - \chi. \tag{24}$$

The relations in Equation (24) can be mathematically described as:

$$L_f(d_1 + d_2e^{\eta} + d_3e^{-\eta}) = 0, \quad L_\Theta(d_4e^{\eta} + d_5e^{-\eta}) = 0,$$
$$L_\Phi(d_6e^{\eta} + d_7e^{-\eta}) = 0, \quad L_\chi(d_8e^{\eta} + d_9e^{-\eta}) = 0. \tag{25}$$

In Equation (25), d_i for $i = 1, 2, 3.....9$ are constants.

4. Results and Discussion

In this work, an attempt is made to explore the characteristics of magnetohydrodynamic hybrid nanofluid flow through two rotating plates. The flow is influenced by the coupled effects of Dufour and Soret diffusions and motile microorganisms. Magnetic field has employed to the flow system with strength B_0 in normal direction to the plates. The system of equations is shifted to dimension-free format by using suitable variables. Various nondimensional factors have been encountered in the process of nondimensionalization which will be discussed in the forthcoming sections.

4.1. Effects of Emerging Parameters on $f(\eta)$ and $g(\eta)$ Profiles. In Figures 2(a) and 2(b), the effect of magnetic factor M upon $f(\eta)$ and $g(\eta)$ is portrayed. Clearly an expansion in M results the creation of Lorentz force in the fluid motion and offer more resistance to linear velocity. In this process, swirling motion is supported by Lorentz force. Hence, the higher values of M decline $f(\eta)$, as shown in Figure 2(a) and augment the profiles of $g(\eta)$, as shown in Figure 2(b). The impact is more significant for hybrid nanoparticles than traditional nanoparticles. The influence of rotational parameter K_r upon $f(\eta)$ and $g(\eta)$ is shown in Figures 3(a) and 3(b). Since augmentation in K_r supports the rotational behavior and opposing linear behavior of fluid motion, hence, higher values of K_r-retard fluid motion $f(\eta)$ and augment $g(\eta)$, as shown in Figures 3(a) and 3(b). From Figures 4(a) and 4(b), it has been noticed that augmentation in volumetric fractions ϕ_1, ϕ_2 retarded the fluid motion linearly and rotationally. This phenomenon can be explained as, with augmentation in ϕ_1, ϕ_2, the dense behavior of nanoparticles enhanced within the fluid motion due to which more constraint is experienced by fluid motion. As a result, the velocity profiles declined in all directions. Since with higher values of Re the viscous forces become dominant due to which fluid motion tends to condense. Hence, the linear as well as microrational velocity profiles retarded for growth in Re, as shown in Figures 5(a) and 5(b).

4.2. Effects of Different Emerging Parameters on Temperature Profiles $\theta(\eta)$. The influence of different emerging factors upon thermal profiles has shown in Figure 6(a)–6(c). The growing values of Dufour number Du results an augmentation in thermal flow of fluid. Actually, for higher values of Du, maximum energy transfer takes place from higher to lower concentration zone, hence, causing a growth in thermal profiles, as shown in Figure 6(a). The higher values of ϕ_1 and ϕ_2 are responsible for generation of more friction to

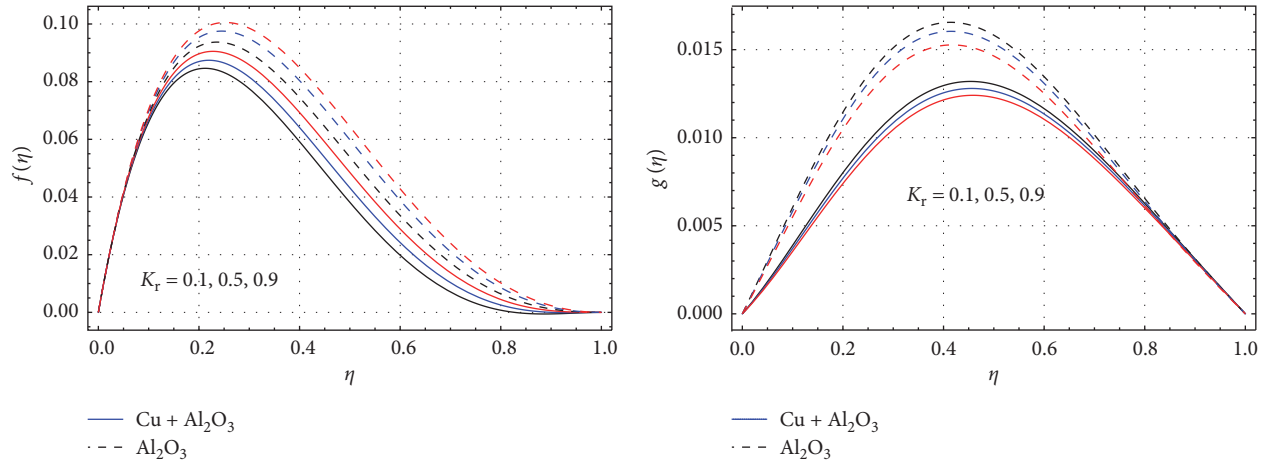

Figure 3: Linear and microrotation velocities vs. variations in K_r.

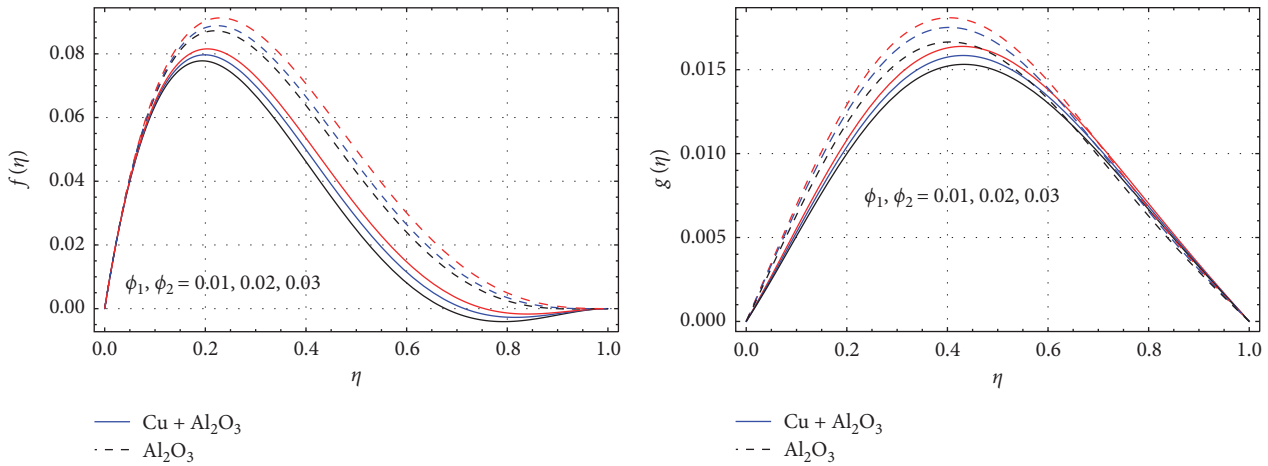

Figure 4: Linear and microrotation velocities vs. variations in ϕ_1 and ϕ_2.

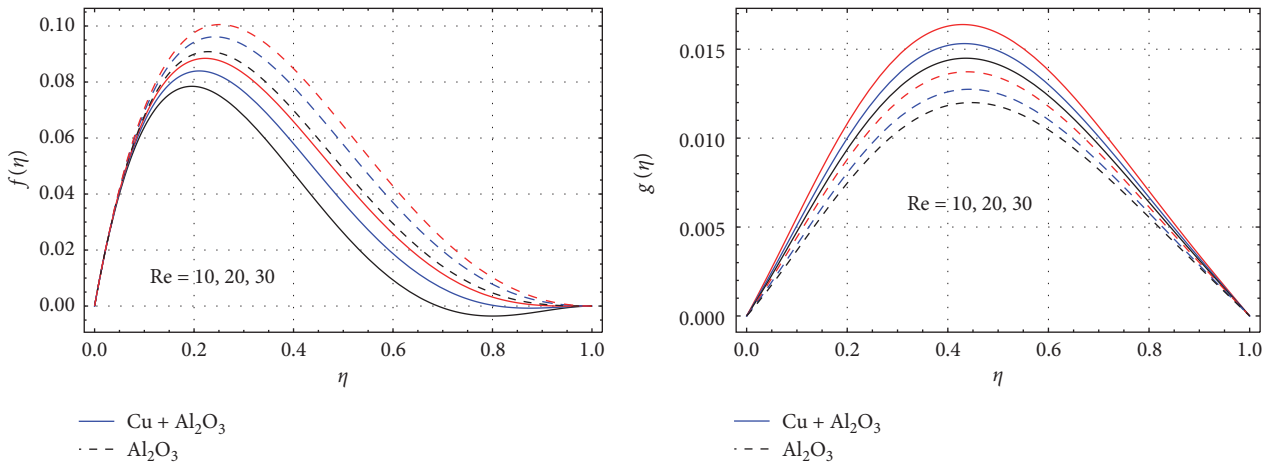

Figure 5: Linear and microrotation velocities vs. variations in Re.

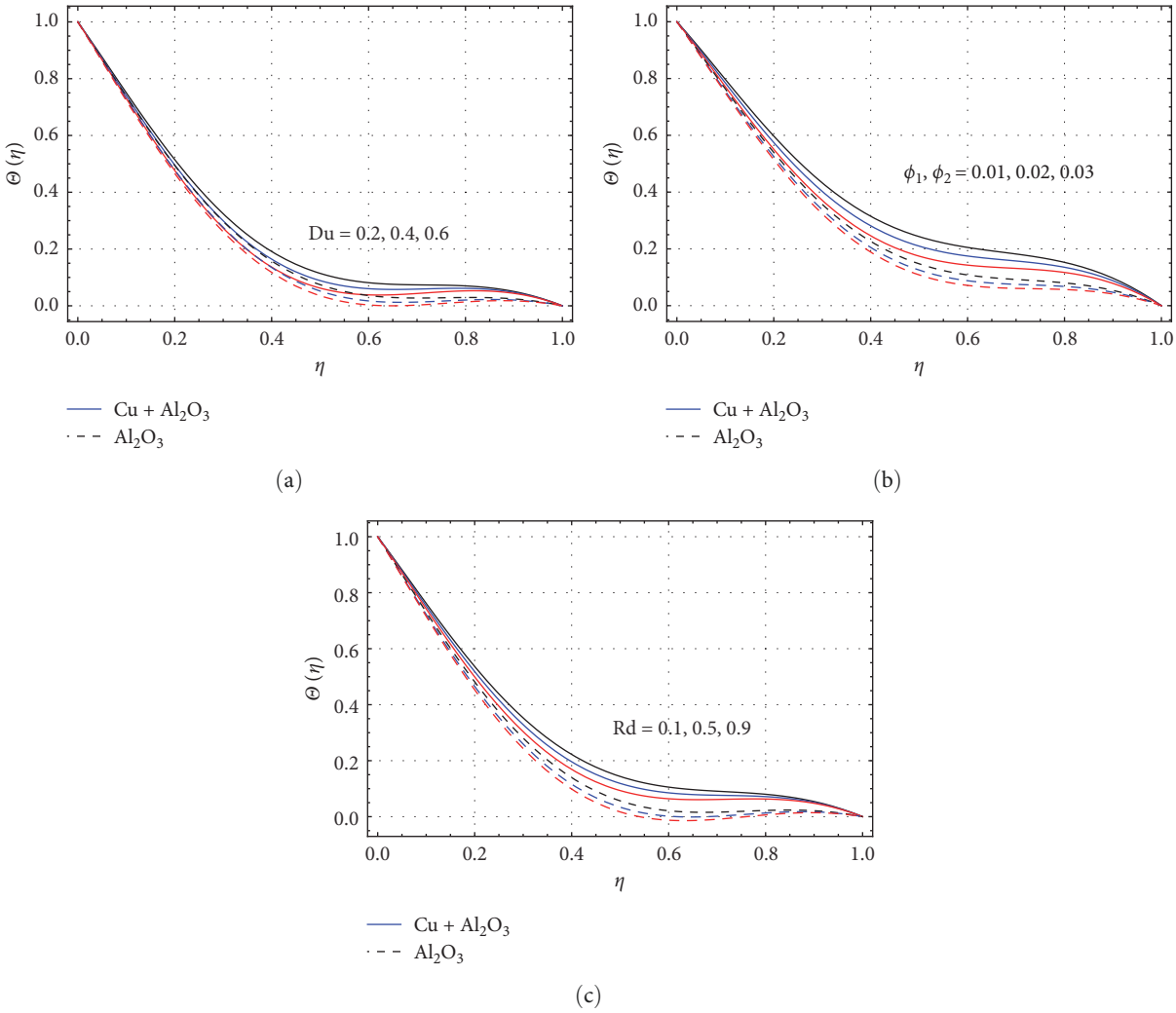

FIGURE 6: Variations in temperature vs. variations in Du, (ϕ_1, ϕ_2), and Rd.

fluid flow in response of resistance to fluid motion. In this process, kinetic energy of fluid particles converted to heat energy that overshoot the thermal flow of fluid, as shown in Figure 6(b). Figure 6(c) shows that augmentation in radiation factor Rd is responsible for growth in temperature. Actually, for higher values of Rd, the thickness of thermal boundary layer grows up due to more transportation of heat that augments the thermal profiles.

4.3. Effects of Different Emerging Parameters on Concentration Profiles $\Phi(\eta)$. The influences of various emerging parameters upon concentration profiles have been shown in Figure 7(a)–7(c). Since the Soret number is mathematically expressed as $\mathrm{Sr} = D_{\mathrm{M}} k_{\mathrm{T}}.(T_0 - T_h)/T_{\mathrm{M}} \upsilon_f.(C_0 - C_h)$, so with upsurge in the values of Sr, the concentration gradient of the fluid flow system will decline due to which less mass diffusivity will occur. In this process, the concentration of the flow system retards, as shown in Figure 7(a). It has been perceived from Figure 7(b) that higher values of activation energy factor E support the mass diffusion. Physically, it can be explained as, a growth in the values of E shoots-up the concentration of molecules with less requisite energy and causes more transportation of mass for fluid flow system that ultimately strengthens the thickness of boundary layer for concentration. In this phenomenon concentration profiles upsurge, as shown in Figure 7(b). The higher values of chemical reaction factor Γ drop the mass diffusion, as shown in Figure 7(c). Actually, with upsurge in Γ, the chemical molecular diffusion declines due to which less diffusion of mass occurs and ultimately retards the concentration profiles.

4.4. Effects of Different Emerging Parameters on Microorganism Profiles $\chi(\eta)$. The influence of bioconvection-Lewis and Peclet numbers (Lb,Pe) over microorganism profiles is shown in Figures 8(a) and 8(b). The augmenting values of both these two parameters weakens the boundary layer thickness of microorganisms due to which less mass diffusions of motile microorganism take place, as shown in Figures 8(a) and 8(b).

4.5. Table Discussions. In Table 1, the thermophysical characteristics for different nanoparticles and base fluid have been depicted numerically. In Tables 2–5, the influence of different emerging parameters has been presented numerically upon various quantities of interest. Since magnetic factor, rotational and viscous parameters are responsible for

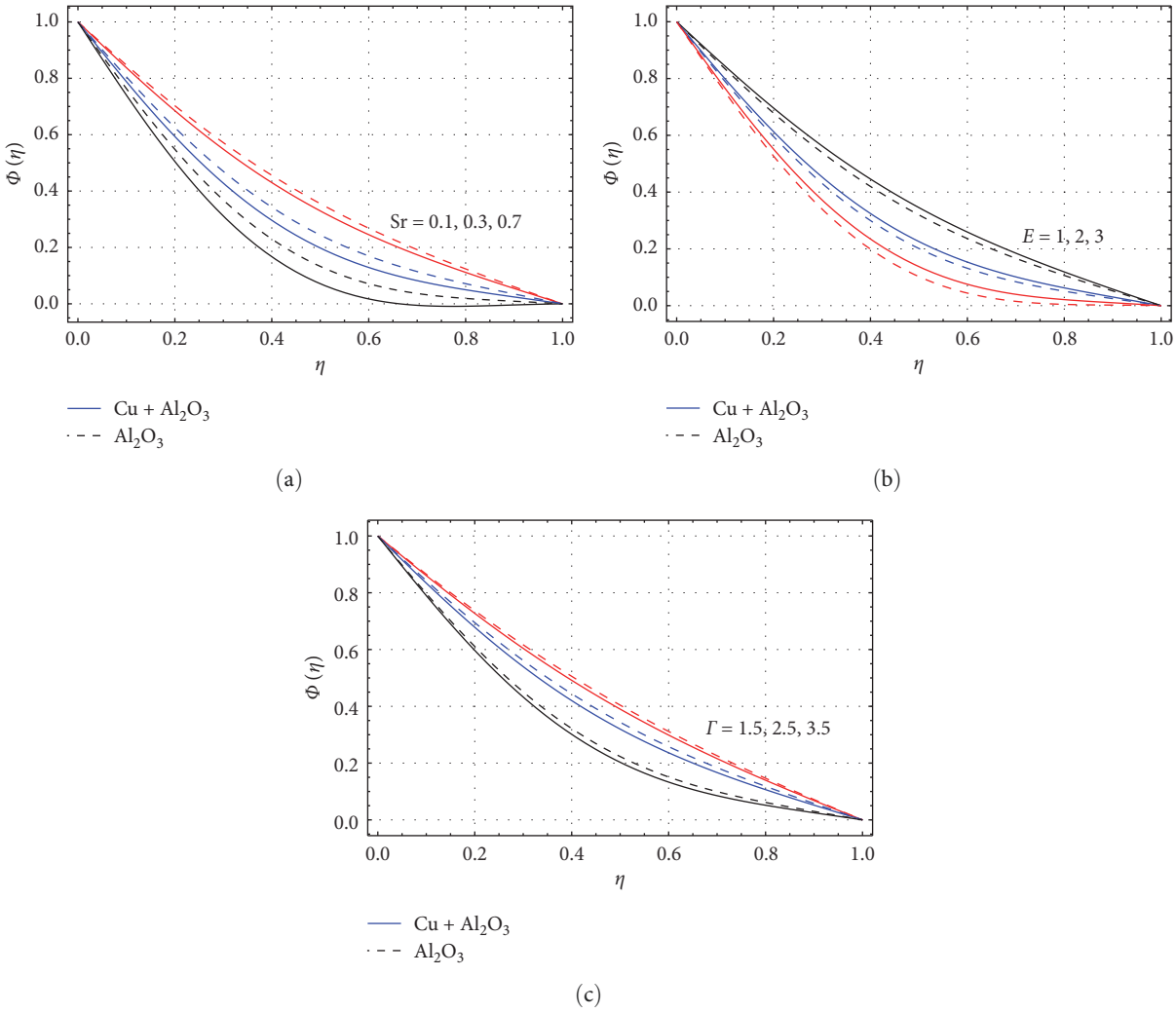

Figure 7: Variations in concentration vs. variations in Sr, E, and Γ.

resistance to fluid flow due to which maximum friction has experienced by fluid's particles. Hence, with growth in these three factors the skin friction grows up as depicted in Table 2. This impact is more visible for hybrid nanoparticles as compared to traditional or single nanoparticles. Table 3 depicts numerically the influence of magnetic, radiation factors, and Dufour number. It is obvious from this table that Nusselt number has increased with growth in radiation parameter whereas upsurge in magnetic parameter and Dufour number has an adverse effect upon Nusselt number. Again the impact is more visible in case of hybrid nanofluid. Table 4 depicts that growing values of Schmidt number upsurge the Sherwood number whereas growing values of Dufour, Soret numbers, and energy activation parameter have declined it. From Table 5 it has revealed that higher values of Lewis and Peclet numbers enhanced the motile rate.

5. Conclusion

This study explores the MHD fluid flow through two rotating plates subject to the effects of microorganisms. The copper and alumina nanoparticles have been mixed with water for formulating hybrid nanofluid. This new combination augments the thermal conductivity of pure fluid. The flow is influenced by the coupled effects of Dufour and Soret diffusions. The joined effects of chemically reactive activation energy have been incorporated in the mass transportation equation. Magnetic effects have been employed to the flow system with strength B_0 in normal direction to the plates. The impact of the embedded parameters has been examined theoretically by employing the graphical view of different flow profiles. After detailed study of the article, it has revealed that:

(i) Linear velocity has declined by augmentation in magnetic factor and rotational parameters, whereas these factors have enhanced microrotational profiles of fluid.

(ii) Augmentation in viscosity parameter and volumetric fractions has declined the fluid motion in all directions.

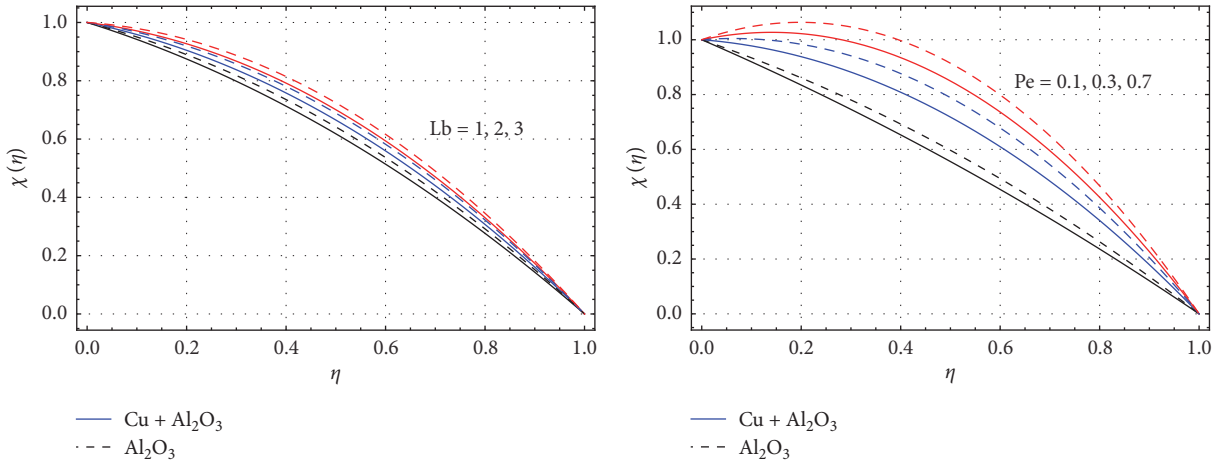

Figure 8: Variations in $\chi(\eta)$ vs. variations in Lb and Pe.

Table 2: Influence of various parameters on skin friction coefficient $-f''(0)$ at lower plate.

K_r	M	Re	$-f''(0)$ $\phi_1 = 0.01$ Nanofluid	$-f''(0)$ $\phi_1, \phi_2 = 0.01$ Hybrid nanofluid	$-f''(0)$ $\phi_1 = 0.02$ Nanofluid	$-f''(0)$ $\phi_1, \phi_2 = 0.02$ Hybrid nanofluid
0.2	0.2	0.2	0.287654	0.3276321	0.29210876	0.33522763
0.4			0.31874532	0.345218745	0.327658745	0.35410452
0.6			0.34568321	0.36543456	0.353256832	0.376426543
	0.4		0.29821087	0.31298210	0.301298210	0.320217129
	0.6		0.3082861	0.33287828	0.31728286	0.34321328
		0.4	0.42765431	0.46743276	0.435427654	0.47542674
		0.6	0.6328761	0.695423287	0.64572876	0.70251954

Table 3: Influence of nanofluid and hybrid nanofluid versus Nusselt number.

Rd	M	Du	$-\theta'(0)$ $\phi_1 = 0.01$ Nanofluid	$-\theta'(0)$ $\phi_1, \phi_2 = 0.01$ Hybrid nanofluid	$-\theta'(0)$ $\phi_1 = 0.03$ Nanofluid	$-\theta'(0)$ $\phi_1, \phi_2 = 0.03$ Hybrid nanofluid
0.2	0.2	0.4	2.46210	2.5203462	2.5421462	2.632152034
0.4			2.698210	2.7421698	2.7532698	2.852374216
0.6			2.8732102	2.94218732	2.9231873	3.103942187
	0.4		2.6732107	2.7356732	2.7724673	2.85473567
	0.6		2.68921255	2.7016892	2.8268921	2.89670168
		0.6	2.21087	2.23421087	2.3232108	2.321234210
		0.8	2.1065922	2.14108065	2.2010659	2.210141080

Table 4: Influence of nanofluid and hybrid nanofluid versus Sherwood number.

Sc	Sr	Du	E	$-\phi'(0)$ Nanofluid	$-\phi'(0)$ Hybrid nanofluid
2	1	1	1	4.63289143	4.673421
3				4.972910	5.0132097
4				5.43210	5.4929432
	2			4.762019	4.78210762
	3			4.89201	4.9432892
		2		4.983201	5.1209832
		3		5.520123	5.6321520
			2	4.103721	4.1215037
			3	3.832019	3.7323201

Table 5: Influence of nanofluid and hybrid nanofluid versus motile rate.

Lb	Pe	$-\chi'(0)$ Nanofluid	$-\chi'(0)$ Hybrid nanofluid
2	2	5.32172744	5.34322172
3		5.3673215	5.38673215
4		5.4227663	5.445227663
	3	5.465321325	5.474653213
	4	5.786635672	5.795635754

(iii) Higher values of radiation parameter, Dufour number, and volumetric fractions have augmented fluid's thermal profiles.

(iv) Concentration of fluid has retarded with upsurge in Soret number and chemical reaction parameter, whereas growth in activation factor of energy has supported the growth in concentration.

(v) Motility of microorganisms has retarded by upsurge in the values of bioconvection Lewis and Peclet numbers.

(vi) It has been noticed that when K_r, M and Re varies from 0.2 to 0.6 then in case of nanofluid, skin friction changes from 0.288 to 0.633 at $\phi_1 = 0.01$ and from 0.292 to 0.646 at $\phi_1 = 0.02$ and in case of hybrid nanofluid the variations in skin friction are from 0.328 to 0.646 at $\phi_1, \phi_2 = 0.01$ and from 0.335 to 0.703 at $\phi_1, \phi_2 = 0.02$

(vii) Numerical influence of different factor upon various physical quantities of interest has been evaluated for single and double nanoparticles. It has revealed that thermal flow rate has augmented more in case of hybrid nanofluid.

Nomenclature

u, v, w: Dimensional velocity components (m/s)
p: Dimensional pressure (Pa)
δ: Microorganism concentration number
h: Channel height (m)
K_r: Rotation parameter
T: Dimensional temperature (K)
C_p: Specific heat ($J\,kg^{-1}K^{-1}$)
Nu: Nusselt number
C_f: Skin friction coefficient
Sh: Sherwood number
η: Similarity variable
k_T: Thermal diffusion ratio
Re: Reynolds number
Du: Dufour number
Pr: Prandtl number
τ: Temperature parameter
Rd: Radiation parameter
Sr: Soret number
E: Activation energy parameter
Sc: Schmidt number
Γ: Chemical reaction parameter
Lb: Bioconvection Lewis number
Pe: Peclet number
C: Dimensional concentration (kg/m^3).

Data Availability

The data that support the findings of this study are available from the corresponding author upon reasonable request.

Conflicts of Interest

The authors declare that they have no conflicts of interest.

Acknowledgments

The authors extend their appreciation to the Deanship of Scientific Research at King Khalid University, Abha, Saudi Arabia, for funding this work through the Research Group Project under grant number (RGP.2/300/44).

References

[1] A. J. Chamkha and A. Ben-Nakhi, "MHD mixed convection–radiation interaction along a permeable surface immersed in a porous medium in the presence of Soret and Dufour's effects," *Heat and Mass Transfer*, vol. 44, pp. 845–856, 2008.

[2] G. Rasool, A. Shafiq, and D. Baleanu, "Consequences of Soret–Dufour effects, thermal radiation, and binary chemical reaction on Darcy–Forchheimer flow of nanofluids," *Symmetry*, vol. 12, no. 9, Article ID 1421, 2020.

[3] S. A. Khan, T. Hayat, M. Ijaz Khan, and A. Alsaedi, "Salient features of Dufour and Soret effect in radiative MHD flow of viscous fluid by a rotating cone with entropy generation," *International Journal of Hydrogen Energy*, vol. 45, no. 28, pp. 14552–14564, 2020.

[4] K. Vafai, A. A. Khan, G. Fatima, S. M. Sait, and R. Ellahi, "Dufour, Soret and radiation effects with magnetic dipole on Powell-Eyring fluid flow over a stretching sheet," *International Journal of Numerical Methods for Heat & Fluid Flow*, vol. 31, no. 4, pp. 1085–1103, 2020.

[5] S. A. Khan, T. Hayat, and A. Alsaedi, "Irreversibility analysis in Darcy–Forchheimer flow of viscous fluid with Dufour and Soret effects via finite difference method," *Case Studies in Thermal Engineering*, vol. 26, Article ID 101065, 2021.

[6] M. B. Hafeez, W. Sumelka, U. Nazir, H. Ahmad, and S. Askar, "Mechanism of solute and thermal characteristics in a Casson hybrid nanofluid based with ethylene glycol influenced by Soret and Dufour effects," *Energies*, vol. 14, no. 20, Article ID 6818, 2021.

[7] G. C. Layek, B. Mandal, and K. Bhattacharyya, "Dufour and Soret effects on unsteady heat and mass transfer for Powell-Eyring fluid flow over an expanding permeable sheet," *Journal of Applied and Computational Mechanics*, vol. 6, no. 4, pp. 985–998, 2020.

[8] A. S. Kotnurkar and D. C. Katagi, "Thermo-diffusion and diffusion-thermo effects on MHD third-grade nanofluid flow driven by peristaltic transport," *Arabian Journal for Science and Engineering*, vol. 45, pp. 4995–5008, 2020.

[9] S. U. S. Choi and J. A. Eastman, "Enhancing thermal conductivity of fluids with nanoparticles," in *1995*

International Mechanical Engineering Congress and Exhibition, Argonne National Lab., IL (United States), 1995.

[10] M. Sheikholeslami, M. Hatami, and D. D. Ganji, "Nanofluid flow and heat transfer in a rotating system in the presence of a magnetic field," *Journal of Molecular Liquids*, vol. 190, pp. 112–120, 2014.

[11] Z. Said, P. Sharma, N. Aslfattahi, and M. Ghodbane, "Experimental analysis of novel ionic liquid-MXene hybrid nanofluid's energy storage properties: model-prediction using modern ensemble machine learning methods," *Journal of Energy Storage*, vol. 52, Part B, Article ID 104858, 2022.

[12] P. Sharma, Z. Said, A. Kumar et al., "Recent advances in machine learning research for nanofluid-based heat transfer in renewable energy system," *Energy & Fuels*, vol. 36, no. 13, pp. 6626–6658, 2022.

[13] L. Ahmad and M. Khan, "Numerical simulation for MHD flow of Sisko nanofluid over a moving curved surface: a revised model," *Microsystem Technologies*, vol. 25, pp. 2411–2428, 2019.

[14] S. Islam, A. Khan, W. Deebani, E. Bonyah, N. A. Alreshidi, and Z. Shah, "Influences of Hall current and radiation on MHD micropolar non-Newtonian hybrid nanofluid flow between two surfaces," *AIP Advances*, vol. 10, no. 5, Article ID 055015, 2020.

[15] Z. Said, P. Sharma, R. M. Elavarasan, A. K. Tiwari, and M. K. Rathod, "Exploring the specific heat capacity of water-based hybrid nanofluids for solar energy applications: a comparative evaluation of modern ensemble machine learning techniques," *Journal of Energy Storage*, vol. 54, Article ID 105230, 2022.

[16] Y.-X. Li, M. I. Khan, R. J. Punith Gowda et al., "Dynamics of aluminum oxide and copper hybrid nanofluid in nonlinear mixed Marangoni convective flow with entropy generation: applications to renewable energy," *Chinese Journal of Physics*, vol. 73, pp. 275–287, 2021.

[17] Z. Said, P. Sharma, A. K. Tiwari et al., "Application of novel framework based on ensemble boosted regression trees and Gaussian process regression in modelling thermal performance of small-scale Organic Rankine Cycle (ORC) using hybrid nanofluid," *Journal of Cleaner Production*, vol. 360, Article ID 132194, 2022.

[18] G. I. Taylor, "Experiments with rotating fluids," *Proceedings of the Royal Society of London. Series A, Containing Papers of a Mathematical and Physical Character*, vol. 100, no. 703, pp. 114–121, 1921.

[19] H. P. Greenspan, *The Theory of Rotating Fluids*, CUP Archive, 1968.

[20] M. Turkyilmazoglu, "Fluid flow and heat transfer over a rotating and vertically moving disk," *Physics of Fluids*, vol. 30, no. 6, Article ID 063605, 2018.

[21] L. K. Forbes, "Steady flow of a Reiner–Rivlin fluid between rotating plates," *Physics of Fluids*, vol. 30, no. 10, Article ID 103104, 2018.

[22] A. S. Dogonchi, D. D. Ganji, and O. D. Makinde, "Impact of stretching and penetration of walls on nanofluid flow and heat transfer in a rotating system," *Defect and Diffusion Forum*, vol. 387, pp. 37–50, 2018.

[23] S. Muhammad, S. I. A. Shah, G. Ali, M. Ishaq, S. A. Hussain, and H. Ullah, "Squeezing nanofluid flow between two parallel plates under the influence of MHD and thermal radiation," *Asian Research Journal of Mathematics*, vol. 10, no. 1, pp. 1–20, 2018.

[24] T. Salahuddin, M. Arshad, N. Siddique, and I. Tlili, "Change in internal energy of viscoelastic fluid flow between two rotating parallel plates having variable fluid properties," *Indian Journal of Physics*, vol. 95, pp. 1801–1811, 2021.

[25] A. R. Bestman, "Natural convection boundary layer with suction and mass transfer in a porous medium," *International Journal of Energy Research*, vol. 14, no. 4, pp. 389–396, 1990.

[26] N. S. Khan, P. Kumam, and P. Thounthong, "Second law analysis with effects of Arrhenius activation energy and binary chemical reaction on nanofluid flow," *Scientific Reports*, vol. 10, Article ID 1226, 2020.

[27] M. M. Bhatti and E. E. Michaelides, "Study of Arrhenius activation energy on the thermo-bioconvection nanofluid flow over a Riga plate," *Journal of Thermal Analysis and Calorimetry*, vol. 143, pp. 2029–2038, 2021.

[28] A. Khan, A. Saeed, A. Tassaddiq et al., "Bio-convective micropolar nanofluid flow over thin moving needle subject to Arrhenius activation energy, viscous dissipation and binary chemical reaction," *Case Studies in Thermal Engineering*, vol. 25, Article ID 100989, 2021.

[29] T. Muhammad, H. Waqas, S. A. Khan, R. Ellahi, and S. M. Sait, "Significance of nonlinear thermal radiation in 3D Eyring-Powell nanofluid flow with Arrhenius activation energy," *Journal of Thermal Analysis and Calorimetry*, vol. 143, pp. 929–944, 2021.

[30] M. Asma, W. A. M. Othman, and T. Muhammad, "Numerical study for Darcy–Forchheimer flow of nanofluid due to a rotating disk with binary chemical reaction and Arrhenius activation energy," *Mathematics*, vol. 7, no. 10, Article ID 921, 2019.

[31] R. Kumar, A. Bhattacharyya, G. S. Seth, and A. J. Chamkha, "Transportation of magnetite nanofluid flow and heat transfer over a rotating porous disk with Arrhenius activation energy: fourth order Noumerov's method," *Chinese Journal of Physics*, vol. 69, pp. 172–185, 2021.

[32] B. Ali, P. K. Pattnaik, R. A. Naqvi, H. Waqas, and S. Hussain, "Brownian motion and thermophoresis effects on bioconvection of rotating Maxwell nanofluid over a Riga plate with Arrhenius activation energy and Cattaneo–Christov heat flux theory," *Thermal Science and Engineering Progress*, vol. 23, Article ID 100863, 2021.

[33] D. U. Sarwe, B. Shanker, R. Mishra, R. S. Varun Kumar, and M. R. Raja Shekar, "Simultaneous impact of magnetic and Arrhenius activation energy on the flow of Casson hybrid nanofluid over a vertically moving plate," *International Journal of Thermofluid Science and Technology*, vol. 8, no. 2, Article ID 080202, 2021.

[34] S. A. Shehzad, T. Hayat, M. S. Alhuthali, and S. Asghar, "MHD three-dimensional flow of Jeffrey fluid with Newtonian heating," *Journal of Central South University*, vol. 21, pp. 1428–1433, 2014.

[35] L. Ahmad, S. Javed, M. I. Khan, M. Riaz Khan, E. R. El-Zahar, and A. A. A. Mousa, "Non-axisymmetric Homann stagnation-point flow of unsteady Walter's B nanofluid over a vertical cylindrical disk," *Proceedings of the Institution of Mechanical Engineers, Part E: Journal of Process Mechanical Engineering*, 2022.

[36] M. Usman, T. Gul, A. Khan, A. Alsubie, and M. Z. Ullah, "Electromagnetic couple stress film flow of hybrid nanofluid over an unsteady rotating disc," *International Communications in Heat and Mass Transfer*, vol. 127, Article ID 105562, 2021.

[37] L. Ahmad and M. Khan, "Importance of activation energy in development of chemical covalent bonding in flow of Sisko magneto-nanofluids over a porous moving curved surface,"

International Journal of Hydrogen Energy, vol. 44, no. 21, pp. 10197–10206, 2019.

[38] L. Ahmad, A. Munir, and M. Khan, "Locally non-similar and thermally radiative Sisko fluid flow with magnetic and Joule heating effects," *Journal of Magnetism and Magnetic Materials*, vol. 487, Article ID 165284, 2019.

[39] W. N. Mutuku and O. D. Makinde, "Hydromagnetic bioconvection of nanofluid over a permeable vertical plate due to gyrotactic microorganisms," *Computers & Fluids*, vol. 95, pp. 88–97, 2014.

[40] Z. Shah, S. Islam, T. Gul, E. Bonyah, and M. A. Khan, "The electrical MHD and Hall current impact on micropolar nanofluid flow between rotating parallel plates," *Results in Physics*, vol. 9, pp. 1201–1214, 2018.

[41] H. A. Attia and N. A. Kotb, "MHD flow between two parallel plates with heat transfer," *Acta Mechanica*, vol. 117, pp. 215–220, 1996.

[42] M. Sheikholeslami and D. D. Ganji, "Three dimensional heat and mass transfer in a rotating system using nanofluid," *Powder Technology*, vol. 253, pp. 789–796, 2014.

[43] M. Hatami, J. Hatami, and D. D. Ganji, "Computer simulation of MHD blood conveying gold nanoparticles as a third grade non-Newtonian nanofluid in a hollow porous vessel," *Computer Methods and Programs in Biomedicine*, vol. 113, no. 2, pp. 632–641, 2014.

[44] C. Zhang, L. Zheng, X. Zhang, and G. Chen, "MHD flow and radiation heat transfer of nanofluids in porous media with variable surface heat flux and chemical reaction," *Applied Mathematical Modelling*, vol. 39, no. 1, pp. 165–181, 2015.

[45] S.-J. Liao, "An explicit, totally analytic approximate solution for Blasius' viscous flow problems," *International Journal of Non-Linear Mechanics*, vol. 34, no. 4, pp. 759–778, 1999.

[46] S. Liao, "An optimal homotopy-analysis approach for strongly nonlinear differential equations," *Communications in Nonlinear Science and Numerical Simulation*, vol. 15, no. 8, pp. 2003–2016, 2010.

Hindawi
Journal of Nanomaterials
Volume 2022, Article ID 7158228, 12 pages
https://doi.org/10.1155/2022/7158228

Research Article

Study on Sintered Wick Heat Pipe (SWHP) with CuO Nanofluids under Different Orientation

P. Manoj Kumar,[1] **Rajasekaran Saminathan**,[2] **Mohammed Tharwan**,[2] **Haitham Hadidi**,[2] **P. Michael Joseph Stalin**,[3] **G. Kumaresan**,[4] **S. Ram**,[5] **Moti Lal Rinawa**,[6] **P. T. Saravanakumar**,[7] **K. Karthikeyan**,[8] **and Dawit Tafesse Gebreyohannes**[9]

[1]*Department of Mechanical Engineering, KPR Institute of Engineering and Technology, Coimbatore, 641407 Tamil Nadu, India*
[2]*Department of Mechanical Engineering, College of Engineering, Jazan University, Saudi Arabia*
[3]*Department of Mechanical Engineering, Audisankara College of Engineering & Technology, Gudur, 524101 Andhra Pradesh, India*
[4]*Department of Mechanical Engineering, Bannari Amman Institute of Technology, Sathyamangalam, 638401 Tamil Nadu, India*
[5]*Department of Mechanical Engineering, Gokaraju Rangaraju Institute of Engineering and Technology, Hyderabad, 500090 Telangana, India*
[6]*Department of Mechanical Engineering, Government Engineering College, Jhalawar, Rajasthan 326023, India*
[7]*Department of Mechatronics Engineering, Hindusthan College of Engineering and Technology, Coimbatore, 641032 Tamil Nadu, India*
[8]*Department of Mechanical Engineering, Sri Ramakrishna Engineering College, Coimbatore, 641022 Tamil Nadu, India*
[9]*Department of Mechanical Engineering, Faculty of Manufacturing, Institute of Technology, Hawassa University, Hawassa, Ethiopia*

Correspondence should be addressed to Dawit Tafesse Gebreyohannes; dawitt@hu.edu.et

Received 28 March 2022; Revised 4 July 2022; Accepted 8 August 2022; Published 25 August 2022

Academic Editor: Zafar Said

The current work investigates the performance of cylindrical-shaped sintered wick heat pipe at different orientations, numerically. The results are compared and validated with the experimental findings. The study is extended by using a nanofluid (comprising nano-Curo in deionized water) as a working fluid and the thermal performance of heat pipe with deionized (DI) water has been compared with that of heat pipe with nanofluid (containing various concentrations of CuO nanoparticles in DI water). During the investigation, the nanofluid with 1.0 weight fraction of CuO nanopaticles found to be optimum, which has produced the better results. The numerical analysis has been carried out to study the temperature difference, fluid velocity, and pressure drop of the sintered wick heat pipe using the commercial CFD software, Ansys Fluent R14.5. The computational results are observed to be much closer to the experimental data, and the vapor velocity at the heat pipe's core has been determined to be 64.54% higher than the liquid flow over the wick structure. Interestingly, the heat pipe pressure drop has been reduced by adding CuO nanoparticles to the working fluid. Finally, the heat pipe loaded with a 1.0% concentration of nano-CuO in nanofluid has exhibited a notable reduction in pressure drop of 35.33%.

1. Introduction

The nanofluids are the recently developed fluids, which can be considered the sustainable medium of heat transfer applications. They are also called as the heat transfer fluids for the next generation [1, 2]. The majority of industries are being forced to implement Industry 4.0 to enhance the production rate and to improve the quality of their products. The

equipment used in industries is integrated with the Internet of Things and machine learning technologies [3]. Implementing new ideas will increase plant efficiency; meanwhile, the size and weight of the equipment will also increase. Electronics-based industries are inevitable, which are facing a lot of challenges and undergoing day-by-day changes to compete with the markets in the present and future [4]. The heat pipe works as a superconductor, which has more than 100 times higher thermal conductivity comparing to the copper rod. Owing to their high conductance, these are preferred in lab tops, high-end computers, microprocessors, and solar systems. In IBM computers and workstations, the higher-end processors are producing more heat; the dissipation of the heat from the confined spaces is difficult with conventional sources like blowers. Due to deprived heat removal rate, the CPU's temperature may rise abruptly, which can cause a permanent damage.

The heat management in electronic devices has become complicated because the size reduction and productivity improvement generate high heat flux, which produces mechanical failures in the system or part of the device. Another study [5] analyzed the effectiveness of mesh wick heat pipes filled with CuO nanoparticles based on deionized water. The heat pipe capacity is enhanced by about 31.5% by the delayed dry-out condition. Adham Makki et al. [6] investigated a solar photovoltaic-thermoelectric generator system based on heat pipes. A theoretical model was made, and the performance of the PV cell was improved by putting together PV and TEC parts.

The thermal efficacy of the copper cylindrical heat pipe (HP) using alumina suspended DI water was studied [7]. The efficacy of the HP increased by 16.8% comparing to the base fluid. Yunhua Gan et al. [8] premeditated the heat management of battery packs using cylindrical cell-based heat pipes. A mathematical model had been formed to analyze the distinct achievement of the battery cells and the outcomes had been validated by comparing them with experimental results. They concluded that the upsurge in the length of the heat dissipation section and aluminum sleeves improved the thermal capacity of the system. Wisoot Sanhan et al. [9] experimented with the thermal analysis of the flattened heat pipe with a double heat source to cool the condenser section effectively from the CPU and GPU in laptops. The results indicated that the flat-shaped heat pipe from the circular section reduces the heat resistance by 5.2%. Hassan and Harmand analyzed [10] the effect of a flat-shaped heat pipe which is used to cool the electronic components. A numerical approach was carried out, because the impact of various permeability of the wick structure would be time consuming to attain with the experimental analysis. They revealed that increasing the permeability of the wick structure could lead to a 19.0% drop in heat pipe surface temperature and pressure. Samiya Amir et al. [11] steered a numerical study on solar photovoltaic panels to analyze the capability of heat pipes to remove excessive heat. The incorporation of heat pipes into PV cells attains a temperature reduction of 9°C as compared to the normal panels. Another numerical study [12] was conducted on a U-shaped pulsating heat pipe. The increase in evaporator side temperature shows a uni-directional effect and increases convection as well as boiling heat transfer.

Kumaresan et al. [13] characterized the function of heat pipes by altering the wick structures. They have used sintered, mesh, and sintered-mesh wicks in cylindrical heat pipes. The heat transport capability of the device has increased by about 18.75% as sintered wick structure compared with mesh wicks. Miao et al. [14] identified phase change heat transfer as the best method to transfer high heat flux with minimal losses; a bent copper heat pipe was used in the investigation. The copper-water heat pipe's critical heat flux has been enhanced, and when the working temperature is above 50°C, the increasing slap was obtained. The feasible analysis of sintered copper heat pipes was studied [15] and the notable changes in the distribution of temperature with respect to the axial distance in the heat pipe, and characteristics limits are evaluated. When the bend angle of the copper heat pipe is raised, the thermal efficacy of the HP is seen to be lowered. Jing et al. [16] explored the capacity and transport limitations of the HP by varying the wick structure's permeability. The capillary limitation is measured in the way of accounting for the capillary pressure, porosity, and permeability of the heat pipe. The results proved that the irregular powder surface of the sintered wick structure reduces 30% of the capillary pressure compared with spherical-shaped powders.

A study was conducted on the heat pipe porous wick structure by Hui Li et al. [17]. The authors confirmed that the capillary limitation of the heat pipe is directly influenced because of the particle size of the powder used to prepare the wick structure. Jafari et al. [18] analyzed the thermal characteristics of additively manufactured wick for heat pipes. The wick structure is manufactured with a multi-scale sintered powder that improves the properties of the wick structure. The flat heat pipe's thermal efficacy had been improved, when it was occupied with 110% of working fluid. Vijayakumar et al. [19] used CuO and alumina nanoparticles in the sintered wick HP to improve the convection heat transmission properties and permeability of the HP. The author found the optimum concentration achieved for CuO nanoparticles at 1.0 wt%. The optimum results were obtained for both CuO- and alumina-based heat pipes at a 45° inclination angle. The thermal characteristics at the evaporator as well as condenser regions had been increased to 32.90% and 24.51%, respectively, at the optimum tilt angle. Brautsch and Kew [20] used different kinds of mesh wicks in the HP. The outcomes confirmed the number of layers wounded in the tube could develop the heat pipe's effectiveness.

As of now, the literature does not justify the impact of porosity and permeability of the wick structure on the thermal performance enhancement of the HP. Ich-Long Ngo and Chan Byon [21] numerically investigated the performance of sintered wick heat pipes measuring their porosity and permeability. They proved that the permeability of microporous inverse wicks produces high performance depending on the wick configuration and porosity. Shiwei Zhang et al. [22] analyzed the capillarity characteristics of sintered powder-based wicks in stainless steel heat pipes. The authors experimentally measured the permeability and porosity of irregular- and regular-sized particles. The irregular-sized particles had proved a better permeability in

terms of 1.5–4.8 factors. The hybrid nanofluids are another variety of heat transfer mediums with a wide range of uses, including electronic cooling, IC engine cooling, heat pipes, and heat exchangers, coolants in welding and machining, nuclear facilities, and many more. Bumataria et al. [23] premeditated the use of heat pipes with the presence of different nanoparticle combinations with the base fluids. The nanofluids containing CuO as well as ZnO nanoparticles and their hybrid mixture in 25 : 75, 50 : 50, and 25 : 75 mass ratios had been chosen by Bumataria et al. [24] while preparing aqueous nanofluids with 1.0 wt. percent of aforementioned nanoparticle combinations. In a copper heat pipe with a straight tube shape, a two-phase heat transfer study had been accomplished using 60% of the evaporator volume to fill the working fluid. The heat input was adjusted from 60 W to 160 W, and the tilt was accustomed from 0° to 90° in 15° and 20 W steps. The hybrid nanofluid comprising nanoparticles of CuO and ZnO (75 : 25) in water demonstrated the least increase in thermal resistance compared to base fluid. The authors speculated that individual nanostructures in the base medium might have induced a synergistic impact, which would have demonstrated the hybrid's improved behavior. At 60° inclination angle and a 160 W heat input, the nanofluids have performed in a better manner comparing to other tilt angles and heat inputs. A cylinder-shaped heat pipe with a copper screen mesh type of wick structure was explored by another literature [25] and its construction was improved by utilizing the investigational data for nanofluids. The base fluid had been mixed with Al_2O_3, CuO, and ZnO nanoparticles at a concentration of 1.0 wt percent. The experimental results were compared, particularly in terms of heat load (in a range of 60-160 W with 20 W incremental steps) and inclination angle (in a range of 0° to 90° with 15° incremental steps). The results ascertained that the nanofluids with CuO nanoparticles displayed a better thermal enhancement comparing to other working fluid at the inclination of 60°.

The extensive review on the published literature revealed that the incorporation of sintered wicks with regular-sized particles could increase strength and durability of the wicks; however, the effect of such particles on the permeability characteristics and performance of the HP wick had not been properly dealt. The use of sintered wick in heat pipes proved to have the greatest influence on the capillary action of the working medium. The novelty of the present work is that it has proposed and experimented the application of irregular-sized copper particles to produce non-uniform pores in the sintered wick structure for enhancing the permeability as well as performance of the heat pipe, which was not adequately addressed in the literature. The numerical analysis of the sintered wick heat pipe has also been performed and the obtained results are validated by comparing them with the experimental results. Further, the investigation has been extended with the aid of nanofluid containing different weight fraction of nano-CuO particles within the heat pipe as working medium and the optimum operating condition and orientation angle are explored.

2. Properties of CuO nanofluid

The CuO nanoparticle (97.5% pure) is a commercial product of Alfa Aesar, USA. However, CuO nanoparticles are allowed for a high-energy ball milling process, which is operated at a 1200 rpm speed to uniform its size. The ball to particle ratio is chosen as 5.21 and the process is extended to a 12-hour period. After the process, the size of nanoparticles is confirmed using HRTEM characterization. Thereafter, the crushed copper (II) oxide nanoparticles are suspended in 250 ml of DI water and taken in a flask. The ultrasonicated (duration of one hour) solution is brought into the stability analysis. This fluid is kept statically for two months. During this period of time, no particles settle, and it confirms that the prepared solution is stable.

The dimension and morphology of the nanoparticles show a major impact on the thermophysical properties of prepared nanofluids [26]. The particles that are larger than 100 nm could be easily settled in the prepared solution, and irregular-shaped nanoparticles may affect the fluid flow properties [27]. Figure 1 reports the HRTEM of nano-CuO particles used in this study. The report confirms the size of the nanoparticles is around 40 nm and fully spherical-shaped nanoparticles are suspended in the fluid to improve the Brownian motion and viscosity of the nanofluid. Figure 1 attests to the size and shape of CuO nanoparticles used in this study.

3. Experimental Facility

The experimental test facility is created using calibrated instruments and the layout setup given in Figure 2. Copper element is selected as pipe wall material, sintered wick powder, and nanoparticles in this study because it is having highest thermal conductivity value in the metal segment, as well as flexible for fabrication. The outer surface and inner core temperature, volume flow rate of cooling water supplied for the condensation process, and heat distributed to the ceramic heater are measured. The heat pipe test section is coupled with ten T-type thermocouples. Five of each thermocouple are fixed at the outer surface and inner core of the HP. A refrigerant-based temperature control unit is attached to the experimentation, used to remain the cooling water entry temperature to the condenser section. An AC power variac controls the electric power supply to the ceramic heater, which confirms the correct heat input at the primary part of the HP. A digital logger is used to examine the steady-state values from the investigations. The experimentation was conducted under atmospheric conditions, i.e., 1 bar pressure and a 27°C temperature. The observations are made at steady-state conditions. Approximately 45 minutes duration is maintained between each measurement.

4. Uncertainty Results

The uncertainty involved in the experimental work is evaluated based on Holman [28]. The surface temperature and mass flow rate of cooling water are the derivatives measured during the experimentation. The uncertainty of experimental values has been determined and given in Table 1.

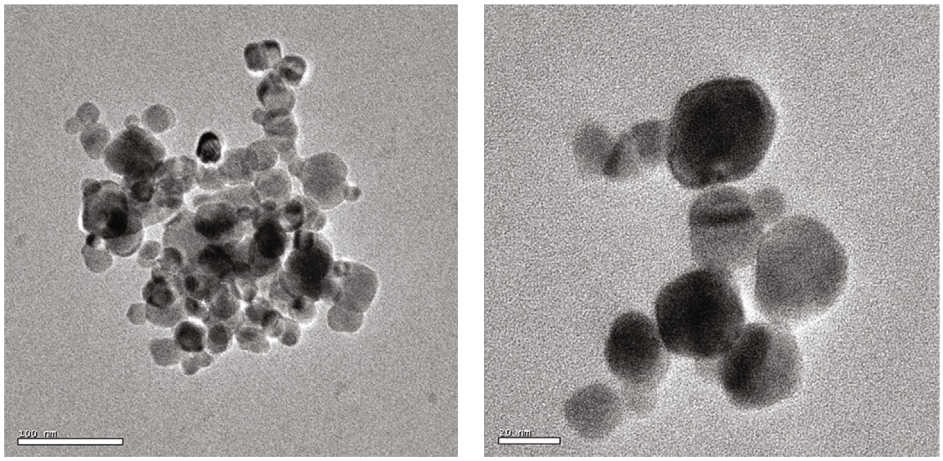

(a) (b)

Figure 1: High-resolution TEM images of CuO nanoparticles with (a) 100 nm and (b) 20 nm magnification.

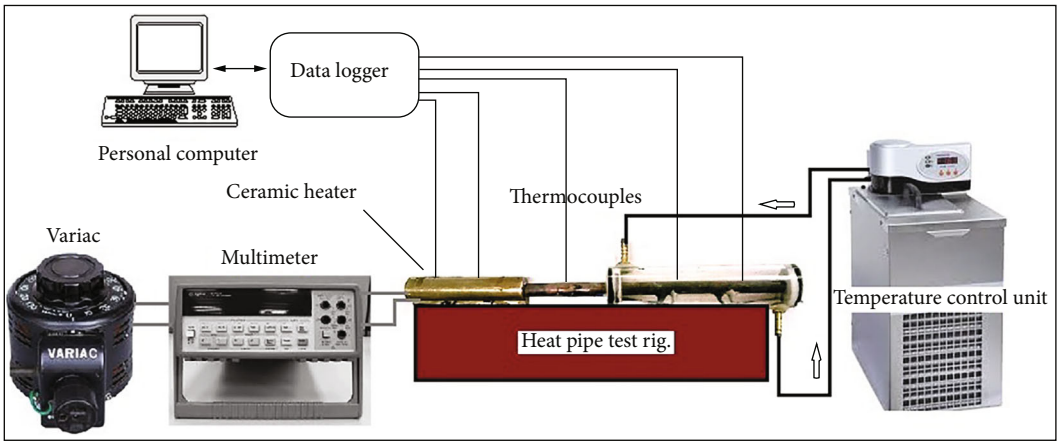

Figure 2: Schematic layout of experimental test rig.

Table 1: Uncertainty of the quantities.

S. No	Quantity	Uncertainty (%)
1.	Heat input	0.329
2.	Temperature difference	0.12
3.	Thermal resistance	1.716

5. Numerical Procedure

Experimental investigations of engineering problems are essential in order to know the physical phenomena of the problem. Moreover, solution accuracy and reliability are also high in the experimental study. However, it has a few limitations, such as high cost, more time, equipment cost, and maintaining steady-state conditions and operating parameters. Under these circumstances, numerical analysis comes in handy [11]. In this study, a two-dimensional numerical analysis was performed using the commercial CFD software ANSYS FLUENT R 14.5. The CFD results were verified by the experimental results. Further, the application of CFD is rapidly expanding with the growth in computational resources. The verification is helpful in identifying and quantifying the errors in modeling and the solution. The accuracy of the numerical analysis is affected by the assumptions made in the boundary conditions applied and the errors like discretization, truncation, and rounding off. In the current investigation, a numerical approach was performed for the copper sintered HP to easily tackle the design complications of two-phase heat transfer, liquid state fluid flow through the wick structure, the interface between the gaseous, and liquid regions.

The geometrical dimensions of the HP used in the experimental investigations are shown in Table 2. A chemically cleaned copper pipe was selected to fabricate the HP with the outer section and a copper powder-based sintered wick with a 1 mm thickness is the wick structure of the heat pipe. Sintered wick with a thickness and porosity of 1 mm and 0.48, respectively, are considered. Because of symmetry about the axis, only half of the section was taken in the analysis. In this work, the grid dependence test was conducted in

Table 2: Specifications of sintered wick heat pipe.

Sl. No	Description	Value
1.	Heat pipe material	Copper
2.	Total length	330 mm
3.	Evaporator length	100 mm
4.	A diabatic length	80 mm
5.	Condenser length	150 mm
6.	Outer diameter	12 mm
7.	Wick material	Copper
8.	Wick thickness	1 mm
9.	Wick type	Sintered wick
10.	Quantity of working fluid	7.3 ml
11.	Working pressure	13.45 kPa

order to ensure the optimized number of grids and size. For this test, the heat pipe's surface temperature was measured. Its values were compared to three different grid sizes and a grid size of 112 x 86 gave a surface temperature value closer to the experimental value and was taken as the optimum.

6. Boundary Conditions

The following assumptions were made in the numerical analysis of the heat pipe [12].

(i) Laminar and incompressible liquid flows

(ii) At $t = 0$ (time), the vapor was saturated

(iii) All of the thermophysical properties of CuO nanofluid/DI water are assumed to stay the same throughout the experiment, except for the vapor flow density, which is calculated based on the pressure at a certain point

(iv) Except for the evaporator and condenser units, the entire heat pipe region has been insulated

(v) The heat pipe saturation temperature was estimated at each location depending on the local pressure

The working fluid, i.e. 1.0% weight concentration of CuO nanofluid/deionized water, is considered in the surface area of the wick structure and the gaseous state in the central core area of the HP. When heat is given in the evaporator region, the CuO nanofluid/DI water gets vaporized and is converted to a gaseous state, and the vapor travels to the condenser region. The vapor reaches the cooling side at the opposite end of the HP. It follows the wick surfaces back to the starting point of the heat pipe.

7. Governing Equations

The fundamental principles governing liquid/vapor flow and heat density variation are mathematically formulated using the PDE (partial differential equation) equation. When the Reynolds number for the vapor flow was in the range of 50 to 500, the laminar flow was taken. Also, when the temperature varies with time at a point, the problem is called unsteady.

7.1. Vapor Flow Region. Continuity equation:

$$\frac{\partial \rho_v}{\partial t} + \frac{1}{r}\frac{\partial}{\partial r}(\rho_v r V_v) + \frac{\partial}{\partial z}(\rho_v W_v) = 0. \tag{1}$$

Momentum equation:
R-momentum

$$\rho_v\left[\frac{\partial V_v}{\partial t} + V_v\frac{\partial V_v}{\partial r} + W_v\frac{\partial V_v}{\partial z}\right] = -\frac{\partial p_v}{\partial r} + \mu_v\left[\frac{\partial^2 V_v}{\partial z^2} + \frac{4}{3r}\frac{\partial}{\partial r}\left(r\frac{\partial V_v}{\partial r}\right) + \frac{1}{3}\frac{\partial^2 W_v}{\partial z \partial r} - \frac{4}{3}\frac{V_v}{r^2}\right]. \tag{2}$$

Z-momentum

$$\rho_v\left[\frac{\partial W_v}{\partial t} + V_v\frac{\partial W_v}{\partial r} + W_v\frac{\partial W_v}{\partial z}\right] = -\frac{\partial p_v}{\partial z} + \mu_v\left[\frac{4}{3}\frac{\partial^2 W_v}{\partial z^2} + \frac{1}{r}\frac{\partial}{\partial r}\left(r\frac{\partial W_v}{\partial r}\right) + \frac{1}{r}\frac{\partial}{\partial r}\left(r\frac{\partial V_v}{\partial z}\right) - \frac{2}{3}\frac{\partial}{\partial z}\left[\frac{1}{r}\frac{\partial}{\partial r}(rV_v)\right]\right]. \tag{3}$$

Energy equation

$$\rho_v C_{pv}\left[\frac{\partial T_v}{\partial t} + V_v\frac{\partial T_v}{\partial r} + W_v\frac{\partial T_v}{\partial z}\right] = k_v\frac{1}{r}\frac{\partial}{\partial r}\left(r\frac{\partial T_v}{\partial r}\right) + \frac{\partial^2 T_v}{\partial z^2} + V_v\frac{\partial p}{\partial r} + W_v\frac{\partial p}{\partial z} + \mu_v\varphi, \tag{4}$$

where φ = dissipation rate, given by

$$\varphi = Z\left[\frac{\partial V_v}{\partial r} + \left(\frac{V_v}{r}\right)^2 + \left(\frac{\partial W_v}{\partial z}\right)^2\right] + \left[\frac{\partial V_v}{\partial z} + \left(\frac{\partial W_v}{\partial r}\right)^2\right] - \frac{2}{3}\left[\frac{1}{r}\frac{\partial}{\partial r}(rV_v) + \left(\frac{\partial W_v}{\partial r}\right)^2\right]. \tag{5}$$

7.2. CuO Nanofluid/DI Water Region. The working fluid passes by capillary action and is primarily influenced by the flow through a porous material. Porosity and permeability are the important parameters that decide the capillary function of the wick structure. The experimentally measured values of the copper sintered wick structure were used in this analysis [29]. The CuO nanofluid/DI water flow is assumed as an incompressible medium. The viscosity between the layers is high (laminar) and unsteady flow conditions.

Continuity equation:

$$\frac{1}{r}\frac{\partial}{\partial r}(rV_l) + \frac{\partial W_l}{\partial z} = 0. \tag{6}$$

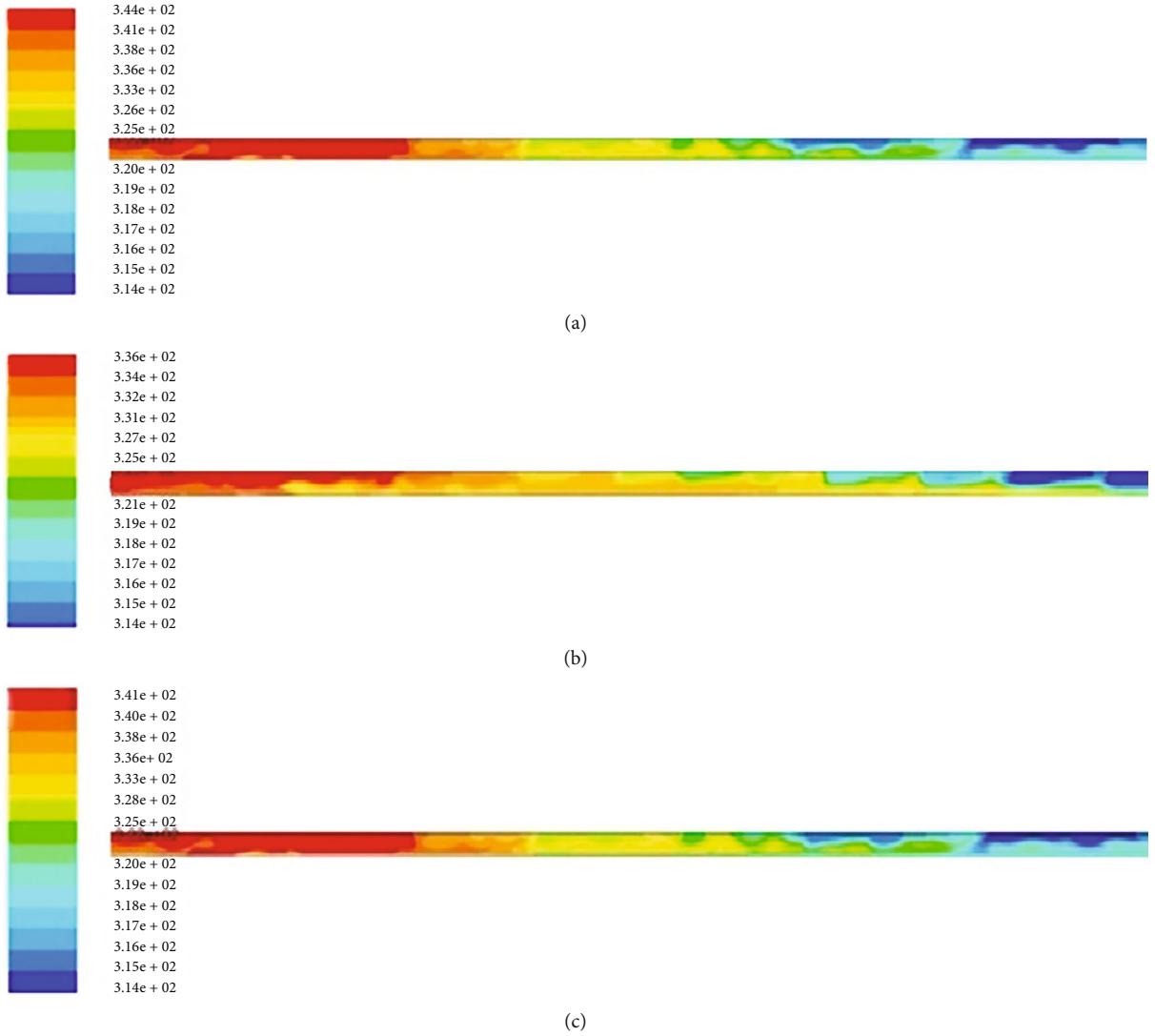

Figure 3: Surface temperature distribution (in Kelvin) over the length of heat pipe with DI water for various tilt angles: (a) 0°, (b) 45°, and (c) 90°.

R-momentum

$$\frac{1}{\varepsilon}\left[\frac{\partial V_l}{\partial t}+\frac{1}{\varepsilon}\left(V_l\frac{\partial V_l}{\partial r}+W_l\frac{\partial V_l}{\partial z}\right)\right]=-\frac{1}{P_l}\frac{\partial P_l}{\partial r}-\frac{\mu_l V_l}{P_l k_l}+\frac{\mu_l}{P_l\varepsilon}\left[\frac{\partial^2 V_l}{\partial z^2}+\frac{1}{r}\frac{\partial}{\partial r}\left(r\frac{\partial V_l}{\partial r}\right)-\frac{V_l}{r^2}\right], \tag{7}$$

where ε is the wick porosity.

Z-momentum

$$\frac{1}{\varepsilon}\left[\frac{\partial W_l}{\partial t}+\frac{1}{\varepsilon}\left(V_l\frac{\partial W_l}{\partial r}+W_l\frac{\partial W_l}{\partial z}\right)\right]=-\frac{1}{P_l}\frac{\partial P_l}{\partial z}-\frac{\mu_l W_l}{P_l k_l}+\frac{\mu_l}{P_l\varepsilon}\left[\frac{\partial^2 W_l}{\partial z^2}+\frac{1}{r}\frac{\partial}{\partial r}\left(r\frac{\partial W_l}{\partial r}\right)\right]. \tag{8}$$

Energy equation

$$\rho_l C_{pl}\left[\frac{\partial T_l}{\partial t}+V_l\frac{\partial T_l}{\partial r}+W_l\frac{\partial T_l}{\partial z}\right]=\frac{1}{r}\frac{\partial}{\partial r}\left(rk_{\text{eff}}\frac{\partial T_l}{\partial r}\right)+\frac{\partial}{\partial z}\left(k_{\text{eff}}\frac{\partial T_l}{\partial z}\right), \tag{9}$$

where, the effective thermal conductivity, k_{eff} is given by

$$K_{\text{eff}}=\frac{K_l[(K_l+K_s)-(1-\varepsilon)(K_l-K_s)]}{(K_l+K_s)+(1-\varepsilon)(K_l-K_s)}. \tag{10}$$

7.3. Heat Pipe Wall Region.

$$\rho_w C_{pw}\frac{\partial T_w}{\partial t}=k_w\left[\frac{1}{r}\frac{\partial}{\partial r}\left(r\frac{\partial T_w}{\partial r}\right)+\frac{\partial^2 T_w}{\partial z^2}\right]. \tag{11}$$

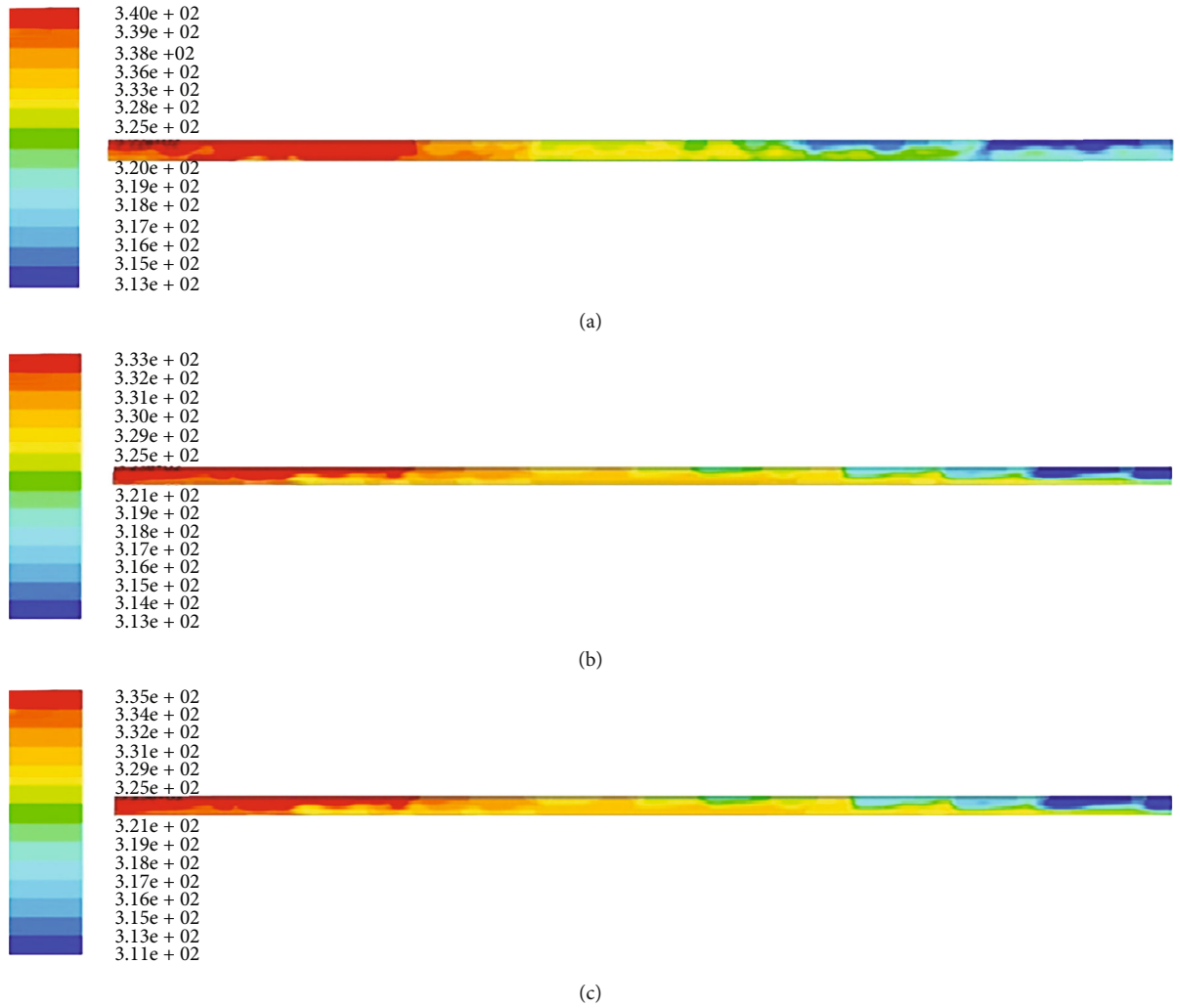

FIGURE 4: Surface temperature distribution (in Kelvin) over the length of the heat pipe with 1.0 wt.% of CuO/DI water nanofluid for various tilt angles: (a) 0°, (b) 45°, and (c) 90°.

8. Results and Discussion

A numerical analysis has been carried out to study the temperature difference, fluid velocity, and pressure reduction in the sintered wick HP using the commercial CFD software Ansys Fluent R14.5. The surface and vapor core temperatures of the SWHP are continuously monitored using a personnel computer followed by a high-accuracy data acquisition system. After that, numerical results are validated by comparing them with experimental values.

8.1. Temperature Distribution. The outer side temperature for SWHP with deionized water and a 1.0% weight concentration of CuO-based nanofluid is seen in Figures 3(a)–3(c) and 4(a)–4(c). In these conditions, 300 K and 13.45 kPa are considered to represent the starting temperatures and pressures, respectively. All the temperature contours are plotted at 100 W of heat input. The analysis was conducted for the varying tilt angles of 0, 45, and 90°. The outside temperature of the heating region is drastically higher than the vapor passage temperature. The temperature difference between the evaporator and condenser regions is approximately 30°C, as observed for deionized water heat pipes in a parallel orientation. The distribution of temperature decreased during the tilted condition of HP, because of the lower thermal resistance at the tilted position.

The surface temperature is considerably decreased when the HP has been angled to a 45°. The temperature distribution follows the same trend as that of the horizontal position, but a significant decrease has been noticed. This is because the leaning of the HP increases the capillary function, which makes the return of the condensate to the evaporator section easy. However, the performance deteriorates once the heat pipe has been tilted to 90°, For 0°, 45°, and 90°, the thermal gradient between the heating and cooling region is 30°C, 23°C, and 27°C, respectively. The larger inclination angle helps to enhance rate of return of working fluid from the cooling region.

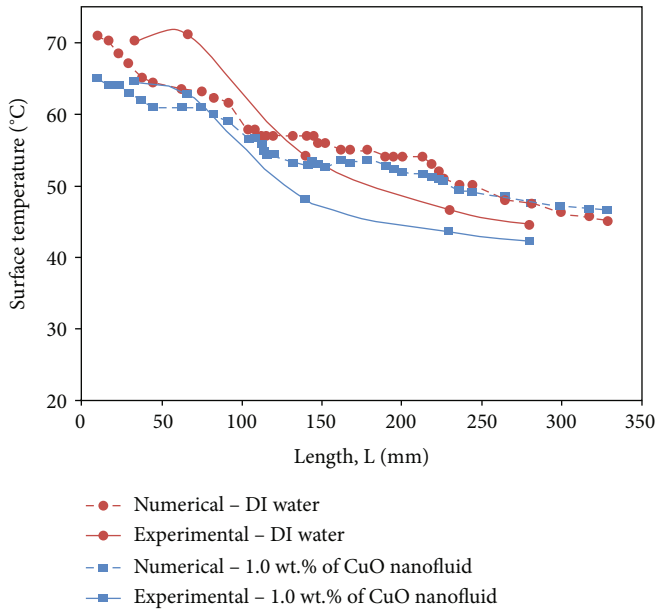

Figure 5: Surface temperature distributions (in Kelvin) along its length for a tilt angle of 45°.

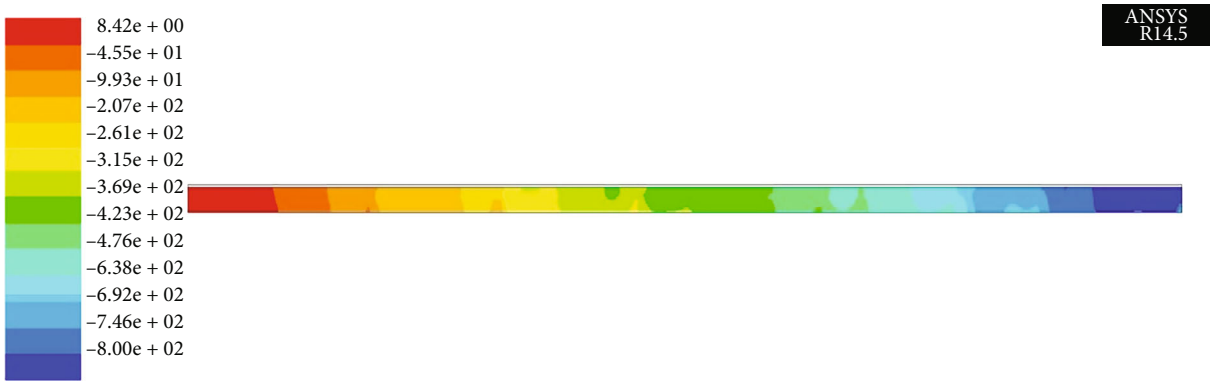

Figure 6: Pressure contour (in Pa) of the heat pipe along with its axial length for DI water.

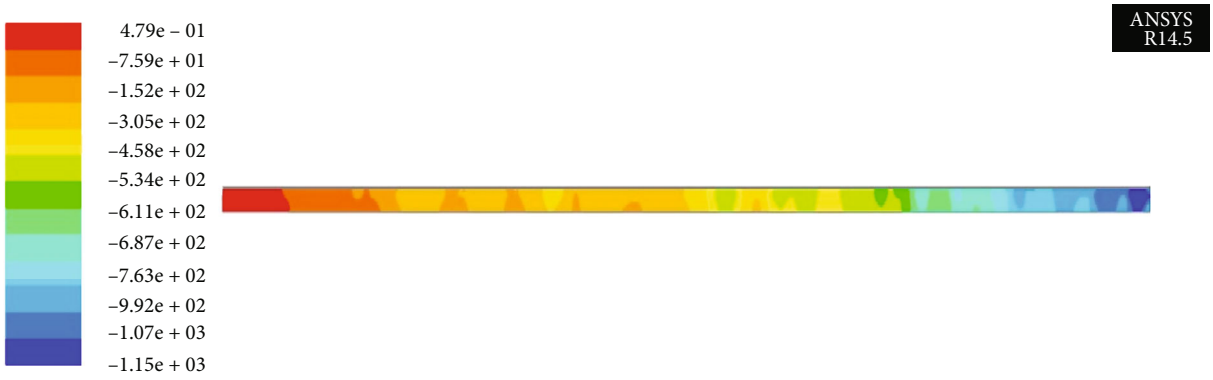

Figure 7: Pressure contour of the heat pipe along its axial length for CuO nanofluid with 1.0 wt.%.

The liquid film formation at the condenser part may also affect the heat removal rate. Hence, the surface temperature increases for the heat pipe at the vertical position.

The spherical-shaped, 40 nm (preferably small in size) CuO nanoparticles improved the thermal as well as fluid flow properties of the working medium. The heat-

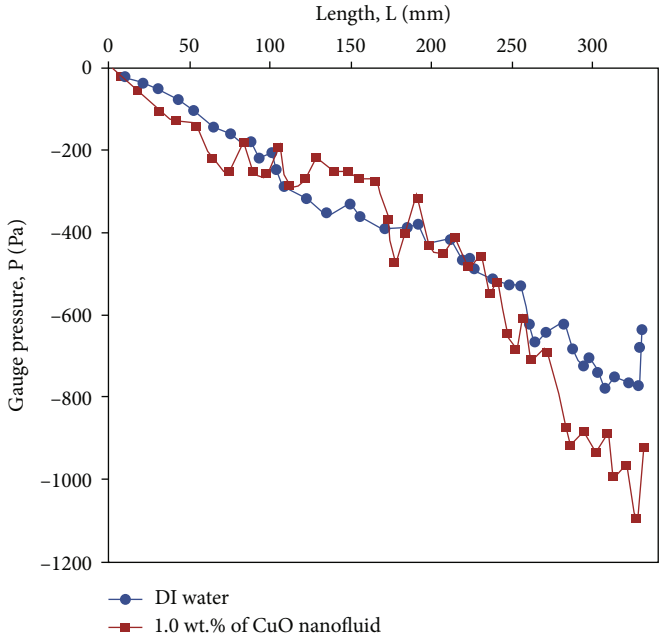

Figure 8: Comparison of vapor pressure of heat pipe working without and with CuO nanofluid for 45° orientation angle.

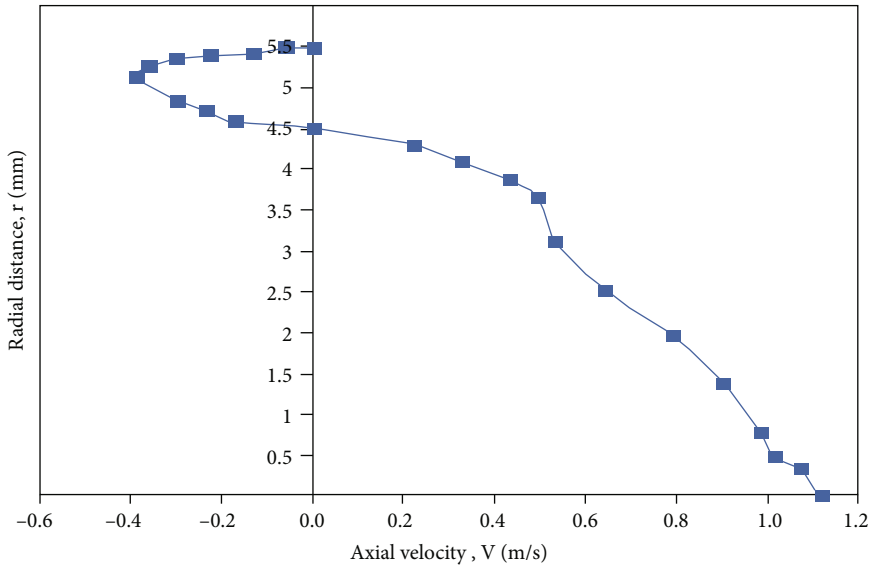

Figure 9: Axial velocity distribution at a diabatic section (X =135 mm from evaporator end) in radial direction of the heat pipe with nanofluid concentration 1% at tilt angle of 45°.

absorbing capacity of the base fluid will be increased by adding uniform-sized nanoparticles. Moreover, the liquid-vapor interface is properly steam lined and thus also shows enhancement in the results. The observed T values are 27, 20, and 24°C, respectively, which are considerably lower as compared to the DI water results.

Figure 5 depicts the heat pipe's surface temperature distribution obtained from experimental and numerical studies at 100 W of heat input. In the experimental analysis, thermocouples are located at fixed intervals, with the last thermocouple at a distance of 50 mm from the condenser, whereas in the numerical analysis, the full length of the heat pipe is considered. Moreover, the inclusion of copper (II) oxide nanoparticles results in the surface temperature reduction of the HP. The minimum and maximum deviations in the temperature distributions for the numerical and experimental values are 4.77% and 13.64%, respectively. This difference is greatest in the condenser section, because of the uncertainties associated with condenser cooling. The temperature difference is the dominant parameter in the present work. The main objective of the study is to enhance the capacity of the heat pipe

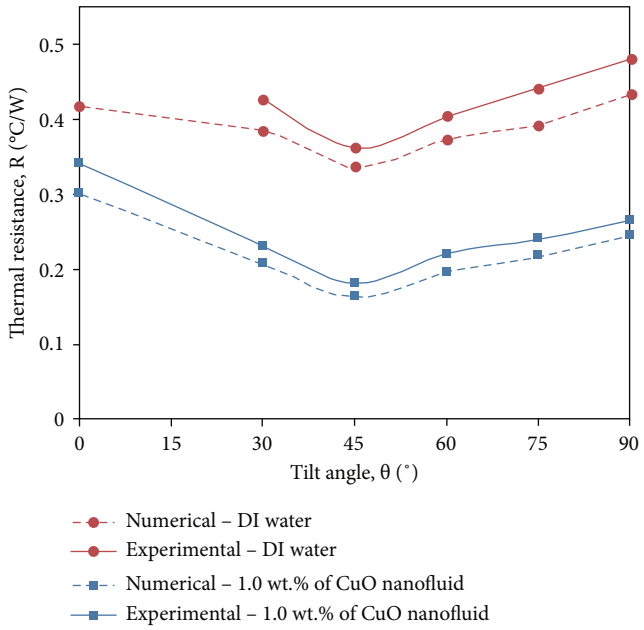

Figure 10: Effect of orientation angle on the thermal resistance of deionized water and CuO nanofluid heat pipe (input = 120 W) compared with Kumaresan et al. [30].

by changing the orientation as well as functioning conditions. The operation of the heat pipe is absolutely dependent on the dry-out condition. It may be postponed by lowering the temperature between the evaporator and condenser section. So, the difference between the surface temperature and the vapor temperature is the most important factor in how well heat pipes work.

8.2. Pressure Distribution. The pressure distribution of the SWHP for DI water and CuO-based working fluid with a 1.0% weight concentration is presented in Figures 6 and 7. The temperature, pressure, and velocity distribution in a heat pipe are calculated using the mass, momentum, and energy equations. At each point, the pressure value varies because of the temperature and phase changes. In the evaporator region, the pressure is at its maximum because of its higher temperature. The vapor core pressure gradually decreases over the length of the condenser.

The local pressure has a direct effect on the saturation temperature of the liquid, which is given by the equation,

$$T_0 = \left[\frac{1}{T_o} - \frac{R}{h_{fg}}.\ln\frac{P_s}{P_o}\right], \tag{12}$$

where P_o and T_o are the saturation pressure and temperature, respectively, and P_s is the vapor pressure.

In addition, it is observed that due to the inclusion of the CuO nanoparticles, the local pressure deteriorated due to the reduction in temperature at all the locations. The suspension of CuO nanoparticles suppressed the thermal resistance and thus the capillary action of the liquid from the condenser section is increased. It results in a drop in vapor core and surface temperature. The pressure gets proportionally reduced with respect to the temperature as per Charles's law. It is also perceived that the pressure drop in the case of a nanofluid is more than the base fluid as the suspended CuO particles raise the viscosity and give rise to more pressure drop. Figure 8 illustrates the gauge pressure of the heat pipe with respect to the axial length. The pressure distribution curve is formed in the negative direction because the heat pipe is working under vacuum pressure. The pressure is evenly distributed for DI water heat pipe comparing to the CuO nanofluid. The heat pipe using CuO nanofluid, on the other hand, achieves the lowest pressure.

8.3. Axial Velocity Distribution. The axial velocity variation of the SWHP in the radial direction is plotted in Figure 9. The readings are taken from the adiabatic section of the HP. The axial velocity of the vapor flow is extremely high at the center core of the heat pipe and zero at the surface region due to the no-slip conditions. After that, the graph passes in the negative direction, because the working fluid is flowing in the reverse direction. The maximum velocity of vapor flow is 1.1 m/s whereas it is only 0.39 m/s for liquid flow, which clearly shows the vapor velocity is more than double the time of that of nanofluid/DI water flow in the vapor core region.

8.4. Result Validation. The SWHP heat resistance is estimated experimentally using the temperature differential between the heating and cooling regions. The heat delivered to the heating end is estimated from the current and voltage values noted from the data logger. It can be found in [19].

$$R_{\text{hp}} = \frac{\Delta T_s}{\text{Q}_{\text{in}}}, \tag{13}$$

where $\Delta T_s = \bar{T}_e - \bar{T}_c$.

Figure 10 represents the heat resistance of SWHP for the cases of CuO nanofluid and DI water at a 120 W heat supply. The heat resistance reduces with the upsurge tilt angle till 45° but tends to rise for inclination angles greater than that. At a 45° inclination angle, 1.0 wt.% CuO/DI water nanofluid shows a maximum decrease of 49.46% when compared to DI water. The experimental results of the horizontal DI water heat pipe are not represented in the graph. This is due to the attainment of dry-out at this angle. The results obtained from the numerical study show lower thermal resistance than the experimental value, and this may be due to the approximation made in the numerical analysis. A maximum of 13.06% deviation is observed between the studies for heat pipes filled with deionized water.

The heat flux of the heat pipe is compared with [29] for the optimal weight concentration of 1.0% of CuO-based working fluid. The tilt angle of the heat pipe increases from a flat to a perpendicular position. The numerical findings match well with the experimental results. The thermal resistance is high irrespective of the working fluid when the HP is operating in a horizontal position. Thermal resistance attained its lowest value at an ideal tilt angle of 45°. Numerical values registered the lowest thermal resistance value compared with experiments. This is because the data prediction is more accurate in numerical, whereas the experimental uncertainties influence the

experimental values. The greatest drop in heat resistance is 0.181°C/W for numerical prediction, which is 5.78% lower than the experimental values. Zafar Said et al. [31] and Stalin et al. [32] confirmed that the introduction of high conductive nanoparticles within the working medium could enhance the heat transfer properties at a determined optimum weight fraction.

9. Conclusion

The numerical analysis of the irregular-shaped copper particles imposed sintered wick heat pipe was conducted using CuO nanofluids as working fluid, and the findings were validated by comparing them with the experimental data. The following observations are made after critical analysis:

(i) A strong consensus was observed between the numerical and experimental investigations. The minimum and maximum deviations in surface temperature had found to be 4.77% and 13.64%, respectively

(ii) The pressure at the evaporator section was at its maximum, and it had been gradually reduced, while moving towards the condenser section. When 1.0% weight fraction of CuO nanoparticles was supplemented, the heat pipe's vapor pressure had gone down compared to heat pipe with plain DI water

(iii) The pressure drop, which occurred in the heat pipe using CuO nanofluids, was greater compared with the plain DI water, because of the restriction to fluid flow created by the nanofluid

(iv) With a weight concentration of 1.0% nano-CuO in nanofluid, the pressure drop in heat pipe had been decremented by 35.33%.

(v) The axial velocity of the vapor core was high at the heat pipe's central core and zero velocity was found near the surface of the sintered wick structure. The vapor velocity at the heat pipe's core was 64.54% higher than the liquid flow over the wick structure. Axial vapor flow velocity was found to be 2.8 times greater than the liquid phase

(vi) The thermal resistance of the heat pipe was reduced by 49.46%, when 1.0% CuO nanoparticles had been used. Contrarily, the required values had not been obtained, when the heat pipe was being operated in a horizontal orientation due to its dry-out condition. However, the data was predicted during the numerical analysis

Nomenclature

A: Area (m^2)
d: Particle size (nm), thickness of heat pipe
g: Body force/gravity
I: Current
k: Effective thermal conductivity (W/m°C)
m: Mass (kg)
P: Pressure (N/m^2)
r: Radius (mm)
T: Temperature (°C)
V: Voltage (Volts), velocity (m/s)
W: Axial flow velocity (m/s)
ΔT: Difference in temperature (°C).

Subscript

bf: CuO nanofluid/DI water
c: Cooling end/condenser
e: Heating end/evaporator
eff: Effective
fg: Phase change
hp: Heat pipe
max: Maximum
ph: Phase transition
Q: Power input
q: Heat density
r: Radial coordinate
th: Thermal
v: Vapor
w: Wick.

Greek Symbols

θ: Orientation of heat pipe (degree)
ε: Wick porosity
μ: Dynamic viscosity (Ns/m^2)
ρ: Density (kg/m^3)
φ: Volume fraction (%)
ω: Weight concentration (wt.%)
Δ: Increment/decrement.

Data Availability

The data used to support the findings of this study are included within the article.

Conflicts of Interest

The authors declare that there is no conflict of interest regarding the publication of this paper.

References

[1] P. M. J. Stalin, T. V. Arjunan, M. M. Matheswaran, and N. Sadanandam, "Effects of CeO_2/water nanofluid on the efficiency of flat plate solar collector," *Journal of the Chinese Society of Mechanical Engineers*, vol. 41, pp. 75–83, 2020.

[2] M. Vijayakumar, S. Sivankalai, P. Michael Joseph Stalin, G. Kumaresan, P. Selvakumar, and V. Manikandan, "A scientometric analysis on development of nanofluids for heat transfer and fluid flow applications," *Solid State Technology*, vol. 64, pp. 3667–3684, 2021.

[3] V. Alcácer and V. Cruz-Machado, "Scanning the Industry 4.0: a literature review on technologies for manufacturing systems," *Engineering Science and Technology, an International Journal*, vol. 22, no. 3, pp. 899–919, 2019.

[4] P. M. Kumar, R. Saminathan, A. Sumayli et al., "Experimental analysis of a heat sink for electronic chipset cooling using a

nano improved PCM (NIPCM)," *Materials Today: Proceedings*, vol. 56, pp. 1527–1531, 2022.

[5] G. Kumaresan, S. Venkatachalapathy, and I. C. Naik, "An experimental study on improvement in thermal efficiency of mesh wick heat pipe," *Applied Mechanics and Materials*, vol. 592-594, pp. 1423–1427, 2014.

[6] A. Makki, S. Omer, Y. Su, and H. Sabir, "Numerical investigation of heat pipe-based photovoltaic–thermoelectric generator (HP-PV/TEG) hybrid system," *Energy Conversion and Management*, vol. 112, pp. 274–287, 2016.

[7] T.-P. Teng, H.-G. Hsu, H.-E. Mo, and C.-C. Chen, "Thermal efficiency of heat pipe with alumina nanofluid," *Journal of Alloys and Compounds*, vol. 504, Supplement 1, pp. S380–S384, 2010.

[8] Y. Gan, L. He, J. Liang, M. Tan, T. Xiong, and Y. Li, "A numerical study on the performance of a thermal management system for a battery pack with cylindrical cells based on heat pipes," *Applied Thermal Engineering*, vol. 179, article 115740, 2020.

[9] W. Sanhan, K. Vafai, N. Kammuang-Lue, P. Terdtoon, and P. Sakulchangsatjatai, "Numerical simulation of flattened heat pipe with double heat sources for CPU and GPU cooling application in laptop computers," *Journal of Computational Design and Engineering*, vol. 8, no. 2, pp. 524–535, 2021.

[10] H. Hassan and S. Harmand, "An experimental and numerical study on the effects of the flat heat pipe wick structure on its thermal performance," *Heat Transfer Engineering*, vol. 36, no. 3, pp. 278–289, 2015.

[11] S. A. Al-Mabsali, H. N. Chaudhry, and M. S. Gul, "Numerical investigation on heat pipe spanwise spacing to determine optimum configuration for passive cooling of photovoltaic panels," *Energies*, vol. 12, no. 24, p. 4635, 2019.

[12] S. Arabnejad, R. Rasoulian, M. B. Shafii, and Y. Saboohi, "Numerical investigation of the performance of a U-shaped pulsating heat pipe," *Heat Transfer Engineering*, vol. 31, no. 14, pp. 1155–1164, 2010.

[13] G. Kumaresan, P. Vijayakumar, M. Ravikumar, R. Kamatchi, and P. Selvakumar, "Experimental study on effect of wick structures on thermal performance enhancement of cylindrical heat pipes," *Journal of Thermal Analysis and Calorimetry*, vol. 136, no. 1, pp. 389–400, 2019.

[14] S. Miao, J. Sui, Y. Zhang, F. Yao, and X. Liu, "Experimental study on thermal performance of a bent copper-water heat pipe," *International Journal of Aerospace Engineering*, vol. 2020, Article ID 8632152, 10 pages, 2020.

[15] D. D. Odhekar and D. K. Harris, "Experimental investigation of bendable heat pipes using sintered copper felt wick," in *Thermal and Thermomechanical Proceedings 10th Intersociety Conference on Phenomena in Electronics Systems, 2006. ITHERM 2006*, pp. 570–577, San Diego, CA, USA, 2006.

[16] J. Zhang, L. X. Lian, Y. Liu, and R. Q. Wang, "The heat transfer capability prediction of heat pipes based on capillary rise test of wicks," *International Journal of Heat and Mass Transfer*, vol. 164, article 120536, 2021.

[17] H. Li, X. Fang, G. Li, G. Zhou, and Y. Tang, "Investigation on fabrication and capillary performance of multi-scale composite porous wick made by alloying-dealloying method," *International Journal of Heat and Mass Transfer*, vol. 127, pp. 145–153, 2018.

[18] D. Jafari, W. W. Wits, and B. J. Geurts, "Phase change heat transfer characteristics of an additively manufactured wick for heat pipe applications," *Applied Thermal Engineering*, vol. 168, p. 114890, 2020.

[19] M. Vijayakumar, P. Navaneethakrishnan, and G. Kumaresan, "Thermal characteristics studies on sintered wick heat pipe using CuO and Al_2O_3 nanofluids," *Experimental Thermal and Fluid Science*, vol. 79, pp. 25–35, 2016.

[20] A. Brautsch and P. A. Kew, "Examination and visualisation of heat transfer processes during evaporation in capillary porous structures," *Applied Thermal Engineering*, vol. 22, no. 7, pp. 815–824, 2002.

[21] I. L. Ngo and C. Byon, "Permeability of microporous wicks with geometric inverse to sintered particles," *International Journal of Heat and Mass Transfer*, vol. 92, pp. 298–302, 2016.

[22] S. Zhang, C. Chen, G. Chen, Y. Sun, Y. Tang, and Z. Wang, "Capillary performance characterization of porous sintered stainless steel powder wicks for stainless steel heat pipes," *International Communications in Heat and Mass Transfer*, vol. 116, article 104702, 2020.

[23] R. K. Bumataria, N. K. Chavda, and H. Panchal, "Current research aspects in mono and hybrid nanofluid basedheat pipe technologies," *Heliyon*, vol. 5, no. 5, article e01627, 2019.

[24] R. K. Bumataria, N. K. Chavda, and A. H. Nalbandh, "Performance evaluation of the cylindrical shaped heat pipe utilizing water-based CuO and ZnO hybrid nanofluids," *Energy Sources, Part A: Recovery, Utilization, and Environmental Effects*, pp. 1–16, 2020.

[25] R. Bumataria and N. Chavda, "Heat load and orientation impacts in cylindrical heat pipes using copper oxide, aluminium oxide, and zinc oxide nanofluids," *International Journal of Ambient Energy*, pp. 1–11, 2021.

[26] P. M. J. Stalin, T. V. Arjunan, M. Almeshaal, P. Murugesan, B. Prabu, and P. M. Kumar, "Utilization of zinc-ferrite/water hybrid nanofluids on thermal performance of a flat plate solar collector—a thermal modeling approach," *Environmental Science and Pollution Research*, pp. 1–14, 2022.

[27] R. Sharma, P. Chauhan, A. K. Sharma et al., "Characterization of ZnO/Nanofluid for Improving Heat Transfer in Thermal Systems," *Materials Today: Proceedings*, vol. 62, pp. 1904–1908, 2022.

[28] J. P. Holman, *Experimental Methods for Engineers*, McGraw Hill, 2001.

[29] G. Kumaresan, S. Venkatachalapathy, L. G. Asirvatham, and S. Wongwises, "Comparative study on heat transfer characteristics of sintered and mesh wick heat pipes using CuO nanofluids," *International Communications in Heat and Mass Transfer*, vol. 57, pp. 208–215, 2014.

[30] G. Kumaresan, S. Venkatachalapathy, and L. G. Asirvatham, "Experimental investigation on enhancement in thermal characteristics of sintered wick heat pipe using CuO nanofluids," *International Journal of Heat and Mass Transfer*, vol. 72, pp. 507–516, 2014.

[31] Z. Said, P. S. ShekRahmana, A. A. Hachicha, and S. Issa, "Performance characterization of a solar-powered shell and tube heat exchanger utilizing MWCNTs/water- based nanofluids: an experimental, numerical, and artificial intelligence approach," *Applied Thermal Engineering*, vol. 212, no. 25, 2022.

[32] P. M. J. Stalin, T. V. Arjunan, M. M. Matheswaran, P. M. Kumar, and N. Sadanandam, "Investigations on thermal properties of CeO2/water nanofluids for heat transfer applications," *Materials Today: Proceedings*, vol. 47, pp. 6815–6820, 2021.

Hindawi
Journal of Nanomaterials
Volume 2022, Article ID 7398110, 14 pages
https://doi.org/10.1155/2022/7398110

Research Article

Thermal Management of the Melting Process in a Latent Heat Triplex Tube Storage System Using Different Configurations of Frustum Tubes

Mohammadreza Ebrahimnataj Tiji,[1] Waleed Khalid Al-Azzawi,[2] Hayder I. Mohammed,[3] Anmar Dulaimi,[4] Farhan Lafta Rashid,[5] Jasim M. Mahdi,[6] Hasan Sh. Majdi,[7] Pouyan Talebizadehsardari,[8] and Hafiz Muhammad Ali[9,10]

[1]*Department of Mechanical Engineering, Qom University of Technology, Qom, Iran*
[2]*Department of Medical Instrumentation Engineering Techniques, Al-Farahidi University, Baghdad 10015, Iraq*
[3]*Department of Physics, College of Education, University of Garmian, Kurdistan, Kalar 46021, Iraq*
[4]*College of Engineering, University of Warith Al-Anbiyaa, Karbala 56001, Iraq*
[5]*Petroleum Engineering Department, College of Engineering, University of Kerbala, Karbala 56001, Iraq*
[6]*Department of Energy Engineering, University of Baghdad, Baghdad 10071, Iraq*
[7]*Department of Chemical Engineering and Petroleum Industries, Al-Mustaqbal University College, Babylon 51001, Iraq*
[8]*Centre for Sustainable Energy use in Food Chains, Institute of Energy Futures, Brunel University London, Kingston Lane, Uxbridge, Middlesex UB8 3PH, UK*
[9]*Mechanical Engineering Department, King Fahd University of Petroleum and Minerals, Dhahran 31261, Saudi Arabia*
[10]*Interdisciplinary Research Center for Renewable Energy and Power Systems (IRC-REPS), King Fahd University of Petroleum and Minerals, Dhahran 31261, Saudi Arabia*

Correspondence should be addressed to Pouyan Talebizadehsardari; pouyan.talebizadehsardari@brunel.ac.uk and Hafiz Muhammad Ali; hafiz.ali@kfupm.edu.sa

Received 21 March 2022; Revised 9 June 2022; Accepted 5 July 2022; Published 4 August 2022

Academic Editor: Hui Yao

In this study, the energy charging mechanism is mathematically modeled to determine the impact of design modifications on the thermofluidic behavior of a phase change material (PCM) filled in a triplex tube containment geometry. The surface area of the middle tube, where the PCM is placed, is supported by single or multi-internal frustum tubes in vertical triplex tubes to increase the performance of the heating and cooling of the system. In addition to the ordinary straight triplex tubes, three more scenarios are considered: (1) changing the middle tube to the frustum tube, (2) changing the inner tube to the frustum tube, and (3) changing both the internal and central tubes to the frustum tubes. The impact of adopting the tube designs and gap width were studied. The outcomes reveal that the heat storage rates are increased for all frustum tube systems compared to the straight tube system. According to the results, the case of a gap width of 5 mm is the optimal one among the studied cases in terms of the melting time and the heat storage rate. Employing the frustum tube configuration with a 5-mm gap width would save the melting time by 25.6% and increase the rate of heat storage by 32.8% compared to the base case of straight tubes.

1. Introduction

Saving global energy resources requires efficient conversion methods and consistent renewable energy sources [1, 2]. Almost 1/3 of the worldwide energy supply is wasted because of ineffective energy conversion techniques, harming the environment [3, 4]. Some renewable energy sources like wind, geothermal, and solar thermal energies suffer from erratically power supply, which creates a significant imbalance between the production and consumption of energy

[5–7]. Thermal energy storage (TES) system is a promising technique to cover the gap; for instance, a thermal storage system can store energy from the sun throughout the day and utilize it during the night or when the demand is high [8–10]. TES is classified into three modes: sensible heat, latent heat, and thermochemical storage. The primary purpose of TES mechanisms is to lower the energy loss and the cost to permit the manufacture of well cost-efficient energy conversion units [11, 12]. Phase change materials (PCMs) are considered one category of the most encouraging materials to store and recover the thermal energy in demand [13, 14].

Recently, the research interest regarding latent heat thermal energy storage (LHTES) increased due to the high thermal efficiency and low phase change temperature point; however, the thermal conductivity of the PCM is generally poor and inappropriate for many applications [15–17]. Accordingly, various techniques have been modelled to improve the heat transfer efficiency of the PCM during the charging and discharging methods [18]. These techniques include a combination with the high conductive materials (nanoparticles) [19–23], utilizing an extended surface area for the heat transfer (fins) [21, 24–26], combinations with the metal foam [27–31], and using more efficient geometries designs [28, 32, 33]. Moreover, natural convection is a critical mechanism that can assist the phase change heat transfer in molten regions. The magnetic field can influence natural convection heat transfer in molten regions of a PCM [34] and viscosity alteration [35].

Many investigations have been achieved to improve the thermofluidic behavior during the PCM's melting and solidification processes, which saves the required time for these operations [36, 37]. Various geometrical aspects have been considered for the LHTES system regarding the design and the shape of the heat transfer fluid (HTF), number of the channels, their positions, and distributions [38]. Park et al. [39] numerically studied the melting process of the PCM in a multichannel HEX LHTES. The impact of the channel number and design on the melting performance of the PCM was investigated regarding thermal management, provided power, and charging period. They found that the melting rate increases by increasing the number of the channels in the early stage, whereas the volumetric energy increases by 18.2% using eight HTF channels compared to a single large channel. Kousha et al. [40] experimentally examined the influences of utilizing different numbers and locations of the HTF channels on the phase change processes of the PCM at various temperatures of the inlet HTF (water). They found that the phase change time reduces using multi-HTF channels compared with the case of a single channel. They also found that increasing the inlet temperature to 80°C accelerates the charging and the discharging rate by 43% and 50%, respectively. Talebizadehsardari et al. [41] studied the effect of various designs and the number of HTF channels utilizing a serpentine tube. They found that the discharging time and the output temperature of the HTF in the case of the serpentine tube were 6 hours and 56°C compared with the straight tube, which was 13.6 hours and 41°C. Mohammed [42] studied the discharge improvement of a phase change material-air-based thermal energy storage unit for space heating applications using metal foams in the air sides. The results showed that the HTF flow rate has a great influence on the discharging rate. The presence of the porous medium in the system improves the discharging process by 116% compared with a non-porous medium system at the same flow rate.

Heat exchangers (HEX) significantly impact manufacturing and engineering functions [43, 44]. Because of limited energy sources and cost considerations, more attention has been paid to improving the performance of the HEX [45, 46]. Thus, there is a significant demand to improve the thermal efficiency of the HEX, which managed to be employing and emerging various enhancement methods [47, 48]. The most common HEX utilized in the factories is shell and tube heat exchanger (STHE). A standard STHE contains a cylindrical shell, including many channels. Pourakabara and Darzi [49] performed a numerical model to predict the charging and discharging processes using different numbers of HTF tubes in the cylindrical and elliptical shapes of the shell embedded in the metal foam. They found that the peaks of the charging and discharging rates achieve 92% and 94%, respectively, when the porous medium is used compared with the system of alone PCM. Likely, Qaiser et al. [50] performed a numerical and experimental study by applying multi-finned channels with various designs of shell form (circular, elliptical, and rectangular). The thermal rate improved by 34% and 24%, and the charging rate was increased by 28% and 22% when utilizing two-vertical channels and v-array triple-channel design, respectively, in the circular shell of the LHTES system as compared to those in the reference case. Yang et al. [51] studied the Design of non-uniformly distributed annular fins for a shell-and-tube thermal energy storage unit. They found that moving fins down effectively improves the melting fraction of middle and bottom PCMs. Also, they detected that an 84.7% improvement in melting uniformity was achieved by a non-uniform design. Guo et al. [52] studied the compression effect of metal foam on melting phase change in a shell-and-tube unit. Yang et al. [53] investigated the effect of fin number on the melting phase change in a horizontal finned shell-and-tube thermal energy storage unit, and they found that the melting time can maximally be saved as high as 72.85% by increasing fin number. Guo et al. [54] examined the thermal assessment of a solid-liquid energy storage tube packed with non-uniform angled fins. In a different work, Guo et al. [55] studied the melting assessment on the angled fin design for a novel latent heat thermal energy storage tube, and they stated that the angled fins with small angles (5°, 10°, and 15°) markedly reduced full melting time for the TES unit. Eisapour et al. [56] optimized the configuration of a double elliptical LHTES through the charging process. They found that the efficiency of the system increases as the gap between the inner channel and the lower wall of the external channel reduces. The best place was located when the internal channel is at the minimum distance of the elliptical wall by 2 mm. Ren et al. [57] investigated the efficiency of shell-and-tube PCM in TES. They found that the spiral tube design and the double serpentine

tube design mostly have an advantage over the single serpentine tube design. The melting duration 95% of the PCM decreased by 16% if the single serpentine design was replaced to spiral (at the tube length of 4055 mm). Further, Patel et al. [58, 59] investigated the impact of the longitudinal fin inside the triplex tube in two different studies, and they found that each parameter related to the fins, including the arrangement, length, width and the number, has a great impact on the thermal performance of the heat storage unit.

Alnakeeb et al. [60] modeled the thermal parameters of the charging process influenced by a single planed tube with various inside eccentricities (0, 0.25, 0.5, and 0.75) and aspect ratios (0.5, 0.6, 0.7, 0.8, 0.9, and 1). The highest charging rate was found at 218.5% for the circular tube (aspect ratio of 1). Zheng et al. [61] examined the impact of internal circular tube eccentricity and Rayleigh number (Re) on phase change material melting and solidification heat transfer. They found that the highest eccentricity in the internal channel to the shell bottom did not necessarily offer the fastest melting rate. The best eccentricity was detected to have a linear relation with Re. The growth in the eccentricity increased the discharging rate just when the Re ratio (Re of discharging divided by charging) was greater than 2.0. Pahamli et al. [62] performed a numerical analysis to examine the impact of eccentricity, velocity, and inlet temperature of heat transfer fluid (HTF) on PCM charging characteristics. Raising the eccentricity from 0 to 0.75 increased the charging rate by 64% and 27%, respectively; simultaneously, the velocity had a minimal effect on the charging rate. Faghani et al. [63] modelled the behavior of the PCM charging in a variety of internal and exterior channel configurations, including vertical, horizontal, and circular ellipses. The shell's horizontal ellipse configuration and the channel's vertical ellipse demonstrated the maximum charging rate. Faghani et al. [63] modeled the operation of PCM charging by utilizing various designs of internal and external channels (circular, horizontal, and vertical ellipses). The arrangement of the horizontal ellipse form of the shell and the vertical ellipse form of the channel showed the highest charging rate. Gorzin et al. [64] conducted a model to examine the impact of various multi-tube LHTES system formations and PCM mass allocations on the discharging rate at different concentrations of nanoparticles. The appropriate allocation of PCM volume increases the discharging rate by 62%, while increasing the loading of the nanoparticles to 4 wt% reduces the discharging time by 15%.

The studies in the literature confirmed that the phase change process of PCM in TES systems is highly influenced by the number of HTF tubes and their geometries, which influence the melting rate and the required duration to complete one cycle. Therefore, a comprehensive investigation has been performed, including studying the angle of the PCM shell. Instead of three circular tubes, a combination of cone and frustum tubes has been utilized in the TES, which may improve the heat transfer in the system through the melting process. Thus, the current study aims to achieve the fastest melting rate and the best thermal performance at the specific distance between the internal and external channels (middle tube hydraulic diameter). The simulation of the melting processes in the different cases was achieved using ANSYS-Fluent software. Eventually, to improve the performance of the novel combination of cone and frustum tube latent heat thermal energy storage, sensitivity analysis of the solidification process could be achieved with the same procedures as the melting process.

2. Problem Description

A vertical triplex tube is examined as a latent heat TES in this study. The surface area of the middle tube, where the PCM is placed, is supported by single or multi-internal frustum tubes to increase the rate of heat transfer during the melting process. In the heat exchanger, the inner and outer tubes pass the heat transfer fluid (HTF), considered water in this study. The HTF flows in the opposite direction in both the internal and the external channels. The direction of the flow is affecting on temperature differences. The maximum temperature is shown at the inlet section and the minimum at the outlet section. The temperature differences directly affect the heat transfer by convection and conduction as well. The height of the tube is considered 250 mm. In the system with straight tubes, the hydraulic diameters of the inner, middle, and outer tubes are considered 20 mm, and the thickness of the inner and outer tubes is also considered 1 mm. It should be noted that the dimensions of the base system are chosen based on the triplex tube latent heat storage systems in the literature [65, 66]. In addition to the ordinary straight triplex tubes shown in Figure 1(a), there are three more scenarios considered in this study, including changing the middle tube to a frustum tube (Figure 1(b)), changing the inner tube to a frustum tube (Figure 1(c)), and changing both the inner and middle tube to frustum tubes (Figure 1(d)). In addition to the various tube designs, different gap widths are assessed considering the hydraulic diameters of 5, 10, and 15 mm for the middle tube at the bottom of the heat exchanger. The hydraulic diameter of the middle tube at the top of the heat exchanger is then determined considering a constant volume for the PCM equal to the PCM volume in the straight triplex tube heat exchanger. It should be noted that in scenario 2 (changing the inner tube to frustum tube), it is not possible to use 5 mm as the hydraulic diameter of the pipe at the bottom due to the slope of the frustum and dimensions of the system.

Because of the nature of the heat transfer issue being examined and the scarcity of circumferential flow difference, the unit is regarded as axisymmetric, as seen in Figure 2. The boundary conditions and directions of the HTF flow, and gravity, are also illustrated in Figure 2.

Table 1 presents the width of the PCM channel at the bottom of the heat exchanger for different proposed scenarios. As mentioned, the widths of the PCM at the top and HTF channels at the bottom and top are then determined according to the volume of the PCM compared with the base case (straight pipes).

Paraffin RT-35 is used as the PCM, whose thermophysical characteristics are listed in Table 2. The HTF's input temperature and flow Reynolds number are set to 50 °C

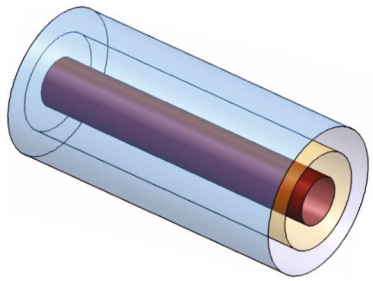

(a) Base case: straight tubes with no tube geometry modification

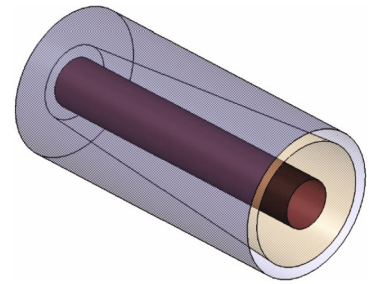

(b) Scenario 1: changing the middle tube to the frustum

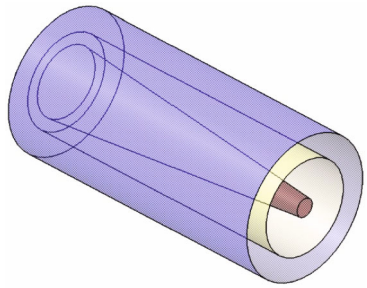

(c) Scenario 2: changing the inner tube to the frustum

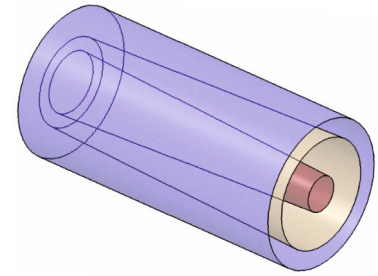

(d) Scenario 3: changing both the inner and middle tube to the frustum

Figure 1: The schematic of the vertical triplex tube TES system with different tube geometry modifications.

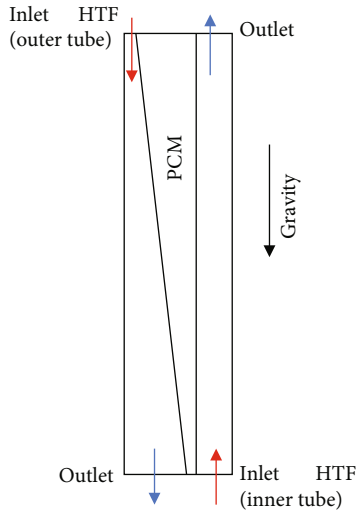

Figure 2: A schematic of the studied triplex tube in axisymmetric condition.

and 1000, respectively, to determine the optimal design. The PCM's initial temperature is regarded to be 15 °C.

3. Mathematical Modeling

In order to simulate the phase change of PCM, the enthalpy-porosity approach developed by Brent et al. [67, 68] was implemented. In this method, the liquid part and the porosity were presumed to be the same in all cells of the computational domain. To simplify the numerical solution of the governing differential equations, the following assumptions are considered as follows:

(i) Utilizing the Boussinesq approximation to control the density and buoyant force.

(ii) The fluid flow of molten PCM is transient, laminar, and incompressible.

(iii) Gravitation acceleration is positive in the – (Ve) y -axis direction.

(iv) The Boussinesq approximation is applicable to control the density and buoyant force.

(v) Perfect insulations are considered at the external boundaries.

(vi) The no velocity-slip condition is applied at the solid boundaries.

For the HTF and the molten PCM, the continuity, momentum, and energy are then defined as follows [8]:

$$\frac{\partial \rho}{\partial t} + \nabla . \rho \vec{V} = 0, \tag{1}$$

$$\rho \frac{\partial \vec{V}}{\partial t} + \rho\left(\vec{V}.\nabla\right)\vec{V} = -\nabla P + \mu\left(\nabla^2 \vec{V}\right) - \rho\beta\left(T - T_{ref}\right)\vec{g} - \vec{S}, \tag{2}$$

$$\frac{\rho C_p \partial T}{\partial t} + \nabla\left(\rho C_p \vec{V} T\right) = \nabla(k\nabla T) - S_L, \tag{3}$$

The factor $(\vec{S})$ in the momentum formula is involved to measure the impact of phase change, which is identified as

Table 1: The dimensions of the PCM width at the bottom of the heat exchanger in various studied scenarios for various cases.

Base case	Scenario 1		Scenario 2		Scenario 3			
Case 0 $\delta = 20$ mm	Case 1 $\delta = 5$ mm	Case 2: $\delta = 10$ mm	Case 3: $\delta = 15$ mm	Case 4: $\delta = 10$ mm	Case 5: $\delta = 15$ mm	Case 6: $\delta = 5$ mm	Case 7: $\delta = 10$ mm	Case 8: $\delta = 15$ mm

Table 2: Thermodynamic properties of the utilized PCM [35].

Properties	ρl [kg/m^3]	ρs [kg/m^3]	L_f [kJ/kg]	C_p [kJ/kg.K]	K [W/m.K]	μ [N.s/m^2]	T_L [°C]	T_S [°C]	β [J/K]
Values	770	860	170	2	0.2	0.023	36	29	0.0006

Table 3: Effect of grid size and time step size on the charging time.

Number of cells	28500		43000		81620
Time step size (s)	0.2	0.1	0.2	0.4	0.2
Melting time	4644	4733	4727	4701	4739

the velocity inhibiting term in Darcy law [69] :

$$\vec{S} = A_m \frac{(1-\lambda)^2}{\lambda^3 + 0.001} \vec{V} \tag{4}$$

The parameter of the mushy zone A_m is taken as 10^5 based on the literature [68, 70]. To evaluate the phase transition progression, λ (liquid part of PCM) is announced as follows [71]:

$$\lambda = \frac{\Delta H}{L_f} = \begin{Bmatrix} 0 & \text{if } T < T_S \\ 1 & \text{if } T > T_L \\ \dfrac{T - T_S}{T_L - T_S} & \text{if } T_S < T < T_L \end{Bmatrix} \tag{5}$$

The Boussinesq approximation is used to calculate the density variations because of the temperature variation through the PCM's phase change course. In this calculation, mass density is treated as fix value, excluding in the gravity term of the momentum formula, where density is observed as a temperature-dependent variable [72]:

$$\rho = \rho_{ref}\left(1 - \beta\left(T - T_{ref}\right)\right) \tag{6}$$

In the above equation, the reference temperature is the melting point (Tl + Ts/2), and the density is calculated at the reference temperature which is the average density of the PCM at the liquid and solid states. Then, the buoyancy effect is calculated for the temperatures higher than the melting temperature.

The source term S_L in the energy formula is found as

$$S_L = \frac{\rho \partial \lambda L_f}{\partial t} + \rho \nabla\left(\vec{V} \lambda L_f\right). \tag{7}$$

The rate of energy stored through the charging progression is calculated as

$$\dot{E_T} = \frac{E_{end} - E_{ini}}{t_m}, \tag{8}$$

where t_m is the charging time and E_e and E_i are the whole PCM's energy at the start and the endpoints of the charging progress. E is the total heat the sensible $(MC_p dT)$ and latent (ML_f) cases of the PCM.

4. Numerical Modeling, Grid Analysis, and Validation

A combination of the SIMPLE algorithm for pressure-velocity coupling and the Green-Gauss cell-based approach was utilized within the ANSYS-FLUENT solver to assess the heat transfer and fluid flow governing equations of PCM through the phase transition progress. For the momentum and energy equations, the QUICK differencing technique was utilized with the PRESTO scheme for the pressure correction equations. The under-relaxation factors are adopted after careful selection as 0.3, 0.3, 0.5, and 1 for pressure correction, velocity components, liquid fraction, and energy equation, respectively. The convergence criteria for terminating the iterative solution are set to be 10^{-4}, 10^{-4}, and 10^{-6} for the continuity, momentum, and energy equations, respectively.

The mesh and the time step size independency tests are performed. Accordingly, the various grid size of 28500, 43000, and 81620 are assessed utilizing the time step size of 0.2 s for the straight triplex system. Table 3 presents the melting time for various mesh densities. As illustrated, the outcomes are almost the same for the cell numbers 43000 and 81620; the mesh size of 43000 is selected for the next steps of this study. Table 3 also presents the melting time for various sizes of time step sizes for the nominated cell number. As demonstrated, the outcomes data are virtually identical for the time step of 0.1, 0.2, and 0.4 s, especially for the values 0.2 and 0.1 s. Thus, 0.2 s is selected as the time step size in the current work.

To verify the appropriateness of the simulation model describe above, the outcomes of Mat et al. [71] were utilized

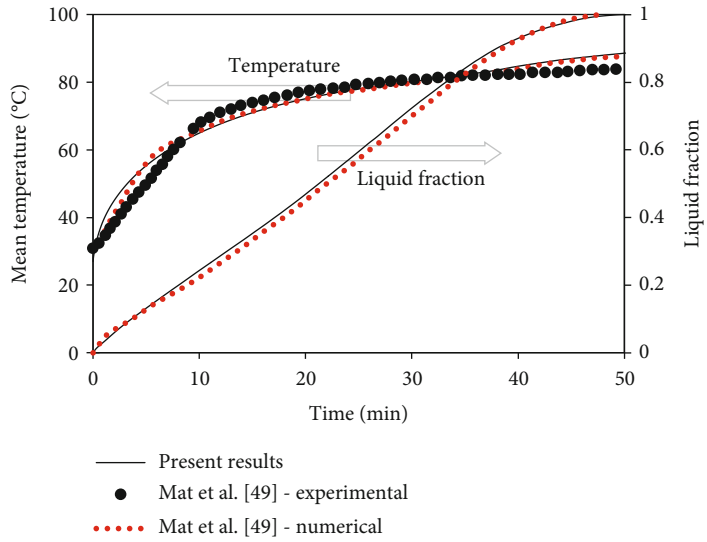

Figure 3: Evaluation of the current model's temperature and liquid-fraction results compared to those of Mat et al. [71].

as a benchmark since the designs analyzed in the two studies are primarily the same. The system configuration investigated in that work along with the boundary conditions and governing equations was revised using the present simulation model. The cited reference work examined the influence of integrated fins attached to both the internal and external tubes of the PCM shell at uniform wall-temperature conditions. Two performance parameters were applied to evaluate the validity of this model: the PCM's thermal conduct and the liquid fraction's growth. Figure 3 illustrates the outcomes of the validation case, which confirms that the numerical and experimental data of Mat et al. [71] are close to the current model estimates for both the liquid fraction and the average temperature of PCM. A maximum percentage error of less than 2% is reported in this validation test. Thus, the current model can be adopted for examining the thermal characteristics of the PCM-based triple-tube system with a frustum tube.

5. Results and Discussion

A series of numerical simulation tests were conducted based on the mathematical model formulated in the preceding section to evaluate the tube geometry modification on the thermal response of PCM contained in a triplex tube containment design during the mode of the energy charging (melting phase). The tube surface area, which is exposed to the heating effect according to the target phase change method, is enhanced by implementing a single internal frustum tube in a vertical triplex tube system keeping the outer shell unchanged. Frustum tube allows for a more comprehensive modification of the tube geometry over the heat-transfer flow direction, making the approach relevant in more design situations. Gap width, which denotes the radial distance between the inner and middle tubes, was used as the characteristic length of the PCM domain. Different gap widths for the annulus holding the PCM between the middle and inner tubes were investigated as the critical design parameter to explore the benefits of the tube geometry variation along the heat-transfer flow direction. Three scenarios were adopted to investigate the possible thermal response improvement due to the tube geometry modification: Scenario 1: changing the middle tube to a frustum tube; scenario 2: changing the inner tube to a frustum tube; and scenario 3: changing both the inner and middle tube to frustum tubes. In each scenario, as indicated in Figure 1, there are three cases with three different gap widths ($\delta = 5$, 10, and 15 mm) except scenario 2 where only two gap widths ($\delta = 10$ and 15 mm) were used. The effects of modifying the tube geometry and gap width were evaluated by examining the contour lines and the profiles of liquid fraction and average PCM temperature and the melting time and heat storage/recovery rates.

5.1. Liquid-Fraction Evolution. Figure 4 illustrates the liquid-fraction **evolution contours at four different periods of melting (600, 1200, 2400, and 3600 s) for all scenarios, as mentioned earlier. Heat conduction dominates the heat transfer process initially for (t = 600 s). The melting fronts marked in light green appear to be nearly parallel to the tube walls, but there are no significant differences between all cases throughout this period. As time proceeds to (t = 1200 s), a role appears for natural convection, which mainly accelerates the melting rate in the upper zones of the PCM domain. This indicates that warm streams of liquid PCM always tend to be settled at the top since the weight of warm liquid PCM is less than the density of cold solid PCM.

Meanwhile, the melting front movement does not progress much at the bottom, as seen in all cases considered in Figure 4. As time proceeds to (t = 2400 s), the melting fronts show more uniformity in movement through the unsolidified layers of PCM. In contrast, liquid-fraction contours show increasing shrinking in the blue zones, especially in the upper parts. This is because natural convection predominates the melting process over thermal conduction during this period. This drives the melting fronts to show faster

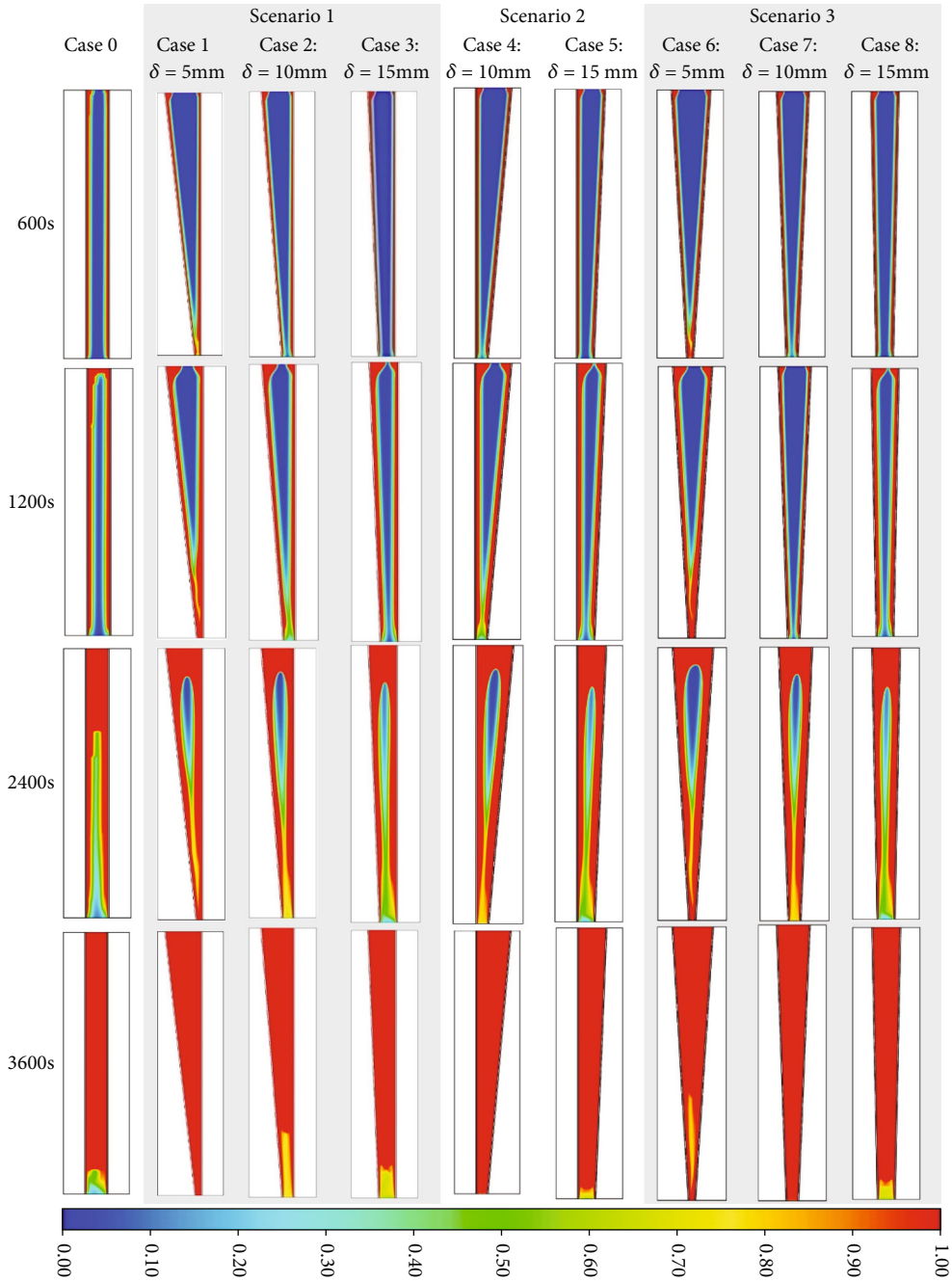

Figure 4: Contours of the liquid-fraction evolution for the investigated tube geometries over various melting times.

movement than in the preceding period. Through the last period (t = 3600 s), even melting is terminated in the upper parts of the domain in all cases; it ultimately terminated in the whole domain only in case 1 ($\delta = 5$ mm) of scenario 1 and case 7 ($\delta = 10$ mm) of scenario 2. The reasons are as follows: (i) the heat exchanging area between HTF and PCM of case 1 is bigger than that of other cases owing to its gap width value (i.e., $\delta = 5$ mm), which is the smallest one used, and (ii) the tilted heating wall from both sides in case 7 gives the melted portions of PCM the potential to move faster and better wash the not yet melted portions as the tilted heating wall can provide a better buoyancy effect than a vertical heating wall. Therefore, these findings suggest that applying a smaller gap width leads to a higher tilt angle of the heating walls, which provides a better potential for more vigorous washing action at the melting fronts.

5.2. Velocity Field. Figure 5 provides a visual representation of the velocity field for all cases within the three scenarios considered for the tube geometry modification and over various melting periods (600, 1200, 2400, and 3600 s). Through the early period ($t \leq 600\,s$), the major PCM domain experienced no movement of liquid PCM as the major PCM has not melted yet. Therefore, the velocity contours are almost

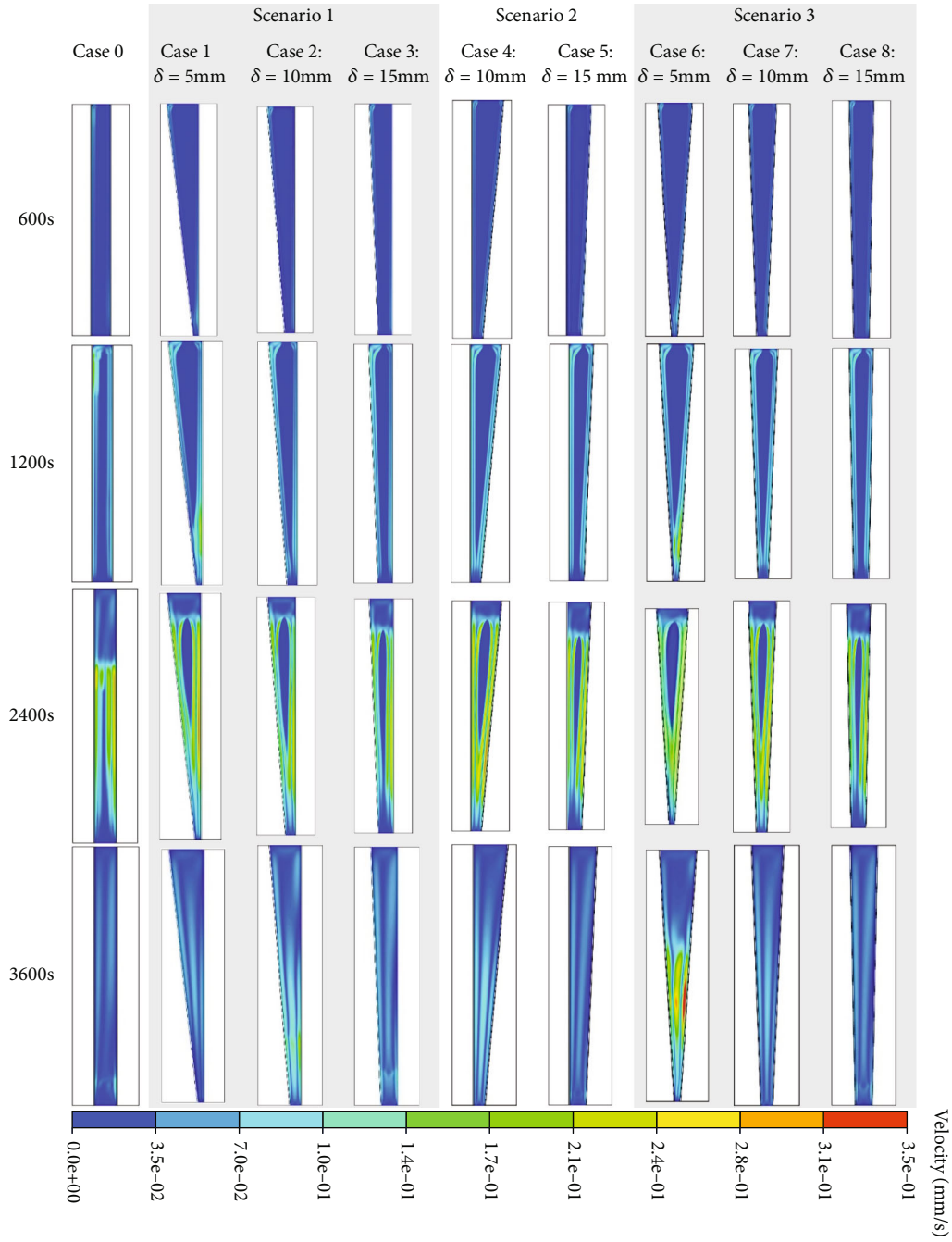

Figure 5: Contours of the velocity field for the investigated tube geometries over various melting times.

identical and marked by blue as a sign of zero velocities. Though this scenario is thermally unstable, the mode of heat transfer is soon altered to contribute from natural convection and conduction during the second period ($600 < t \leq 1200$ s). This period also witnesses the appearance of velocity boundary layers adjacent to the heating walls. However, the values of velocities remain relatively low within the order of 1×10^{-1} mm/s. Furthermore, modifying the tube geometry into frustum results in minor changes in flow velocity over the aforementioned periods. As moving to the next period, the convection movement becomes stronger and more effective at higher portions of the annulus, where the convection rotating part start to expand from below, moving warm liquid to the upper part, while cold liquid with relatively high densities remains trapped below, allowing the melting rate to increase more rapidly in this region. Also explained by this is the production of comparatively high velocities at the top of the domain, which progressively decreases as the rotating cell moves lower, as shown in Figure 5 ($t = 2400$ s). The velocity field appears to show faster movement as the blue color of the velocity field turns red with relatively big rotating cells at the top half of the domain during the final period ($t = 3600$ s). The modification of tube geometry as that in case 1 helps the better

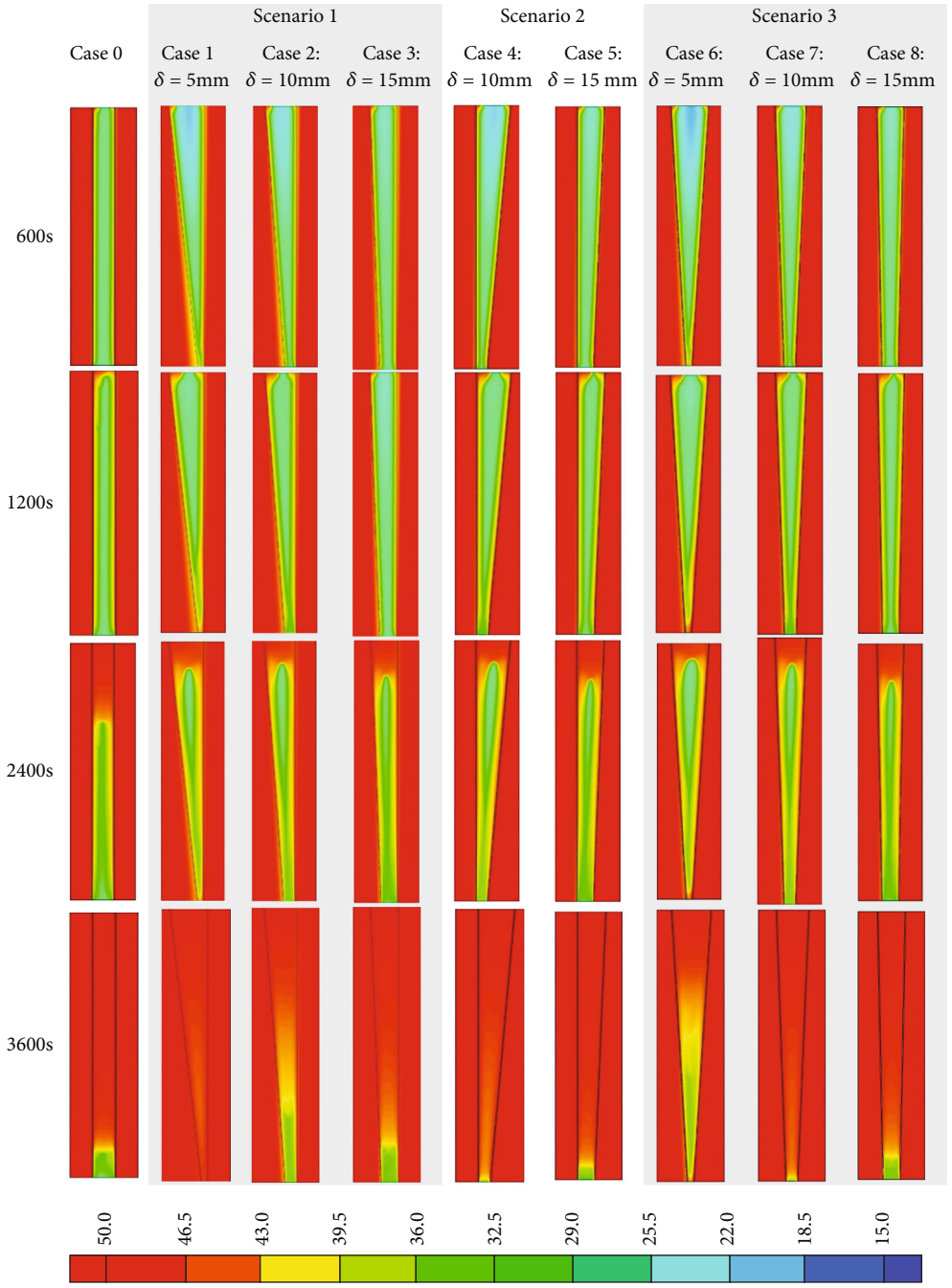

Figure 6: Contours of the temperature distribution for the investigated tube geometries over various melting times.

movement of buoyancy-driven flow, which results in a further increase in flow velocity over the final melting stages. This is expected as the modification of tube geometry into the frustum, especially in cases 1 and 7, helps the formation of bigger rotating cells compared to other cases due to the good role of natural convection, which empowers a substantial propagation of melting as earlier indicated in discussing the dynamic behavior of melting front movement.

5.3. Temperature Distribution. In Figure 6, the isotherm distribution contours for all cases in the discussion and over different melting periods (600, 1200, 2400, and 3600 s) for the studied scenarios of tube geometry modification are given. During the initial stages (t = 600 and 1200 s), the inhomogeneity of local natural convection across the different parts of the PCM domain triggers the PCM temperature to be higher at the bottom than the temperature at the top or center of the PCM domain in all studied cases except case 1. This implies that case 1 has a higher temperature gradient in the gravity direction than other cases, which is advantageous for developing natural convection during the later periods. During the third period (t = 2400 s), the isotherms almost have a similar appearance to each other, and some recirculation cells started to appear near the center of the PCM

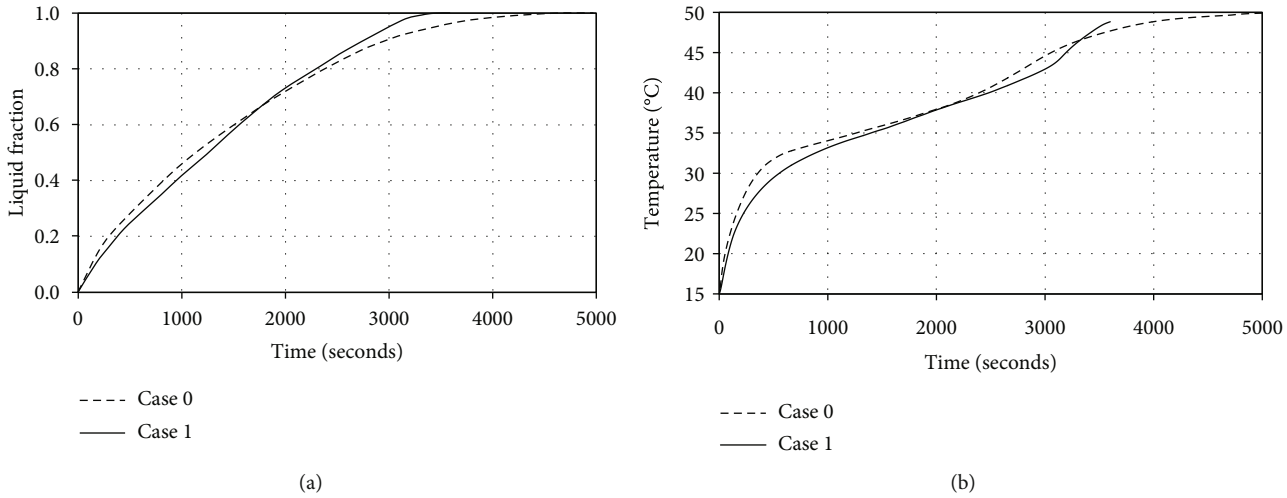

Figure 7: The time-wise variation of (a) liquid-fraction and (b) average temperature for the PCM melting for cases 0 and 1.

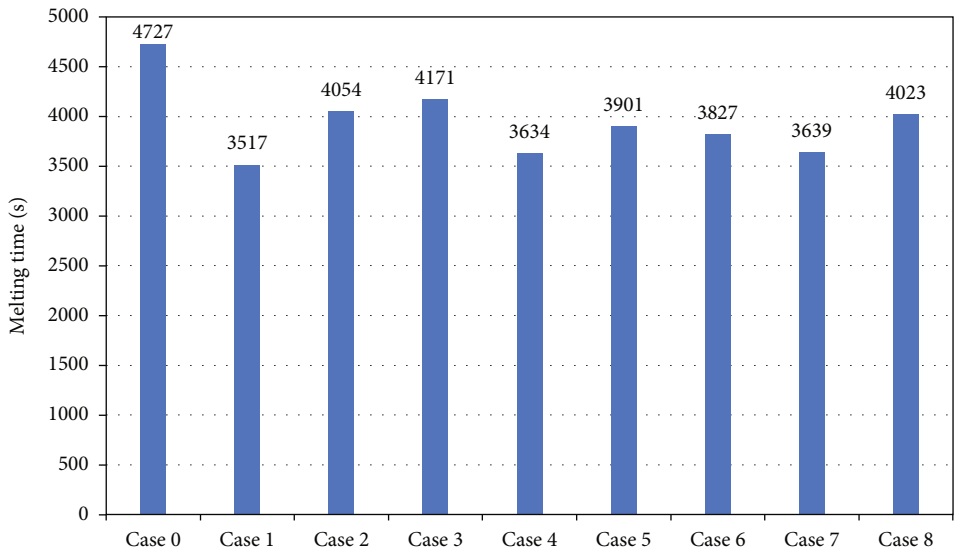

Figure 8: The melting time required for the melting completion for different tube configurations.

domain, especially in the upper half of the domain. This is because the buoyancy effect which originates from the temperature gradient in the vertical direction, outweighs the gravity impact, and triggers the melted portions of PCM to flow, resulting in the formation of recirculation cells. Therefore, natural convection has a greater impact on the temperature field than conduction does during this time. This confirms that during this period, modifying the tube geometry into frustum further enhances the heat transfer by natural convection between the liquid PCM and the HTF during the melting mode. For frustum tubes, a bigger one with smaller gap width such as that in case 1 helps faster heat diffusion across the PCM domain so that the whole PCM reaches the highest temperature in the range, marked in red at t = 3600 s. This indicates that the strength of natural convection further improves as the gap width between the frustum tubes decreases.

5.4. Melting Behavior Profiles. As the best performing among the eight cases of frustum tubes, case 1, which involves Changing the middle tube to a frustum tube with the gap width ($\delta = 5$ mm), is selected to compare the effect of employing frustum tubes over the straight tubes on melting behavior of PCM in a triplex tube storage system. The time histories for liquid-fraction profile and average temperature behavior for cases, case 0 (straight tubes) and case 1 (frustum tube), are compared in Figures 7(a) and 7(b), respectively. As seen in the figure, modifying the tube geometry does not significantly improve the PCM liquid-fraction profile or average temperature behavior at the early durations of melting (i.e., for $t \leq 2400$ s). However, as time advances, it can be observed that employing frustum tubes in case 1 typically provides better heat transfer into the PCM due to the larger heat-exchanging area with the HTF than in the base (case 0). This allows the PCM in case 1 to terminate melting

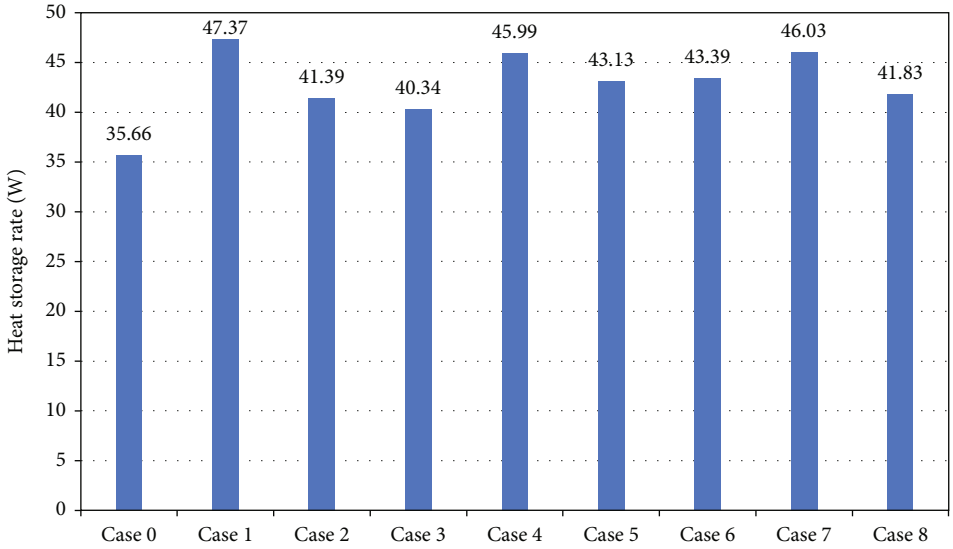

Figure 9: The heat storage rate during melting mode for different tube configurations.

within 3500 s of operation while case 0 needed about 5000 s to complete melting. Moreover, the whole PCM in case 1 reaches the melting temperature (Tl = 49°C) in Figure 7(b) faster than that in case 0 by about 600 s. The reason is that the heat transport from HTF to the PCM during the early periods via conduction is later stored as sensible heat in the residual parts of PCM, leading to a rapid increase in the PCM average temperature during the final periods. The other reason is that the geometry of the frustum tube in case 1 enables a better dominating role of natural convection during the final periods. It should be noted that natural convection in such a situation could serve as a further supply of heat transport into PCM, helping the average temperature of PCM to reach its maximum value in a shorter melting duration in case 1. In fact, the higher the average temperature of PCM, the faster the melting rate and the better the thermal storage process in the PCM-based energy storage system.

5.5. Heat Storage Rates. Figures 8 and 9 show the values of melting time and heat storage rate for each of the cases under discussion. Data from Figure 8 indicates that the time needed to melt the PCM completely is 4727, 3517, 4054, 4171, 3634, 3901, 3827, 3639, and 4023 seconds for cases 0, 1, 2, 3, 4, 5, 6, 7, and 8, respectively. By using case 0 as a referential case to compare with, the results reveal that the melting time could be reduced by 25.6, 14.2, 11.8, 23.1, 17.5, 19.0, 23.0, and 14.9% for cases 1, 2, 3, 4, 5, 6, 7, and 8, respectively. Thus, altering the geometry of the triplex tubes into frustum significantly improves the energy storage process during the melting mode. As a result, all frustum tube systems have shorter melting times than the straight tube system. Furthermore, data from Figure 9 indicates that the heat added to the PCM during the melting mode can be stored at the rate of 35.66, 47.37, 41.39, 40.34, 45.99, 43.13, 43.39, 46.03, and 41.83 watts for cases 0, 1, 2, 3, 4, 5, 6, 7, and 8, respectively. Therefore, when compared to case 0, the heat storage rate could be increased by 32.8, 16.1, 13.1, 29.0, 21.0, 21.7, 29.1, and 17.3% for cases 1, 2, 3 4, 5, 6, 7, and 8, respectively. As a result, heat storage rates are increased for all frustum tube systems compared to straight tube systems. To sum up, data from Figures 8 and 9 also indicates that case 1 performs the best, reducing 25.6% of melting time and increasing the heat storage rate by 32.8%. This suggests that among the tested cases, changing the geometry of the central tube to a frustum and employing a smaller gap width ($\delta = 5$ mm) has the most potential for improving the PCM thermal response during the melting mode.

6. Conclusions

Numerical analyses of the melting process are performed to evaluate the effects of the configuration modification on the thermal response of the PCM contained in a triplex tube storage system. The model is investigated in a three-dimensional configuration via commercial software (ANSYS-FLUENT). To enhance the heating and cooling processes in the system, the surface area of the tube is treated by single or multi-internal frustum tubes in vertical triplex tubes, including the ordinary straight triplex tubes. There are eight cases prepared in this work based on three scenarios: scenario 1: changing the middle tube to a frustum tube; scenario 2: changing the inner tube to a frustum tube; and scenario 3: changing both the inner and middle tube to frustum tubes. The cases were evaluated considering the charging duration and the heat storage rates. The main conclusions can be summarized as follows:

(1) Heat storage rates for all frustum tube systems are higher than those for straight tube systems. Because of the small gap width of case 1, which makes the surface area between heat transfer fluid and PCM bigger than that of other cases, case 1 was found to be the optimal case for the melting time-saving potential and the overall heat storage rate

(2) Using smaller values for the gap width between the tubes currying the heat-transfer fluid (HTF) increases the heat-exchanging areas between the PCM and HTF in charge. Therefore, the frustum tube configurations with smaller gap widths have a better potential for enhancing the PCM thermal response during the melting process

(3) In comparison to the straight tube configuration, the total melting times could be saved by 25.6, 14.2, 11.8, 23.1, 17.5, 19.0, 23.0, and 14.9% for the studied cases from 1 to 8, respectively. The results also indicate that the heat storage rate for the same studied cases could be raised by 32.8%, 16.1%, 13.1%, 29.0%, 21.0, 21.7, 29.1%, and 17.3%, respectively

Data Availability

Data will be provided on request.

Conflicts of Interest

The authors declare that they have no conflicts of interest.

References

[1] B. Ji, F. Zhang, X. Song, and Y. Tang, "A novel potassium-ion-based dual-ion battery," *Advanced Materials*, vol. 29, no. 19, p. 1700519, 2017.

[2] H. Xu, T. He, N. Zhong, B. Zhao, and Z. Liu, "Transient thermomechanical analysis of micro cylindrical asperity sliding contact of SnSbCu alloy," *Tribology International*, vol. 167, article 107362, 2022.

[3] M. S. Mahdi, H. B. Mahood, A. A. Khadom, A. N. Campbell, M. Hasan, and A. O. Sharif, "Experimental investigation of the thermal performance of a helical coil latent heat thermal energy storage for solar energy applications," *Thermal Science and Engineering Progress*, vol. 10, pp. 287–298, 2019.

[4] M. Wang, C. Jiang, S. Zhang, X. Song, Y. Tang, and H.-M. Cheng, "Reversible calcium alloying enables a practical room-temperature rechargeable calcium-ion battery with a high discharge voltage," *Nature Chemistry*, vol. 10, no. 6, pp. 667–672, 2018.

[5] X. Zhang, Y. Tang, F. Zhang, and C. S. Lee, "A novel aluminum–graphite dual-ion battery," *Advanced energy materials*, vol. 6, no. 11, p. 1502588, 2016.

[6] S. Mu, Q. Liu, P. Kidkhunthod, X. Zhou, W. Wang, and Y. Tang, "Molecular grafting towards high-fraction active nanodots implanted in N-doped carbon for sodium dual-ion batteries," *National science review*, vol. 8, no. 7, p. nwaa178, 2020.

[7] W. Qiao, W. Liu, and E. Liu, "A combination model based on wavelet transform for predicting the difference between monthly natural gas production and consumption of US," *Energy*, vol. 235, article 121216, 2021.

[8] M. S. Mahdi, H. B. Mahood, A. A. Khadom, and A. N. Campbell, "Numerical simulations and experimental verification of the thermal performance of phase change materials in a tube-bundle latent heat thermal energy storage system," *Applied Thermal Engineering*, vol. 194, article 117079, 2021.

[9] P. Yang, H. D. Ng, and H. Teng, "Numerical study of wedge-induced oblique detonations in unsteady flow," *Journal of Fluid Mechanics*, vol. 876, pp. 264–287, 2019.

[10] W. Qiao, Y. Wang, J. Zhang, W. Tian, Y. Tian, and Q. Yang, "An innovative coupled model in view of wavelet transform for predicting short- term PM10 concentration," *Journal of Environmental Management*, vol. 289, article 112438, 2021.

[11] H. Wu, X. Hu, X. Li et al., "Large-scale fabrication of flexible EPDM/MXene/PW phase change composites with excellent light-to-thermal conversion efficiency via water-assisted melt blending," *Composites Part A: Applied Science and Manufacturing*, vol. 152, article 106713, 2022.

[12] J. He, P. Xu, R. Zhou et al., "Combustion synthesized electrospun InZnO nanowires for ultraviolet photodetectors," *Advanced Electronic Materials*, vol. 8, no. 4, p. 2100997, 2022.

[13] P. Talebizadehsardari, J. M. Mahdi, H. I. Mohammed, M. Moghimi, A. H. Eisapour, and M. Ghalambaz, "Consecutive charging and discharging of a PCM-based plate heat exchanger with zigzag configuration," *Applied Thermal Engineering*, vol. 193, article 116970, 2021.

[14] R. B. Mahani, H. I. Mohammed, J. M. Mahdi et al., "Phase change process in a zigzag plate latent heat storage system during melting and solidification," *Molecules*, vol. 25, no. 20, p. 4643, 2020.

[15] M. Ghalambaz, H. I. Mohammed, A. Naghizadeh et al., "Optimum placement of heating tubes in a multi-tube latent heat thermal energy storage," *Materials*, vol. 14, no. 5, p. 1232, 2021.

[16] X. Sun, H. I. Mohammed, M. E. Tiji et al., "Investigation of heat transfer enhancement in a triple TUBE latent heat storage system using circular fins with inline and staggered arrangements," *Nanomaterials*, vol. 11, no. 10, p. 2647, 2021.

[17] Y. Ju, T. Zhu, R. Mashayekhi et al., "Evaluation of multiple semi-twisted tape inserts in a heat exchanger pipe using Al2O3 nanofluid," *Nanomaterials*, vol. 11, no. 6, p. 1570, 2021.

[18] M. Yang, C. Li, L. Luo, R. Li, and Y. Long, "Predictive model of convective heat transfer coefficient in bone micro- grinding using nanofluid aerosol cooling," *International Communications in Heat and Mass Transfer*, vol. 125, article 105317, 2021.

[19] X. Liu, H. I. Mohammed, A. Z. Ashkezari, A. Shahsavar, A. K. Hussein, and S. Rostami, "An experimental investigation on the rheological behavior of nanofluids made by suspending multi-walled carbon nanotubes in liquid paraffin," *Journal of Molecular Liquids*, vol. 300, article 112269, 2020.

[20] A. D. Farahani, S. D. Farahani, and E. Hajian, "Efficacy of magnetic field on nanoparticle-enhanced phase change material melting in a triple tube with porous fin," *Heat Transfer Research*, vol. 52, no. 12, 2021.

[21] R. D. C. Oliveski, F. Becker, L. A. O. Rocha, C. Biserni, and G. E. S. Eberhardt, "Design of fin structures for phase change material (PCM) melting process in rectangular cavities," *Journal of Energy Storage*, vol. 35, article 102337, 2021.

[22] A. Chamkha, A. Doostanidezfuli, E. Izadpanahi, and M. Ghalambaz, "Phase-change heat transfer of single/hybrid nanoparticles-enhanced phase- change materials over a heated horizontal cylinder confined in a square cavity," *Advanced Powder Technology*, vol. 28, no. 2, pp. 385–397, 2017.

[23] Y. Zhang, C. Li, D. Jia, D. Zhang, and X. Zhang, "Experimental evaluation of the lubrication performance of MoS_2/CNT nanofluid for minimal quantity lubrication in Ni-based alloy

grinding," *International Journal of Machine Tools and Manufacture*, vol. 99, pp. 19–33, 2015.

[24] N. S. Bondareva, M. Ghalambaz, and M. A. Sheremet, "Influence of the fin shape on heat transport in phase change material heat sink with constant heat loads," *Energies*, vol. 14, no. 5, p. 1389, 2021.

[25] A. Kumar, R. Kothari, S. K. Sahu, S. I. Kundalwal, and M. P. Paulraj, "Numerical investigation of cross plate fin heat sink integrated with phase change material for cooling application of portable electronic devices," *International Journal of Energy Research*, vol. 45, no. 6, pp. 8666–8683, 2021.

[26] S. Tuly, M. Rahman, M. Sarker, and R. Beg, "Combined influence of fin, phase change material, wick, and external condenser on the thermal performance of a double slope solar still," *Journal of Cleaner Production*, vol. 287, article 125458, 2021.

[27] P. Talebizadeh Sardari, H. I. Mohammed, J. M. Mahdi et al., "Localized heating element distribution in composite metal foam-phase change material: Fourier's law and creeping flow effects," *International Journal of Energy Research*, vol. 45, no. 9, pp. 13380–13396, 2021.

[28] C. Nie, J. Liu, and S. Deng, "Effect of geometry modification on the thermal response of composite metal foam/phase change material for thermal energy storage," *International Journal of Heat and Mass Transfer*, vol. 165, article 120652, 2021.

[29] J. Duan and F. Li, "Transient heat transfer analysis of phase change material melting in metal foam by experimental study and artificial neural network," *Journal of Energy Storage*, vol. 33, article 102160, 2021.

[30] M.-R. Wang, L. Deng, G.-C. Liu et al., "Porous organic polymer-derived nanopalladium catalysts for chemoselective synthesis of antitumor benzofuro [2, 3-b] pyrazine from 2-bromophenol and isonitriles," *Organic Letters*, vol. 21, no. 13, pp. 4929–4932, 2019.

[31] H. Teng, H. D. Ng, K. Li, C. Luo, and Z. Jiang, "Evolution of cellular structures on oblique detonation surfaces," *Combustion and Flame*, vol. 162, no. 2, pp. 470–477, 2015.

[32] M. S. Mahdi, H. B. Mahood, A. A. Alammar, and A. A. Khadom, "Numerical investigation of PCM melting using different tube configurations in a shell and tube latent heat thermal storage unit," *Thermal Science and Engineering Progress*, vol. 25, article 101030, 2021.

[33] B. Debich, A. El Hami, A. Yaich, W. Gafsi, L. Walha, and M. Haddar, "Design optimization of PCM-based finned heat sinks for mechatronic components: a numerical investigation and parametric study," *Journal of Energy Storage*, vol. 32, article 101960, 2020.

[34] M. Ghalambaz, S. M. H. Zadeh, S. Mehryan, I. Pop, and D. Wen, "Analysis of melting behavior of PCMs in a cavity subject to a non-uniform magnetic field using a moving grid technique," *Applied Mathematical Modelling*, vol. 77, pp. 1936–1953, 2020.

[35] S. Mehryan, M. Vaezi, M. Sheremet, and M. Ghalambaz, "Melting heat transfer of power-law non-Newtonian phase change nano-enhanced n-octadecane-mesoporous silica ($MPSiO_2$)," *International Journal of Heat and Mass Transfer*, vol. 151, article 119385, 2020.

[36] W. Qiao, Z. Li, W. Liu, and E. Liu, "Fastest-growing source prediction of US electricity production based on a novel hybrid model using wavelet transform," *International Journal of Energy Research*, vol. 46, no. 2, pp. 1766–1788, 2022.

[37] Y. Zhang, C. Li, D. Jia, D. Zhang, and X. Zhang, "Experimental evaluation of MoS_2 nanoparticles in jet MQL grinding with different types of vegetable oil as base oil," *Journal of Cleaner Production*, vol. 87, pp. 930–940, 2015.

[38] T. Gao, C. Li, Y. Zhang et al., "Dispersing mechanism and tribological performance of vegetable oil-based CNT nanofluids with different surfactants," *Tribology International*, vol. 131, pp. 51–63, 2019.

[39] S. H. Park, Y. G. Park, and M. Y. Ha, "A numerical study on the effect of the number and arrangement of tubes on the melting performance of phase change material in a multi-tube latent thermal energy storage system," *Journal of Energy Storage*, vol. 32, article 101780, 2020.

[40] N. Kousha, M. Rahimi, R. Pakrouh, and R. Bahrampoury, "Experimental investigation of phase change in a multitube heat exchanger," *Journal of Energy Storage*, vol. 23, pp. 292–304, 2019.

[41] P. Talebizadehsardari, H. I. Mohammed, J. M. Mahdi et al., "Effect of airflow channel arrangement on the discharge of a composite metal foam-phase change material heat exchanger," *International Journal of Energy Research*, vol. 45, no. 2, pp. 2593–2609, 2021.

[42] H. I. Mohammed, "Discharge improvement of a phase change material-air-based thermal energy storage unit for space heating applications using metal foams in the air sides," *Heat Transfer*, vol. 51, no. 5, 2002.

[43] M. Trafczynski, M. Markowski, K. Urbaniec, P. Trzcinski, S. Alabrudzinski, and W. Suchecki, "Estimation of thermal effects of fouling growth for application in the scheduling of heat exchangers cleaning," *Applied Thermal Engineering*, vol. 182, article 116103, 2021.

[44] B. Li, C. Li, Y. Zhang et al., "Heat transfer performance of MQL grinding with different nanofluids for Ni- based alloys using vegetable oil," *Journal of Cleaner Production*, vol. 154, pp. 1–11, 2017.

[45] A. Piccolo and A. J. Jaworski, "Experimental study of heat transfer characteristics of finned-tube and circular-pore heat exchangers in oscillatory flow," *Applied Thermal Engineering*, vol. 181, article 116022, 2020.

[46] E. M. El-Said, M. Abdulaziz, and M. M. Awad, "Thermodynamic performance evaluation for helical plate heat exchanger based on second law analysis," *Proc Roman Acad Ser A*, vol. 19, pp. 237–242, 2018.

[47] E. M. El-Said, M. Abdulaziz, and M. M. Awad, ""A numerical investigation on heat transfer enhancement and the flow characteristics in a new type plate heat exchanger using helical flow duct, " cogent," *Engineering*, vol. 4, no. 1, article 1396638, 2017.

[48] T. Gao, C. Li, D. Jia et al., "Surface morphology assessment of CFRP transverse grinding using CNT nanofluid minimum quantity lubrication," *Journal of Cleaner Production*, vol. 277, article 123328, 2020.

[49] A. Pourakabar and A. A. R. Darzi, "Enhancement of phase change rate of PCM in cylindrical thermal energy storage," *Applied Thermal Engineering*, vol. 150, pp. 132–142, 2019.

[50] R. Qaiser, M. M. Khan, L. A. Khan, and M. Irfan, "Melting performance enhancement of PCM based thermal energy storage system using multiple tubes and modified shell designs," *Journal of Energy Storage*, vol. 33, article 102161, 2021.

[51] X. Yang, J. Guo, B. Yang, H. Cheng, P. Wei, and Y.-L. He, "Design of non-uniformly distributed annular fins for a

shell-and-tube thermal energy storage unit," *Applied Energy*, vol. 279, article 115772, 2020.

[52] J. Guo, Z. Du, G. Liu, X. Yang, and M.-J. Li, "Compression effect of metal foam on melting phase change in a shell-and-tube unit," *Applied Thermal Engineering*, vol. 206, article 118124, 2022.

[53] X. Yang, X. Wang, Z. Liu, X. Luo, and J. Yan, "Effect of fin number on the melting phase change in a horizontal finned shell- and-tube thermal energy storage unit," *Solar Energy Materials and Solar Cells*, vol. 236, article 111527, 2022.

[54] J. Guo, X. Wang, B. Yang, X. Yang, and M.-J. Li, "Thermal assessment on solid-liquid energy storage tube packed with non-uniform angled fins," *Solar Energy Materials and Solar Cells*, vol. 236, article 111526, 2022.

[55] J. Guo, Z. Liu, B. Yang, X. Yang, and J. Yan, "Melting assessment on the angled fin design for a novel latent heat thermal energy storage tube," *Renewable Energy*, vol. 183, pp. 406–422, 2022.

[56] A. H. Eisapour, M. Eisapour, H. I. Mohammed, A. Shafaghat, M. Ghalambaz, and P. Talebizadehsardari, "Optimum design of a double elliptical latent heat energy storage system during the melting process," *Journal of Energy Storage*, vol. 44, article 103384, 2021.

[57] H. Ren, M. He, W. Lin, L. Yang, W. Li, and Z. Ma, "Performance investigation and sensitivity analysis of shell-and-tube phase change material thermal energy storage," *Journal of Energy Storage*, vol. 33, article 102040, 2021.

[58] J. R. Patel, M. K. Rathod, R. M. Elavarasan, and Z. Said, "Influence of longitudinal fin arrangement on the melting and solidification inside the triplex tube latent heat thermal storage system," *Journal of Energy Storage*, vol. 46, article 103778, 2022.

[59] J. R. Patel, M. K. Rathod, and M. Sheremet, "Heat transfer augmentation of triplex type latent heat thermal energy storage using combined eccentricity and longitudinal fin," *Journal of Energy Storage*, vol. 50, article 104167, 2022.

[60] M. A. Alnakeeb, M. A. Abdel Salam, and M. A. Hassab, ""Eccentricity optimization of an inner flat-tube double-pipe latent-heat thermal energy storage unit, " case studies," *Thermal Engineering*, vol. 25, article 100969, 2021.

[61] Z.-J. Zheng, Y. Xu, and M.-J. Li, "Eccentricity optimization of a horizontal shell-and-tube latent-heat thermal energy storage unit based on melting and melting-solidifying performance," *Applied Energy*, vol. 220, pp. 447–454, 2018.

[62] Y. Pahamli, M. J. Hosseini, A. A. Ranjbar, and R. Bahrampoury, "Analysis of the effect of eccentricity and operational parameters in PCM- filled single-pass shell and tube heat exchangers," *Renewable Energy*, vol. 97, pp. 344–357, 2016.

[63] M. Faghani, M. J. Hosseini, and R. Bahrampoury, "Numerical simulation of melting between two elliptical cylinders," *Alexandria Engineering Journal*, vol. 57, no. 2, pp. 577–586, 2018.

[64] M. Gorzin, M. J. Hosseini, M. Rahimi, and R. Bahrampoury, "Nano-enhancement of phase change material in a shell and multi-PCM-tube heat exchanger," *Journal of Energy Storage*, vol. 22, pp. 88–97, 2019.

[65] K. Chen, H. I. Mohammed, J. M. Mahdi, A. Rahbari, A. Cairns, and P. Talebizadehsardari, "Effects of non-uniform fin arrangement and size on the thermal response of a vertical latent heat triple-tube heat exchanger," *Journal of Energy Storage*, vol. 45, article 103723, 2022.

[66] F. T. Najim, H. I. Mohammed, H. M. T. Al-Najjar et al., "Improved melting of latent heat storage using fin arrays with non-uniform dimensions and distinct patterns," *Nanomaterials*, vol. 12, no. 3, p. 403, 2022.

[67] P. Talebizadeh Sardari, G. S. Walker, M. Gillott, D. Grant, and D. Giddings, "Numerical modelling of phase change material melting process embedded in porous media: effect of heat storage size," *Proceedings of the Institution of Mechanical Engineers, Part A: Journal of Power and Energy*, vol. 234, no. 3, pp. 365–383, 2020.

[68] J. M. Mahdi and E. C. Nsofor, "Melting enhancement in triplex-tube latent heat energy storage system using nanoparticles-metal foam combination," *Applied Energy*, vol. 191, pp. 22–34, 2017.

[69] M. Esapour, M. Hosseini, A. Ranjbar, Y. Pahamli, and R. Bahrampoury, "Phase change in multi-tube heat exchangers," *Renewable Energy*, vol. 85, pp. 1017–1025, 2016.

[70] W.-B. Ye, D.-S. Zhu, and N. Wang, "Numerical simulation on phase-change thermal storage/release in a plate-fin unit," *Applied Thermal Engineering*, vol. 31, no. 17-18, pp. 3871–3884, 2011.

[71] S. Mat, A. A. Al-Abidi, K. Sopian, M. Y. Sulaiman, and A. T. Mohammad, "Enhance heat transfer for PCM melting in triplex tube with internal-external fins," *Energy Conversion and Management*, vol. 74, pp. 223–236, 2013.

[72] J. M. Mahdi and E. C. Nsofor, "Solidification enhancement in a triplex-tube latent heat energy storage system using nanoparticles-metal foam combination," *Energy*, vol. 126, pp. 501–512, 2017.

Hindawi
Journal of Nanomaterials
Volume 2022, Article ID 5531041, 16 pages
https://doi.org/10.1155/2022/5531041

Research Article

Prescribed Thermal Activity in the Radiative Bidirectional Flow of Magnetized Hybrid Nanofluid: Keller-Box Approach

Iftikhar Ahmad,[1] Qazi Zan-Ul-Abadin,[1] Muhammad Faisal,[1] K. Loganathan,[2,3] Tariq Javed,[4] and Dinesh Kumar Chaudhary[5]

[1]*Department of Mathematics, Azad Jammu & Kashmir University, Muzaffarabad 13100, Pakistan*
[2]*Research and Development Wing, Live4Research, Tiruppur, Tamilnadu 638106, India*
[3]*Department of Mathematics and Statistics, Manipal University Jaipur, Jaipur, 303007 Rajasthan, India*
[4]*Department of Mathematics and Statistics, International Islamic University, Islamabad 44000, Pakistan*
[5]*Department of Physics, Amrit Campus, Tribhuvan University, Kathmandu, Nepal*

Correspondence should be addressed to Qazi Zan-Ul-Abadin; qazi.zain@ajku.edu.pk, K. Loganathan; loganathankaruppusamy304@gmail.com, and Dinesh Kumar Chaudhary; din.2033@gmail.com

Received 5 May 2022; Revised 9 June 2022; Accepted 16 July 2022; Published 27 July 2022

Academic Editor: Zafar Said

In this exploration, we decided to investigate the significance of prescribed thermal conditions on unsteady 3D dynamics of water-based radiative hybrid nanofluid with the impact of cylindrical-shaped nanosized particles (alumina (Al_2O_3) and titania (TiO_2)). For physical relevancy, the impact of the Lorentz force is also included. The combination of suitable variables has been used to transform the transport equations into the system of ordinary differential equations and then numerically solved via the Keller-Box approach. Graphical illustrations have been used to predict the impact of the involved parameters on the thermal setup. Convergence analysis is presented via the grid independence approach. Skin frictions and local Nusselt numbers against various choices of involved parameters are plotted and arranged in tabular forms. It is observed through the present investigation that temperature distribution is increased with the higher choices of radiation parameter $0.0 \le R_d \le 2.0$ and decreased with the improvement in the choices of temperature maintaining indices (i.e., $-2.0 \le r, s \le 2.0$). Moreover, the thermophysical properties except specific heat for hybrid nanofluid are improved with the involvement of cylindrical-shaped nanoparticles. The temperature of the hybrid nanofluid is observed to be higher for variable thermal conditions as compared to uniform thermal conditions. Outfalls for a limited version of the report have been compared with a previous published paper.

1. Introduction

Nanofluids have been widely used in many technological and industrial processes like nuclear reactors, automobile radiators, and solar aircrafts because their superior thermal conductivity as compared to conventional fluids as the rate of heating/cooling is extremely reliant on the performance of thermal conductivity of the nanosized particles. Various mathematical relations [1, 2] have been adopted to investigate the thermophysical properties of nanosized particles but the most appropriate mathematical relations regarding these properties are developed/discussed by Masoumi et al. [3]. The boundary regime flow of nanofluid due to an expanding device is firstly numerically deliberated by Khan and Pop [4] with random motion and thermodiffusion effects of tiny-sized particles. Sheikholeslami and Rokni et al. [5] elaborated the heat transfer mechanism by using single-phase and double-phase estimations of magneto-nanofluid and proved that higher estimation of tiny particle concentration augments the temperature gradient. Ganvir et al. [6] summarized the combined performance of convective heat transference, particle size, thermophysical properties, inlet velocity, volume concentration, and liquid temperature, both analytically and numerically.

An improved approach to overcome the thermal needs of industrial and engineering processes is famous with the name of hybrid nanofluid. The investigation about the

importance of hybrid nanofluid has gained a tremendous height due to their wide applications in domestic refrigerators, engine cooling, microelectronics, heat exchanger devices, pharmaceutical processes, fuel cells, grinding processes, ultrasonic radiations, thermal diffusion processes, and many more. Hybrid nanofluid can be formed by submerging two or more nanoparticles into the host liquid. These nanoparticles may include metals, dielectrics, liquid materials, polymeric, lipids, and semiconductors. Some common examples of nanoparticles are copper, zinc-oxide, carbon nanotubes, phosphates, zinc sulfide, cadmium telluride, etc. Alumina and titania nanoparticles are widely used in engineering applications, and these are prepared from metal precursors. These tiny-sized particles can be synthesized by electrochemical, chemical, or photochemical methods. These nanoparticles have commercial applications due their structure, high strength, electron affinity, and electrical conductivity. The most widely used oxide ceramic material is alumina, and it has applications in cutting tools, tap washers, spark plugs, etc. The most abundantly used nanomaterial for human life is titania, and it is used in sunscreen, biomedical applications, photovoltaic devices, pharmaceutical drugs, and waste water treatment and as a food additive. Sarkar et al. [7] reviewed the advantages and disadvantages of nano as well as hybrid nanofluids and recommended that hybrid nanofluids have various advantages as compared to conventional nanofluids because of their auspicious heat transference enhancement, pressure drop ability, improved thermal network, and favorable aspect ratio. Sidik et al. [8] disclosed the recent progress related to the field of hybrid nanofluids by discussing the factors affecting their thermal properties and stability. Unsteady dynamics of hybrid nanofluid with heat transference characteristic due to the expanding/contracting device is numerically explored by Waini et al. [9] and presented the stability analysis regarding the dual solutions. Numerical evaluation regarding pure water-based hybrid nanofluids with the combination of nanoparticles (alumina, titania, and silica) is explored by Minea [10]. Investigation concerning water-based hybrid nanofluids with the optical properties of titania and alumina nanoparticles is made by Leong et al. [11] along the stability of the obtained solution. Moldoveanu et al. [12] glimpsed the experimental evaluation regarding the hybrid mixture of alumina and titania nanoparticles with viscosity as the main focus of the investigation. Moldoveanu et al. [13] also evaluated the hybrid mixture of titania and alumina nanoparticles with thermal conductivity as the foremost point of the exploration. Shirazi et al. [14] experimentally discussed the mixture of titania nanoparticles and water in order to observe the level of the oil recovery enhancement process. Khan et al. [15] elaborated the mixed convective stagnation dynamics of the radioactive mixture of titania, copper, and water in the magnetic environment towards an expandable device. An experimental evaluation regarding the stability, characterization, and dynamic viscosity of the hybrid mixture of titania and cupric oxide with water as working fluid is completed by Asadi et al. [16]. Ahmad et al. [17] explained the heat/mass transference attributes in the hybrid interpretation of alumina and copper nanoparticles through porous media. A comparative depiction regarding unsteady transport of magnetically influenced water-based fluid with the hybrid mixture of nanoparticle combinations (copper-alumina and alumina-titania) towards an expanding device using finite element approach is elaborated by Ali et al. [18]. Some recent scientific contributions about hybrid nanofluids have been addressed by some scholars/researchers (refs. [19–21]) and their applications (refs. [22–26]).

In the last few years, researchers are interested to discuss the novel impact of the shape of nanoparticles in the improvement of heating/cooling processes, solar aircrafts, effective thermal conductivity, and other thermophysical characteristics. Zhang et al. [27] measured the values of effective thermal conductivity and thermal diffusivity of nanofluids by considering the spherical as well as cylindrical-shaped nanoparticles using transient technique and predicted that Hamilton and Crosser models provide the best approximation for these thermophysical characteristics. Later on, Timofeeva et al. [28] theoretically explained the effect of the nanoparticle shape on thermophysical behaviour of alumina with the help of experimental data. Yang and Ma [29] provided the computer simulation for the understanding of translocation processes of nanoparticles with the usages of different shapes (ellipsoids, discs, rods, and spheres) of nanoparticles across a lipid bilayer. Maheshwary et al. [30] experimentally discussed the significance of the particle shape, particle size, and concentration on thermal conductivity of water-conveying titania nanofluid and predicted that thermal conductivity of the mixture is improved by intensifying the choices of the particle shape, size, and concentration. Sheikholeslami [31] discussed the effect of various shapes (platelet, brick, cylinder, and sphere) of nanoparticles on the forced convective flow of water-conveying cupric oxide nanofluid within a permeable lid-driven enclosure in the magnetic environment by using CVFEM and indicated that the Nusselt number declines with the augments of the Lorentz force. Rashid and Liang [32] numerically investigated the implication of the nanoparticle shape (sphere and lamina) on the dynamics of magnetized nanofluid with heat transference phenomenon, thermal radiation effect, and joule heating process towards an expanding disk through a porous space in a rotating frame. Dinarvand and Rostami [33] analyzed the shape factor influence of nanoparticles (graphene oxide and magnetite) for bidirectional unsteady dynamics of water-conveying hybrid nanofluid squeezed between two parallel surfaces using the Tiwari-Das model and predicted that the shape factor effect of nanoparticles has a crucial role in food processing, polymer processing, injection modeling, lubrication, etc. Bhattad and Sarkar [34] theoretically examined the significances of the nanoparticle size and shapes (brick, platelet, sphere, and cylinder) on the thermohydraulic enactment of a sheet evaporator by using hybrid nanofluids having various combinations of mixtures.

The combined significances of thermal radiation and Lorentz force space contribute a vital role in the development of combustion processes, nuclear weapons, electron ramifications, polarization process, stellar evolution, heat conduction process, petroleum reservoirs, etc. Turkyilmazoglu and Pop [35] numerically addressed the natural convection dynamics of radiative water-conveying nanofluid containing copper, alumina, titania, cupric oxide, and silver nanoparticles across a flat device. Devi and Devi [36] numerically examined the

effects of Newtonian heating and Lorentz force on bidirectional dynamics of water-conveying hybrid nanofluid with the mixture of copper and alumina. From this exploration, it is conveyed that hybrid nanofluid provides the better rate of heat transference than conventional nanofluid. Sheikholeslami and Sadoughi [37] numerically disclosed the MHD effect on the flow of nanofluid inside a porous enclosure with four square heat sources by considering the importance of nanoparticle shapes. Hayat et al. [38] discussed the radiative and heat transfer characteristics for hybrid mixture of silver and cupric oxide nanoparticles with water as base liquid in a rotating frame. It is deduced that rotation and radiation phenomena boost the thermal environment of the hybrid mixture. Some more recent exploration regarding the implications of the Lorentz force and porous media is found in the refs. [39–43].

The variation in the temperature fluctuation at the geometric surfaces is beneficial for several industrial and engineering applications. Liu and Andersson [44] implemented the variable thermal conditions to investigate the heat transference characteristics for 3D dynamics of a liquid towards a bidirectional expanding device. Both the heating processes, namely, PST (prescribed surface temperature) and PHF (prescribed heat flux), have been discussed by Liu and Andersson, and it was predicted that variable thermal conditions provide an improved rate of heat transference than arbitrary thermal conditions at the geometric surface. Oliveira et al. [45] discussed the practical applications of variable thermal conditions in the engineering processes like power converters, motor controllers, passive thermosyphons, and air conditioning process. Waini et al. [46] discussed the heat transference characteristic for the steady dynamics of hybrid nanofluid past a vertical thin needle by considering the variable heat flux at the geometric surface. Waini et al. [47] also investigated the heat transference process along with variable heat flux for the stagnated dynamics of hybrid nanofluid (alumina and copper) with water as working liquid on a contracting cylindrical geometry. Some more recent contributions related to the variable temperature of the geometrical surfaces are found in the refs. [48–52].

In the view of abovementioned comprehensive literature survey, it is noticed that much attention has not been given to the dynamics of hybrid nanofluid towards bidirectional elongating geometry. The main theme of the present contribution is to predict the effects of cylindrical-shaped nanoparticles (alumina and titania) for radiative water-conveying hybrid nanofluid flow towards an unsteady bidirectional elongating device with prescribed thermal conditions, and this type of contribution is not found in literature to the best of the author's knowledge. Additionally, influence of the Lorentz force is also incorporated in the mathematical model. Suitable mathematical relations have been used to transform the transport equations into dimensionless forms, and then, computer simulation is made via the Keller-Box method [53–59]. Finally, the foremost outcomes obtained through present numerical investigation are presented through various plots and tables.

2. Mathematical Formulation

In order to frame the unsteady mathematical model for bidirectional dynamics of water-conveying hybrid nanofluid with cylindrical-shaped nanoparticles (alumina (Al_2O_3) and titania (TiO_2)), the Cartesian configuration is adopted. The mathematical relation of the Lorentz force is used to inspect the MHD (magnetohydrodynamics) effects with strength $B_0 = b_0/\sqrt{1-ct}$ (b_0 represents the initial strength of the magnetic field). The mathematical relation of Rosseland approximation is then followed to examine the effects of thermal radiation. The tiny particles are considered in thermal equilibrium. The no-slip phenomenon is considered at the surface to keep the flow incompressible as well as laminar. Expansion velocity $u_w = ax/(1-ct)\,; a > 0, c > 0$ is opted along the x-axis, and the expansion velocity $v_w = by/(1-ct)\,; b \geq 0$ is decided along the y-axis, whereas $0 < z < \infty$ is the region covered by the hybrid nanofluid (as sketched in Figure 1). In order to provide the variable temperature mechanism at the surface, two types of thermal conditions, namely, PST and PHF, are applied. Table 1 is constructed to summarize the thermophysical characteristics of water H_2O, alumina, and titania.

In the continuation of the abovementioned assumptions with a boundary layer theory, the transport equations are manifested as follows (refs. [38, 52]):

$$\begin{aligned}
&\frac{\partial u}{\partial x} + \frac{\partial v}{\partial y} + \frac{\partial w}{\partial z} = 0,\\
&\frac{\partial u}{\partial t} + u\frac{\partial u}{\partial x} + v\frac{\partial u}{\partial y} + w\frac{\partial u}{\partial z} = \frac{\mu_{\mathrm{hnf}}}{\rho_{\mathrm{hnf}}}\frac{\partial^2 u}{\partial z^2} - \frac{\sigma_{\mathrm{hnf}}}{\rho_{\mathrm{hnf}}}{B_0}^2 u,\\
&\frac{\partial v}{\partial t} + u\frac{\partial v}{\partial x} + v\frac{\partial v}{\partial y} + w\frac{\partial v}{\partial z} = \frac{\mu_{\mathrm{hnf}}}{\rho_{\mathrm{hnf}}}\frac{\partial^2 v}{\partial z^2} - \frac{\sigma_{\mathrm{hnf}}}{\rho_{\mathrm{hnf}}}{B_0}^2 v,\\
&\frac{\partial T}{\partial t} + u\frac{\partial T}{\partial x} + v\frac{\partial T}{\partial y} + w\frac{\partial T}{\partial z} = \alpha_{\mathrm{hnf}}\frac{\partial^2 T}{\partial z^2} - \frac{1}{\left(\rho C_p\right)_{\mathrm{hnf}}}\frac{\partial q_{\mathrm{rad}}}{\partial z}.
\end{aligned} \tag{1}$$

The velocity and thermal conditions for equation (1) are conveyed as follows (ref. [41]):

$$\begin{aligned}
&z = 0 : u = u_w(x,t) = \frac{ax}{1-ct},\\
&v = v_w(y,t) = \frac{by}{1-ct},\\
&w = 0,\\
&z \longrightarrow \infty : u \longrightarrow 0,\\
&v \longrightarrow 0,\\
&\text{PST case} : z = 0 : T = T_w(x,y,t) = T_\infty + T_0\left(\frac{x^r y^s}{1-ct}\right),\\
&z \longrightarrow \infty : T \longrightarrow T_\infty,\\
&\text{PHF case} : z = 0 : -k_{\mathrm{hnf}}\left(\frac{\partial T}{\partial z}\right)_w = q_w(x,y,t) = T_1\left(\frac{x^r y^s}{1-ct}\right),\\
&z \longrightarrow \infty : T \longrightarrow T_\infty.
\end{aligned} \tag{2}$$

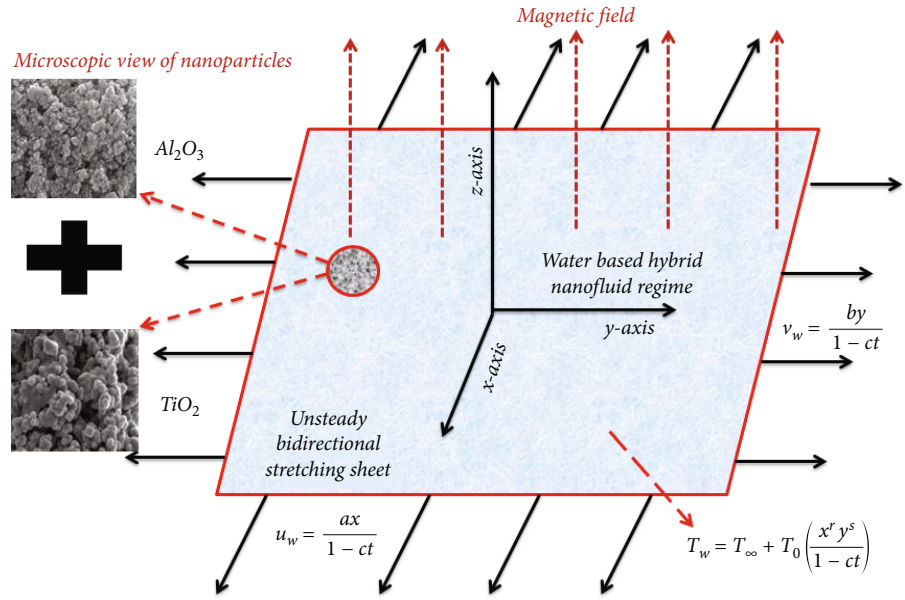

Figure 1: Graphical abstract of the considered hybrid nanofluid model.

Table 1: Thermophysical features of water, alumina, and titania nanoparticles (refs. [15, 17, 18]).

Thermophysical features	Base fluid	Nanoparticles	
	H_2O	$Al_2O_3(\psi_1)$	$TiO_2(\psi_2)$
Density (ρ): kg/m^3	997.1	3970	4250
Thermal conductivity (k): W/mK	0.613	40.0	8.9538
Specific heat (C_p): J/kgK	4179	765	686.2
Electrical conductivity: (σ): S/m	5.5×10^{-6}	35×10^6	0.24×10^7
Prandtl number: Pr	6.20	—	—

Here, (u, v, w) designates the velocity components along the x-, y-, and z-directions, respectively, T shows the temperature at the surface, time factor is symbolized by t, (r, s) are the indices that are used to control the temperature at the surface, T_0 and T_1 are dimensional constants, μ_{hnf} is opted to describe the effective viscosity of the hybrid mixture, ρ_{hnf} is chosen to label the density of the hybrid mixture, k_{hnf} is taken to mark the thermal conductivity of the hybrid mixture, $\alpha_{\text{hnf}} = k_{\text{hnf}}/(\rho C_p)_{\text{hnf}}$ is picked to state the thermal diffusivity of the hybrid mixture, $C_{p_{\text{hnf}}}$ is selected to represent the specific heat capacity, and σ_{hnf} is typified to express the influence of electrical conductivity of the hybrid nanofluid.

The mathematical relations to introduce the cylindrical shaped nanoparticles for present evolution of hybrid nanomaterial are composed as follows (refs. [2, 27, 31]):

$$\rho_{\text{hnf}} = \psi_1\rho_{p1} + \psi_2\rho_{p2} + (1-\psi_1-\psi_2)\rho_f,$$

$$(\rho C_p)_{\text{hnf}} = \psi_1(\rho C_p)_{p1} + \psi_2(\rho C_p)_{p2} + (1-\psi_1-\psi_2)(\rho C_p)_f,$$

$$\frac{k_{\text{hnf}}}{k_{\text{bf}}} = \frac{(k_{p2}+3.82k_{\text{bf}}) - 3.82\psi_2(k_{p2}-k_{\text{bf}})}{(k_{p2}+3.82k_{\text{bf}}) + \psi_2(k_{p2}-k_{\text{bf}})},$$

$$\frac{k_{\text{bf}}}{k_f} = \frac{(k_{p1}+3.82k_f) - 3.82\psi_1(k_{p1}-k_f)}{(k_{p1}+3.82k_f) + \psi_1(k_{p1}-k_f)},$$

$$\frac{\sigma_{\text{hnf}}}{\sigma_{\text{bf}}} = 1 + \frac{3\left((\sigma_{p2}/\sigma_{\text{bf}})-1\right)\psi_2}{(\sigma p_2/\sigma_{\text{bf}}) + 2 - \left((\sigma_{p2}/\sigma_{\text{bf}})-1\right)\psi_2},$$

$$\frac{\sigma_{\text{bf}}}{\sigma_f} = 1 + \frac{3\left((\sigma_{p1}/\sigma_f)-1\right)\psi_1}{(\sigma_{p1}/\sigma_f) + 2 - \left((\sigma_{p1}/\sigma_f)-1\right)\psi_1},$$

$$\alpha_{\text{hnf}} = \frac{k_{\text{hnf}}}{(\rho C_p)_{\text{hnf}}},$$

$$\frac{\mu_{\text{hnf}}}{\mu_{\text{bf}}} = 1 + 13.5\psi_2 + 904.4{\psi_2}^2,$$

$$\frac{\mu_{\text{bf}}}{\mu_f} = 1 + 13.5\psi_1 + 904.4{\psi_1}^2. \quad (3)$$

Here, quantities of volume fractions for alumina and titania nanoparticles are expressed through ψ_1 and ψ_2, respectively. The case of conventional fluid can be recovered by considering $\psi_1 = \psi_2 = 0$.

The equation for radiative heat transfer is defined as follows (refs. [35, 38]):

$$q_{\text{rad}} = -\frac{16\sigma^*}{3k^*} T_\infty{}^3 \frac{\partial T}{\partial z}. \tag{4}$$

Here, q_{rad} describes the radiative heat transference, σ^* illustrates the Stefan Boltzmann factor, and k^* explains the effect of the mean absorption factor.

The set of relations used to nondimensionalize the present mathematical model is conveyed as follows (refs. [41, 52]):

$$\begin{aligned} u &= \frac{ax}{1-ct} f'(\eta), \\ v &= \frac{ay}{1-ct} g'(\eta), \\ w &= -\left(\frac{a\vartheta_f}{1-ct}\right)^{1/2} [f(\eta) + g(\eta)], \\ \eta &= \left(\frac{a}{\vartheta_f(1-ct)}\right)^{1/2} z, \end{aligned} \tag{5}$$

$$\begin{aligned} &\text{PST case} : \theta(\eta) = \frac{T(x,y,z,t) - T_\infty}{T_w(x,y,t) - T_\infty}, \\ &\text{PHF case} : T - T_\infty = \frac{T_1}{k_f}\left(\frac{\vartheta_f}{a(1-ct)}\right)^{1/2} x^r y^s \phi(\eta). \end{aligned} \tag{6}$$

With the involvement of equations (6) and (7), the transport equations become

$$\varepsilon_1 f''' - f'^2 + (f+g)f'' - S\left(f' + \frac{\eta}{2} f''\right) - \varepsilon_2 M^2 f' = 0, \tag{7}$$

$$\varepsilon_1 g''' - g'^2 + (f+g)g'' - S\left(g' + \frac{\eta}{2} g''\right) - \varepsilon_2 M^2 g' = 0, \tag{8}$$

$$\text{PST case} : \varepsilon_3(1+R_d)\theta'' + \Pr\left((f+g)\theta' - \left(rf' + sg'\right)\theta - S\left(\theta + \frac{\eta}{2}\theta'\right)\right) = 0, \tag{9}$$

$$\text{PHF case} : \varepsilon_3(1+R_d)\phi'' + \Pr\left((f+g)\phi' - \left(rf' + sg'\right)\phi - S\left(\phi + \frac{\eta}{2}\phi'\right)\right) = 0, \tag{10}$$

with boundary restrictions

$$\begin{aligned} f(0) + g(0) &= 0, \\ f'(0) &= 1, \\ g'(0) &= \alpha, \\ f'(\infty) &\longrightarrow 0, \\ g'(\infty) &\longrightarrow 0, \\ \text{PST case} : \theta(0) &= 1, \\ \theta(\infty) &\longrightarrow 0, \\ \text{PHF case} : \phi'(0) &= -\frac{k_f}{k_{\text{hnf}}}, \phi(\infty) \longrightarrow 0. \end{aligned} \tag{11}$$

Here, the Hartmann number is recognized by $M = (\sigma_f/a\rho_f)^{1/2} b_0$, the unsteady factor is stated by $S = c/a$, the elongation ratio is expressed by $\alpha = b/a$, the Prandtl factor is indicated by $\Pr = \upsilon_f/\alpha_f$, $R_d = (16\sigma^*/3k^*k_f)T_\infty{}^3$ is the radiation factor, and $(\varepsilon_1, \varepsilon_2, \varepsilon_3)$ are the relations for the present hybrid mixture and these relations are elaborated as follows:

$$\begin{aligned} \varepsilon_1 &= \frac{\left(1 + 13.5\psi_2 + 904.4\psi_2{}^2\right)\left(1 + 13.5\psi_1 + 904.4\psi_1{}^2\right)}{\left(\psi_1\left(\rho_{p1}/\rho_f\right) + \psi_2\left(\rho_{p2}/\rho_f\right) + (1-\psi_1-\psi_2)\right)}, \\ \varepsilon_2 &= \frac{\left(1 + \left(\left(3\left(\left(\sigma_{p2}/\sigma_{\text{bf}}\right) - 1\right)\psi_2\right)/\left(\left(\sigma_{p2}/\sigma_{\text{bf}}\right) + 2 - \left(\left(\sigma_{p2}/\sigma_{\text{bf}}\right) - 1\right)\psi_2\right)\right)\right)\left(1 + \left(\left(3\left(\left(\sigma_{p1}/\sigma_f\right) - 1\right)\psi_1\right)/\left(\left(\sigma_{p1}/\sigma_f\right) + 2 - \left(\left(\sigma_{p1}/\sigma_f\right) - 1\right)\psi_1\right)\right)\right)}{\psi_1\left(\rho_{p1}/\rho_f\right) + \psi_2\left(\rho_{p2}/\rho_f\right) + (1-\psi_1-\psi_2)}, \\ \varepsilon_3 &= \frac{\left(\left(\left(k_{p2} + 3.82k_{\text{bf}}\right) - 3.82\psi_2\left(k_{p2} - k_{\text{bf}}\right)\right)/\left(\left(k_{p2} + 3.82k_{\text{bf}}\right) + \psi_2\left(k_{p2} - k_{\text{bf}}\right)\right)\right)\left(\left(\left(k_{p1} + 3.82k_f\right) - 3.82\psi_1\left(k_{p1} - k_f\right)\right)/\left(\left(k_{p1} + 3.82k_f\right) + \psi_1\left(k_{p1} - k_f\right)\right)\right)}{\psi_1\left(\left(\rho C_p\right)_{p1}/\left(\rho C_p\right)_f\right) + \psi_2\left(\left(\rho C_p\right)_{p2}/\left(\rho C_p\right)_f\right) + (1-\psi_1-\psi_2)}. \end{aligned} \tag{12}$$

The most fascinating quantities for thermal processes and most used in the improvement of heat exchanger devices are termed as skin-friction coefficients (i.e., C_{fx} and C_{fy}) and the local Nusselt number (i.e., Nu_x). The

mathematical formulations of these quantities are communicated as follows (refs. [36, 44, 51]):

$$
\begin{aligned}
C_{fx} &= \frac{\tau_{wx}}{\rho_f {u_w}^2},\\
C_{fy} &= \frac{\tau_{wy}}{\rho_f {v_w}^2},\\
\tau_{wx} &= \mu_{\mathrm{hnf}} \left(\frac{\partial u}{\partial z}\right)_{z=0},\\
\tau_{wy} &= \mu_{\mathrm{hnf}} \left(\frac{\partial v}{\partial z}\right)_{z=0},\\
\text{PST case} : Nu_x &= \frac{x q_h}{k_f (T_w - T_\infty)},\\
q_h &= -k_{\mathrm{hnf}} \left(\frac{\partial T}{\partial z}\right)_{z=0} + (q_{\mathrm{rad}})_w,\\
\text{PHF case} : Nu_x &= \frac{x q_h}{k_f (T - T_\infty)},\\
q_h &= -k_{\mathrm{hnf}} \left(\frac{\partial T}{\partial z}\right)_{z=0} + (q_{\mathrm{rad}})_w.
\end{aligned}
\tag{13}
$$

The dimensionless formulations of the abovementioned quantities using Reynold's numbers $\mathrm{Re}_x = x u_w/\vartheta_f$, $\mathrm{Re}_y = y v_w/\vartheta_f$ are transported as follows:

$$
\begin{aligned}
{\mathrm{Re}_x}^{1/2} C_{fx} = {} & \left(1 + 13.5\psi_1 + 904.4{\psi_1}^2\right)\\
& \cdot \left(1 + 13.5\psi_2 + 904.4{\psi_2}^2\right) f''(0),
\end{aligned}
\tag{14}
$$

$$
\begin{aligned}
{\mathrm{Re}_y}^{1/2} C_{fy} = {} & \alpha^{-3/2} \left(1 + 13.5\psi_1 + 904.4{\psi_1}^2\right)\\
& \cdot \left(1 + 13.5\psi_2 + 904.4{\psi_2}^2\right) g''(0),
\end{aligned}
\tag{15}
$$

$$
{\mathrm{Re}_x}^{-1/2} Nu_x = \begin{cases} -\dfrac{k_{\mathrm{hnf}}}{k_f}(1 + R_d)\theta'(0) & \text{(PST case)},\\ (1 + R_d)\dfrac{1}{\phi(0)} & \text{(PHF case)}. \end{cases}
\tag{16}
$$

3. Keller-Box Simulation

The final form of the system of equations obtained through the aforementioned modeling along with boundary conditions is simulated via the Keller-Box approach. This numerical approach has accuracy of up to second order and has rapid convergence ability than other routine work numerical approaches (shooting method, RK-method, BVP4c, etc.). This approach also provides the flexibility about adoption of the step size for the computational domain and is more appropriate for the solution of boundary layer flow problems. The major advantage of this method over other numerical methods is its unique conversion procedure of differential equations into algebraic equations using central difference approximations. Foremost steps to implement this numerical approach are stated below and summarized via the flow chart (Figure 2):

(i) The first step is to transform the higher-order differential equations into first-order differential equations

(ii) The next step is to transmute the obtained differential system into the difference equation system via central difference numerical approximations

(iii) Linearization of the system of difference equations is completed with the courtesy of Newton's linearization standard method

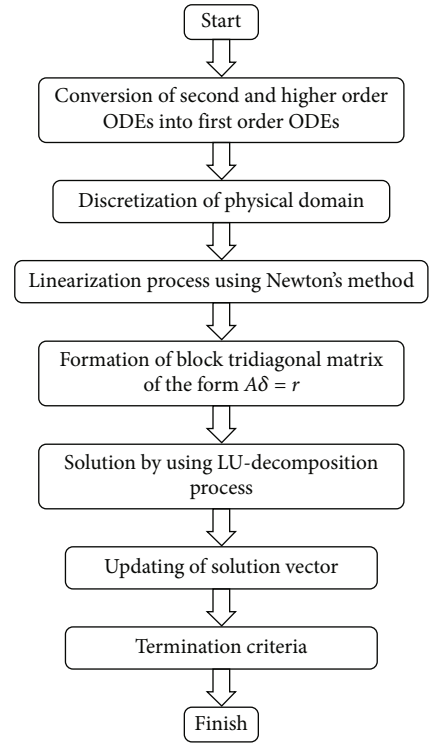

Figure 2: Flow chart of numerical procedure.

Table 2: Convergence of the Keller-Box simulation for $\alpha = S = M = 0.5$, $r = s = 1.0$, $\psi_1 = \psi_2 = 0.04$, $R_d = 0.5$.

n_p	$-f''(0)$	$-g''(0)$	$-\theta'(0)$	$1/\phi(0)$
500	0.6718217	0.317969	2.631693	3.556174
1000	0.6718218	0.317969	2.631367	3.555733
1500	0.6718218	0.317969	2.631306	3.555651
2000	0.6718218	0.317969	2.631285	3.555623
2500	0.6718218	0.317969	2.631275	3.555609
3000	0.6718218	0.317969	2.63127	3.555602
3500	0.6718218	0.317969	2.631267	3.555598
4000	0.6718218	0.317969	2.631265	3.555595
4500	0.6718218	0.317969	2.631263	3.555593
5000	0.6718218	0.317969	2.631262	3.555592
10000	0.6718218	0.317969	2.631262	3.555592

Table 3: Outcomes in the nonappearance of nanoparticles, magnetic and unsteadiness aspects.

$\alpha = 1.0$	$-f''(0)$	$f(\infty)$	$-g''(0)$	$g(\infty)$
Present	1.173722	0.751498	1.173722	0.751498
Liu and Andersson [44]	1.173721	0.751494	1.173721	0.751494
$\alpha = 0.5$	$-f''(0)$	$f(\infty)$	$-g''(0)$	$g(\infty)$
Present	1.093095	0.842387	0.465205	0.451678
Liu and Andersson [44]	1.093096	0.842360	0.465206	0.451663
$\alpha = 0.0$	$-f''(0)$	$f(\infty)$	$-g''(0)$	$g(\infty)$
Present	−1.0	1.0	0.0	0.0
Liu and Andersson [44]	−1.0	1.0	0.0	0.0

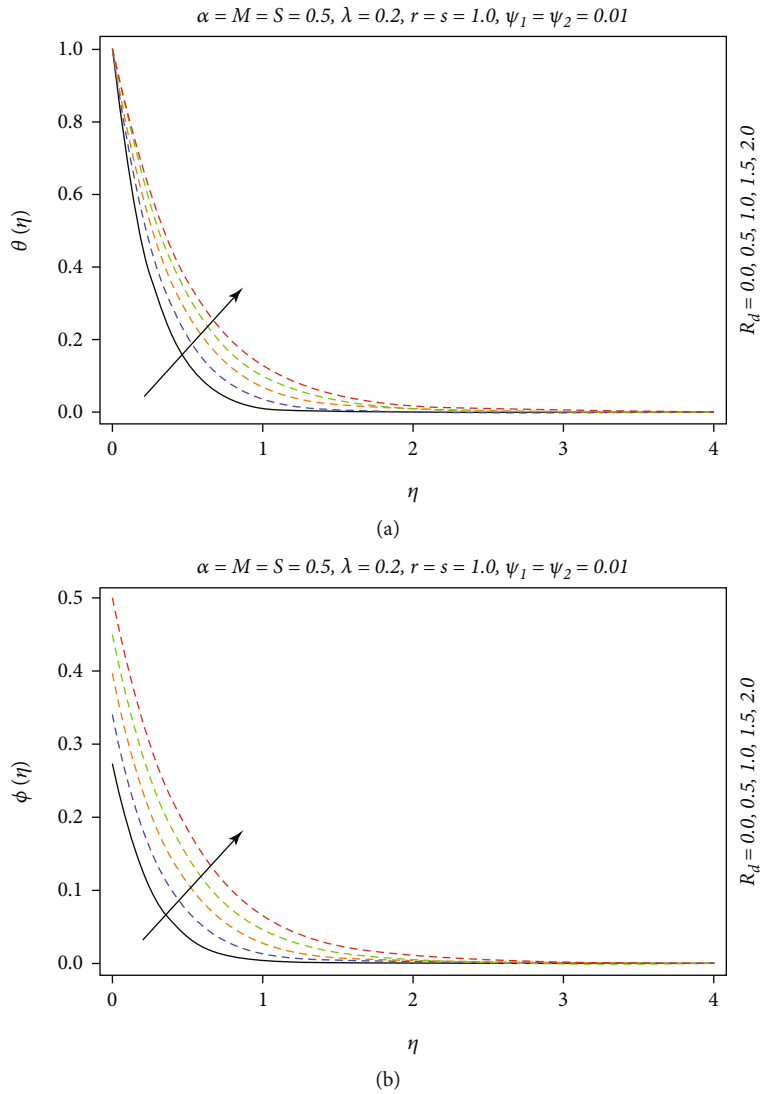

Figure 3: (a, b) Temperature fluctuation against the variation of radiation factor R_d for the PST case and for the PHF case.

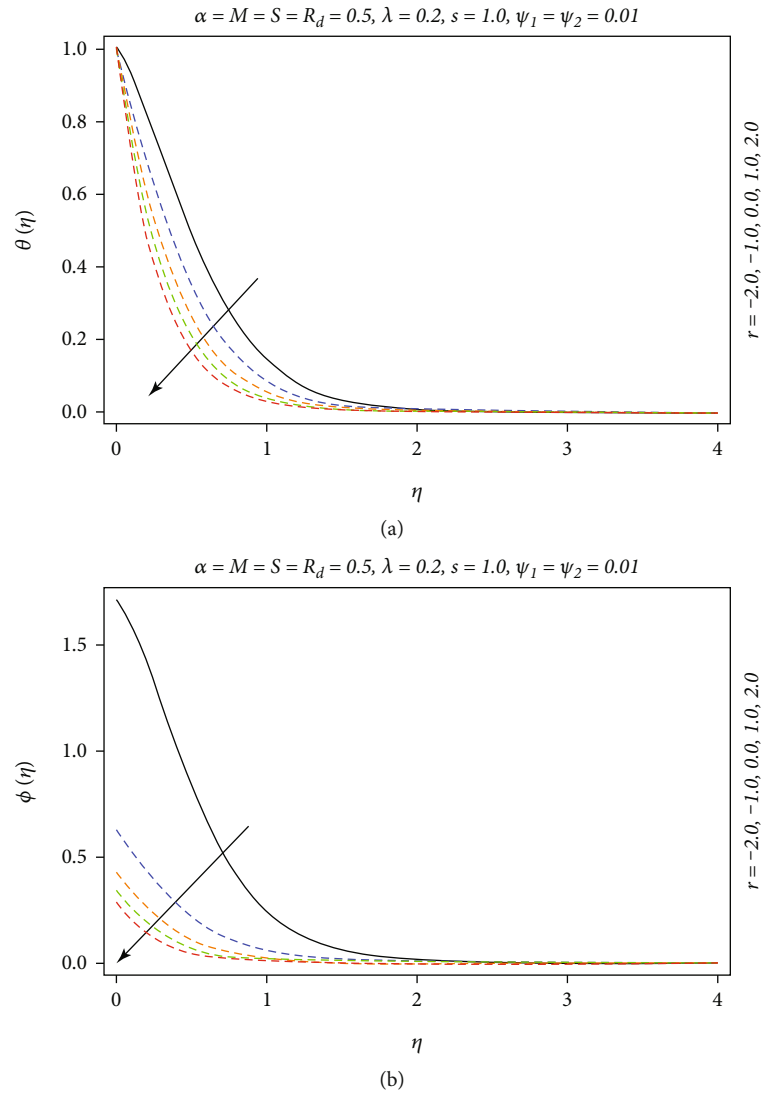

Figure 4: (a, b) Temperature fluctuation against the variation of the index r for the PST case and for the PHF case.

(iv) The linearized equations are then arranged into matrix-vector forms

(v) The LU decomposition technique is opted to solve the obtained matrix-vector problem

(vi) Finally, the value of the unknown vector provides the numerical solution of the aforementioned mathematical problem

During the implementation of the abovementioned steps, the computational domain $[0\infty)$ is truncated into the finite domain $[\eta_0\, \eta_\infty]$. In order to obtain the first approximation of the numerical solution, we selected $\eta_0 = 0, \eta_\infty = 20$, $n_p = 500, h = (\eta_\infty - \eta_0)/n_p$, and then, the desired accuracy, i.e., $\varepsilon = 10^{-6}$, is achieved by varying the value of n_p (the numbers of grid points) with the reduction in the value of h (step size).

Table 2 is designed to estimate the rate of convergence of the Keller-Box simulation as well as to find the best choice of n_p for the simulation of the local Nusselt number and skin-friction coefficients. It is deduced through Table 2 that one thousand grid points are enough for the convergent solution of $f''(0)$ and five hundred grid points are sufficient to achieve the convergence criteria for $g''(0)$, whereas five thousand grid points are necessary to attain the convergent approximation for both $\theta'(0)$ as well as $1/\phi(0)$. In order to check the stability of the Keller-Box solution, the value of n_p is increased up to ten thousand and the solution is found consistent. The convergent solution obtained through Table 2 is used for further manipulations in order to find the impact of involved parameters on the thermal setup, local Nusselt number, and skin-friction coefficients.

4. Code Validation

In order to validate the numeric code for the solution of the considered problem, the outfalls reported in the present contribution have been compared with the outfalls discussed in

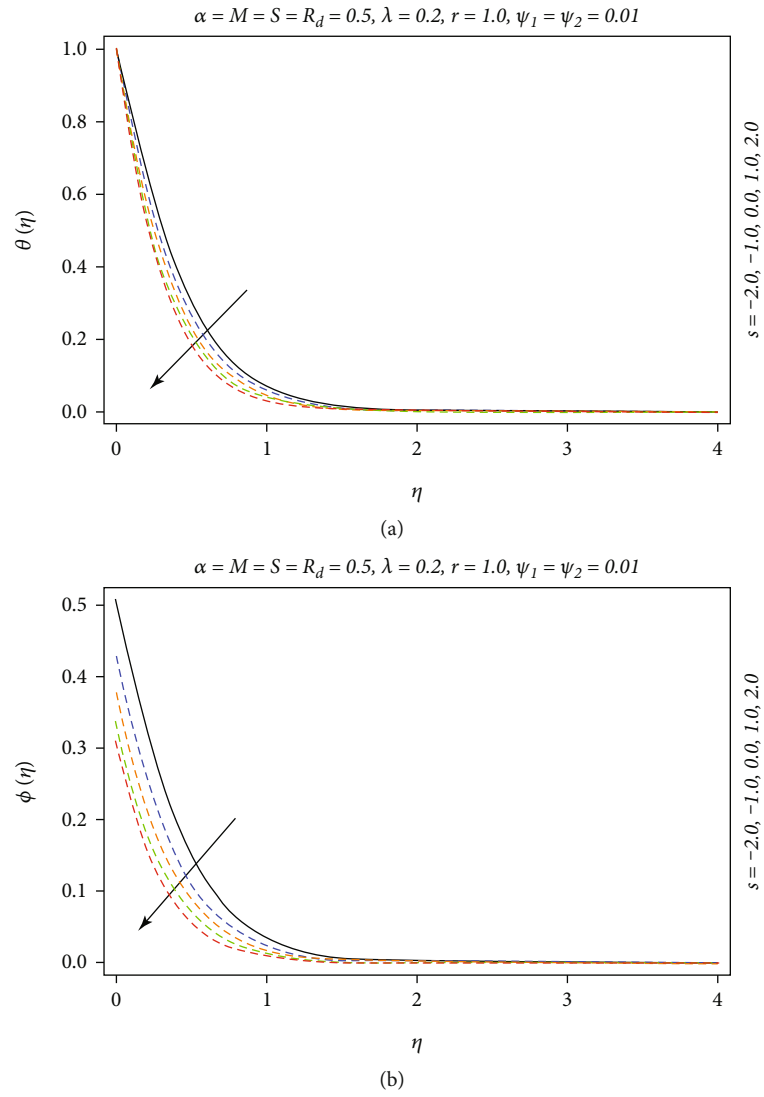

Figure 5: (a, b) Temperature fluctuation against the variation of the index s for the PST case and for the PHF case.

the article (Liu and Andersson [44]) for $f''(0), g''(0), f(\infty)$ and $g(\infty)$ in the absence of nanoparticles. A convincing scientific connection has been found between the present scrutiny and the published activity. In this regard, Table 3 is arranged in the analysis.

5. Results and Discussion

The present heading describes the importance of the involved important parameters like radiation factor R_d and temperature maintaining indices (r, s) on thermal setups $[\theta(\eta), \phi(\eta)]$ via various plots, whereas the physical quantities like the local Nusselt number and skin friction coefficients are discussed for various estimations of involved constraints via various graphs and tables. Moreover, the thermophysical properties for the present hybrid mixture are also computed at the end of this section and discussed deeply. Figure 3 describes the impact of radiation factor R_d on $\theta(\eta)$ and on $\phi(\eta)$. It is detected through Figures 3(a) and 3(b) that the escalating choice of R_d enhances the worth of thermal setups. The thickness of the thermal layer is observed larger for smaller choices of R_d as compared to larger estimations of R_d. The maximum temperature for the PST mechanism is observed as one, whereas the maximum temperature for the PHF case is noticed as 0.5 when R_d is increased from 0 to 2.0. Overall, the strength of the thermal setup for the PHF case is observed to be more prominent than that for the PST case. Physically, the abovementioned changes are produced because R_d is the mathematical ratio of Stefan Boltzman number σ^* to mean absorption factor k^*. The value of σ^* is increased whereas the value of k^* is diminished with the positive tendency of R_d. Figure 4 explains the influence of temperature maintaining index r corresponding to the x-direction on $\theta(\eta)$ and on $\phi(\eta)$ while other parameters are being fixed. The temperature of hybrid nanofluid is diminished for both the PST and PHF cases with the escalating amount of r. The value of temperature is detected higher for the PHF case than the PST case for $r \leq -2$ and is deduced

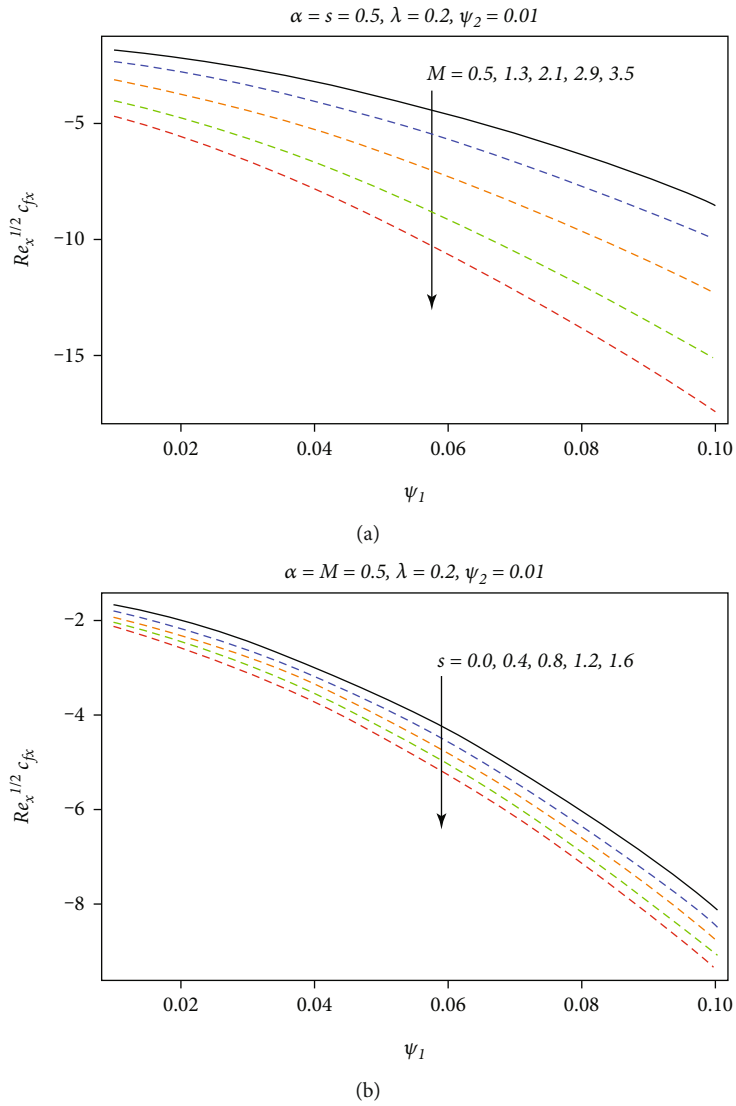

FIGURE 6: (a, b) Skin-friction coefficient C_{fx} against the variations in ψ_1&M and ψ_1&S.

higher for the PST case than the PHF case for other choices of r. Physically, the temperature distribution is well dominant for variable thermal conditions than arbitrary thermal conditions. The wideness of the thermal layer is larger in the PHF case than the PST case. Figure 5 is plotted to explain the worth of temperature maintaining index s corresponding to the y-direction on $\theta(\eta)$ and on $\phi(\eta)$ by keeping the other involved factors fixed. The temperature with the higher estimations of s is reduced for both the PHF and PST mechanisms. The value of temperature fluctuation is attained higher for PST conditions than PHF conditions for all the choices of s, but the thermal thickness is achieved quite dominant for the PHF case as associated with the PST case.

Figure 6(a) manifests the combined influence of ψ_1 and M on C_{fx} for fixed values of other involved parameters. Skin-friction coefficient C_{fx} is reduced with increasing amounts of both M and ψ_1. Physically, more electric conduction is produced in the flow of the hybrid mixture with the positive growth in M from 0.5 to 3.5. Skin-friction coefficient C_{fx} is reduced with the phenomenon of electric conduction. Moreover, the electrical conductivity of alumina is much higher than the electrical conductivity of host liquid and this phenomenon produces the reduction in the value of C_{fx}. The smaller selection of ψ_1 produces the stream of moderate thickness, whereas the thickness of the stream is observed to be double when ψ_1 reached 0.10. Figure 6(b) explains the combined influence of ψ_1 and S on C_{fx} for fixed selections of other involved constraints. Skin-friction coefficient C_{fx} is reduced with the higher estimation of S. Physically, expansion rate a is reduced with the improvement in the value of S, and therefore, reduction in the computation of C_{fx} is attained. Figure 7(a) reveals the collective effect of ψ_2 and λ on C_{fy} with other parameters being kept fixed. Skin-friction coefficient C_{fy} is abridged with growing amounts of both λ and ψ_2. Actually, a less elongation rate is produced with the development in λ from 0.2 to 1.4.

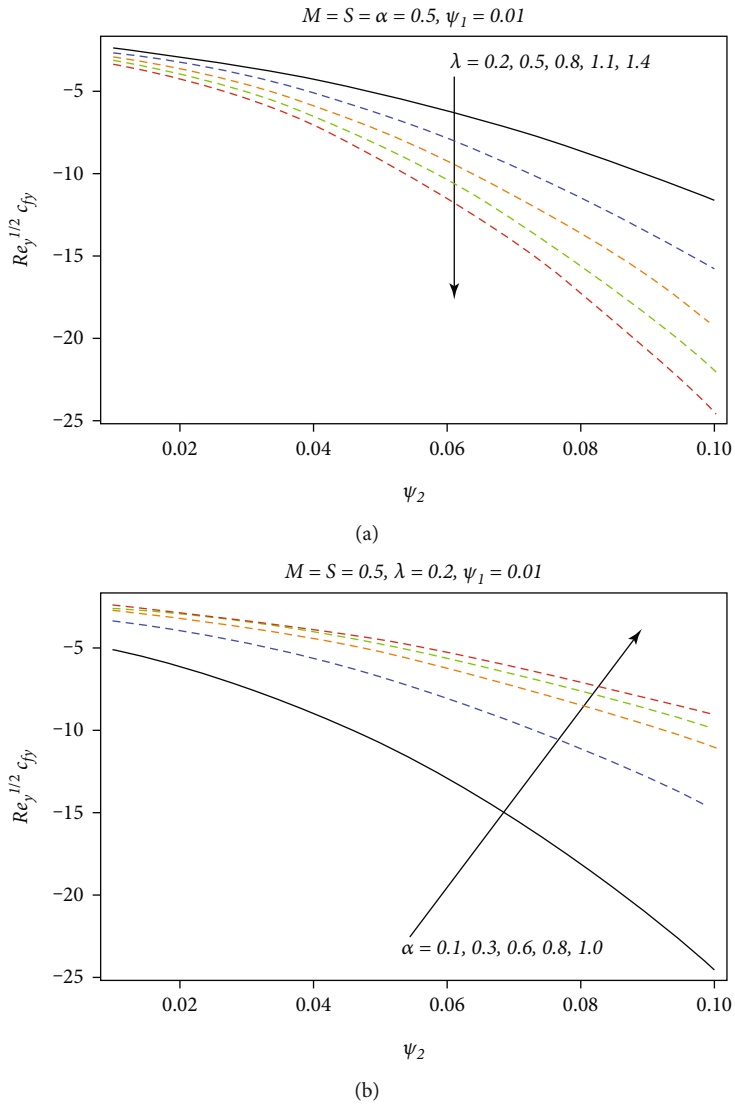

Figure 7: (a, b) Skin-friction coefficient C_{fy} against the variations in ψ_2&λ and ψ_2&α.

Skin-friction coefficient C_{fy} is diminished with the productions of a less elongation rate. Moreover, the electrical conductivity of titania is much higher than the electrical conductivity of host liquid and this phenomenon produces the reduction in the computation of C_{fy}. As electrical conductivity of titania is higher than the electrical conductivity of alumina, therefore, faster reduction in C_{fy} is achieved than C_{fx}. The smaller assortment of ψ_2 yields the stream of minute thickness, whereas the thickness of the stream is observed triple when ψ_2 reached 0.10. Figure 7(b) elucidates the joined impact of ψ_2 and α on C_{fy} for stationary values of other mathematical constraints. Skin-friction coefficient C_{fy} is enhanced with the advancement in α. Precisely, expansion rate b is enhanced and expansion rate a is diminished with the development in α, and therefore, enhancement in the computation of C_{fy} is attained.

Figure 8(a) explores the graphical assessment of Nusselt number Nu_x against the variations in R_d and r with other parameters being retained as fixed. Nusselt number Nu_x is improved with the enhancement in r from −2.0 to 2.0, and also, it is increased with the escalation in R_d from 0.0 to 2.0. Energy is transformed in the form of electromagnetic waves with the involvement of thermal radiation, and it is more efficient in porous space or vacuum because it is the ideal situation for full transmission of the radiation energy. The value of Nu_x is augmented with the escalation in R_d from 0.0 to 2.0. The rate of heat transference is observed slower for negative values of r than positive values of r because the surface temperature is mentioned higher for the negative value of r than the positive value of r, and therefore, the thermal flux across the surface will be higher for the positive value of r than its negative value. As a result, the Nusselt number Nu_x is tremendously improved.

Figure 8(b) describes the graphical evaluation of Nusselt number Nu_y against the variations in S and s with other parameters being taken as fixed. Nusselt number Nu_y is improved with the enhancement in s from −2.0 to 2.0, and

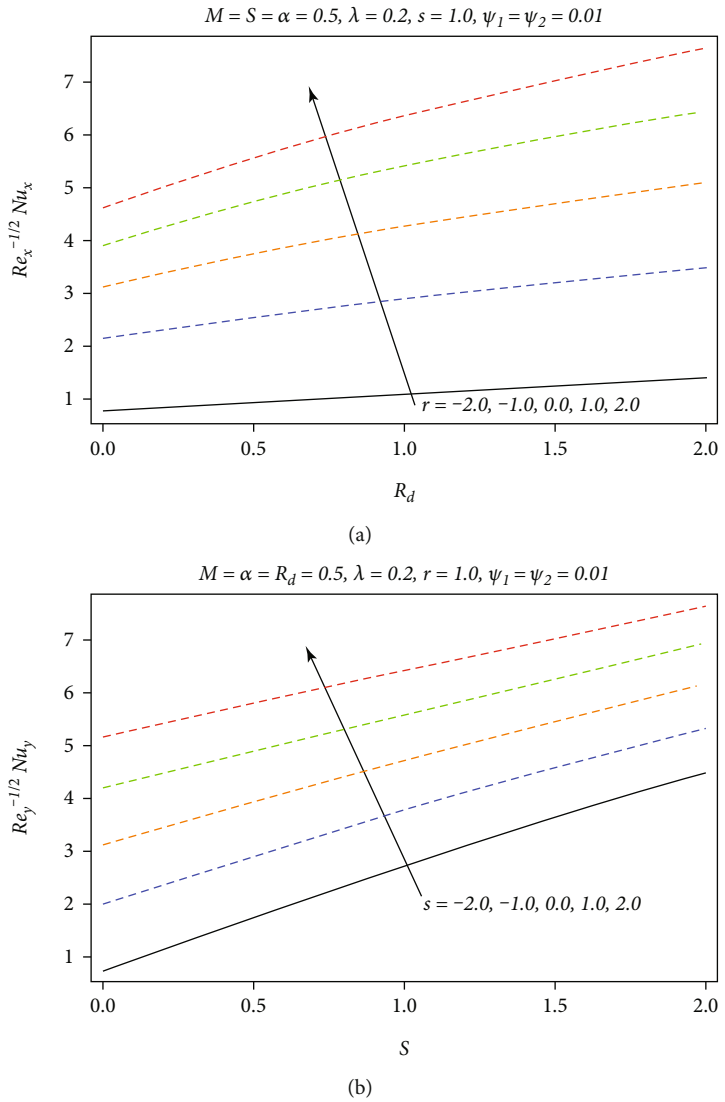

Figure 8: Nusselt number Nu_x against the variations in (a) R_d&r and Nu_y against the variations in (b) S&s.

Table 4: Contribution of solid volume fractions ψ_1 and ψ_2 on thermal interest quantities for $\alpha = S = M = 0.5, r = s = 1.0, R_d = 0.5$.

Nanoparticle volume fractions		$-\mathrm{Re}_y^{1/2} C_{fx}$	$-\mathrm{Re}_y^{1/2} C_{fy}$	$(\mathrm{Re}_x^{-1/2}/(1+R_d))Nu_x$	
ψ_1	ψ_2			VST case	VHF case
0.01	0.01	1.818652	2.354086	3.165999	3.165999
0.04	0.01	3.199621	4.200442	3.392241	3.392241
0.07	0.01	5.443228	7.263307	3.584352	3.584352
0.10	0.01	8.510418	11.50723	3.751383	3.751383
0.13	0.01	12.42493	16.96354	3.903712	3.903712
0.16	0.01	17.20563	23.65449	4.046176	4.046176
0.01	0.04	3.207035	4.209267	3.351655	3.351655
0.01	0.07	5.46183	7.285107	3.50311	3.50311
0.01	0.10	8.542308	11.54414	3.630213	3.630213
0.01	0.13	12.47104	17.01642	3.743252	3.743252
0.01	0.16	17.26637	23.72367	3.846784	3.846784

Table 5: Fluctuations in the thermophysical behaviours for the existing hybrid mixture with $\psi_1 = 0.01$.

ψ_2	ρ_{hnf}	$(\rho C_p)_{\text{hnf}} \times 10^3$	k_{hnf}	$\sigma_{\text{hnf}} \times 10^{-6}$
0.00	1026.829	4.14486	0.6407428664	5.666667
0.01	1059.358	4.109932	0.6634263686	5.838384
0.03	1124.416	4.040076	0.7098079091	6.19244
0.05	1189.474	3.97022	0.7575933453	6.561404
0.07	1254.532	3.900364	0.8068473972	6.946237
0.09	1319.59	3.830508	0.8576388251	7.347985

Table 6: Fluctuations in the thermophysical behaviours for the existing hybrid mixture with $\psi_2 = 0.01$.

ψ_1	ρ_{hnf}	$(\rho C_p)_{\text{hnf}} \times 10^3$	k_{hnf}	$\sigma_{\text{hnf}} \times 10^{-6}$
0.00	1029.629	4.144072	0.6349801229	5.666667
0.01	1059.358	4.109932	0.6634263686	5.838384
0.03	1118.816	4.041652	0.7218911348	6.19244
0.05	1178.274	3.973372	0.7825545636	6.561404
0.07	1237.732	3.905092	0.8455479603	6.946237
0.09	1297.19	3.836812	0.9110132942	7.347985

also, it is increased with the escalation in S from 0.0 to 2.0. The transmission of heat is perceived slower for negative selections of s than positive selections of s because the stretching device is maintained at higher temperature for the negative value of s than the positive value of s, and therefore, thermal flux across the stretching device will be higher for the positive value of s than its negative value. As a result, the Nusselt number Nu_y is extremely enriched. Physically, unsteady expansion parameter S is involved in equation (9) with the sum of dimensionless temperature and its derivative with respect to η. As a result, the rate of heat transference across the yz plane is increased.

Roles of solid volume fractions ψ_1 for alumina and ψ_2 for titania on the local Nusselt number as well as on skin friction coefficients are discussed in Table 4. It is attained in Table 4 that escalating selections of ψ_1 and ψ_2 improve the skin-friction coefficients for the present model. It is also observed that the impact of ψ_1 and ψ_2 is more dominant for the flow along the y-direction as compared to the x-direction. Mathematically, the involvement of α is absent in equation (14), whereas it is involved in the reciprocal form as described in equation (15). As in our study, the value of α is selected to be 0.5, so the numerical value of $g''(0)$ is observed to be higher than the numerical value of $f''(0)$. Moreover, the roles of ψ_1 and ψ_2 on the local Nusselt number are also discussed in Table 3 and it is deduced that higher estimations of ψ_1 and ψ_2 in the range $[0.01\, 0.16]$ improve the rate of heat transference which is beneficial for many industrial and engineering applications. Furthermore, the rate of heat transference is observed to be equal quantitatively for both the PST and PHF mechanisms. The thermophysical features for the present hybrid mixture are discussed in Table 5 for various choices of ψ_2 (the weightage of titania) by adjusting $\psi_1 = 0.01$. The escalating estimation of ψ_2 enhances the density, thermal conductivity, and electrical conductivity of the hybrid mixture whereas the heat capacity is reduced with the present development in ψ_2. Physically, the mixture of alumina and titania with the working fluid, i.e., water, provides the improvement in the thermophysical features as compared to that in Table 1. In Table 6, thermophysical characteristics for present hybrid combination are computed for different selections of ψ_1 (the solid volume fraction of alumina) by taking $\psi_2 = 0.01$. With the increase of ψ_1, the density, the electrical conductivity, and the thermal conductivity are improved but the heat capacity is condensed with this variation. The base fluid, i.e., water, delivers enlargement in thermophysical properties of hybrid nanofluid associated to Table 1 with the chemically mixture of alumina and titania.

6. Conclusions

This study provides the mathematical analysis for unsteady bidirectional dynamics of radiative water-conveying hybrid nanofluid (i.e., the combination of titania and alumina) with the significance of variable thermal conditions (PST and PHF) and impact of the cylindrical shape of nanoparticles. The influence of the Lorentz force is also incorporated to make the investigation more impactful. Numerical simulation is made via the Keller-Box approach, and key observations are listed as follows:

(i) The thermophysical features of the hybrid nanofluid except specific heat are improved with the involvement of the cylindrical shape of nanoparticles, i.e., titania and alumina

(ii) The rate of heat transference is observed identical for both the PST and PHF cases

(iii) The magnitude of the stress applied on the y-direction is observed to be higher than the magnitude of the stress applied along the x-direction with the positive estimations of volume fractions of nanoparticles

(iv) The temperature of the hybrid nanofluid is increased with the development in the choice of R_d and decreased with the improvement in the choices of temperature maintaining indices (r, s)

(v) Skin-friction coefficients are reduced with progressions in the values of the Hartmann number, unsteady parameter, and volume percentages of nanoparticles

(vi) The local Nusselt number is improved with developments in the amounts of radiation and unsteady parameters

This scientific contribution has many mechanical, biomedical, and commercial applications. These are coating a sheet with hybrid nanomaterials, manufacturing of printing ink, degrading organic contaminants, manufacturing of sodium vapour lamps, etc. This study is also really helpful

for the researchers working in the field of nanomaterials and can be protracted in the future by considering different geometries.

Nomenclature

B_0: Strength of magnetic field
a, b: Stretching rates
t: Time
c: Time coefficient
x, y, z: Space coordinates
u_w, v_w: Stretching velocities
PST: Prescribed surface temperature
PHF: Prescribed heat flux
T_w: Surface temperature
r, s: Thermal indices
T_0, T_1: Dimensional constants
T_∞: Ambient temperature
u, v, w: Velocity field components
T: Temperature
hnf: Hybrid nanofluid
μ_{hnf}: Dynamic viscosity of hnf
ρ_{hnf}: Density of hnf
σ_{hnf}: Electrical conductivity of hnf
k_{hnf}: Thermal conductivity of hnf
α_{hnf}: Thermal diffusivity of hnf
$C_{p_{\text{hnf}}}$: Specific heat capacity of hnf
ψ_1: Volume fraction of alumina
ψ_2: Volume fraction of titania
f: Fluid
bf: Base fluid
$p1$: Alumina nanoparticles
$p2$: Titania nanoparticles
q_{rad}: Radiative heat transfer
σ^*: Stefan Boltzmann constant
k^*: Mean absorption coefficient
η: Similarity variable
f', g': Dimensionless velocities
θ, ϕ: Dimensionless temperatures
Pr: Prandtl number
R_d: Radiation parameter
S: Unsteady parameter
M: Hartmann number
$\varepsilon_1, \varepsilon_2, \varepsilon_3$: Dimensionless quantities
Re_x, Re_y: Reynolds numbers
Nu_x: Nusselt number
C_{fx}, C_{fy}: Skin friction coefficients
α: Stretching ratio parameter
ρ, k, C_p, σ: Thermophysical properties
h: Step size
ε: Convergence criterion
n_p: Numbers of grid points.

Data Availability

The raw data supporting the conclusion of this report will be made available by the corresponding author without undue reservation.

Conflicts of Interest

The authors declare that they have no competing interests.

Authors' Contributions

All authors contributed equally to this work, and all the authors have read and approved the final version of the report.

References

[1] J. C. Maxwell, *A Treatise on Electricity and Magnetism*, vol. 1, Clarendon Press, Oxford, 1873.

[2] R. L. Hamilton and O. K. Crosser, "Thermal conductivity of heterogeneous two-component systems," *Industrial & Engineering Chemistry Fundamentals*, vol. 1, no. 3, pp. 187–191, 1962.

[3] N. Masoumi, N. Sohrabi, and A. Behzadmehr, "A new model for calculating the effective viscosity of nanofluids," *Journal of Physics D: Applied Physics*, vol. 42, no. 5, article 055501, 2009.

[4] W. A. Khan and I. Pop, "Boundary-layer flow of a nanofluid past a stretching sheet," *International Journal of Heat and Mass Transfer*, vol. 53, no. 11-12, pp. 2477–2483, 2010.

[5] M. Sheikholeslami and H. B. Rokni, "Simulation of nanofluid heat transfer in presence of magnetic field: a review," *International Journal of Heat and Mass Transfer*, vol. 115, pp. 1203–1233, 2017.

[6] R. B. Ganvir, P. V. Walke, and V. M. Kriplani, "Heat transfer characteristics in nanofluid–a review," *Renewable and Sustainable Energy Reviews*, vol. 75, pp. 451–460, 2017.

[7] J. Sarkar, P. Ghosh, and A. Adil, "A review on hybrid nanofluids: recent research, development and applications," *Renewable and Sustainable Energy Reviews*, vol. 43, pp. 164–177, 2015.

[8] N. A. C. Sidik, M. M. Jamil, W. M. A. A. Japar, and I. M. Adamu, "A review on preparation methods, stability and applications of hybrid nanofluids," *Renewable and Sustainable Energy Reviews*, vol. 80, pp. 1112–1122, 2017.

[9] I. Waini, A. Ishak, and I. Pop, "Unsteady flow and heat transfer past a stretching/shrinking sheet in a hybrid nanofluid," *International Journal of Heat and Mass Transfer*, vol. 136, pp. 288–297, 2019.

[10] A. A. Minea, "Hybrid nanofluids based on Al_2O_3, TiO_2 and SiO_2: numerical evaluation of different approaches," *International Journal of Heat and Mass Transfer*, vol. 104, pp. 852–860, 2017.

[11] K. Y. Leong, Z. A. Najwa, K. K. Ahmad, and H. C. Ong, "Investigation on stability and optical properties of titanium dioxide and aluminum oxide water-based nanofluids," *International Journal of Thermophysics*, vol. 38, no. 5, p. 77, 2017.

[12] G. M. Moldoveanu, A. A. Minea, M. Iacob, C. Ibanescu, and M. Danu, "Experimental study on viscosity of stabilized Al_2O_3, TiO_2 nanofluids and their hybrid," *Thermochimica Acta*, vol. 659, pp. 203–212, 2018.

[13] G. M. Moldoveanu, A. A. Minea, G. Huminic, and A. Huminic, "Al2O3/TiO2 hybrid nanofluids thermal conductivity," *Journal of Thermal Analysis and Calorimetry*, vol. 137, no. 2, pp. 583–592, 2019.

[14] M. Shirazi, S. Kord, and Y. Tamsilian, "Novel smart water-based Titania nanofluid for enhanced oil recovery," *Journal of Molecular Liquids*, vol. 296, p. 112064, 2019.

[15] S. A. Khan, M. I. Khan, T. Hayat, M. F. Javed, and A. Alsaedi, "Mixed convective non-linear radiative flow with TiO2-cu-water hybrid nanomaterials and induced magnetic field," *International Journal of Numerical Methods for Heat & Fluid Flow*, vol. 29, no. 8, pp. 2754–2774, 2019.

[16] A. Asadi, I. M. Alarifi, and L. K. Foong, "An experimental study on characterization, stability and dynamic viscosity of CuO-TiO_2/water hybrid nanofluid," *Journal of Molecular Liquids*, vol. 307, p. 112987, 2020.

[17] S. Ahmad, K. Ali, M. Rizwan, and M. Ashraf, "Heat and mass transfer attributes of copper-aluminum oxide hybrid nanoparticles flow through a porous medium," *Case Studies in Thermal Engineering*, vol. 25, p. 100932, 2021.

[18] B. Ali, R. A. Naqvi, L. Ali, S. Abdal, and S. Hussain, "A comparative description on time-dependent rotating magnetic transport of a water base liquid H2O with hybrid nanomaterials Al2O3-Cu and Al2O3-TiO2 over an extending sheet using Buongiorno model: finite element approach," *Chinese Journal of Physics*, vol. 70, pp. 125–139, 2021.

[19] P. K. Kanti, K. V. Sharma, A. A. Minea, and V. Kesti, "Experimental and computational determination of heat transfer, entropy generation and pressure drop under turbulent flow in a tube with fly ash-Cu hybrid nanofluid," *International Journal of Thermal Sciences*, vol. 167, p. 107016, 2021.

[20] I. S. Okeke, K. K. Agwu, A. A. Ubachukwu, and F. I. Ezema, "Influence of transition metal doping on physiochemical and antibacterial properties of ZnO nanoparticles: a review," *Applied Surface Science Advances*, vol. 8, p. 100227, 2022.

[21] P. Sharma, Z. Said, S. Memon et al., "Comparative evaluation ofAI-based intelligentGEPandANFISmodels in prediction of thermophysical properties ofFe3O4-coatedMWCNThybrid nanofluids for potential application in energy systems," *International Journal of Energy Research*, 2022.

[22] A. K. Tiwari, V. Kumar, Z. Said, and H. K. Paliwal, "A review on the application of hybrid nanofluids for parabolic trough collector: recent progress and outlook," *Journal of Cleaner Production*, vol. 292, p. 126031, 2021.

[23] Z. Said, M. Ghodbane, L. S. Sundar, A. K. Tiwari, M. Sheikholeslami, and B. Boumeddane, "Heat transfer, entropy generation, economic and environmental analyses of linear fresnel reflector using novel rGO- Co_3O_4 hybrid nanofluids," *Renewable Energy*, vol. 165, pp. 420–437, 2021.

[24] F. Ali, K. Loganathan, S. Eswaramoorthi, K. Prabu, A. Zaib, and D. K. Chaudhary, "Heat Transfer Analysis on Carboxymethyl Cellulose Water-Based Cross Hybrid Nanofluid Flow with Entropy Generation," *Journal of Nanomaterials*, vol. 2022, Article ID 5252918, 11 pages, 2022.

[25] A. K. Tiwari, N. S. Pandya, Z. Said, H. F. Öztop, and N. Abu-Hamdeh, "4S consideration (synthesis, sonication, surfactant, stability) for the thermal conductivity of CeO2 with MWCNT and water based hybrid nanofluid: an experimental assessment," *Colloids and Surfaces A: Physicochemical and Engineering Aspects*, vol. 610, p. 125918, 2021.

[26] N. A. Zainal, R. Nazar, K. Naganthran, and I. Pop, "Unsteady three-dimensional MHD non-axisymmetric Homann stagnation point flow of a hybrid Nanofluid with stability analysis," *Mathematics*, vol. 8, no. 5, p. 784, 2020.

[27] X. Zhang, H. Gu, and M. Fujii, "Effective thermal conductivity and thermal diffusivity of nanofluids containing spherical and cylindrical nanoparticles," *Journal of Applied Physics*, vol. 100, no. 4, article 044325, 2006.

[28] E. V. Timofeeva, J. L. Routbort, and D. Singh, "Particle shape effects on thermophysical properties of alumina nanofluids," *Journal of Applied Physics*, vol. 106, no. 1, article 014304, 2009.

[29] K. Yang and Y. Q. Ma, "Computer simulation of the translocation of nanoparticles with different shapes across a lipid bilayer," *Nature Nanotechnology*, vol. 5, no. 8, pp. 579–583, 2010.

[30] P. B. Maheshwary, C. C. Handa, and K. R. Nemade, "A comprehensive study of effect of concentration, particle size and particle shape on thermal conductivity of titania/water based nanofluid," *Applied Thermal Engineering*, vol. 119, pp. 79–88, 2017.

[31] M. Sheikholeslami, "Magnetic field influence on CuO-H_2O nanofluid convective flow in a permeable cavity considering various shapes for nanoparticles," *International Journal of Hydrogen Energy*, vol. 42, no. 31, pp. 19611–19621, 2017.

[32] U. Rashid and H. Liang, "Investigation of nanoparticles shape effects on MHD nanofluid flow and heat transfer over a rotating stretching disk through porous medium," *International Journal of Numerical Methods for Heat & Fluid Flow*, vol. 30, no. 12, pp. 5169–5189, 2020.

[33] S. Dinarvand and M. N. Rostami, "Three-dimensional squeezed flow of aqueous magnetite–graphene oxide hybrid nanofluid: a novel hybridity model with analysis of shape factor effects," *Proceedings of the Institution of Mechanical Engineers, Part E: Journal of Process Mechanical Engineering*, vol. 234, no. 2, pp. 193–205, 2020.

[34] A. Bhattad and J. Sarkar, "Effects of nanoparticle shape and size on the thermohydraulic performance of plate evaporator using hybrid nanofluids," *Journal of Thermal Analysis and Calorimetry*, vol. 143, no. 1, pp. 767–779, 2021.

[35] M. Turkyilmazoglu and I. Pop, "Heat and mass transfer of unsteady natural convection flow of some nanofluids past a vertical infinite flat plate with radiation effect," *International Journal of Heat and Mass Transfer*, vol. 59, pp. 167–171, 2013.

[36] S. S. U. Devi and S. A. Devi, "Numerical investigation of three-dimensional hybrid cu–Al2O3/water nanofluid flow over a stretching sheet with effecting Lorentz force subject to Newtonian heating," *Canadian Journal of Physics*, vol. 94, no. 5, pp. 490–496, 2016.

[37] M. Sheikholeslami and M. Sadoughi, "Mesoscopic method for MHD nanofluid flow inside a porous cavity considering various shapes of nanoparticles," *International Journal of Heat and Mass Transfer*, vol. 113, pp. 106–114, 2017.

[38] T. Hayat, S. Nadeem, and A. U. Khan, "Rotating flow of Ag-CuO/H2O hybrid nanofluid with radiation and partial slip boundary effects," *The European Physical Journal E*, vol. 41, no. 6, pp. 1–9, 2018.

[39] K. Loganathan, N. Alessa, and S. Kayikci, "Heat transfer analysis of 3-D viscoelastic nanofluid flow over a convectively heated porous Riga plate with Cattaneo-Christov double flux," *Frontiers of Physics*, vol. 9, article 641645, 2021.

[40] H. A. Nabwey and A. Mahdy, "Transient flow of micropolar dusty hybrid nanofluid loaded with Fe3O4-ag nanoparticles through a porous stretching sheet," *Results in Physics*, vol. 21, p. 103777, 2021.

[41] H. U. Rasheed, S. Islam, Z. Khan et al., "Computational analysis of hydromagnetic boundary layer stagnation point flow of nano liquid by a stretched heated surface with convective

conditions and radiation effect," *Advances in Mechanical Engineering*, vol. 13, no. 10, 2021.

[42] K. Loganathan, G. Muhiuddin, A. M. Alanazi, F. S. Alshammari, B. M. Alqurashi, and S. Rajan, "Entropy optimization of third-grade Nanofluid slip flow embedded in a porous sheet with zero mass flux and a non-Fourier heat flux model," *Frontiers of Physics*, vol. 8, p. 250, 2020.

[43] Zeeshan, "Second law and entropy generation analysis of magnetized viscous fluid flow over a permeable expandable sheet with nonlinear thermal radiation: Brownian and thermophoresis effect," *Advances in Mechanical Engineering*, vol. 14, no. 1, 2022.

[44] I. C. Liu and H. I. Andersson, "Heat transfer over a bidirectional stretching sheet with variable thermal conditions," *International Journal of Heat and Mass Transfer*, vol. 51, no. 15-16, pp. 4018–4024, 2008.

[45] J. L. G. Oliveira, C. Tecchio, K. V. Paiva, M. B. H. Mantelli, R. Gandolfi, and L. G. S. Ribeiro, "Passive aircraft cooling systems for variable thermal conditions," *Applied Thermal Engineering*, vol. 79, pp. 88–97, 2015.

[46] I. Waini, A. Ishak, and I. Pop, "Hybrid nanofluid flow and heat transfer past a vertical thin needle with prescribed surface heat flux," *International Journal of Numerical Methods for Heat & Fluid Flow*, vol. 29, no. 12, pp. 4875–4894, 2019.

[47] I. Waini, A. Ishak, and I. Pop, "Hybrid nanofluid flow on a shrinking cylinder with prescribed surface heat flux," *International Journal of Numerical Methods for Heat & Fluid Flow*, vol. 31, no. 6, pp. 1987–2004, 2021.

[48] I. Ahmad, M. Faisal, T. Javed, A. Mustafa, and M. Z. Kiyani, "Numerical investigation for mixed convective 3D radiative flow of chemically reactive Williamson nanofluid with power law heat/mass fluxes," *Ain Shams Engineering Journal*, vol. 13, no. 1, p. 101508, 2022.

[49] N. S. Khashi'ie, I. Waini, N. A. Zainal, K. Hamzah, and A. R. Mohd Kasim, "Hybrid nanofluid flow past a shrinking cylinder with prescribed surface heat flux," *Symmetry*, vol. 12, no. 9, p. 1493, 2020.

[50] M. Faisal, I. Ahmad, and T. Javed, "Dynamics of MHD tangent hyperbolic nanofluid with prescribed thermal conditions, random motion and thermo-migration of nanoparticles," *Journal of dispersion science and technology*, pp. 1–15, 2021.

[51] T. Javed, M. Faisal, and I. Ahmad, "Dynamisms of solar radiation and prescribed heat sources on bidirectional flow of magnetized Eyring-Powell nanofluid," *Case Studies in Thermal Engineering*, vol. 21, p. 100689, 2020.

[52] I. Ahmad, M. Faisal, and T. Javed, "Dynamics of copper–water nanofluid with the significance of prescribed thermal conditions," *Heat Transfer*, vol. 50, no. 5, pp. 4248–4263, 2021.

[53] S. Mosayebidorcheh, M. Vatani, M. Hatami, and D. Domiri Ganji, "Two-phase nanofluid thermal analysis over a stretching infinite solar plate using Keller box method (KBM)," *Iranian Journal of Chemistry and Chemical Engineering (IJCCE)*, vol. 37, no. 6, pp. 247–256, 2018.

[54] M. Faisal, I. Ahmad, and T. Javed, "Keller–box simulation for nonzero and zero mass fluxes of nanofluid flow impinging over a bi-directional stretching sheet: an unsteady mathematical model," *International Journal of Modern Physics C*, vol. 32, no. 4, p. 2150052, 2021.

[55] I. Ahmad, M. Faisal, and T. Javed, "Unsteady rotating flow of nanofluid with prescribed thermal aspects," *International Journal of Modern Physics C (IJMPC)*, vol. 32, no. 7, p. 2150093, 2021.

[56] A. Abbasi and W. Farooq, "A numerical simulation for transport of hybrid nanofluid," *Arabian Journal for Science and Engineering*, vol. 45, no. 11, pp. 9249–9265, 2020.

[57] M. Faisal, I. Ahmad, and T. Javed, "Numerical assessments of prescribed heat sources on unsteady 3D flow of Williamson nanoliquid through porous media," *Special Topics & Reviews in Porous Media: An International Journal*, vol. 12, no. 2, pp. 71–92, 2021.

[58] T. Sajid, W. Jamshed, F. Shahzad et al., "Study on heat transfer aspects of solar aircraft wings for the case of Reiner-Philippoff hybrid nanofluid past a parabolic trough: Keller box method," *Physica Scripta*, vol. 96, no. 9, article 095220, 2021.

[59] I. Ahmad, M. Faisal, and T. Javed, "Unsteady flow of Walters-B magneto-nanofluid over a bidirectional stretching surface in a porous medium with heat generation," *Special Topics & Reviews in Porous Media: An International Journal*, vol. 12, no. 3, pp. 49–70, 2021.

Hindawi
Journal of Nanomaterials
Volume 2022, Article ID 2446972, 27 pages
https://doi.org/10.1155/2022/2446972

Research Article

Analysis of Forced Convection with Hybrid Cu-Al_2O_3 Nanofluids Injected in a Three-Dimensional Rectangular Channel Containing Three Perpendicular Rotating Blocks with $\kappa - \varepsilon$ Turbulent Modeling

S. H. Elhag,[1] Abid A. Memon,[2] M. Asif Memon,[2,3] Kaleemullah Bhatti,[2] Kavikumar Jacob,[3] Samirah Alzahrani,[1] and Jamel Seidu[4]

[1]*Department of Mathematics and Statistics, College of Science, Taif University, P.O. Box 11099, Taif 21944, Saudi Arabia*
[2]*Department of Mathematics and Social Sciences, Sukkur IBA University, Sukkur, 65200 Sindh, Pakistan*
[3]*Department of Mathematics and Statistics, Faculty of Applied Sciences and Technology, Universiti Tun Hussein Onn Malaysia, Batu Pahat, 86400 Johor, Malaysia*
[4]*School of Railways and Infrastructure Development, University of Mines and Technology (UMaT) Essikado, Sekondi-Takoradi, Ghana*

Correspondence should be addressed to Jamel Seidu; jseidu@umat.edu.gh

Received 18 May 2022; Revised 18 June 2022; Accepted 28 June 2022; Published 19 July 2022

Academic Editor: Zafar Said

In this paper, the flow of hybrid nanofluids in a three-dimensional rectangular channel consisting of three perpendicular blocks will be analyzed in terms of heat transfer. The two perpendicular rectangular blocks are rotating with speed ω. The hybrid mixture consists of aluminum oxide and copper, and each of them will contain in volume fraction of 0.001 to 0.25. The κ-ε model of turbulent flow along with Navier and energy equation will be brought into action by using the finite element package COMSOL Multiphysics 5.6. Volume fraction and speed of rotation will be used as the parameters, and a parameter study will be done by fixing the Reynolds number Re = 50,000 with energy dissipation rate (ε) (m^2/s^3) ($3.46E-6$ to $3.76E-5$), kinetic energy (κ) (m^2/s^2) ($2.50E-06$ to $1.23E-05$), and the Prandtl number (0.98506 to 1.2625). It was deducted that the local Nusselt number is minimized at the outlet for stationary blocks and the maximum for the moving blocks. In addition, the mean number of Nusselt on the upper surface of the rectangular channel increases when the blocks are stationary and decreases when the blocks are moving. The study suggests that to maximize the conduction process in the channel the blocks must rotate with a certain velocity. This study also determined that with increasing the total viscosity of hybrid nanofluids, the average temperature is decreasing linearly in the middle of the channel whether the blocks are rotating or not. The temperature gradient along the z-axis decreases with increasing volume fraction only when blocks are stationary. In addition, it has been determined that the maximum average temperature occurs when the volume fractions of copper and oxide are equal to 0.001.

1. Introduction and Literature Survey

The study of imposing a hybrid nanofluid in the domain to increase the heat transfer rate is increasing these days due to having a large number of applications in industrial development. The hybrid nanofluid can be a mixture of metallic, nonmetallic, and polymeric nanosized particles which are suspended in pure fluid like water and ethanol glycol. It was approved by many researchers with and without experiment, adding nanofluid in the pure fluid will increase the heat transfer rate. At Argonne National Laboratory, the first experiment based on nanofluid was performed [1]. In this experiment for the first time, the tremendous properties of the nanofluid in terms of heat transfer were explained. In

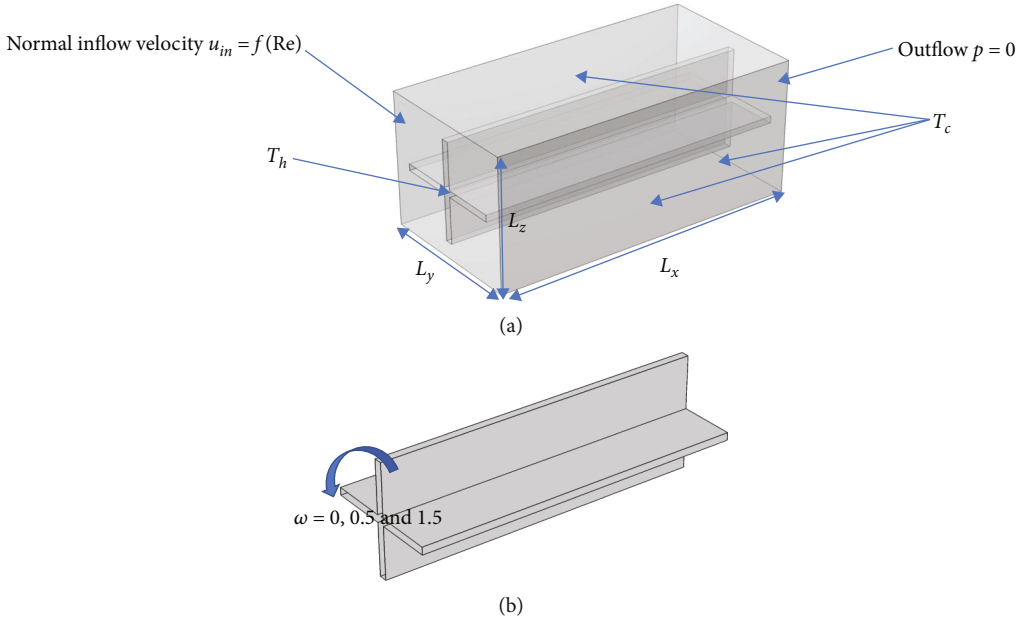

Figure 1: (a, b) Schematic diagram of the three-dimensional rectangular channel containing the perpendicular blocks.

the experiment, it was also suggested to improve these properties by certain modifications. The study beings a revolution in the field of engineering due to having a large number of applications of heat production. Later, several experimental and numerical investigations for heat transfer have been done by taking nanofluids under consideration [2, 3]. The applications of the nanofluids can also be seen in making efficient heat exchanger tubes. In the research study [4], WO_3/water-based nanofluids were investigated in the triple tube for the purpose to produce an efficient heat exchanger. The tube was comprised of a porous plate along with the rib type and twisted tape. In [5], a survey was written about the advantage of nanofluids when used as the coolant to make the efficient heat exchangers. In the survey, the author reported several findings regarding the previous literature which contribute to increasing the rate of heat transfer, like pressure drop, Reynolds number, flow regime, temperature, kind of base fluid, and the size of nanomaterials. Later on, the recent advancements in the thermophysical properties of the nanofluid were discussed in [6] along with the heat transport, dynamic motion, and the new challenges while studying the heat transportation with the help of nanofluids. The author of this article specially discussed the heat transport and the dynamic motion of the nanofluids in the media. The applications of nanofluids can largely be seen in making efficient solar collectors. For example, in [7], the hybrid nanofluids were used to observe the heat transfer by using the two nanofluids copper and aluminum oxide in the solar collector. It was found that the copper nanofluids have a finer capability than the aluminum oxide to hike up the heat transfer up to 6.4%. In producing efficient batteries, the flow of nanofluid along the heat transfer was also investigated in [8]. In this article, the author used the most advanced technique of machine learning on the experimental data of viscosity and density of the ternary nanofluids at various temperatures to improve the performance of the battery. Recently, the study of mixing the different nanofluids is gaining importance due to their reliable results for heat production in the interested domain. The concept of hybrid nanofluid was initiated [9, 10] with experiments and numerical solutions. It was suggested by them that the usage of hybrid nanofluid will increase more heat transfer rate as compared to an individual nanofluid through the base fluid. After that idea, several researchers started working on better understanding the hybrid nanofluids. A copper tube was investigated for the Al_2O_3-water nanofluid flow through several experiments [11–14]. With these experiments, it was explained that including the Al_2O_3 nanoparticles will boost the convection process in the copper tube, and also, it is much enhanced by increasing the Reynolds number and the concentration of the nanoparticles. The impact on the heat transfer by the constant magnetic effect as well as radiation on the stretching sheets was investigated in [15] while taking the water as the base fluid with copper and aluminum oxide as nanofluids. It was found that the constant magnetic effect and the radiation both enhance the rate of heat transfer. From many experiments [16–20], it is proved that even mixing a small amount of any nanoparticles or copper with the aluminum oxide will improve the thermal conductivity without harming the strongness of the nanofluids. The tremendous mixture of Cu-Al_2O_3 which is mostly used to analyze the convection process in the channel is formed by implementing the hydrogen reduction reaction on the CuO-Al_2O_3 combination [21]. It can also be produced by blending the pure Al_2O_3 and the very small-sized nanoparticles of CuO [22–24]. Also, the mixture CuO-Al_2O_3 has various importance in the engineering field. Among them, one of the applications is used there for the heat distribution in the electronic heat sink production [25–27]. The application of this mixture can widely be found in making efficient solar collectors [28, 29].

Table 1: Thermophysical properties of the nanofluid and parameters to geometry building [30].

Symbol	Value	Explanation
ϕ_1	0.001, 0.01, 0.09, 0.1, and 0.25	Volume fraction of aluminum oxide
ϕ_2	0.001, 0.01, 0.09, 0.1, and 0.25	Volume fraction of copper
ρ_{np1}	3880 (kg/m^3)	Density of alumina
ρ_{np2}	8954 (kg/m^3)	Density of copper
ρ_{np}	$\left(\phi_1\rho_{np1} + \phi_2\rho_{np2}\right)/\phi_1 + \phi_2$	The total density of the nanoparticles
$(c_p)_{np1}$	765 (J/kgK)	Specific heat of aluminum oxide
$(c_p)_{np2}$	383.1 (J/kgK)	Specific heat of copper
$(c_p)_{np}$	$\phi_1\rho_{np1}(c_p)_{np1} + \phi_2\rho_{np2}(c_p)_{np2}/\varphi\rho_{np}$	Specific heat of particles
ϕ	$\phi_1 + \phi_2$	The total volume fraction of nanoparticles
κ_{np1}	40 (W/mK)	Thermal conductivity of the aluminum oxide
κ_{np2}	386 (W/mK)	Thermal conductivity of copper
κ_{np}	$\phi_1\kappa_{np1} + \phi_2\kappa_{np2}/\phi_1 + \phi_2$	Total thermal conductivity of nanofluids
ρ_{bf}	998 (kg/m^3)	The density of the base fluid
ρ_{nf}	$\rho_{bf}(1-\phi) + \phi\rho_{np}$	Density of nanofluid
$(c_p)_{bf}$	4182 (J/kgK)	Specific heat of the base fluid
$(c_p)_{nf}$	$\rho_{bf}(1-\phi)(c_p)_{bf} + \rho_{np}(1-\phi)(c_p)_{np}/\rho_{nf}$	Specific heat capacity of nanofluid
κ_{bf}	0.597 (W/mK)	Thermal conductivity of the base fluid
κ_{nf}	$\kappa_{bf}\left(\kappa_{np} + 2\kappa_{bf} + 2\left(\kappa_{np} - \kappa_{bf}\right)\phi/\kappa_{np} + 2\kappa_{bf} - \left(\kappa_{np} - \kappa_{bf}\right)\phi\right)$	Thermal conductivity of the nanofluids
μ_{bf}	0.000998 (Pa s)	The viscosity of the base fluid
μ_{hnf}	$\mu_{bf}/(1-\phi)^{2.5}$ (Pa s)	Viscosity of nanofluid
D_h	0.333 (cm)	Hydraulic diameter
Re	50,000	Reynolds number
u_{in}	μ_{hnf} Re$/\rho_{nf}D_h$	Inlet velocity
L_x	1 (cm)	Length along the x-axis
L_y	0.5 (cm)	Length along the y-axis
L_z	0.5 (cm)	Length along the z-axis
ω	0, 0.5, and 1.5 (m/s)	The rotational velocity of perpendicular blocks along the z-direction
T_c	293.15 (K)	Cold temp
T_h	323.15 (K)	Hot temp

The object of this study is to observe the heat distribution by passing a hybrid mixture of Cu-Al_2O_3 through the three-dimensional rectangular channel which contained the perpendicular blocks of a certain thickness. The perpendicular blocks are rotated with some speed. The problem is simulated by using the latest and emerging finite element package COMSOL Multiphysics 5.6 by using the Navier-Stokes equation, energy equation, and $\kappa - \varepsilon$ model of turbulent flow. By considering different volume fractions of the contents of the mixture with some speed of the perpendicular blocks, the parametric study for the heat transfer of the mixture contents will be observed. In the first section, we will describe the problem formulation along with the thermophysical properties of the chosen nanofluid. In the 2nd section, we will apply the mesh independent study and compare the results for the average Nusselt number with the available correlations from the literature. In the 3rd section, we will calculate the results for average temperature, temperature gradient, local Nusselt number, and average Nusselt number on the chosen domain. And, finally, we will write the conclusion. The selected geometry has not been discussed in the previous research work.

2. Problem Formulation

In the current research article, we are going to establish a simulation for the heat transfer and a turbulent flow in the three-dimensional rectangular channel containing the two

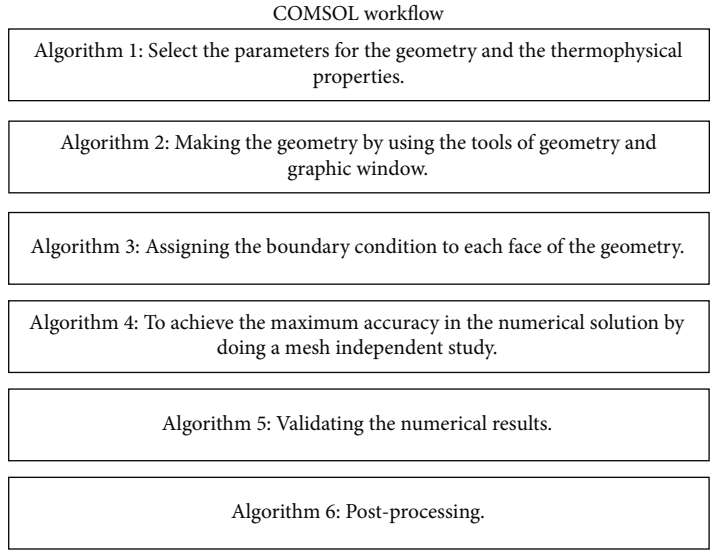

Figure 2: Working wagon wheel of COMSOL Multiphysics 5.6.

perpendicular rectangular blocks with a certain thickness. A hybrid-type nanofluid containing the aluminum oxide and copper in the water base fluid will be undergone from the inlet of the channel. The perpendicular blocks inside the three-dimensional channel are capable to rotate along the z -axis at the speed of ω. Let $L_x \times L_y \times L_z$ be the dimensions of the three-dimensional rectangular channel, and then, the thickness of perpendicular blocks will be taken as 5% of the length of the channel L_x and the gap ratio from the side of the channel is taken to $12.5\%L_y$; see Figures 1(a) and 1(b). A zero-pressure value is taken at the outlet of the channel and an average velocity u_{in} profile which is the function of the Reynolds number will be imposed from the left entrance of the channel. The perpendicular block will be allowed to rotate along the z-axis at a uniform speed ω. Let the surrounding of the channel bear a cool temperature T_c and the perpendicular blocks are facing a hot temperature T_h. A hybrid nanofluid composed of aluminum oxide and copper mixed with the water is under observation. Let subscript (1) present the aluminum oxide and subscript (2) present the thermophysical properties of copper, and then, we are in a position to explain all parameters to develop this simulation in Table 1.

The present model of hybrid nanofluid will be investigated by using the finite element package of COMSOL Multiphysics 5.6 in the space coordinate system. The three-dimensional incompressible Navier-Stokes is along with $\kappa - \varepsilon$ turbulence model of Reynolds Navier-Stokes equations. Let the velocity field of the flow be presented by the vector $\mathbf{u} = <u, \text{v}, \text{w}>$, and then, the governing partial differential equations and the energy equations are given as follows:

Continuity equation:

$$\rho_{\text{nf}}(\nabla \cdot \mathbf{u}) = 0. \tag{1}$$

Momentum equation:

$$\rho_{\text{nf}}(\mathbf{u} \cdot \nabla)\mathbf{u} = \nabla \cdot \left[-pI + (\mu_{\text{hnf}} + \mu_T)(\nabla \mathbf{u} + (\nabla \mathbf{u})^T\right]. \tag{2}$$

$\kappa - \varepsilon$ turbulence model:

$$\begin{aligned}
\rho_{\text{nf}}(\mathbf{u} \cdot \nabla)\kappa &= \nabla \cdot \left[\left(\mu_{\text{hnf}} + \frac{\mu_T}{\sigma_\kappa}\right)\nabla\kappa\right] + p_\kappa - \rho_{\text{nf}}\varepsilon, \\
\rho_{\text{nf}}(\mathbf{u} \cdot \nabla)\varepsilon &= \nabla \cdot \left[\left(\mu_{\text{hnf}} + \frac{\mu_T}{\sigma_\kappa}\right)\nabla\varepsilon\right] + c_{\varepsilon 1}\frac{\varepsilon}{\kappa} - c_{\varepsilon 2}\rho_{\text{nf}}\frac{\varepsilon^2}{\kappa},
\end{aligned} \tag{3}$$

where

$$\begin{aligned}
\mu_T &= \rho_{nf} c_\mu \frac{\kappa^2}{\varepsilon}, \\
p_\kappa &= \mu_T\left[\nabla \mathbf{u} : (\nabla \mathbf{u} + (\nabla \mathbf{u})^T\right], \\
&\rho_{\text{nf}}\left(c_p\right)_{\text{nf}} \mathbf{u} \cdot \nabla T = 0.
\end{aligned} \tag{4}$$

Boundary conditions:

Inlet: $x = 0, 0 \le y \le L_y, 0 \le z \le L_z$: $U_{\text{av}} = u_{\text{in}}$, $\kappa_0 = (3/2)(U_{\text{in}} I_T)^2$, $\varepsilon_0 = c_\mu^{3/2}(\kappa_0{}^{3/2}/L_T)$, $\partial T/\partial n = 0$.

Outlet: $x = \text{L}_x, 0 \le z \le L_z, 0 \le y \le L_y : p = 0, \nabla\kappa \cdot \mathbf{n} = 0$ and $\nabla\varepsilon \cdot \mathbf{n} = 0, \partial T/\partial n = 0$.

Along the outer surface of the rectangular box: a no-slip condition $u = 0, v = 0, w = 0$ will be imposed with $T = T_c$ and $\nabla\kappa \cdot \mathbf{n} = 0, \varepsilon = \rho_{\text{nf}}(c_\mu \kappa^2/\kappa_v \delta_w^+ \mu_{\text{nf}})$.

Along with the blocks $u = 0$, $v = 0$, and $w = \omega$, $\nabla\kappa \cdot \mathbf{n} = 0$ and $\nabla\varepsilon \cdot \mathbf{n} = 0$ and $\text{T} = \text{T}_c$, where n is the normal vector to the surface of the selected boundary $I_T = 0.05$, $L_T = 0.01850$, and $\delta_w^+ = 11.06$.

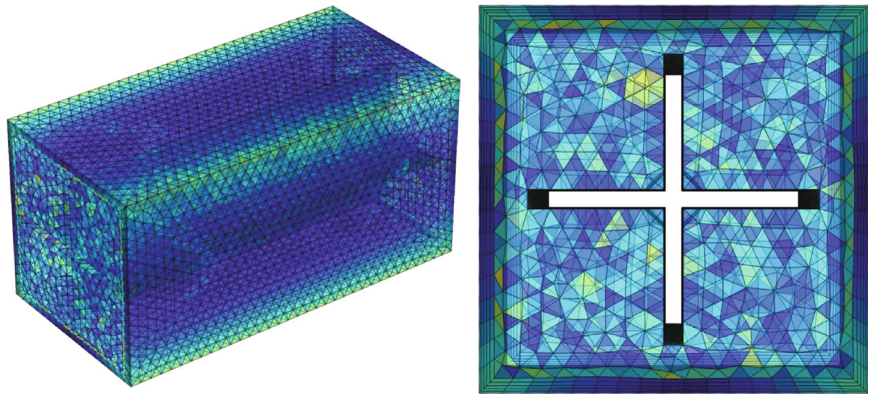

Figure 3: Schematic diagram of the meshing procedure in the twisted rectangular channel with tetrahedral elements.

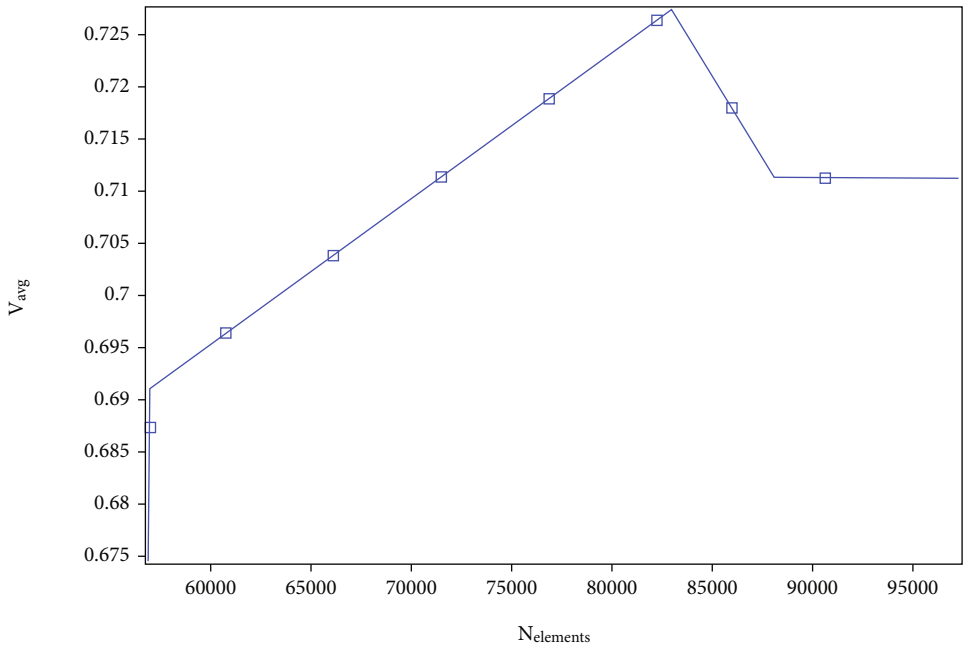

Figure 4: Average velocity magnitude at the outlet of twisted tube channel at Re = 50,000 and $\phi = \phi_1 + \phi_2 = 0.002$.

Turbulence variable:

$C_{\varepsilon 1}$	$C_{\varepsilon 2}$	C_μ	σ_κ	σ_ε	κ_v
1.44	1.92	0.09	1	1.3	0.41

2.1. Computational Parameters. Finally, we are enlisting the computational parameters as follows:

(i) Prandtl number: $\mathrm{Pr} = \mu_{\mathrm{hnf}}(c_p)_{\mathrm{nf}}/\kappa_{\mathrm{nf}}$

(ii) Heat flux: $Q = (\kappa_{\mathrm{nf}}/\kappa_f)\nabla T$

(iii) Heat transfer coefficient: $h = Q/A(T - T_b)$

(iv) Bulk temperature: $T_b = \int_\Omega \mathbf{u}T\, d\Omega / \int_\Omega \mathbf{u}\, d\Omega$

(v) Local Nusselt number: $\mathrm{Nu} = h\,x/k_{\mathrm{nf}}$

(vi) Average Nusselt number: $\mathrm{Nu}_{\mathrm{avg}} = (1/A)\int_\Omega \mathrm{Nu}_x\, dA$ where A is the area of the selected boundary

The governing equations given above subject to the boundary conditions will be considered to obtain the numerical solution by using the COMSOL Multiphysics 5.6 software. The software implements the finite element procedure to discretize the governing partial differential equation into a set of algebraic equations, and then, the set of algebraic equations will be solved by the Newton-Raphson procedure. About 75 simulations will be obtained by using the parametric study for the volume fraction of aluminum oxide and copper along with the rotational speed of the perpendicular blocks. The working algorithms of COMSOL software are given above; see Figure 2.

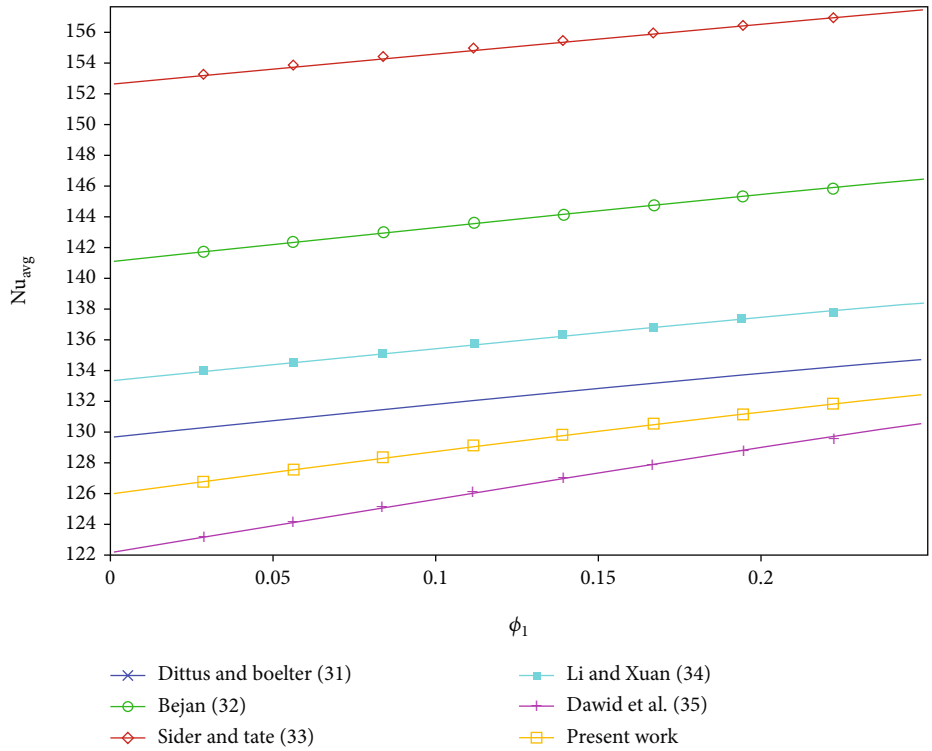

Figure 5: Validation and comparison of average Nusselt number at the exit of the channel against ϕ_1 when Re = 50,000, $\phi_2 = 0.001$, and $\omega = 0$.

Table 2: Average Nusselt number at the outlet of the channel against volume fraction of Al_2O_3.

ϕ_1	[31]	[32]	[33]	[34]	[35]	Present work
0.001	129.6963	141.0264	152.6951	133.3071	122.1352	125.9100
0.01	129.8972	141.245	152.891	133.5125	122.4697	126.1830
0.09	131.6322	143.1327	154.5806	135.2858	125.3763	128.5140
0.1	131.8412	143.3602	154.784	135.4996	125.7287	128.987
0.25	134.612	146.3746	157.4765	138.3343	130.4428	132.5200

3. Mesh Independent Study

To get the maximum accuracy level for a numerical method that is based on the meshing process, the mesh independent procedure will be the crucial step. According to the procedure, a targeted variable will be chosen at a certain boundary or location in the interested domain and then finding the numerical solution by increasing the number of elements. A point is reached where the numerical solution for the targeted variable will not be improved further. It is the stage where the numerical results will have reliable accuracy. For the current problem, the meshing process is applied to the selected three-dimensional geometry by using the various types of elements, i.e., tetrahedral, prisms, triangles, and quads; see Figure 3. The number of elements used is between 55,000 and 100,000; see Figure 4. The average velocity was chosen at the exit of the channel. The numerical results were obtained by using Re = 50,000, $\phi = 0.002$, and $\omega = 0$ where the volume fraction of aluminum oxide and copper is equal by the value of 0.001. It can be seen that as the number of elements is increased, the numerical solution for the average velocity at the outlet of the channel is improved. The solution gets the mesh independent stage when the number of elements is greater than 88,000.

Table 3: The percentage errors with Dittus-Boelter and Dawid et al.

ϕ_1	[31]	[35]
0.001	2.919359	3.09067
0.01	2.859338	3.03202
0.09	2.368873	2.50263
0.1	2.164877	2.59153
0.25	1.554096	1.59242

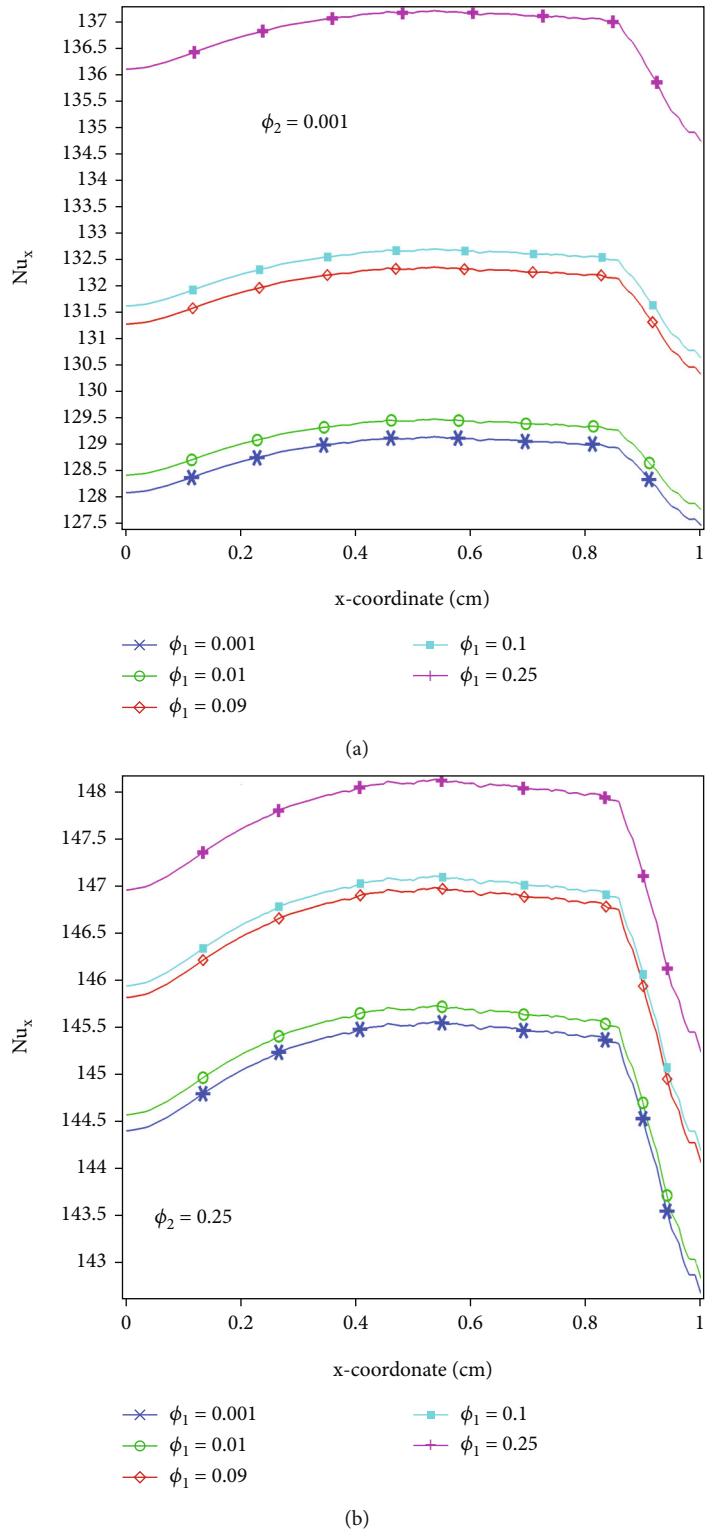

FIGURE 6: (a, b) Local Nusselt number along the length of the channel for all volume fractions of aluminum oxide at $\omega = 0$.

4. Validation and Comparison with Various Correlations

After doing the mesh independent study, the numerical solution obtained with FEM will be compared with the correlations of the average Nusselt number given in the literature [31–35]. Five different correlations are compared with the present work of the average Nusselt number at the outlet of the channel; see Figure 5. It can be seen in Table 2 that the present work for the average Nusselt number nearly satisfies

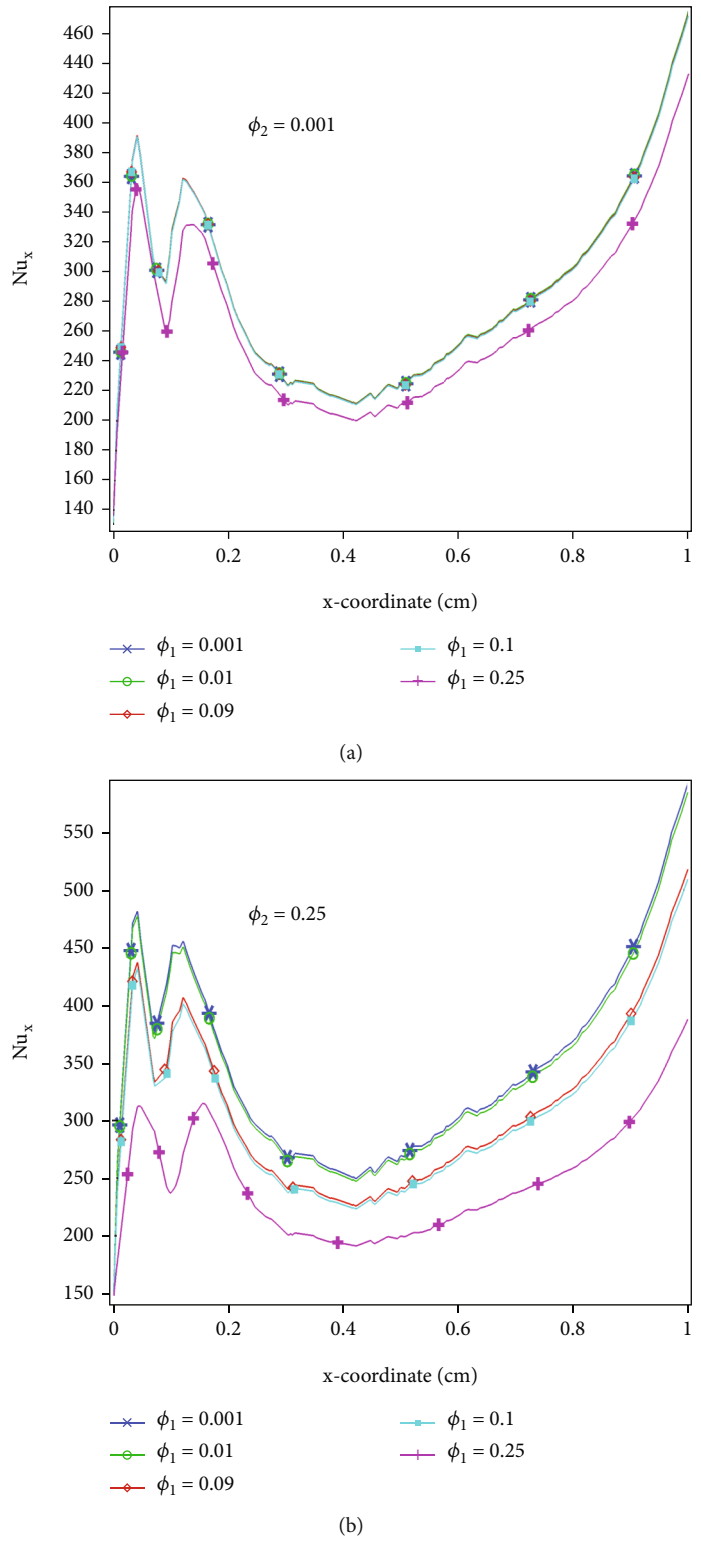

FIGURE 7: (a, b) Local Nusselt number along the length of the channel for all volume fractions of aluminum oxide at $\omega = 0.5$.

the experimental result of the Dittus-Boelter equation [31] and the numerical result of Dawid et al. [35] for the average Nusselt number.

Moreover, it can be perceived from Table 3 that, as we increase the volume fraction of aluminum oxide in the mixture, the percentage error is decreasing.

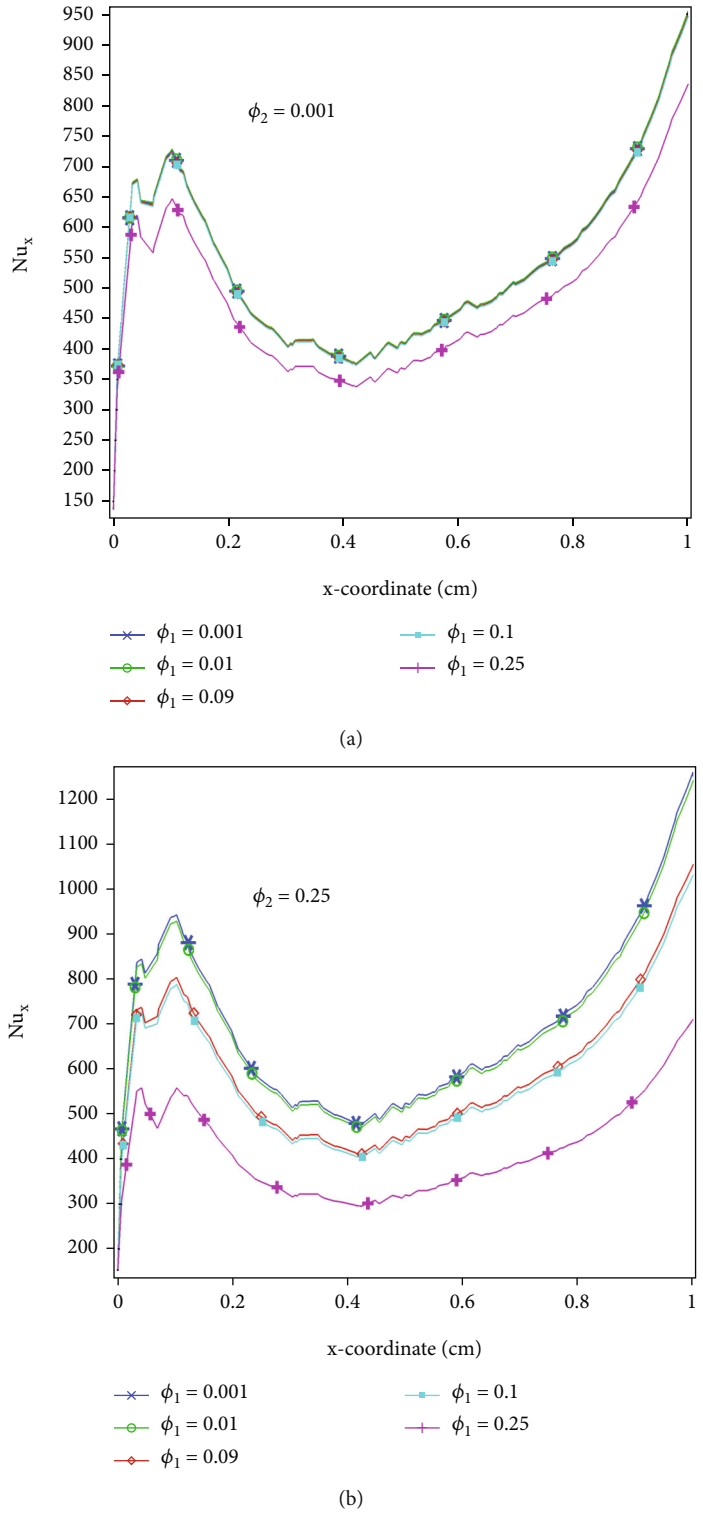

Figure 8: (a, b) Local Nusselt number along the length of the channel for all volume fractions of aluminum oxide at $\omega = 1.5$.

5. Result Discussion

5.1. Local and Average Nusselt Number. In this section, we are going to discuss the impact of the volume fraction of aluminum oxide and the copper on the local and average Nusselt number along the x-direction of the channel and altering the speed of the perpendicular blocks. The schema to check the pattern is like that of any two of the three parameters ϕ_1, ϕ_2, and ω and will be fixed and one will be changed.

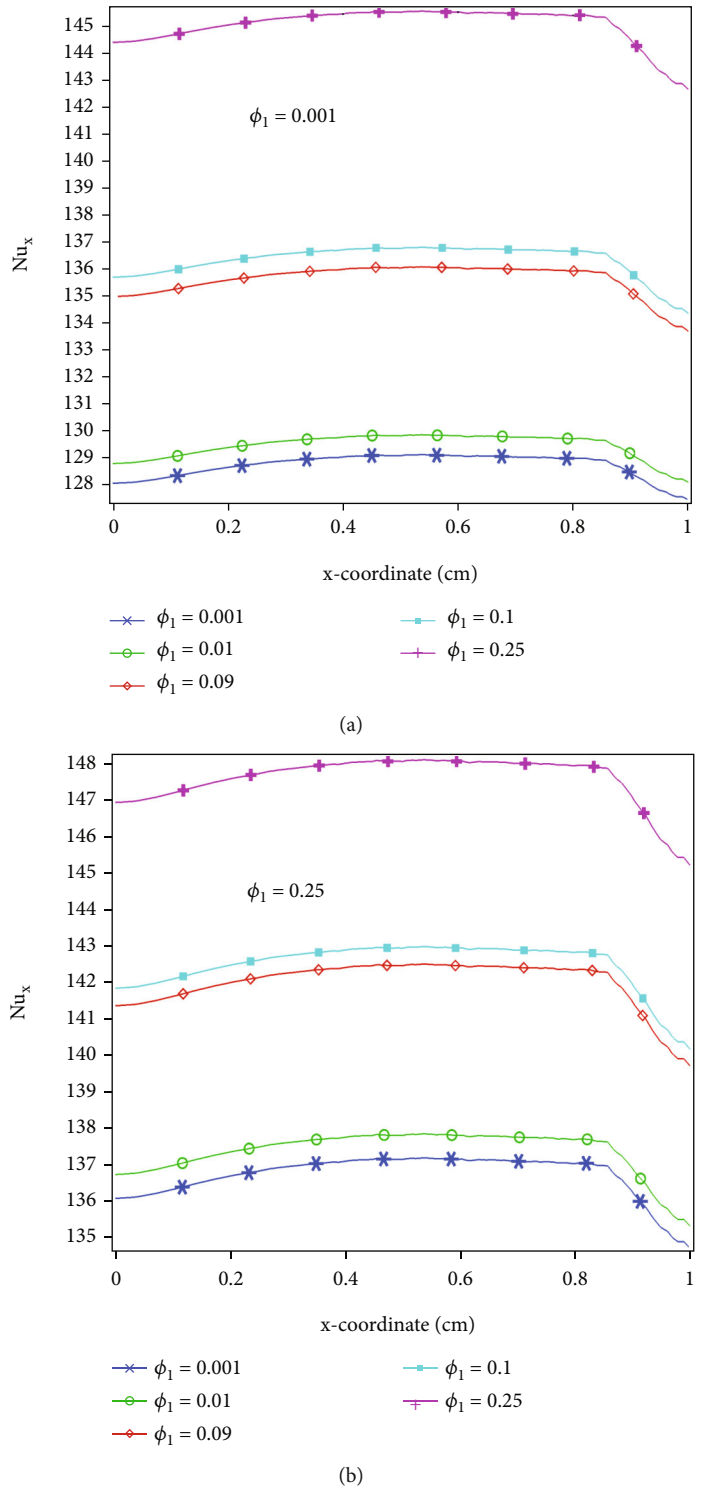

Figure 9: (a, b) Local Nusselt number along the length of the channel for all volume fractions of copper at $\omega = 0$.

Figures 6(a) and 6(b) are produced by fixing the volume fraction of the copper (0.001 and 0.25) and the speed of the perpendicular block ($\omega = 0$), and then, the impact of the local Nusselt number is checked by increasing the volume fraction of aluminum oxide. In Figure 6(a), it can be seen that the local Nusselt number is increasing along the x-direction first and then declined near the outlet of the channel when $\phi_2 = 0.001$, although, with the increasing volume fraction for aluminum oxide (0.001-0.25), the local Nusselt number is improved gradually along the x-direction of the channel. Figure 6(b) is produced by fixing $\phi_2 = 0.25$ and $w = 0$; it can be seen that the local Nusselt number along

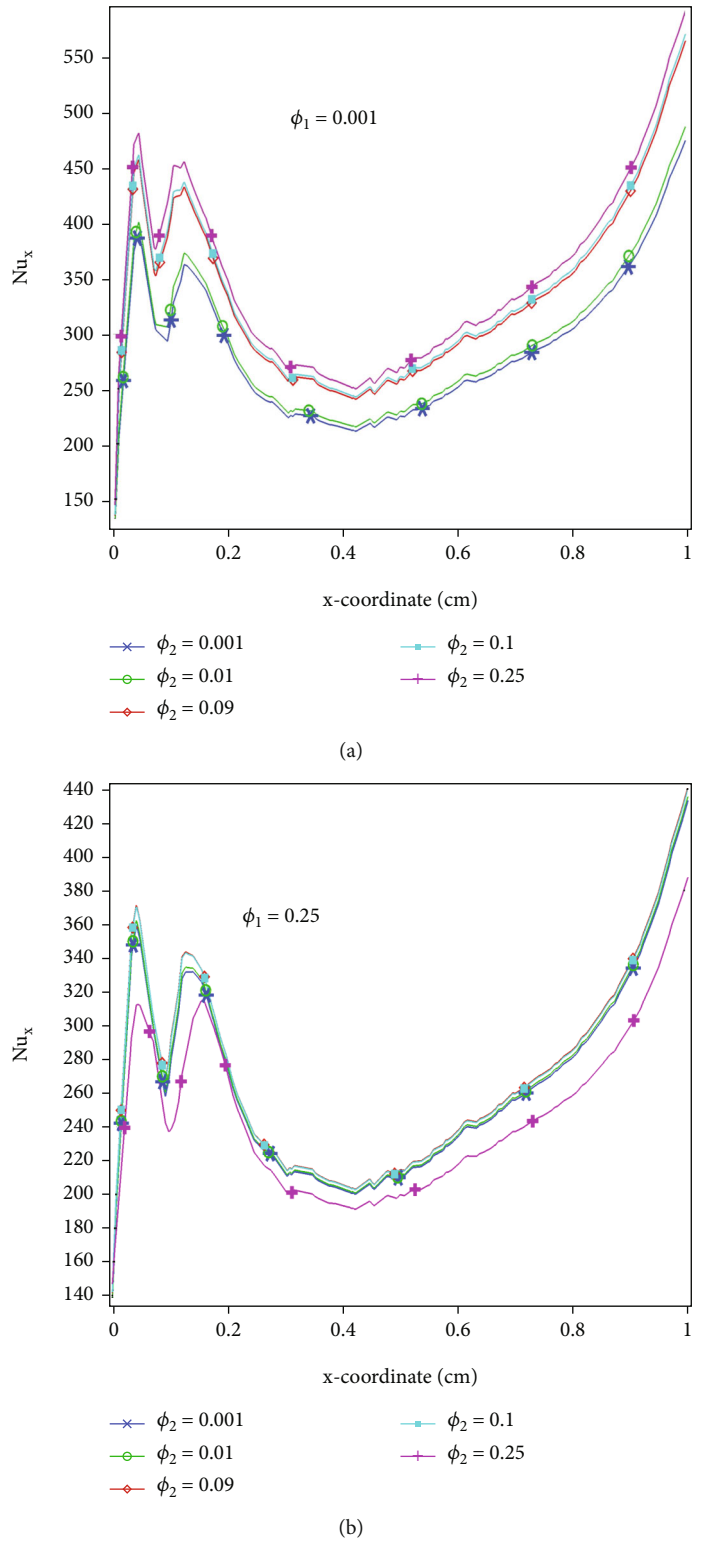

FIGURE 10: (a, b) Local Nusselt number along the length of the channel for all volume fractions of copper at $\omega = 0.5$.

the x-direction is increasing with the higher rate of increase and decrease near the outlet of the channel. Also, the values of the local Nusselt number are improved gradually by adding the volume fraction of the copper in the mixture. In both Figures 6(a) and 6(b), it can be understood that the increasing of the volume fraction of the aluminum oxide will always give favor to increasing the local Nusselt number along the x-direction.

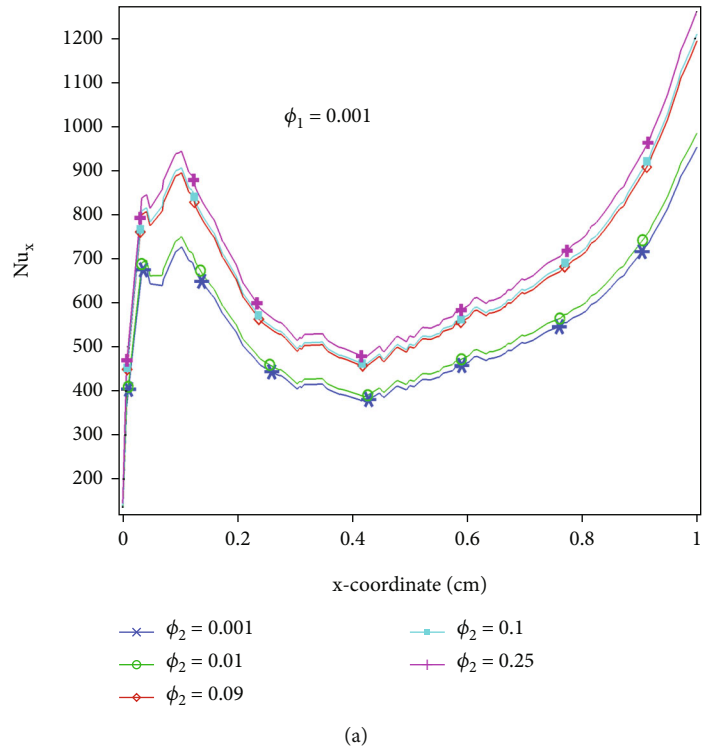

(a)

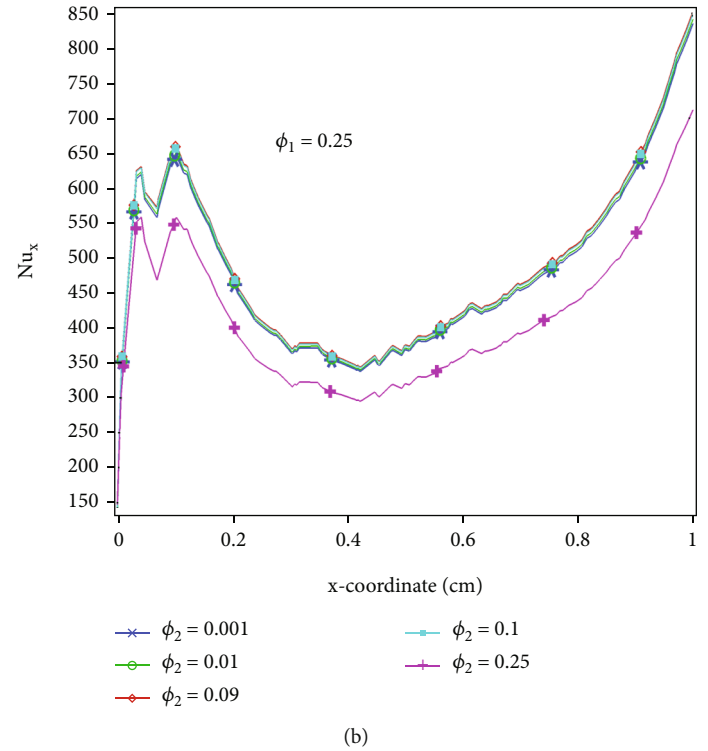

(b)

Figure 11: (a, b) Local Nusselt number along the length of the channel for all volume fractions of copper at $\omega = 1.5$.

Figures 7(a) and 7(b) are produced for $\omega = 0.5$ and $\phi_2 = 0.001, 0.25$. In the case in Figures 2(a) and 2(b), when we have obtained the simulation by increasing the rotational speed of perpendicular blocks, the local Nusselt number along the x-direction is increasing abruptly very near to the entrance of the channel and then decreases up to the middle of the channel and finally increases up to the exit of the channel. Unlike in the case discussed in Figures 6(a) and 6(b), in this case, the local Nusselt number is decreased with the increase in volume fraction

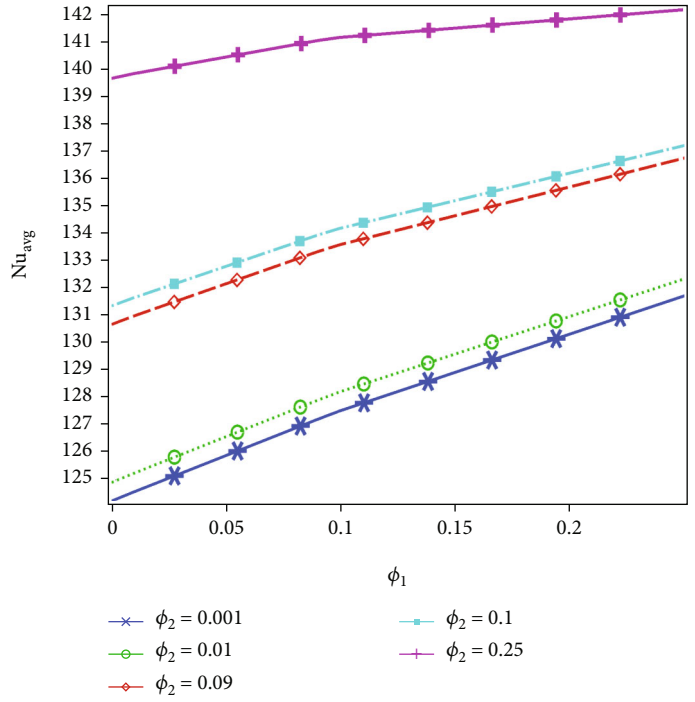

(a)

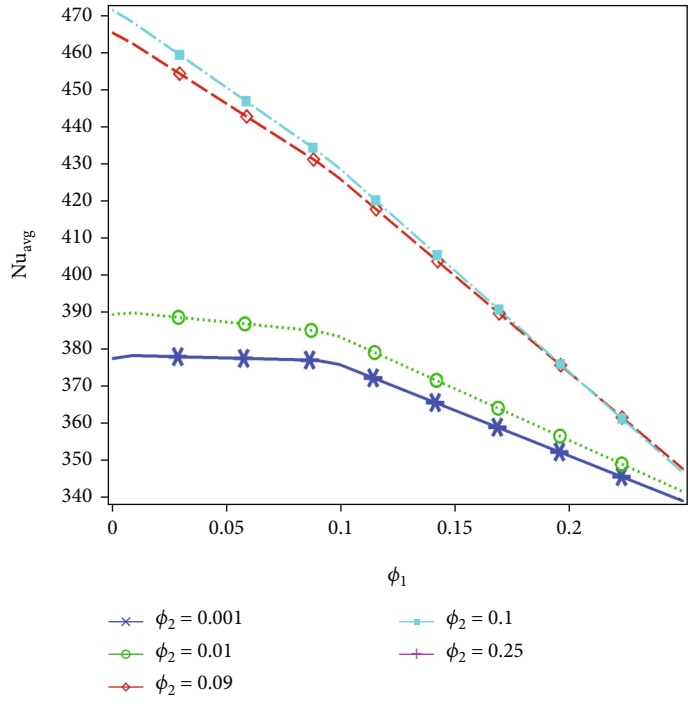

(b)

Figure 12: Continued.

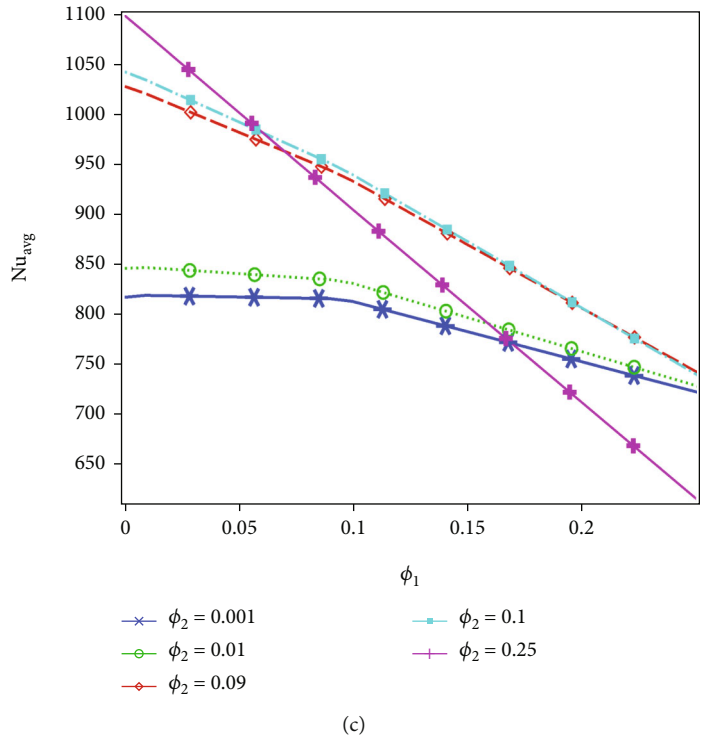

Figure 12: The average Nusselt number at the upper surface of the channel with the increasing volume fraction of the aluminum oxide: (a) $\omega = 0$, (b) $\omega = 0.5$, and (c) $\omega = 1.5$.

of aluminum oxide ϕ_1 from 0.001 to 0.25 as shown in both Figures 2(a) and 2(b). In Figure 7(b), it can be also seen that with increasing the volume fraction of copper, the pattern of the local Nusselt number is changed due to an increase in the volume fraction of alumina. Though, in this case, the local Nusselt number is decreasing with the increase in volume fraction, the pattern is obvious as compared in Figure 6(a). Moreover, the addition of the copper in the hybrid mixture by the fraction of 0.25 will increase the values of the local Nusselt number along the length of the channel.

In Figures 8(a) and 8(b), again we have focused on the pattern of the local Nusselt number with the increase in the rotation of perpendicular blocks by 1.5 in the domain and fixed the volume fraction of the copper by 0.001 and 0.25. The same pattern can be seen along the length of the channel; the local Nusselt number is increasing near the inlet in a very quick manner and then decreasing up to the middle of the channel and finally increasing up to the exit of the channel. But for the fixed volume fraction ϕ_2 of copper oxide, the local Nusselt number along the length of the channel is decreasing with an increase in the volume fraction of the aluminum oxide. Moreover, the speed of rotation of the perpendicular blocks will improve the local Nusselt number values along the length of the channel. It can be concluded that whenever the perpendicular blocks are not rotated, then the local Nusselt number at the exit of the channel is maximum; but when the block is rotating at the same speed, then the local Nusselt number at the outlet of the channel is maximum comparing Figures 6(a) and 6(b) and 7(a) and 7(b).

In Figures 9(a) and 9(b), the local Nusselt number is calculated by fixing the speed of rotation of the block and the volume fraction of the copper. It seems that with an increase in the volume fraction of the copper oxide in both cases of Figures 9(a) and 9(b) by fixing the volume fraction of the aluminum oxide, the local Nusselt number is always increasing along the channel and decreases up to the outlet of the channel. The addition of the aluminum oxide will boost the local Nusselt number along the length of the channel with the same pattern.

In Figures 10(a) and 10(b), the pattern of the local Nusselt number is checked by increasing the speed of rotation of the perpendicular blocks for a particular volume fraction of aluminum oxide. It is obvious that in Figure 10(a) the local Nusselt number is increasing abruptly near the inlet and is maximum at the outlet of the channel. The local Nusselt number is maximum at the outlet of the channel which means that the convection is maximum at the outlet of the channel. It can be seen that in Figure 10(a), with increasing the volume fraction of copper, the local Nusselt number is increasing. In Figure 10(b), it can be seen that adding more volume fraction of aluminum oxide will decrease the local Nusselt number by increasing the volume fraction of copper. Finally, we can see that the speed of rotation of the perpendicular blocks will increase the overall local Nusselt number along the length of the channel.

In Figures 11(a) and 11(b), the local Nusselt number along the length of the channel is presented by increasing

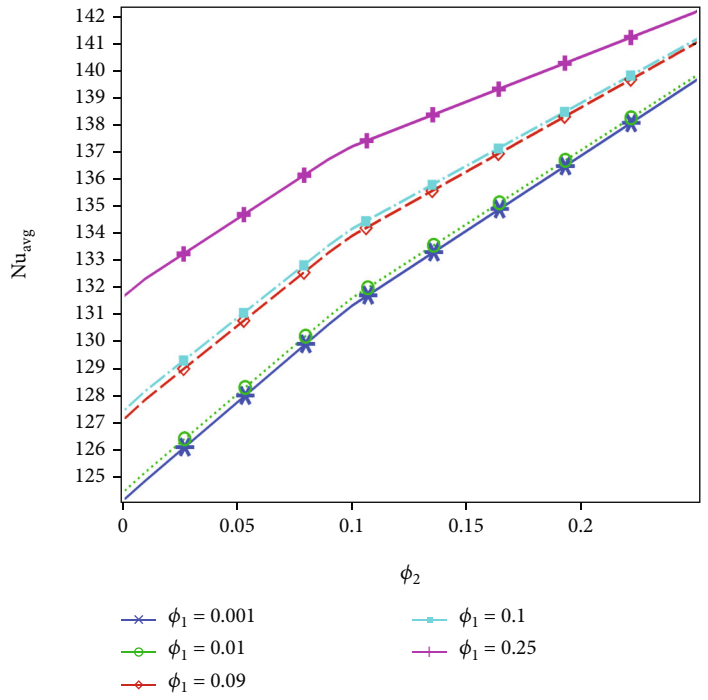

(a)

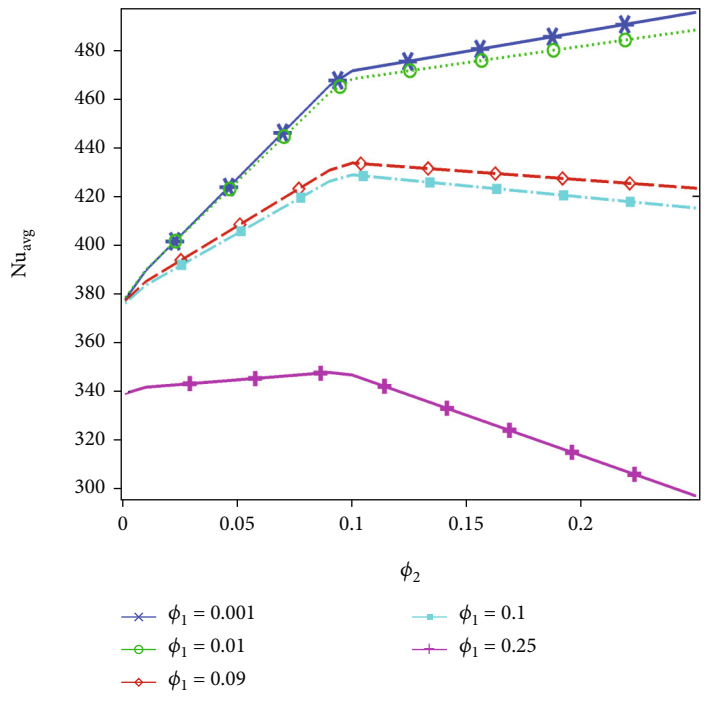

(b)

Figure 13: Continued.

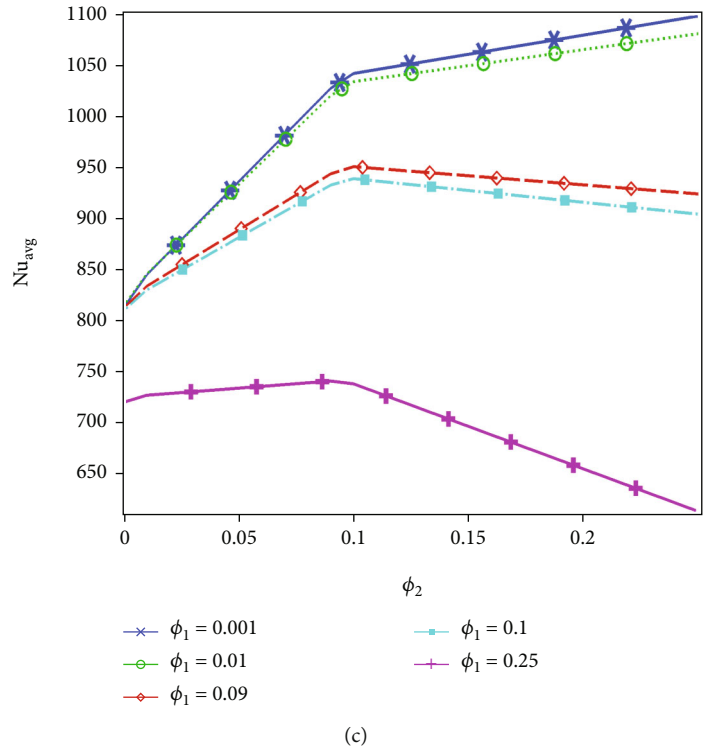

FIGURE 13: The average Nusselt number at the upper surface of the channel with the increasing volume fraction of the copper: (a) $\omega = 0$, (b) $\omega = 0.5$, and (c) $\omega = 1.5$.

the speed of rotation. It can be seen that with the increase in speed of rotation the local Nusselt number along the length of the channel is improved. Also, by adding the volume fraction of the aluminum oxide, the Nusselt number is decreasing by the values along the length of the channel. In Figure 11(a), when the volume fraction of alumina oxide was 0.001, the local Nusselt number is increasing at the outlet of the channel by increasing the volume fraction of the copper from 0.001 to 0.25. If we observe the local Nusselt number at the volume fraction of aluminum oxide at 0.25, the local Nusselt number is minimum at $\phi_2 = 0.25$.

The average Nusselt number against the volume fraction of alumina is calculated at the upper surface of the channel with a fixed volume fraction of the copper with 0.001-0.25 and with a variable speed of rotation of perpendicular blocks in Figures 12(a)–12(c). It can be seen that when $w = 0$ in Figure 12(a), the average Nusselt number is increasing at the upper surface of the channel. But, when the speed of the rotation of the perpendicular blocks is increased as in Figures 12(b) and 12(c), the average Nusselt number at the upper surface of the channel is decreasing. Therefore, it can be said that when the blocks are not moving, the convection is greater than conduction at the upper surface of the channel, and when they are in motion, the situation will be quite different.

In Figures 13(a)–13(c), the average Nusselt number at the upper surface of the rectangular channel has been determined by fixing the volume fraction of the aluminum oxide and rotation of the perpendicular blocks. These graphs perceived that with increasing the volume fraction of the copper, the average Nusselt number at the upper surface of the channel is increasing when the perpendicular blocks are stationary; see Figure 13(a). The pattern of the average Nusselt number is altered when the blocks are rotated $\omega = 0.5$ and 1.5; see Figures 13(b) and 13(c). It can be concluded that the average Nusselt number is increasing for the volume fraction of copper up to 0.1 and then decreasing. The process of declining becomes faster when the aluminum oxide is further added by the volume fraction ϕ_1. Therefore, in the cases when the blocks are rotating with some speed, with the addition of aluminum oxide in the copper, the average Nusselt number is decreasing with increasing the volume fraction of the copper.

5.2. Average Temperature and Gradient of Temperature along the z-Direction. Let μ be the total viscosity of the hybrid nanofluid that was calculated by fixing the volume fraction of the copper and the speed of rotation of the blocks. Now, we are determining the average temperature at the inlet of the channel in Figures 14(a)–14(d). From the graphs, it is obvious that the average temperature at the inlet of the channel is decreasing with the increasing viscosity of the hybrid nanofluid. Also, by increasing the speed of the perpendicular blocks, the average temperature along the middle of the channel further boosts up but shows the same behavior with increasing viscosity of hybrid nanofluids. Also, adding the copper by some volume fraction in the

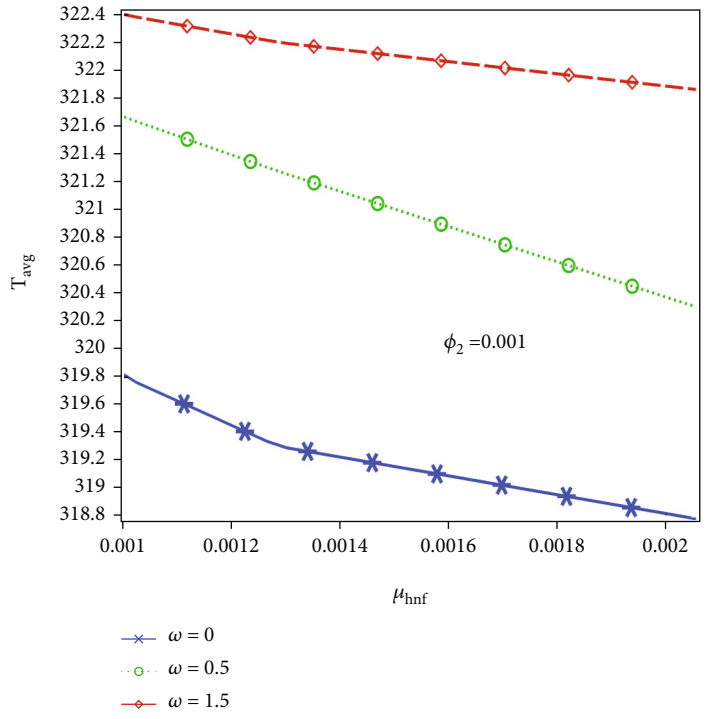

(a)

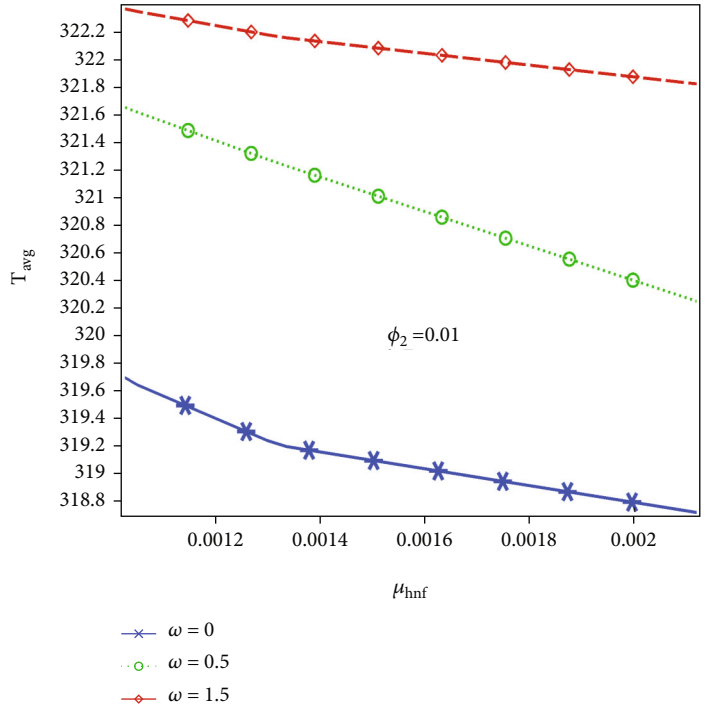

(b)

Figure 14: Continued.

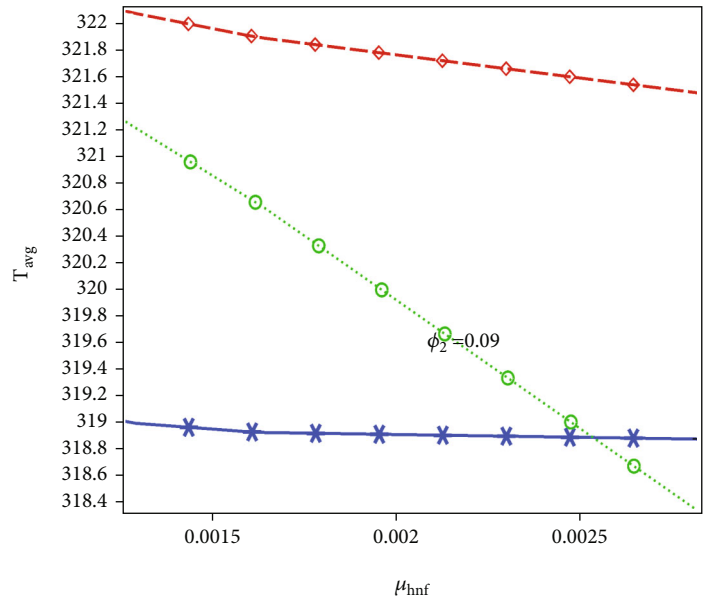

(c)

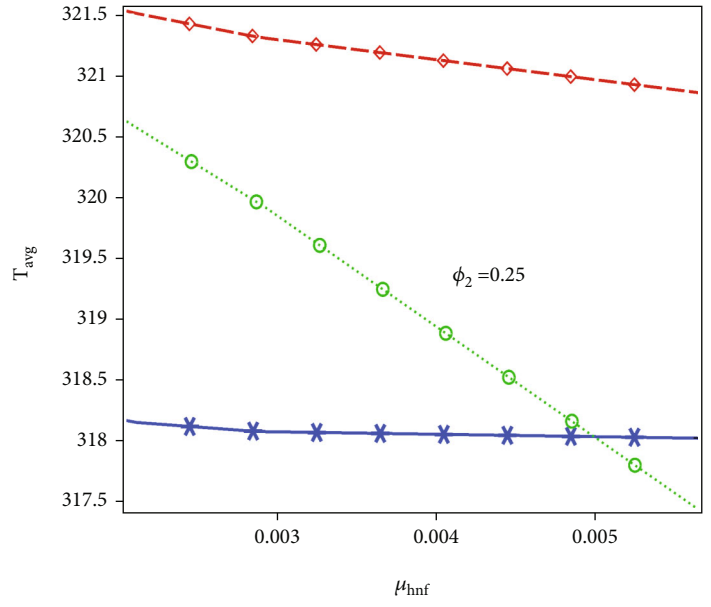

(d)

Figure 14: (a–d) Average temperature vs. the viscosity of the hybrid nanofluid at the inlet of the channel for all the volume fractions of aluminum oxide.

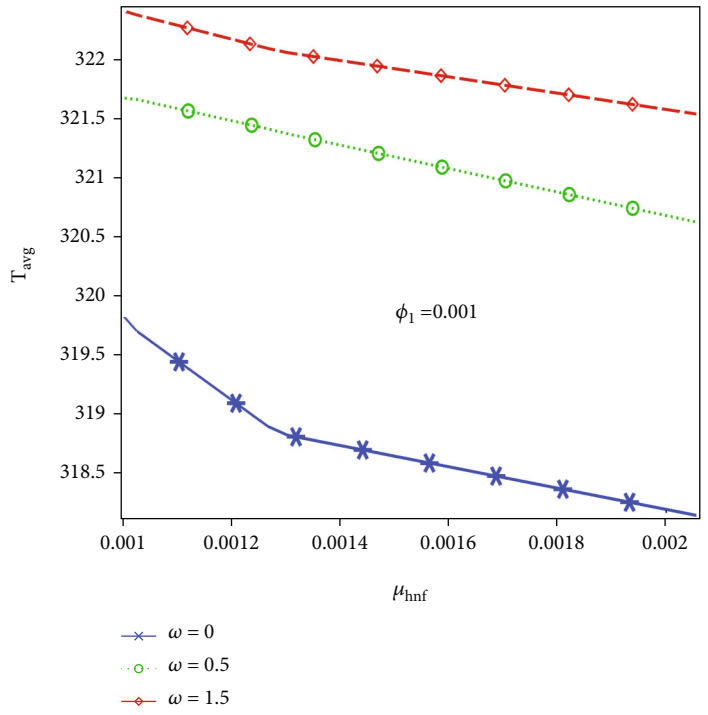

(a)

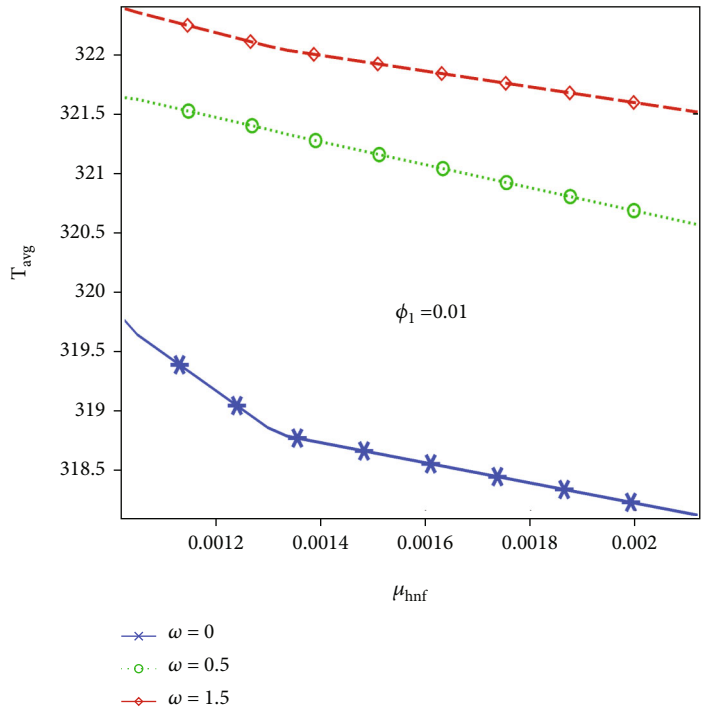

(b)

Figure 15: Continued.

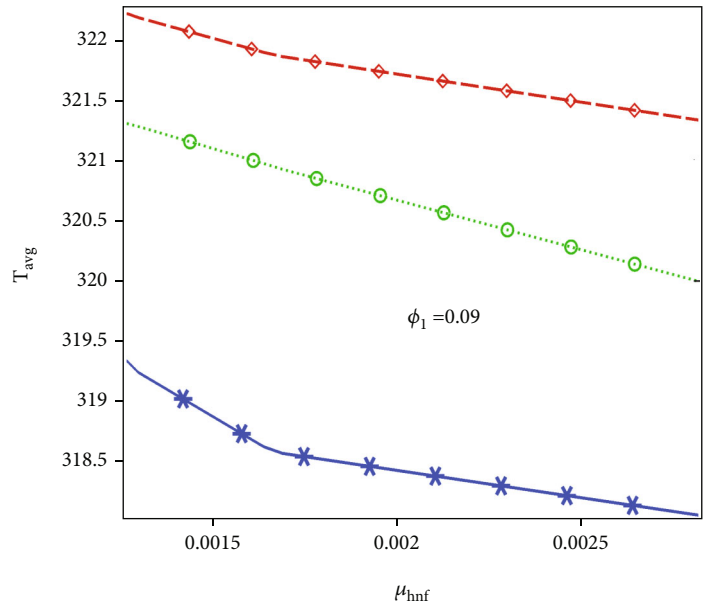

(c)

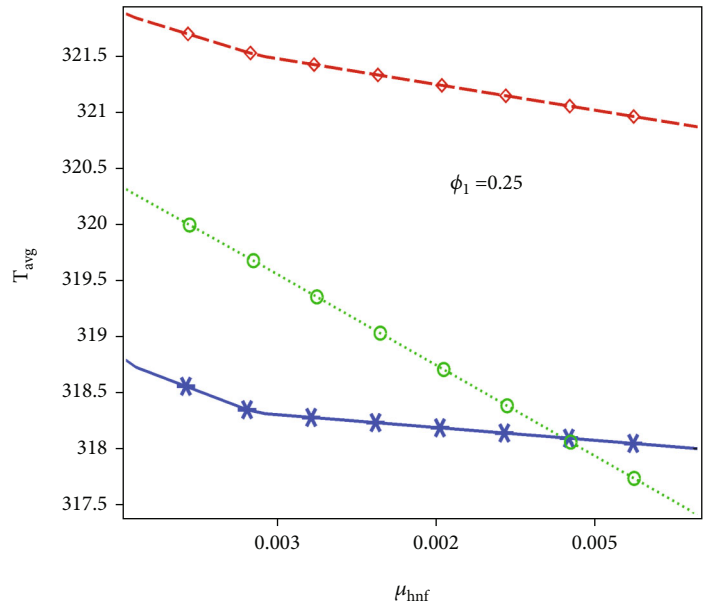

(d)

Figure 15: (a–d) Average temperature vs. the viscosity of the hybrid nanofluid at the inlet of the channel for all the volume fractions of copper.

Table 4: Average temperature at the inlet and the viscosity.

ϕ_1	ϕ_2	$\omega = 0$		$\omega = 0.5$		$\omega = 1.5$	
		μ (Pa·s)	T_{avg} (K)	μ (Pa·s)	T_{avg} (K)	μ (Pa·s)	T_{avg} (K)
0.001	**0.001**	**0.001003**	**319.82**	**0.001003**	**321.67**	**0.001003**	**322.4**
0.001	0.01	0.001026	319.7	0.001026	321.66	0.001026	322.37
0.001	0.09	0.001267	318.9	0.001267	321.41	0.001267	322.09
0.001	0.1	0.001302	318.82	0.001302	321.37	0.001302	322.05
0.001	0.25	0.002056	318.14	0.002056	320.62	0.002056	321.54
0.01	0.001	0.001026	319.76	0.001026	321.64	0.001026	322.39
0.01	0.01	0.00105	319.65	0.00105	321.62	0.00105	322.35
0.01	0.09	0.001299	318.86	0.001299	321.37	0.001299	322.07
0.01	0.1	0.001336	318.79	0.001336	321.33	0.001336	322.03
0.01	0.25	0.002119	318.13	0.002119	320.57	0.002119	321.52
0.09	0.001	0.001267	319.34	0.001267	321.31	0.001267	322.22
0.09	0.01	0.001299	319.24	0.001299	321.28	0.001299	322.18
0.09	0.09	0.001639	318.63	0.001639	320.97	0.001639	321.9
0.09	0.1	0.00169	318.57	0.00169	320.93	0.00169	321.86
0.09	0.25	0.00282	318.06	0.00282	320	0.00282	321.33
0.1	0.001	0.001302	319.29	0.001302	321.26	0.001302	322.2
0.1	0.01	0.001336	319.2	0.001336	321.23	0.001336	322.16
0.1	0.09	0.00169	318.6	0.00169	320.92	0.00169	321.87
0.1	0.1	0.001743	318.55	0.001743	320.87	0.001743	321.84
0.1	0.25	0.00293	318.05	0.00293	319.91	0.00293	321.31
0.25	0.001	0.002056	318.78	0.002056	320.31	0.002056	321.87
0.25	0.01	0.002119	318.72	0.002119	320.25	0.002119	321.83
0.25	0.09	0.00282	318.34	0.00282	319.7	0.00282	321.52
0.25	0.1	0.00293	318.31	0.00293	319.61	0.00293	321.48
0.25	*0.25*	*0.005646*	*318*	*0.005646*	*317.41*	*0.005646*	*320.86*

mixture will lead to a decline a little bit temperature at the inlet of the channel compared to Figures 14(a) and 14(d).

In Figures 15(a)–15(d), the average temperature is measured by fixing the volume fraction of the aluminum oxide and the speed of rotation of the perpendicular blocks, where μ present the viscosity of the hybrid nanofluid when the volume fraction of the copper in the mixture is varying from 0.001 to 0.25. As we found in Figure 15(a), the average temperature is quickly decreasing at the inlet of the channel with the increasing total viscosity of the channel when compared with Figure 14(a), although the addition of the aluminum fraction in the hybrid mixture will give additional support to the decline in the average temperature at the inlet of the channel. All cases can be compared in this regard. In Table 4, the maximum average temperature occurs when $\phi_1 = \phi_2 = 0.001$ (presented in bold) and the minimum average temperature occurs when $\phi_1 = \phi_2 = 0.25$ (presented in italic) for all the cases even if the blocks are rotating or stationary.

As in the current problem, a hybrid nanofluid along the rectangular channel contained the perpendicular moving blocks. A hot temperature was applied to the perpendicular blocks and a cool temperature condition was applied to the upper four-sided surfaces of the rectangular channel. In Figures 16(a)–16(d), the temperature gradient was expressed in terms of the volume fraction of aluminum oxide for a particular volume fraction of copper oxide and the rotational speed of the perpendicular blocks. It can be seen that when the perpendicular blocks are stationary, the temperature gradient along the z-direction is decreasing by increasing the volume fraction of aluminum oxide. As the rotational speed is increasing, the temperature gradient along the z-direction is increasing gradually with the increase of the volume fraction of aluminum oxide. Moreover, an addition of the copper in the mixture will support to decrease in the temperature gradient along the z-direction in the case when the perpendicular blocks are stationary. While the perpendicular blocks are rotating, the temperature gradient along the z-direction is increasing with the increase in volume fraction of the aluminum oxide. A great impact on the temperature gradient along the z-direction can be seen when the blocks are rotating at some speed ω which is obvious when comparing all the cases.

To examine the relationship of the temperature gradient along the z-direction with the volume fraction of copper, see Figures 17(a)–17(d). The temperature gradient along the z-direction is decreasing when the perpendicular blocks are stationary and increases when the perpendicular blocks

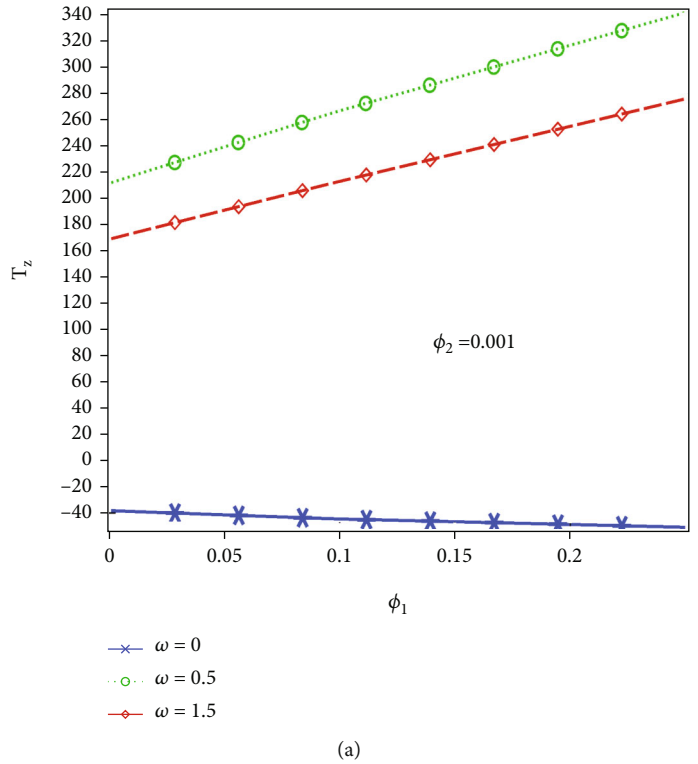

(a)

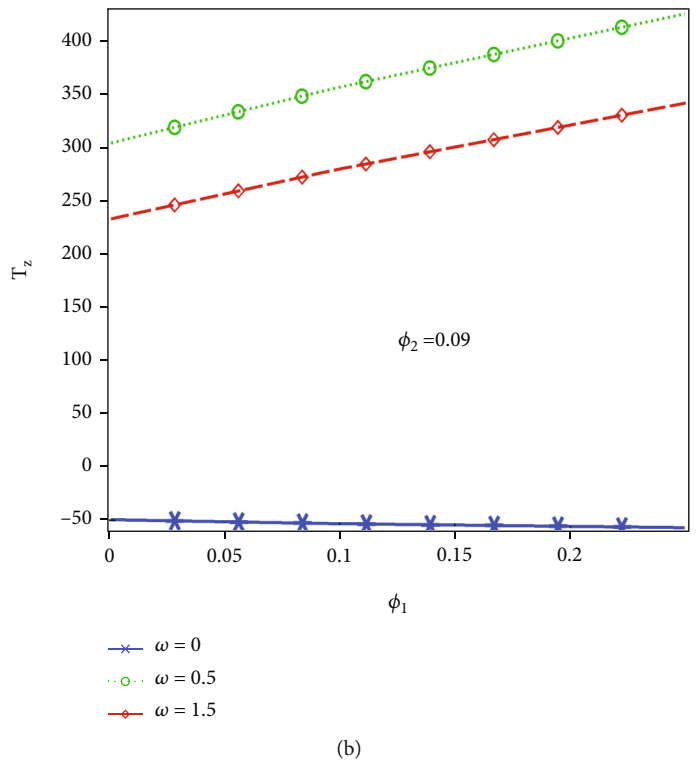

(b)

Figure 16: Continued.

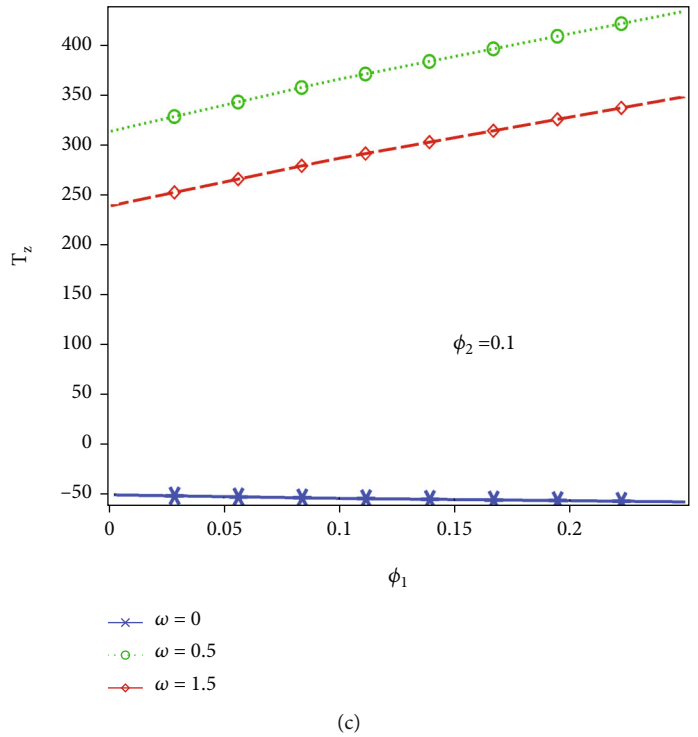

(c)

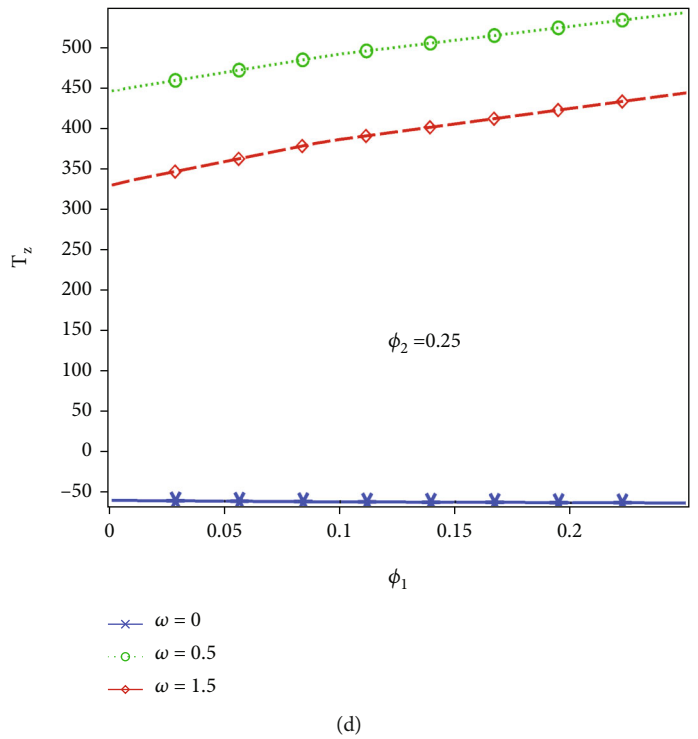

(d)

Figure 16: (a–d) Temperature gradient along the z-axis at the middle of the channel against the volume fraction of alumina oxide.

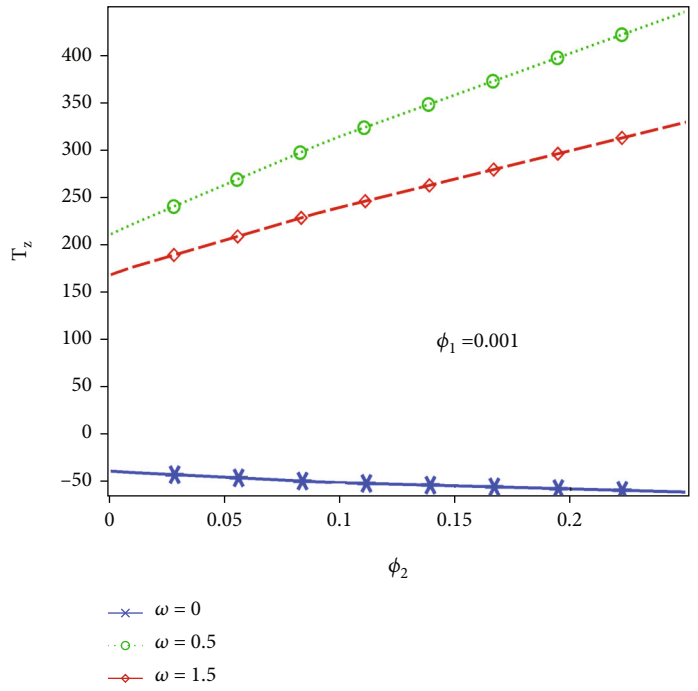

(a)

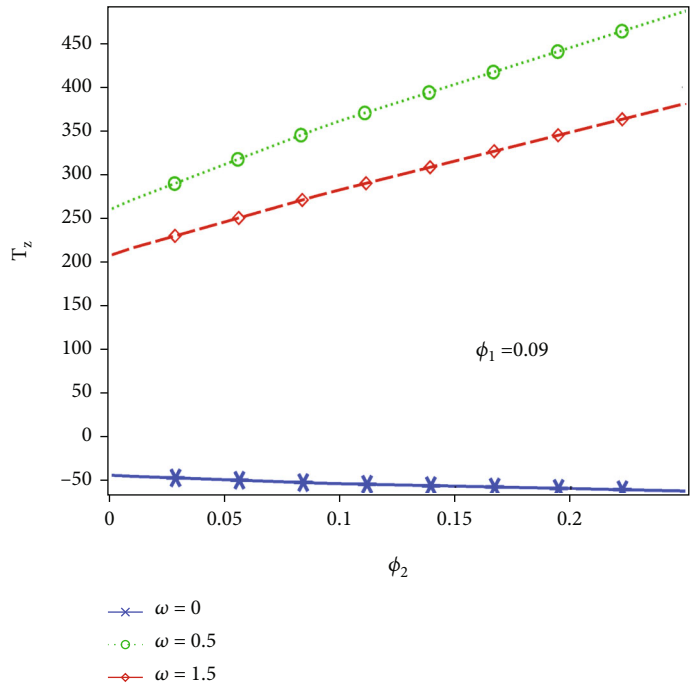

(b)

Figure 17: Continued.

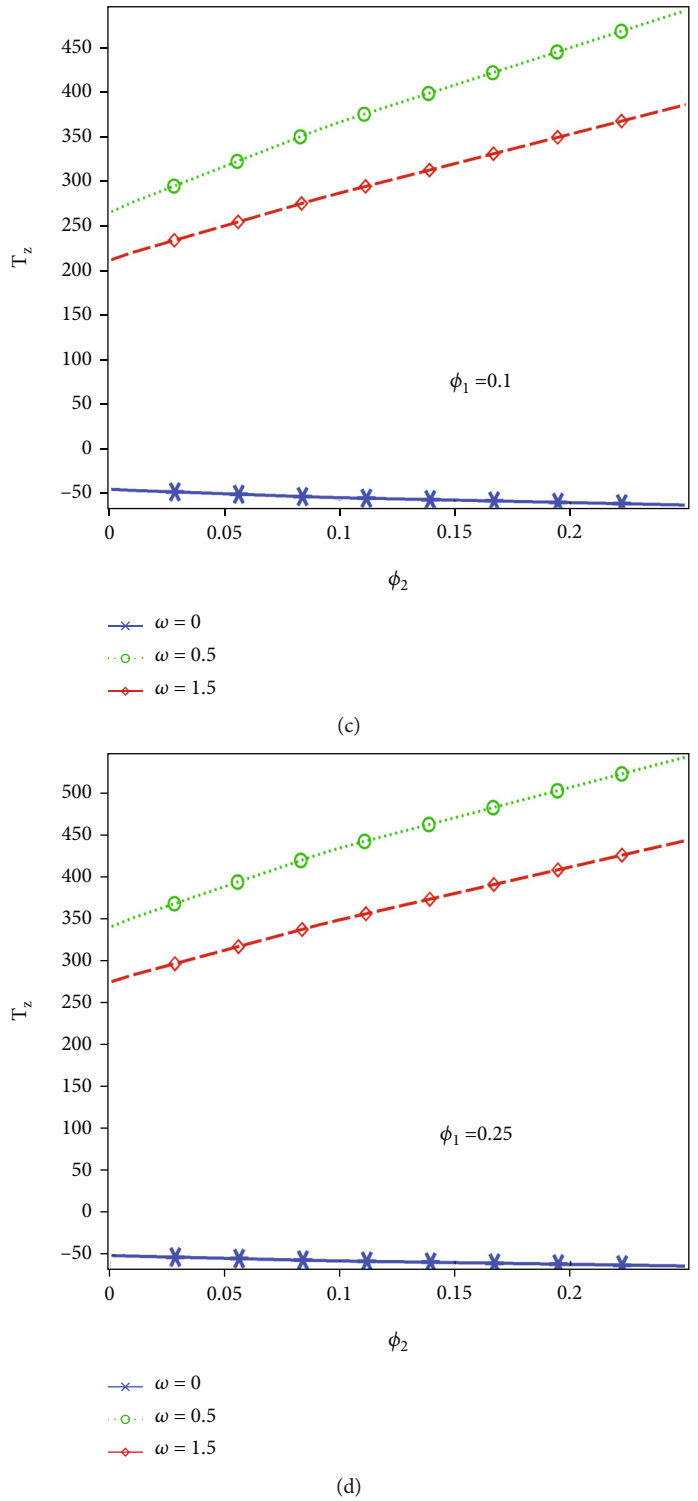

FIGURE 17: (a–d) Temperature gradient along the z-axis at the middle of the channel against the volume fraction of alumina oxide.

are moving with speed $\omega = 0.5$ and 1.5. The addition of the volume fraction of the alumina will lead to a decrease in the temperature gradient for the case when perpendicular blocks are stationary and an increase when the perpendicular blocks are rotating. From all this discussion, we can say that stationary perpendicular blocks are producing a cool environment inside the rectangular channel, while when they are moving, they are increasing the temperature gradient along the z-direction. The motion of the perpendicular blocks will take a great part in heat conduction over all the domains.

6. Conclusion

In the current article, we have analyzed the heat transfer in a three-dimensional rectangular channel containing the perpendicular rotating blocks when a hybrid nanofluid flows which contained a mixture of aluminum oxide and copper. Both the aluminum oxide and the copper were mixed in the volume fraction of 0.001-0.25 in the water base fluid. The study was done by the variation of the speed of rotation of the perpendicular rectangular blocks $\omega = 0$, 0.5, and 1.5. The governing partial differential equations of heat and the Navier-Stokes equations $\kappa - \varepsilon$ were used to develop the simulation into an emerging software COMSOL Multiphysics 5.6. The hybrid mixture was entered from the inlet of the channel with an average speed of Re = 50,000 whereas the turbulence dissipation rate ε and turbulence kinetic energy κ were kept in the range $3.46E-6$ to $3.76E-5$ and $2.50E-06$ to $1.23E-05$. The numerical results are validated by doing the mesh independent study and verified by comparing the average Nusselt number with the available correlations from the literature. The graphs and tables were used to present the numerical results for the local Nusselt number, average Nusselt number, average temperature, and average temperature gradient along the middle of the channel. We have reached the following decisions:

(i) For the fixed rotation of the perpendicular blocks and the volume fraction of copper, the local Nusselt number along the x-direction is increasing with the volume fraction of the aluminum oxide. For a stationary block, the local Nusselt number is found minimum at the outlet of the channel, and for rotational blocks, the local Nusselt number is maximum at the outlet of the channel

(ii) If blocks are rotating, then the volume fraction of the aluminum oxide will decrease the local Nusselt number along the x-direction. It was also perceived that when the blocks are rotating, the addition of the volume fraction of copper will increase the local number along the x-direction

(iii) The average Nusselt number at the upper surface of the channel is increasing by increasing the volume fraction of the aluminum oxide as well as the copper for stationary blocks and decreasing when the perpendicular blocks are in motion

(iv) The average temperature at the inlet of the channel is decreasing by increasing with the total viscosity of the hybrid nanofluid. The average temperature can be readily reduced by fixing the volume fraction of aluminum oxide and changing the volume fraction of copper

(v) Also, the average temperature at the inlet of the channel is increasing by increasing the speed of the rotation of the blocks. Moreover, the average temperature can be minimized by increasing the volume fraction of both nanoparticles

(vi) The temperature gradient along the z-direction is decreasing with the increase in volume fraction of both the nanofluids Al_2O_3 and Cu when the blocks are stationary. The rotational speed of the perpendicular blocks will be the cause to increase in the temperature gradient along the z-direction

Data Availability

No data were required to perform this research.

Conflicts of Interest

The authors declare that they have no conflict of interest.

Acknowledgments

This work was supported by Taif University Researchers Supporting Project Number (TURSP-2020/207), Taif University, Taif, Saudi Arabia.

References

[1] S. U. S. Choi, Z. G. Zhang, W. Yu, F. E. Lockwood, and E. A. Grulke, "Anomalous thermal conductivity enhancement in nanotube suspensions," *Applied Physics Letters*, vol. 79, no. 14, pp. 2252–2254, 2001.

[2] I. Khan, S. Fatima, M. Y. Malik, and T. Salahuddin, "Exponentially varying viscosity of magnetohydrodynamic mixed convection Eyring-Powell nanofluid flow over an inclined surface," *Results in Physics*, vol. 8, pp. 1194–1203, 2018.

[3] N. A. Halim, S. Sivasankaran, and N. F. M. Noor, "Active and passive controls of the Williamson stagnation nanofluid flow over a stretching/shrinking surface," *Neural Computing and Applications*, vol. 28, no. S1, pp. 1023–1033, 2017.

[4] A. K. Tiwari, S. Javed, H. F. Oztop, Z. Said, and N. S. Pandya, "Experimental and numerical investigation on the thermal performance of triple tube heat exchanger equipped with different inserts with WO_3/water nanofluid under turbulent condition," *International Journal of Thermal Sciences*, vol. 164, article 106861, 2021.

[5] N. S. Pandya, H. Shah, M. Molana, and A. K. Tiwari, "Heat transfer enhancement with nanofluids in plate heat exchangers: a comprehensive review," *European Journal of Mechanics-B/Fluids*, vol. 81, pp. 173–190, 2020.

[6] Z. Said, S. Sundar, A. K. Tiwari et al., *Recent advances on the fundamental physical phenomena behind stability, dynamic motion, thermophysical properties, heat transport, applications, and challenges of nanofluids*, Physics Reports, 2021.

[7] S. Samiezadeh, R. Khodaverdian, M. H. Doranehgard, H. Chehrmonavari, and Q. Xiong, "CFD simulation of thermal performance of hybrid oil-Cu-Al2O3 nanofluid flowing through the porous receiver tube inside a finned parabolic trough solar collector," *Sustainable Energy Technologies and Assessments*, vol. 50, article 101888, 2022.

[8] Z. Said, N. K. Cakmak, L. Prabhakar Sharma, and S. Sundar, "Synthesis, stability, density, viscosity of ethylene glycol-based ternary hybrid nanofluids: experimental investigations and model -prediction using modern machine learning techniques," *Powder Technology*, vol. 400, article 117190, 2022.

[9] S. Suresh, K. P. Venkitaraj, P. Selvakumar, and M. Chandrasekar, "Effect of Al_2O_3-Cu/water hybrid nanofluid in heat transfer," *Experimental Thermal and Fluid Science*, vol. 38, pp. 54–60, 2012.

[10] M. Baghbanzadeh, A. Rashidi, D. Rashtchian, R. Lotfi, and A. Amrollahi, "Synthesis of spherical silica/multiwall carbon nanotubes hybrid nanostructures and investigation of thermal conductivity of related nanofluids," *Thermochimica Acta*, vol. 549, pp. 87–94, 2012.

[11] D. Wen and Y. Ding, "Experimental investigation into convective heat transfer of nanofluids at the entrance region under laminar flow conditions," *International Journal of Heat and Mass Transfer*, vol. 47, no. 24, pp. 5181–5188, 2004.

[12] X.-Q. Wang and A. S. Mujumdar, "Heat transfer characteristics of nanofluids: a review," *International Journal of Thermal Sciences*, vol. 46, no. 1, pp. 1–19, 2007.

[13] S. Heris and S. Zeinali, "Experimental investigation of oxide nanofluids laminar flow convective heat transfer," *International communications in heat and mass transfer*, vol. 33, no. 4, pp. 529–535, 2006.

[14] S. Z. Heris, S. G. Etemad, and M. N. Esfahany, "Experimental investigation of convective heat transfer of Al2O3/water nanofluid in circular tube," *International journal of heat and fluid flow*, vol. 28, no. 2, pp. 203–210, 2007.

[15] F. Mabood and A. T. Akinshilo, "Stability analysis and heat transfer of hybrid Cu- Al_2O_3/H_2O nanofluids transport over a stretching surface," *International Communications in Heat and Mass Transfer*, vol. 123, article 105215, 2021.

[16] S. Lee, S. U. S. Choi, S. Li, and J. A. Eastman, "Measuring thermal conductivity of fluids containing oxide nanoparticles," pp. 280–289, 1999.

[17] V. Sridhara and L. N. Satapathy, "Al_2O_3-based nanofluids: a review," *Nanoscale Research Letters*, vol. 6, no. 1, pp. 1–16, 2011.

[18] Z. Said, M. H. Sajid, M. A. Alim, R. Saidur, and N. A. Rahim, "Experimental investigation of the thermophysical properties of AL_2O_3-nanofluid and its effect on a flat plate solar collector," *International Communications in Heat and Mass Transfer*, vol. 48, pp. 99–107, 2013.

[19] M. N. Rostami, S. Dinarvand, and I. Pop, "Dual solutions for mixed convective stagnation-point flow of an aqueous silica-alumina hybrid nanofluid," *Chinese Journal of Physics*, vol. 56, no. 5, pp. 2465–2478, 2018.

[20] R. Taherialekouhi, S. Rasouli, and A. Khosravi, "An experimental study on stability and thermal conductivity of water-graphene oxide/aluminum oxide nanoparticles as a cooling hybrid nanofluid," *International Journal of Heat and Mass Transfer*, vol. 145, article 118751, 2019.

[21] P. K. Jena, E. A. Brocchi, and M. S. Motta, "In-situ formation of Cu-Al_2O_3 nano-scale composites by chemical routes and studies on their microstructures," *Materials Science and Engineering: A*, vol. 313, no. 1-2, pp. 180–186, 2001.

[22] K. Niihara, "New design concept of structural ceramics," *Journal of the Ceramic Society of Japan*, vol. 99, no. 1154, pp. 974–982, 1991.

[23] S. Suresh, K. P. Venkitaraj, and P. Selvakumar, "Synthesis, characterisation of Al_2O_3-Cu nano composite powder and water based nanofluids," *Advanced Materials Research*, vol. 328-330, pp. 1560–1567, 2011.

[24] S.-T. Oh, T. Sekino, and K. Niihara, "Fabrication and mechanical properties of 5 vol% copper dispersed alumina nanocomposite," *Journal of the European Ceramic Society*, vol. 18, no. 1, pp. 31–37, 1998.

[25] P. Selvakumar and S. Suresh, "Use of ${\rm Al}_{2}{\rm O}_{3}\hbox{–}{\rm Cu}$/water hybrid nanofluid in an electronic heat sink," *IEEE Transactions on Components, Packaging and Manufacturing Technology*, vol. 2, no. 10, pp. 1600–1607, 2012.

[26] A. Ijam, R. Saidur, and P. Ganesan, "Cooling of minichannel heat sink using nanofluids," *International Communications in Heat and Mass Transfer*, vol. 39, no. 8, pp. 1188–1194, 2012.

[27] C.-J. Ho and W. C. Chen, "An experimental study on thermal performance of Al_2O_3/water nanofluid in a minichannel heat sink," *Applied Thermal Engineering*, vol. 50, no. 1, pp. 516–522, 2013.

[28] M. S. Tahat and A. C. Benim, "Experimental analysis on thermophysical properties of Al_2O_3/CuO hybrid nano fluid with its effects on flat plate solar collector," in *In Defect and diffusion forum*, vol. 374, pp. 148–156, Trans Tech Publications Ltd, 2017.

[29] A. Yegane, S. Pooya, and A. Kasaeian, "Thermal performance assessment of a flat-plate solar collector considering porous media, hybrid nanofluid and magnetic field effects," *Journal of Thermal Analysis and Calorimetry*, vol. 141, no. 5, pp. 1969–1980, 2020.

[30] A. Azman, M. Z. Yusoff, A. Mukhtar, P. Gunnasegaran, N. A. Hamid, and N. K. Ching, "Numerical study of heat transfer enhancement for mono and hybrid nanofluids flow in a straight pipe," *CFD Letters*, vol. 13, no. 2, pp. 49–61, 2021.

[31] F. W. Dittus and L. M. K. Boelter, "Heat transfer in automobile radiators of the tubular type," *International Communications in Heat and Mass Transfer*, vol. 12, no. 1, pp. 3–22, 1985.

[32] A. Bejan, *Convection heat transfer*, John Wiley & sons, 2013.

[33] E. N. Sieder and G. E. Tate, "Heat transfer and pressure drop of liquids in tubes," *Industrial & Engineering Chemistry*, vol. 28, no. 12, pp. 1429–1435, 1936.

[34] Q. Li and Y. Xuan, "Convective heat transfer and flow characteristics of Cu-water nanofluid," *Science in China Series E: Technological Science*, vol. 45, no. 4, pp. 408–416, 2002.

[35] D. Taler and J. Taler, "Simple heat transfer correlations for turbulent tube flow," in *E3S Web of conferences*, vol. 13, p. 02008, EDP Sciences, 2017.

Hindawi
Journal of Nanomaterials
Volume 2022, Article ID 1859698, 9 pages
https://doi.org/10.1155/2022/1859698

Research Article

Stability Analysis of Fe_3O_4-OA-MWCNT Nanocomposite-Based Nanofluid

Muhammad Nadeem,[1] **Sumbul Purree**,[1] **M. G. B. Ashiq**,[2] **and Hafiz Muhammad Ali**[3,4]

[1]*Department of Basic Sciences, University of Engineering and Technology, Taxila, 47056, Pakistan*
[2]*Department of Physics, College of Science, Imam Abdulrahman Bin Faisal University, P.O. Box 1982, Dammam 31441, Saudi Arabia*
[3]*Department of Mechanical Engineering, King Fahd University of Petroleum and Minerals, Dhahran 31261, Saudi Arabia*
[4]*Interdisciplinary Research Center for Renewable Energy and Power Systems (IRC-REPS), King Fahd University of Petroleum and Minerals, Dhahran 31261, Saudi Arabia*

Correspondence should be addressed to Muhammad Nadeem; nadeem.badani@uettaxila.edu.pk and Hafiz Muhammad Ali; hafiz.ali@kfupm.edu.sa

Received 21 March 2022; Revised 30 May 2022; Accepted 2 June 2022; Published 25 June 2022

Academic Editor: Ibrahim Alarifi

The aim of this project is to fabricate a highly stable Fe_3O_4-OA-MWCNT composite and its colloidal suspension in polyalphaolefin (PAO) base fluid for heat transfer applications. The nanocomposite was produced in three mass ratios (0.5 : 1, 1 : 1, and 1.5 : 1) to explore the concentration effects on the stability of the nanocomposite. XRD analysis and FTIR spectroscopy were conducted to inspect the phase and composition of the synthesized nanocomposite. The crystallite sizes (3.75 nm, 7.74 nm, and 7.52 nm) and dislocation densities of each composite were calculated, and it was revealed that the samples with high concentration of iron oxide nanoparticles showed small defects in their lattices. Dispersion stability of ferrofluids was also examined by natural deposition method for 365 days. The ferrofluids displayed high stability for more than one year with no sign of sedimentation. Thermal conductivity of the nanofluid was also measured via. A transient plane source method and a linear trend with slight deviation were observed.

1. Introduction

Ferrofluids, also known as ferromagnetic fluids, are an innovative class of nanofluids which comprises magnetic nanoparticles suspended into the base fluids like water, EG, and oil [1]. For the past decades, a lot of research has been done on these fluids which revealed that the ferrofluids are beneficial for heat transfer applications, i.e., oil recovery [2], heat exchanger [3], power generation [4], electronics cooling [5], and solar systems [6] because of their unique chemical, thermal, physical, mechanical, and magnetic properties [1]. These ferromagnetic nanomaterials embody maghemite (Fe_2O_3 or γ-Fe_2O_3), magnetite (Fe_3O_4), and ferrites composed of nickel (Ni), cobalt (Co), Manganese (Mn), silver (Ag), barium (Ba), lithium (Li), chromium (Cr), and zinc (Zn) [7].

The superparamagnetic behavior of ferrofluids corresponds to quick and firm response to relatively weak magnetic fields which make them easier to control magnetically [8]. However, the applications of these magnetic fluids have been restricted greatly due to them being heavy causing sedimentation and agglomeration which directly affects the heat transfer capability of nanofluids. This is because soft magnetic materials have very high apparent density value in comparison to other materials. Also, magnetic nanoparticles possess high chemical activity and are oxidized very easily. Such materials are coated with suitable polymers or surfactants, e.g., oleic acid, castor oil, and

sodium lauryl sulphate (SLS) in order to tackle the issue regarding the stability of ferrofluids [9]. Zareei et al. [10] fabricated alumina/water based nanofluid and used three surfactants sodium dodecyl sulphate (SDS), cetyl trimethyl ammonium bromide (CTAB), and Triton X-100 to investigate their effect on pH and particle size. Al-Waeli et al. [11] studied the influence of CTAB, SDS, tannic acid+ammonia, dodecyl benzene sulphonates (SDBS) and sodium deoxycholate on silica-based nanofluid. Chakraborty et al. [12] observed the effect of surfactants like SDS and Tween-20 on Cu-Zn-Al-based nanosuspension and reported 20.9% thermal conductivity with SDS as a surfactant. The choice of surfactants depends upon the types of base fluid. For polar fluids, water-soluble surfactants are used and, for nonpolar, the opposite [13]. Although surfactants reduce the apparent density to some extent, this method is still not considered to be highly effective as it also affects the thermal conductivity. Hence, synthesis of magnetic composites is thought to enhance the thermal efficiency and stability of these innovative fluids by reducing their apparent density [14]. For this purpose, carbon nanotubes are said to possess very small density, unique cylindrical structure, high mechanical strength, and great chemical stability and considered a good choice to reduce agglomeration and enhance the thermal conductivity of ferrofluids by researchers, scientists, and engineers [15–17]. Shi et al. [18] synthesized a superparamagnetic nanofluid using Fe_3O_4@CNT composite and studied the thermal conductivity via controlling the mass ratio of composite and magnetic field. Shahsavar et al. [19] examined heat transfer and entropy generation through natural convection of Fe_3O_4@CNT hybrid nanofluid inside a concentric horizontal annulus. Liu et al. [20] observed thermal conductivity of 24.25% and 22.62% when inquired Fe_3O_4@CNT nanocomposite in water based fluid for the effect of oscillating magnetic field. Saba and Ahmed et al. conducted an investigation on flow and heat transfer properties of Fe_3O_4@CNT/H_2O nanofluid inside a very long asymmetric channel with porous walls and declared that the CNT's dispersion in a nanofluid has a great influence on the transport properties. As mentioned above, several studies with open literature on Fe_3O_4-MWCNT have been reported with high thermal performance. However, nanofluid with Fe_3O_4/MWCNT composite and polyalphaolefin oil as a cooling agent have not been reported yet. PAO has been used in various industries as a lubricant and as a coolant [21]. Also, past literatures reported that nanofluids comprising insulating oil base fluids like PAO with poor heat transfer properties are more stable and homogeneous with high heat transfer rates [22]. In addition, the viscosity of PAO usually decreases with increase in temperature which has a significant effect on thermal conductivity [23, 24].

In this paper, the nanocomposite of Fe_3O_4 blended with multiwalled carbon nanotubes (MWCNT) with low apparent density and a hybrid nanofluid with base fluid of polyalphaolefin (PAO) is synthesized to explore a method to fabricate a highly stable nanofluid with high thermal conductivity for heat transfer application. Thermal conductivity of prepared nanofluid by controlling the morphology of nanoparticles, added volume fraction, minimizing agglomeration, and enhanced stability of the nanoparticles in the base fluid is also analyzed in this work.

2. Materials and Methods

2.1. Chemicals. All the chemicals, ferrous chloride ($FeCl_2$), ferric chloride ($FeCl_3$), ammonium hydroxide (NH_4OH), hydrochloric acid (HCl), deionized water, multiwalled carbon nanotubes (MWCNT), oleic acid, o-xylene, and polyalphaolefin (PAO), are acquired/purchased in Pakistan. All these reagents were analytical grade and were used without further purification.

2.2. Synthesis of Iron Oxide Nanoparticle. Iron oxide nanoparticles were prepared by a modified version of chemical coprecipitation method [25]. At first, ferrous chloride tetrahydrate and ferric chloride hexahydrate were dissolved in 100 ml of distilled water under constant stirring for 20 minutes. After that, the pH of this solution was maintained at 10 by adding 35 ml of ammonium hydroxide dropwise during constant stirring at 1100 rpm for 20 minutes. The solution slowly turned black indicating the formation of precipitates. These precipitates were collected via centrifugation at 4000 rpm for 10 minutes. Then, they were washed with distilled water 4-5 times and dried at 40°C in oven overnight.

2.3. Coating of Iron Oxide Nanoparticles with Oleic Acid. The synthesized iron oxide nanoparticles were coated with oleic acid to reduce the apparent density of nanoparticles. For this, 2 wt.% of Fe_3O_4 nanoparticles was added into the 10% (*v*/*v*) oleic acid solution during constant stirring at 400 rpm at 40°C for 1 hour. The obtained viscous solution was centrifuged at 4000 rpm to collect the nanoparticles. These nanoparticles then washed with alcohol 3-4 times and were dried in an oven for 24 hours.

2.4. Nanocomposite Fabrication. A solution mixing method was used to fabricate the multiwalled carbon nanotubes (MWCNT) based nanocomposite. For this purpose, iron oxide nanoparticles were mixed with MWCNT in three different mass ratios of 0.5 : 1, 1 : 1, and 1.5 : 1 in 50 ml oleic acid solution during rigorous stirring for 1100 rpm at 40°C temperature for 1 hour. The MWCNT were added into the solution during second half, and the solution was sonicated for 2 hours at the same temperature. Residuals were removed through ethanol for several times. Then, obtained composites were dried in oven for a day and grounded to powder form for further proceedings.

2.5. Synthesis of Hybrid Nanofluid. Prepared Fe_3O_4-OA-MWCNT nanocomposites with three different compositional mass ratios of 0.5 : 1, 1 : 1, and 1.5 : 1 were used to create polyalphaolefin-based hybrid nanofluid. Nanofluids were prepared in three different volume fractions of 0.3 wt.%, 0.5 wt.%, and 0.7 wt.% for each composite. Based on known weights and densities of the sample, the required

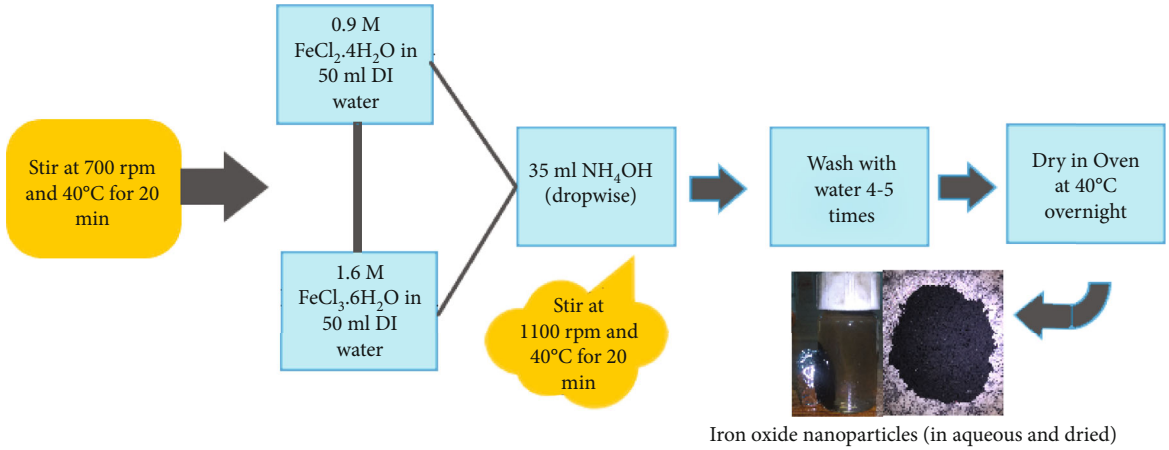

Figure 1: Flow diagram of synthesis of IONPs.

volume fraction of nanocomposite was predicted by following equation:

$$\phi = \frac{\left(W_{\text{Nanocomposite}}/\rho_{\text{Nanocomposite}}\right)}{\left[\left(W_{\text{Nanocomposite}}/\rho_{\text{Nanocomposite}}\right) + \left(W_{\text{Polyalphaolefin}}/\rho_{\text{Polyalphaolefin}}\right)\right]} \times 100. \quad (1)$$

Then nanocomposites were dispersed in 14 ml of polyalphaolefin oil through sonication of 2 hours at 70°C to obtain a stable suspension (see Figure 1).

3. Characterization

Crystal behavior and phase identification were analyzed via XRD analysis. An X-ray diffractometer of D8 Advance (Bruker Germany) (LYNX EYE linear detector) and a diffractometer equipped with copper tube ($\lambda = 1.5406A$) were used for the measurements with an average range of 20° to 80° along with the step size of 0.5. 6300 type A Jasco infrared spectrometer (4 cm^{-1} resolution with a scanning speed of 2 mm/sec) was used to record the complex spectrum of synthesized nanocomposite. The spectral range of 399.193 to 4000 cm^{-1} was used for the compositional analysis of the sample at room temperature. Surface morphology of synthesized pure iron oxide nanoparticles was analyzed via. A JEM-2100 transmission electron microscope (TEM) with 200 kV accelerating voltage was used. Sedimentation photograph technique was used to observe the stability of Fe_3O_4-OA-MWCNT amalgam in polyalphaolefin (PAO) base fluid. It works on the principle that the size of nanocomposite is directly related to the stability of particles in the nanofluid as particle with large size will settle down quickly on the bottom of the container. For this, nanocomposites with mass ratios of 0.5 : 1, 1 : 1, and 1.5 : 1 of IONPs : MWCNT were used to prepare nanofluids of three different volume fractions (i.e.,0.3 wt.%, 0.5 wt.%, and 0.7 wt.%). The photographs were taken at various intervals with maximum after one year. Hot Disc TPS 2500 Thermal Constant Analyzer, which employ transient plane source method, with thermal conductivity range of 0.005 to 1800 Wm/K, and can accommodate the temperature from cryogenic to 1000°C, was used to obtain the heat transfer data of each composition with uncertainty error of 2% to 5%. A thermal conducting plane

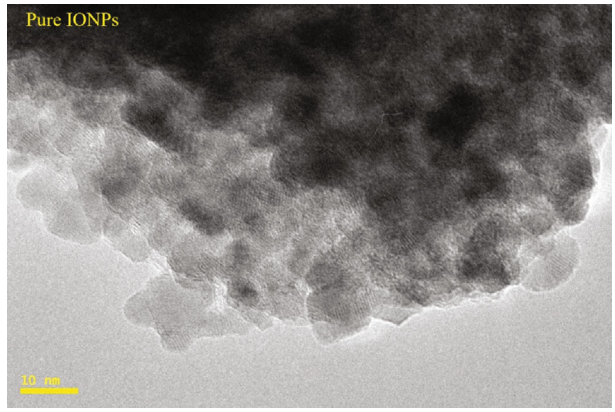

Figure 2: TEM image of pure Fe_3O_4 nanoparticles.

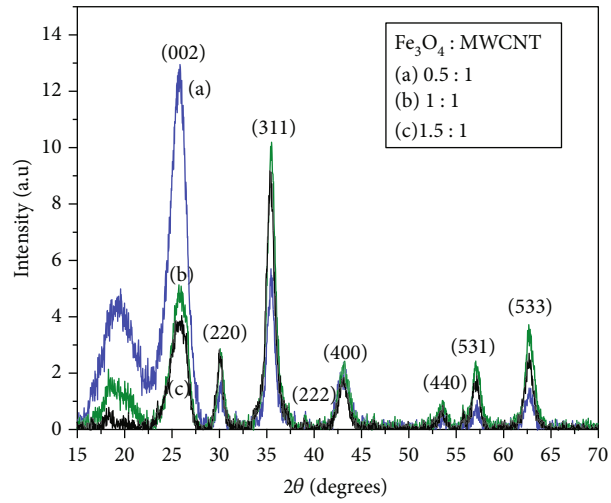

Figure 3: XRD spectra of Fe_3O_4-OA-MWCNT nanocomposite with mass ratios between Fe_3O_4 : MWCNT, i.e., (a) 0.5 : 1, (b) 1 : 1, and (c) 1.5 : 1.

sensor acting as a heat source is placed between two testing sample. The rise in temperature of the source enhances the heat dissipation of the material under examination at a rate that depends on its thermal transport properties. The sample was sonicated at 40°C for 1 hour for homogeneity and then was placed into holders. Thermal transport properties were measured at pr. depth of approx. 1.6 mm of the sample. The equipment was calibrated three times before calculation with standard fluid (PAO) in this case. About five measurements at temperature of 0-100°C were taken for about 4 hours with 25°C intervals in between measurements. The process was repeated several times to ensure the validity of the results.

4. Results and Discussion

Three different samples of Fe_3O_4-OA-MWCNT nanocomposite having compositional ratios: (a) 0.5 : 1 (S1), (b) 1 : 1 (S2), and (c) 1.5 : 1 (S3), between IONPs and MWCNT have been synthesized to investigate its phase, crystal structure, and chemical composition using various techniques like XRD and FTIR. Nanofluids with volume concentration 0.3 wt.%, 0.5 wt.%, and 0.7 wt.% for each sample have also been prepared under suitable conditions to explore its dispersion stability.

4.1. Surface Morphology of IONPs. The stability of nanofluids is directly influenced by the nature of nanoparticles [26]. Therefore, surface morphology and agglomeration behavior of iron oxide nanoparticles were examined in detail using a transmission electron microscope (TEM). Figure 2 clearly confirms the spherical shape and crystalline nature of the pure IONPs. The particles show agglomeration even after sonication of 2 hours in the ethanol (solvent). This is due to the magnetic and inner particle interaction among of Fe_3O_4 nanoparticles. The clusters were formed due to high surface charge and dipolar interactions of particles.

4.2. Phase and Crystal Structure. Figure 3 (a–d) contains the XRD pattern of all samples, i.e., S1, S2, and S3. The reflecting planes (220), (311), (222), (400), (440), (511), (531), and (533) corresponding to 2θ angles 30°, 35.5°, 38°, 43°, 53.7°, 53.4°, 57.3°, and 62.8° show the characteristic peaks of iron oxide nanoparticles. The lack of planes (210), (300), and (320) proves the absence of maghemite phase when compared to JCPD card No. 19-0629, as the obtained peaks match with the standard peaks [27]. The lattice plane (002) at 25.95° of angle 2θ corresponds to the presence of interlayer stacking of graphene sheets embedded together and confirms the multiwalled nature of carbon nanotubes which matches exactly to the JCPD card No. 41-1487 confirming the existence of nanocomposite [28]. Comparing these peaks leads to conclusion that increasing the iron oxide ratio directly affects the crystallinity of the nanocomposite; i.e., the sharpness of peaks has been enhanced.

The crystallite size of nanocomposite was calculated using mostly used the Debye-Scherrer formula from the XRD pattern along with dislocation densities [29]:

$$D_{hkl} = \frac{0.94\lambda}{\beta \cos\theta}, \tag{2}$$

where D_{hkl}, β, λ, and θ corresponds to crystallite size, full wave half maximum, wavelength of Cu-k_α, and diffraction angle, respectively. The dislocation density (δ) is the measure of number of distortions/defects present in a crystal structure and is expressed in lines per square meter. It was also calculated by the following formula:

$$\delta = \frac{1}{D_{hkl}^{\,2}}. \tag{3}$$

Table 1 shows the value of diffraction angle, full wave half maximum (FWHM) in radians, crystallite size, and dislocation density of Fe_3O_4-OA-MWCNT nanocomposite with different mass ratios. Among all three nanocomposites, the one with least iron oxide content has the smallest size of 3.75 nm and increasing the magnetic content resulted in increase in crystallite size and decrease in defects. The maximum crystallite size observed is 7.52 nm of Fe_3O_4 : MWCNT with 1.5 : 1 mass ratios and the smallest dislocation density of 1.77×10^{16} lines/m^2. This is because oxidation or structural interactions due to hydroxyl or

Table 1: XRD parameters of Fe_3O_4-OA-MWCNT.

Fe_3O_4 : MWCNT	θ (degrees)	FWHM (radians)	Crystallite size (nm)	Dislocation density ($\times 10^{16}$) (lines/m^2)
0.5 : 1	25.96	0.03864	3.75	7.12
1 : 1	38.00	0.01871	7.74	1.67
1.5 : 1	35.38	0.01927	7.52	1.77

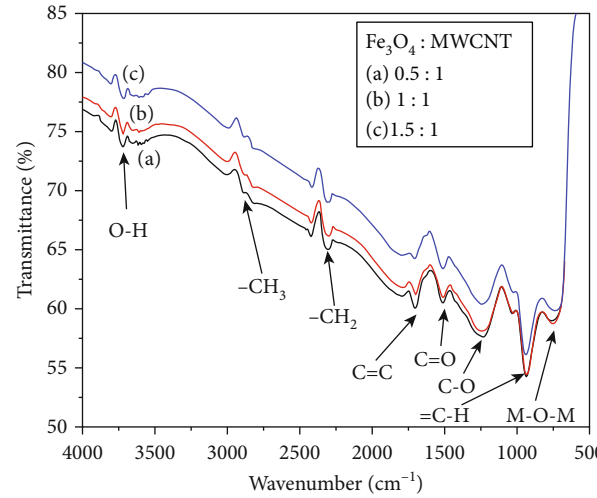

Figure 4: FTIR spectra of Fe_3O_4-OA-MWCNT nanocomposite with mass ratios between Fe_3O_4 : MWCNT, i.e., (a) 0.5 : 1, (b) 1 : 1, and (c) 1.5 : 1.

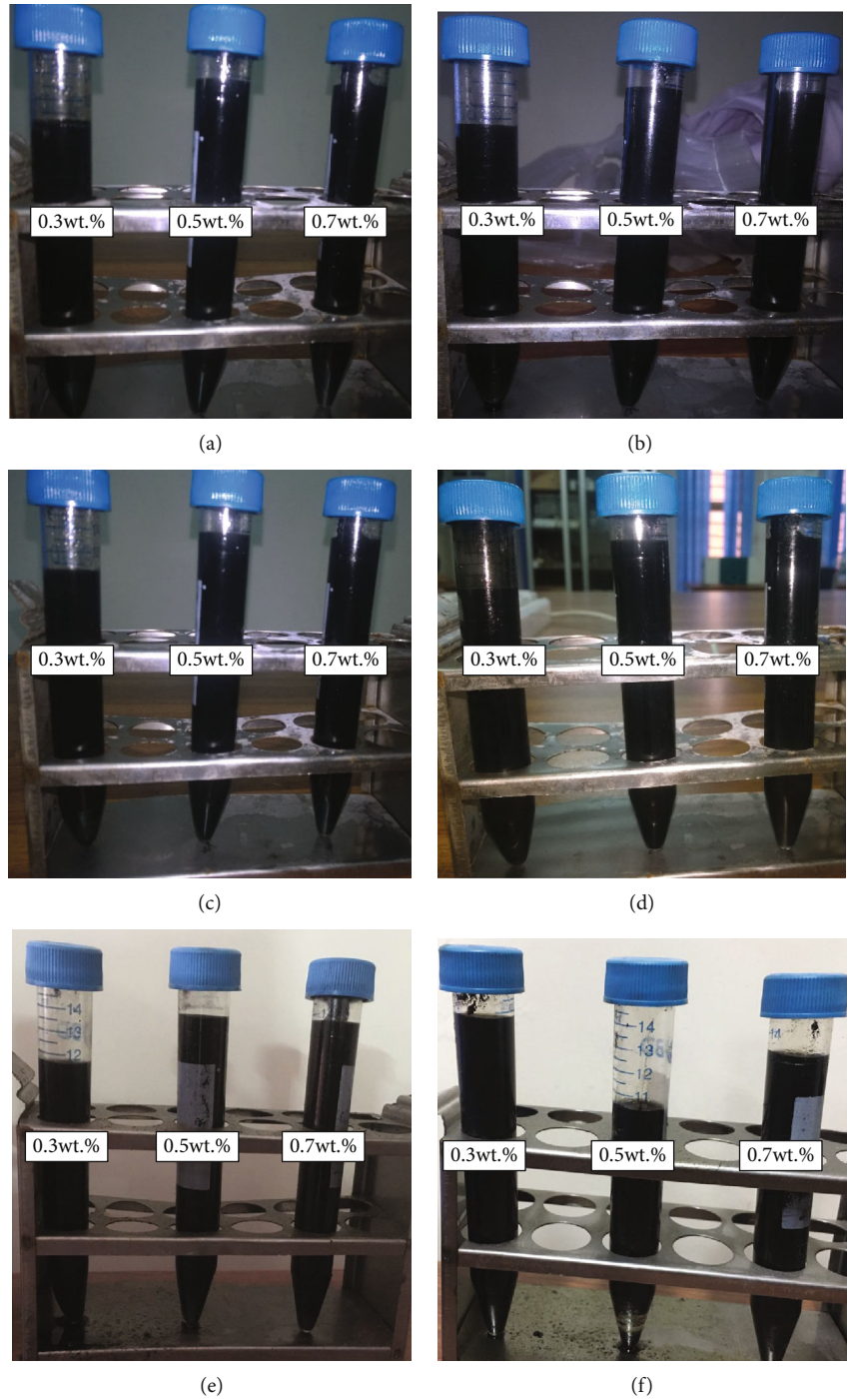

FIGURE 5: Nanofluid containing S1 (Fe_3O_4-OA-MWCNT)/PAO with weight of 0.3 wt.%, 0.5 wt.%, and 0.7 wt.% (2-hour sonication) after (a) one week, (b) one month, (c) four months, (d) six months, (e) eight months, and (f) one year.

carboxyl functional group affects the stacking of tubules causing distortions among the crystal lattices.

4.3. Compositional Analysis. Figure 4 shows the FTIR spectra of Fe_3O_4-OA-MWCNT nanocomposite with three different mass ratios (0.5 : 1, 1 : 1, and 1.5 : 1) of iron oxide and multi-walled carbon nanotubes. The wide absorption band at 929.92 cm^{-1} is due to the out of plane bending of =C-H bond. A broad band at 740.63 cm^{-1} in fingerprint region represents the stretching vibrations of Fe-O bond which shows slight deviations (747.36 cm^{-1} and 754.92 cm^{-1}) due to increase in the mass ratio of iron oxide nanoparticles in the composite. These absorption bands confirm the presence of metallic oxide nanoparticles. The presence of C=C was revealed by the absorption spectra at 1505.41-1695.55 cm^{-1} which indicates the hexagonal structure of the MWCNT.

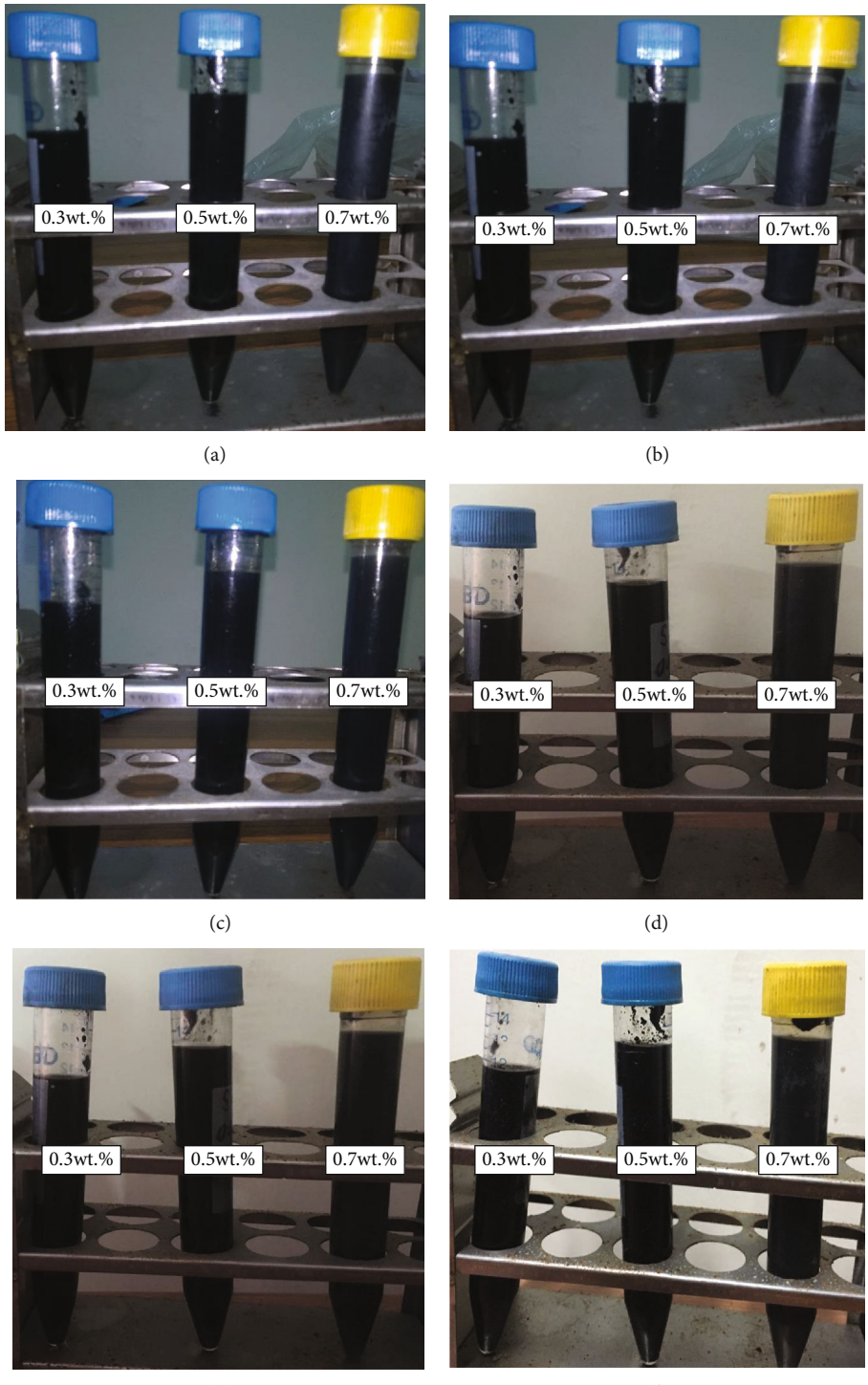

FIGURE 6: Nanofluid containing S2 (Fe_3O_4-OA-MWCNT)/PAO with weight of 0.3 wt.%, 0.5 wt.%, and 0.7 wt.% (2-hour sonication) after (a) one week, (b) one month, (c) four months, (d) six months, (e) eight months, and (f) one year.

The MWCNT shows very weak peaks of C=C aromatic ring stretching around 1600 cm^{-1} which is the indication of a large number of asymmetrical carbons present [30]. The absorption peaks at 1687.98 and 1512.98 cm^{-1} elucidate the presence of C=O. At 1050 cm^{-1}, a strong absorption peak from C-O bond stretching is obtained. The weak absorption peaks at 2313-2847 cm^{-1} indicate the presence of asymmetrical stretching of aromatic bonds of $-CH_2$ and $-CH_3$ which is due to alkyl groups at 3717.31 cm^{-1} shows the presence of O-H stretching vibrations which indicates the modification of MWCNT. Negligible intensity of O-H peak is the evidence that the prepared nanocomposite is hydrophobic in nature.

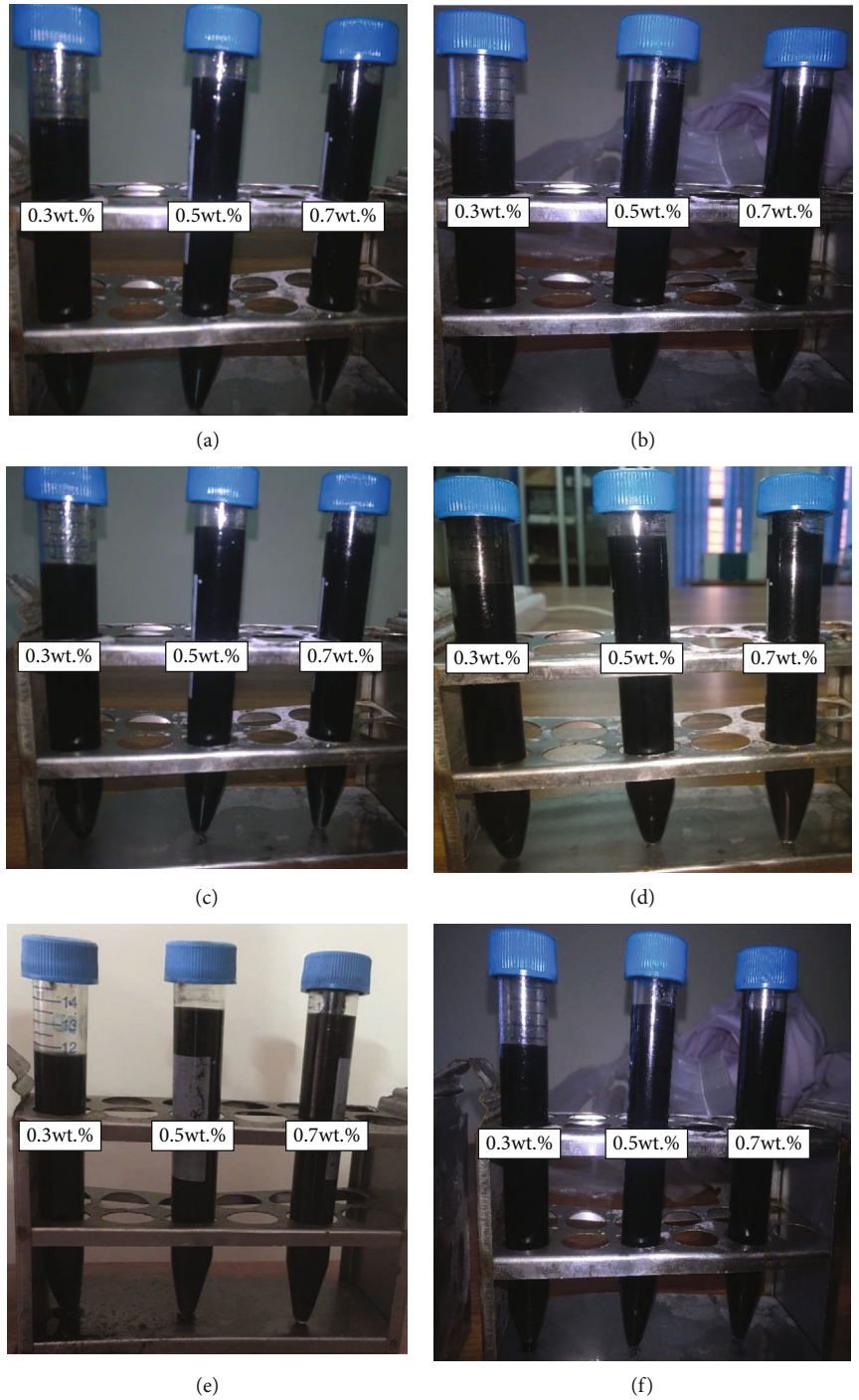

Figure 7: Nanofluid containing S3 (Fe_3O_4-OA-MWCNT)/PAO with weight of 0.3 wt.%, 0.5 wt.%, and 0.7 wt.% (2-hour sonication) after (a) one week, (b) one month, (c) four months, (d) six months, (e) eight months, and (f) one year.

4.4. Dispersion Stability. Dispersion stability is the most debated and important characteristics of nanofluids for thermal applications. The prepared samples were utilized to observe their aggregation behavior in the polyalphaolefin oil with respect to time. Figure 5 illustrates the stability investigation of polyalphaolefin oil containing sample S1 in three different volume fractions. It is evident in the figure that the ferrofluids comprising of S1 nanocomposite are stable after 12 months and negligible sedimentation was observed after six months.

Figure 6 shows the stability of sample S2-based nanofluids with respect to time. No apparent change in the color of suspension was observed even after 12 months indicating its high storage life.

Figure 7 reveals the dispersion behavior of colloids containing sample S3. After 12 months, suspensions showed

very high stability with negligible deposition due to presence of multiwalled carbon nanotubes (MWCNT) which form a complex three-dimensional structure making sedimentation difficult.

4.5. Thermal Conductivity. Thermal conductivity of polyalphaolefin oil-based nanofluid comprising of Fe_3O_4/OA/MWCNT nanocomposite was carefully calculated via a thermal constant analyzer at five different temperature values with 25°C interval among each value. The equipment was standardized using polyalphaolefin oil, and every calculation was repeated three times to ensure the reliability of the calculations.

Figure 8 shows the temperature dependence of the thermal conductivity at various volume fractions for PAO-based hybrid nanofluid measured at temperatures from 0°C to 100°C. It can be observed that the thermal conductivity diminishes with the increase in temperature, and a wide variation is observed at elevated temperature. Deviations in thermal conductivity curves were observed when compared to pure polyalphaolefin oil; i.e., Curve (d) shows rise in thermal behavior, and curve (c) shows reduction in thermal conductivity at high temperatures. This is due to rise in particle interactions which results in the formation of aggregates because of large aggregation time and sharp rise in temperature. This provides new pathways for heat transport, but when the aggregation is very high, it disrupts the thermal transport mechanism causing in the reduction of thermal conductivity, though the heat transfer reduces when temperature is enhanced but the thermal conductivity curve shift towards higher values when the particle concentration is increased. As observed in the above graph, the higher value of thermal conductivity was observed at a volume concentration of 0.7 wt.% and the lowest thermal conductivity was observed at 0.5 wt.% which is almost the same as pure polyalphaolefin oil. The rise of thermal conductivity observed due to the addition of nanocomposite in PAO was also calculated with its heat transfer rates varying from 0.25% to 0.9% as compared to base fluid which is not very high because of large cluster formation and poor heat transfer capacity of the oil. In the incompetent thermal performance of heat transfer fluids, energy loss is observed. This can be prevented with a lubricant consisting of good heat transfer capacity.

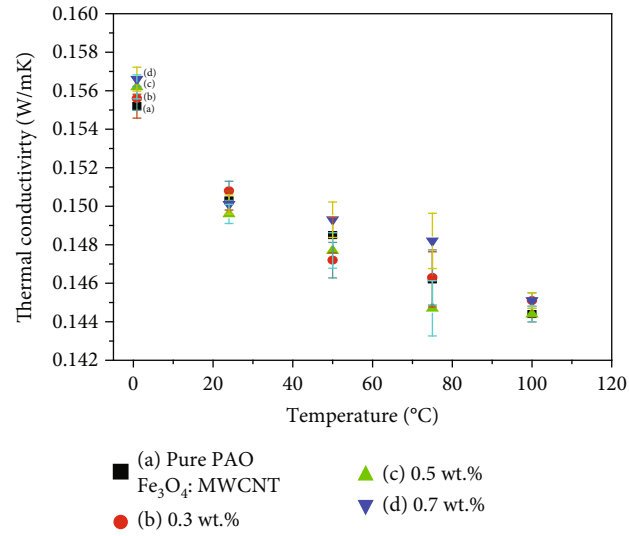

Figure 8: Thermal conductivity trend of Fe_3O_4/MWCNT/PAO nanofluid as a function of temperature. The error bars indicate the standard deviation of the values.

5. Conclusion

Fe_3O_4-OA-MWCNT nanocomposite with weight ratios of 0.5 : 1, 1 : 1, and 1.5 : 1 was magnificently synthesized via solution blend approach of in situ polymerization method, and its ferrofluids were prepared in polyalphaolefin oil with volume fractions, i.e., 0.3 wt.%, 0.5 wt.%, and 0.7 wt.% in the present study. The crystallite sizes of each composition of the sample (S1—0.5 : 1, S2—1 : 1, and S3—1.5 : 1) were carefully calculated (i.e., 3.75 nm, 7.74 nm, and 7.52 nm) using Scherrer's equation with dislocation densities 7.12×10^{16} lines/m^2, 1.67×10^{16} lines/m^2, and 1.77×10^{16} lines/m^2, accordingly. XRD analysis verified the crystal behavior of the nanocomposite while FTIR spectra confirmed the hydrophilic nature and formation of nanocomposite. The stability assessment revealed that each composition showed high aggregation stability and no apparent deposition was observed even after one year. The thermal conductivity of the sample determination showed the linear trend as a function of temperature and volume fraction, and highest thermal conductivity was observed for 0.7 wt.% at 50°C temperature when compared to pure PAO oil. This shows that Fe_3O_4-OA-MWCNT/PAO-based nanofluids have great potential for thermal applications as a lubricant and as a heat exchanger.

Data Availability

Data will be provided on reasonable request.

Conflicts of Interest

The authors declare that they have no conflicts of interest.

References

[1] M. Imran, A. H. Shaik, A. R. Ansari et al., "Synthesis of highly stable γ-Fe_2O_3ferrofluid dispersed in liquid paraffin, motor oil and sunflower oil for heat transfer applications," *RSC Advances*, vol. 8, no. 25, pp. 13970–13975, 2018.

[2] M. Ramezanpour and M. Siavashi, "Application of SiO_2–water nanofluid to enhance oil recovery," *Journal of Thermal Analysis and Calorimetry*, vol. 135, no. 1, pp. 565–580, 2019.

[3] M. U. Sajid and H. M. Ali, "Recent advances in application of nanofluids in heat transfer devices: a critical review," *Renewable and Sustainable Energy Reviews*, vol. 103, pp. 556–592, 2019.

[4] P.-H. Yen and J.-C. Wang, "Power generation and electric charge density with temperature effect of alumina nanofluids using dimensional analysis," *Energy Conversion and Management*, vol. 186, pp. 546–555, 2019.

[5] M. Bahiraei, S. Heshmatian, M. Goodarzi, and H. Moayedi, "CFD analysis of employing a novel ecofriendly nanofluid in a miniature pin fin heat sink for cooling of electronic components: effect of different configurations," *Advanced Powder Technology*, vol. 30, no. 11, pp. 2503–2516, 2019.

[6] H. Olia, M. Torabi, M. Bahiraei, M. H. Ahmadi, M. Goodarzi, and M. R. Safaei, "Application of nanofluids in thermal performance enhancement of parabolic trough solar collector: state-of-the-art," *Applied Sciences*, vol. 9, no. 3, p. 463, 2019.

[7] V. Singh, A. Kumar, M. Alam, A. Kumar, P. Kumar, and V. Goyat, "A study of morphology, UV measurements and zeta potential of zinc ferrite and Al_2O_3 nanofluids," *Materials Today: Proceedings*, vol. 59, pp. 1034–1039, 2022.

[8] X. Zhang, L. Sun, Y. Yu, and Y. Zhao, "Flexible ferrofluids: design and applications," *Advanced Materials*, vol. 31, no. 51, p. 1903497, 2019.

[9] H. Pu and F. Jiang, "Towards high sedimentation stability: magnetorheological fluids based on CNT/Fe_3O_4nanocomposites," *Nanotechnology*, vol. 16, no. 9, pp. 1486–1489, 2005.

[10] M. Zareei, H. Yoozbashizadeh, and H. R. M. Hosseini, "Investigating the effects of pH, surfactant and ionic strength on the stability of alumina/water nanofluids using DLVO theory," *Journal of Thermal Analysis and Calorimetry*, vol. 135, no. 2, pp. 1185–1196, 2019.

[11] A. H. A. Al-Waeli, M. T. Chaichan, H. A. Kazem, and K. Sopian, "Evaluation and analysis of nanofluid and surfactant impact on photovoltaic- thermal systems," *Case Studies in Thermal Engineering*, vol. 13, article 100392, 2019.

[12] S. Chakraborty, I. Sengupta, I. Sarkar, S. K. Pal, and S. Chakraborty, "Effect of surfactant on thermo-physical properties and spray cooling heat transfer performance of Cu-Zn-Al LDH nanofluid," *Applied Clay Science*, vol. 168, pp. 43–55, 2019.

[13] C. Scherer and A. M. Figueiredo Neto, "Ferrofluids: properties and applications," *Brazilian Journal of Physics*, vol. 35, no. 3A, pp. 718–727, 2005.

[14] L. Shi, Y. He, Y. Hu, and X. Wang, "Thermophysical properties of Fe_3O_4@CNT nanofluid and controllable heat transfer performance under magnetic field," *Energy Conversion and Management*, vol. 177, pp. 249–257, 2018.

[15] A. A. Nadooshan, H. Eshgarf, and M. Afrand, "Measuring the viscosity of Fe_3O_4-MWCNTs/EG hybrid nanofluid for evaluation of thermal efficiency: Newtonian and non-Newtonian behavior," *Journal of Molecular Liquids*, vol. 253, pp. 169–177, 2018.

[16] R. Nasrin, N. A. Rahim, H. Fayaz, and M. Hasanuzzaman, "Water/MWCNT nanofluid based cooling system of PVT: experimental and numerical research," *Renewable Energy*, vol. 121, pp. 286–300, 2018.

[17] M. H. Esfe, S. Esfandeh, M. K. Amiri, and M. Afrand, "A novel applicable experimental study on the thermal behavior of SWCNTs(60%)-MgO(40%)/EG hybrid nanofluid by focusing on the thermal conductivity," *Powder Technology*, vol. 342, pp. 998–1007, 2019.

[18] L. Shi, Y. He, Y. Hu, and X. Wang, "Controllable natural convection in a rectangular enclosure filled with Fe_3O_4@CNT nanofluids," *International Journal of Heat and Mass Transfer*, vol. 140, pp. 399–409, 2019.

[19] A. Shahsavar, P. Talebizadeh Sardari, and D. Toghraie, "Free convection heat transfer and entropy generation analysis of water-Fe_3O_4/CNT hybrid nanofluid in a concentric annulus," *International Journal of Numerical Methods for Heat & Fluid Flow*, vol. 29, no. 3, pp. 915–934, 2019.

[20] W. Liu, J. Alsarraf, A. Shahsavar, M. Rostamzadeh, M. Afrand, and T. K. Nguyen, "Impact of oscillating magnetic field on the thermal-conductivity of water- Fe_3O_4 and water- Fe_3O_4/CNT ferro-fluids: Experimental study," *Journal of Magnetism and Magnetic Materials*, vol. 484, pp. 258–265, 2019.

[21] X. Li, F. Yuan, W. Tian et al., "Heat transfer enhancement of nanofluids with non-spherical nanoparticles: a review," *Applied Sciences*, vol. 12, no. 9, p. 4767, 2022.

[22] S. N. Suhaimi, A. R. A. Rahman, M. F. M. Din, M. Z. Hassan, M. T. Ishak, and M. T. . Jusoh, "A review on oil-based nanofluid as next-generation insulation for transformer application," *Journal of Nanomaterials*, vol. 2020, 17 pages, 2020.

[23] A. K. Sleiti, "Heat transfer measurements of polyalpha-olefin-boron nitride nanofluids for thermal management and lubrication applications," *Case Studies in Thermal Engineering*, vol. 22, article 100776, 2020.

[24] S. Purree, M. Nadeem, M. Zubair et al., "Volume fraction effects on thermophysical properties of Fe $_3$ O $_4$/MWCNT based hybrid nanofluid," *International Journal of Nanoelectronics & Materials*, vol. 14, no. 1, 2021.

[25] M. Nadeem, "Synthesis of iron oxide nanoparticles for the anti cancer drugs delivery," *Universiti Teknologi Malaysia*, 2016.

[26] T. Le Ba, O. Mahian, S. Wongwises, and I. M. Szilágyi, "Review on the recent progress in the preparation and stability of graphene-based nanofluids," *Journal of Thermal Analysis and Calorimetry*, vol. 142, pp. 1–28, 2020.

[27] Y. Y. Byong and S. S. Kwak, "Assembly of magnetite nanoparticles into spherical mesoporous aggregates with a 3-D wormhole-like porous structure," *Journal of Materials Chemistry*, vol. 20, pp. 1–9, 2010.

[28] H. Xiong, L. Wang, S. U. Rehman et al., "Carbon coated core-shell FeSiCr/Fe_3C embedded in carbon nanosheets network nanocomposites for improving microwave absorption performance," *Nano*, vol. 15, no. 7, p. 2050094, 2020.

[29] H. Khan, A. S. Yerramilli, A. D'Oliveira, T. L. Alford, D. C. Boffito, and G. S. Patience, "Experimental methods in chemical engineering: X-ray diffraction spectroscopy—XRD," *The Canadian Journal of Chemical Engineering*, vol. 98, no. 6, pp. 1255–1266, 2020.

[30] R. Yudianti, H. Onggo, Y. Saito, T. Iwata, and J. I. Azuma, "Analysis of functional group sited on multi-wall carbon nanotube surface," *The Open Materials Science Journal*, vol. 5, no. 1, pp. 242–247, 2011.

Hindawi
Journal of Nanomaterials
Volume 2022, Article ID 6428469, 15 pages
https://doi.org/10.1155/2022/6428469

Research Article

Numerical Study on the Thermal Enhancement of Phase Change Material with the Addition of Nanoparticles and Changing the Orientation of the Enclosure

P. Narasimha Siva Teja,[1] **S. K. Gugulothu**,[1] **P. Dinesh Sankar Reddy**,[2] **Abdul Ashraf**,[1] **B. Deepanraj**,[3] **and P. Thillai Arasu**[4]

[1]*Department of Mechanical Engineering, National Institute of Technology, Andhra Pradesh, India*
[2]*Department of Chemical Engineering, National Institute of Technology, Andhra Pradesh, India*
[3]*College of Engineering, Prince Mohammad Bin Fahd University, Al Khobar, Saudi Arabia*
[4]*College of Natural and Computational Science, Wollega University, Ethiopia*

Correspondence should be addressed to P. Thillai Arasu; thililaiarasu@wollegauniversity.edu.et

Received 1 April 2022; Accepted 9 May 2022; Published 6 June 2022

Academic Editor: Zafar Said

The global demand of the heating and cooling applications gives a larger potential to study the thermal energy storage system. Phase change materials (PCM) that are used to charge, store, and discharge the heat energy are inferior in heat transfer characteristics. The properties of PCM can be improved by adding nanoparticles, changing the orientation of the enclosure or both. Two-dimensional transient numerical analysis on the effect of Grashoff number (5000, 13000, and 20000), nanoparticle type (Al_2O_3, CuO, and MWCNT), and volume concentration (0%, 1%, 3%, and 5%) added in RT 42 PCM and orientation of square enclosure (30, 45, and 60°) to enhance the heat transfer rate is carried out. The thermophysical properties of the nano-PCM are evaluated and presented. From the results, it is affirmed that the melt fraction of the PCM rises with the increase in Gr and volume concentration of the nanoparticles up to an optimum level. The MWCNT-based nano-PCM attained a larger portion of melt fraction followed by Al_2O_3, CuO, and pure PCM. It is noted that an orientation of 60° and 45° will convert more quantities of pure PCM and nano-PCM into liquid fraction, respectively. The (3% MWCNT/RT-42 PCM) filled in 45° oriented container attained the highest melt fraction by 3.4%, 2.04%, and 2.94% than (3% Al_2O_3/RT-42 PCM), (1%CuO/RT-42 PCM), and pure PCM. The variation in the maximum melt fraction of the nanomaterial is because of the change in thermophysical characteristics of the nano-PCM.

1. Introduction

Renewable energy resources are emerging in the present world to reduce global pollution and replace a portion of conventional fuels. Thermal energy having various industrial and domestic applications can be substituted with solar heat energy which is one of the prominent renewable energy sources. This energy is intermittent and depends on weather conditions. Therefore, storage of low-grade energy is inevitable to provide a sustainable solution to energy demand. Thermal energy storage can be done by using latent heat materials by changing their phase. Also, PCMs can be used in thermal management of different heat transfer applications like electronic cooling, waste heat recovery. Despite the larger heat capacities of phase change materials (PCM), it has a drawback of inferior heat transfer characteristics. Hence, improving the thermal characteristics of PCM is a challenging area in this field. Numerical assessment on thermal conductivity improvement of the PCM under uniform and sinusoidal types of heat flux by incorporating multi-walled carbon nanotubes was carried out by Gupta et al. [1]. An increase in melting rate was observed for higher values of amplitude and wavelength ratio of undulations applied on the vertical wall of the square duct. The charging

process of the thermocline storage tank (TCST) was studied both experimentally and numerically by Xu et al. [2] by developing a 1D model. They introduced the correction coefficient (ε) expresses the enhancement in thermal diffusion. The use of the 1D model predicted the distribution of temperature more accurately and developed a correlation equation between the thickness of thermocline, Fr, and Re. They reported analytical expression between thermocline thickness and time is also obtained with approximately 14% of error. Experimental and computational investigations on the theory of constituent mixtures in the PCM composites were performed by Jiao et al. [3]. In this, the effect of nonequilibrium mixtures and the relation between velocity and change in density during melting were discussed. The temperature contours and streamlines are presented. The numerical and experimental results are compared for different positions and achieved a good agreement. Melting rate analysis of an encapsulated PCM incorporated with metal foam was done numerically by Baruah et al. [4]. The parameters varied in this study are porosity, pore size distribution, capsule size, and thickness of shell. They observed that the melting rate is improved for minimum capsule size and porosity with higher shell thickness. Computational study on the effect of encapsulated geometry filled with PCM for different angular orientations has been carried out by Zhang et al. [5]. They observed that the pyramidal and tetrahedral-shaped capsules with a horizontal base have the highest melting rate due to larger surface area. Comparing angular inclination, the melting rate is more when the center of gravity of capsules was nearer to the bottom of geometry. Huang et al. [6] inspected the rate of melting of double-PCM heat sinks by mixing paraffin with an alloy having lower melting point (LMPA). The performance characteristics are evaluated for different volume fractions of LMPA, the fin shape, and heating power. They reported that, throughout the second melting stage, the double-PCM heat sink and LMPA heat sink were similar in performance. However, during the third melting stage, the temperature control with paraffin gets deteriorated. The fin shape and volume fraction of the LMPA have been optimized by extending the second stage of melting and eliminating the third melting stage. Experimental assessment of the heat transmission enhancement of PCM-based heat energy storage system and its allied applications by incorporating metal fins and foams is performed by Guo et al. [7]. They affirmed that the combination of fin and foam structure reduces the melting time by 83% than bare, ideal fin, or metal foam structures. The uniformity of the temperature field is maintained with the help of foam structure only but not with the fin structure. Nie et al. [8] inspected the impact of geometry with seven different vertical-shell tubes on heat transmission characteristics in a latent thermal energy storage network. They reported that frustum-shaped geometry enhanced both conduction and convection, while the conical shell improved only convection compared to cylindrical geometry. Geometry modification has little effect on heat transfer in composite metal foam/PCM. The impact of thickness and position of the PCM film, different climatic conditions, PCM melting point temperature on the heat transfer analysis in the thermally efficient building are performed by Li et al. [9]. Results suggested proper melting point PCM reduces temperature fluctuations and energy expenditure of air conditioning units, and higher input temperature requires higher melting point PCM. Also, the PCM with melting point near to the occupant's comfort zone increases the thermal comfort especially at moderate climate conditions. Huang et al. [10] evaluated the heat transmission improvement in the composite type PCM by incorporating porosity of metal foams having high conductivity. They noted that the rate of PCM melting is increased with foam porosity. Computational and experimental investigations on the impact of heat sink orientation attached to the PV cell passive cooling system are conducted by Abdulmunem et al. [11]. The heat sink is filled with PCM and studied with different inclinations of 0°, 30°, 60°, and 90°. They observed that the PCM melting speed has been enhanced alongside the advancement of orientation angle from 0 to 90°. The heat transmission analysis of the rectangular latent thermal energy storage network with different partitions (1, 2, 4, 8, 16, and 32) was performed experimentally (1 and 2 partitions) and numerically (for other partitions) by Mahdi et al. [12]. Partitioning of LHSU led to an increase in PCM melting speed, and a partition of 8 was found as the optimum. The amount of increase in melting rate is 31%, 53%, 65%, and 68% for 2, 4, 8, and 16 partitions compared to a single partition. Simulation study of integrated PCM partition and heat transmission fluid is conducted by Sodhi and Muthukumar [13]. The phase change materials selected in this analysis are in the range of 360°C to 305°C. The impact of Fin distribution, Stefan number on heat energy transmission was carried out. They noted that, for $\mathrm{Ste}_{\mathrm{ref}} \geq 1$, the m-PCM system has the same or lesser charging or discharging rate than a single PCM system. However, there was an improvement up to 25% for $\mathrm{Ste}_{\mathrm{ref}} = 0.5$ to 2. Employing different fin-distribution and ratio of PCMs block length reduced the time for charging and discharging as high as 30% compared to a single PCM system. Performance analysis of different PCMs with higher and lower melting temperatures for PVT applications for weather conditions of Iraq in summer is published by Chaichan et al. [14]. The materials selected are paraffin wax, Vaseline-petroleum jelly, and its combination. The outcomes exhibited that the hybrid PCM using Vaseline completely mixed with paraffin wax is formed with a lower melting point. Usage of petroleum jelly, paraffin, and hybrid paraffin (50%wax + 50%Vaseline) in the PVT structure caused a reduction in photovoltaic cell temperature, which led to huge improvements in efficiency of the system. Experimental investigation of a 2-phase closed thermosyphon (TPCT) form of heat pipes is done by Ozbas et al. [15]. The impact of the number of pipes at different positions (types 1, 2, and 3) and different angles of inclinations (26°, 41°, and 56°) on the effectiveness of TPCT is studied. They found that the best results are obtained for 26° and also affirmed that the greater the tilt angle the greater thermic resistance with lesser heat transferability of TPCT. Numerical analysis of melting and heat energy transmission of PCM

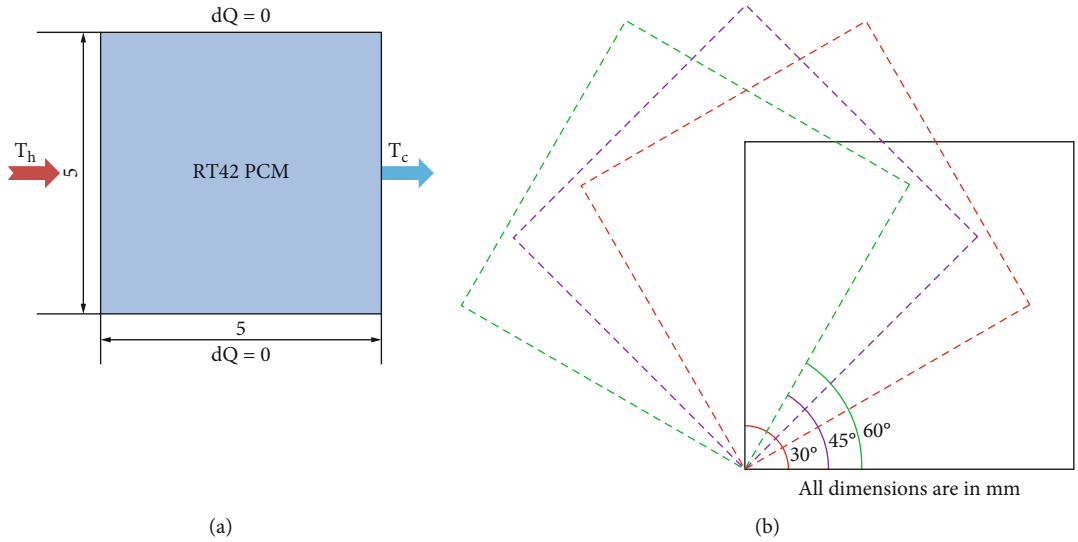

Figure 1: (a) Model geometry with horizontal and vertical sides. (b) Orientation of the enclosure.

in a rectangular block with bilateral flow has been done by Qin et al. [16]. The analysis was done by varying the values of Re number of heat transfer fluids ranging from 10^4 to 7×10^4 and Ra number in range of 3×10^6 to 6×10^6. They reported that the development of natural convection mode is owing to the effects of abnormal HTF heat transmission and cooling among the solid-liquid and the liquid PCM. Investigation on the effect of melting performance of paraffin RT82 PCM with distribution of copper-oxide-nanoparticles (CuO) at varying concentrations has been performed in multitube heat exchange units by Bashirpour-Bonab et al. [17]. The effect of nanoparticle mixture upon flow structure and heat transmission characteristic at different stages of melting of PCM was studied. They observed that with the increase of nanoparticles concentration between 3 and 7% leads to reduction in the time taken for melting by 8.7% to 22.18% though there is a minimal effect in the prime melting stages. It is also noted that the number of internal tubes has positive effects in melting rate and negative effects with distance between the tubes. Gollapudi et al. [18] numerically explored the impact of horizontal fin in a square container packed with Al_2O_3 nanofluid and found that heat transmission characteristics were upgraded with the presence of fin. Additionally, higher conductivity ratio of fins resulted in better heat transmission performance. De Césaro Oliveski et al. [19] investigated the melting method of lauric acid inside a rectangular shaped container with extended surface. The parametric study was performed for 78 different configurations by only changing the fin aspect ratio. They concluded that the total melting time reduced with decrease in aspect ratio of the fin. With increasing value of volume concentration (φ), there was an increase in rate of melt fraction. Furthermore, it is observed that there is a drop in energy accumulation as the value of φ rises. Abidi et al. [20] simulated the charging and discharging procedure of $CaCl_2.6H_2O$ PCM containing graphene in 2D enclosed circular space. The enclosure contains two circles. The inner circle containing 12 blades of rectangular shape incorporated was kept at higher temperature for charging and lower temperature for discharging. The results show that increase in blade length caused a rise in enclosure temperature in charging mode and with a blade length of 1.5, and the Nu is enhanced by 252% in the first 100 s and decreased by a factor of 0.87 in 1000 s while charging whereas it is reduced by 94% and increased by 115% for discharging mode. Computational evaluation on thermal energy storage network employing fins with linear tree-like shapes with the integration of MoS_2-TiO_2 hybrid nanoparticles termed as hybrid nanoenhanced phase-changing material (HNEPCM) was done by Hosseinzadeh et al. [21]. It was found that the tree-shaped fins achieved superior heat transmission characteristics than rectangular fins and absence of fins. Evaluation of enhancement of melting characteristics of PCM by accommodating a new fin design is conducted by Kok [22]. Both types of fins are compared using base and nano-PCMs. They concluded that incorporating heat transfer fins improved the melting rate as well as reduced the cost and weight of thermal energy storage systems (TES). The designed fin reduced the melting time by 63% in the thermal energy storage tank. Design and analysis of a PCM-filled square cavity with thermal heat flux at distinct sites (0.2 L, 0.4 L, 0.6 L, and 0.8 L) were done by Dora et al. [23]. A heating element was positioned at the lowest surface with different locations varied in terms of length. The transient analysis was done for 10 hrs. They concluded that the heater at 0.2 L and 0.4 L assured the complete melting of the PCM than other locations. Experimental analysis was directed by Jevnikar and Siddiqui [24] to know the thermal behaviour of phase change material while melting. The temperature and velocity are measured using thermocouples and particle image velocimetry (PIV), respectively. They observed that velocity has a significant function in melting

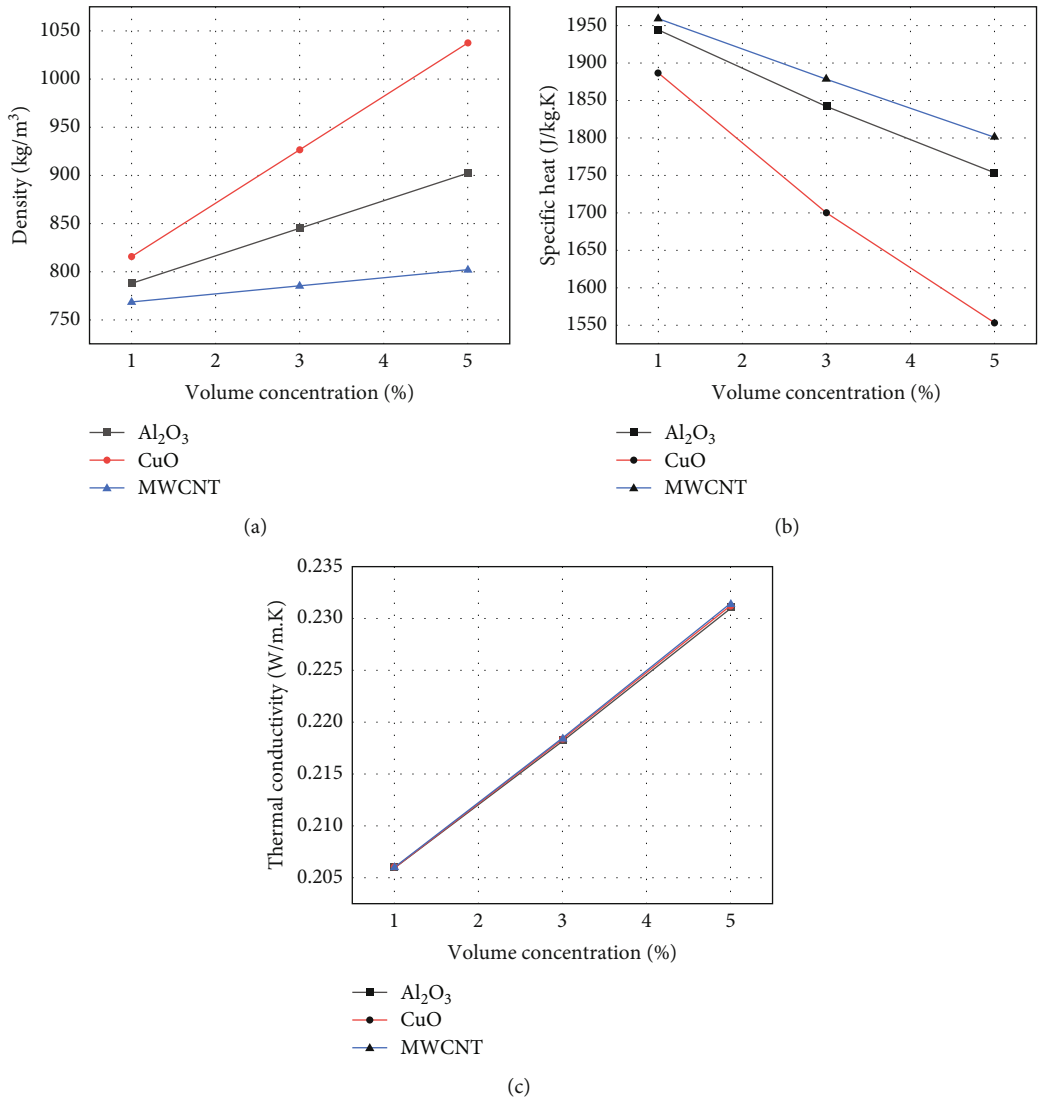

FIGURE 2: Material properties of NEPCM for different concentrations of nanoparticles. (a) Effective density. (b) Effective specific heat. (c) Effective thermal conductivity.

and heat transmission and provided the comprehensive data for heat energy transfer enhancement in numerical models with phase change process. Experimental and computational evaluations of the melting of the PCM 27 in an upright cavity were carried out by Mehdaoui et al. [25]. The simulation is carried out in TRANSYS with the Tunisian climate situations. They concluded that the room temperature with the incorporation of a PCM wall is reduced to 12°C, and the PCM has a calculated stored energy of 1200 kJ/m^2 by increasing 2°C in the night times. Numerical and experimental examinations are performed by Ebadi et al. [26] to understand the effect of addition of Cu nanoparticles at different Rayleigh numbers on the melting of bio-PCM in a thermal energy storage of upright cylindrical type system. They observed that adding nanoparticles has minimal effect on the shapes of melt fraction and stored energy compared to base-PCM. Further, the stored energy difference with Rayleigh numbers was very less at the start of melting, and larger variance was detected at higher Rayleigh numbers. The effect of blending different types of nanoparticles (Silver, CuO, Al_2O_3, and MWCNT) with various volume fractions (1, 3, 6, 8, and 10%) into pure PCM was examined by Bashar and Siddiqui [27]. They affirmed that silver particles provide the highest heat transfer enhancement followed by CuO. The Al_2O_3 and MWCNT nanoparticles however reduce the heat transfer due to higher settlement rates, and the optimum addition of nanoparticles suggested is 6% for 25% higher rate of melting than pure PCM. Tao et al. [28] performed the numerical investigation on the impact of filling position and free convection on the rate of charge and discharge in latent heat storage system of shell and tube type. The analysis is carried out by packing the PCM in tube side in one case and shell side in another case with and without natural convection. They observed that the heat transfer is improved by 54.2% more when the PCM is used in tube side escorted by natural mode of convection with reduced

Table 1: Thermophysical properties of the base materials used.

Properties	Pure PCM (RT-42)	Alumina (Al_2O_3)	Copper oxide (CuO)	Multiwalled carbon nanotube (MWCNT)
Density (kg/m^3)	760	3600	6310	1600
Specific heat (KJ/kg.K)	2000	765	531	8.039
Thermal conductivity (W/m.K)	0.2	36	76	3000
Viscosity (kg/m.s)	0.02351	—	—	—
Thermal expansion coefficient (1/K)	0.0005	—	—	—
Pure solvent melting heat (J/kg)	165000	—	—	—
Solidus temperature (K)	311.15	—	—	—
Liquidus temperature (K)	315.15	—	—	—

Table 2: Number of elements vs. Nusselt number (Nu).

Grid size	Nusselt number (Nu)
61 × 61	2.10952
100 × 100	2.10201
143 × 143	2.09754
179 × 179	2.09348
200 × 200	2.08958

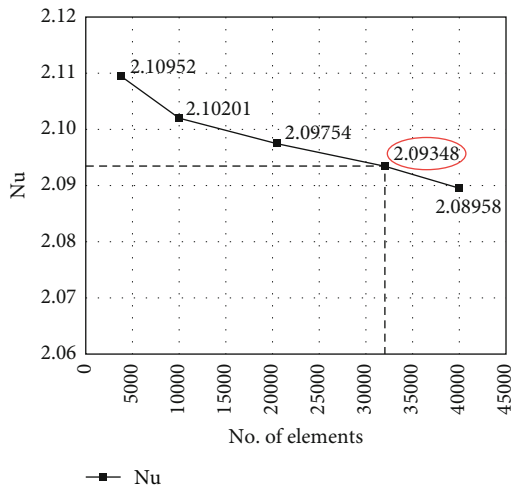

Figure 3: Grid independence study.

melting time of 34.4% and 36.6% more with the PCM present in tube side without the free convection at a melting rate of 25.4% compared to the PCM in shell side. Joneidi et al. [29] investigated the impact of thermal heat flux and alignment of the enclosure on the heat transmission and melt fraction of PCM filled in a rectangular container. The rectangular cavity is heated with different heat fluxes (4.4 W, 5 W, and 5.6 W) oriented in different inclinations (0°, 45°, and 90°), and the analysis was carried with the help of thermocouples and camera. They concluded that the increase in heat flux led to reduction in the rate of melting of the PCM and an increase in inclination angle results in maximization of the final stored energy. The numerical analysis of a n-octadecane PCM filled in a container incorporated with silicone heating generating element was done by Bondareva and Sheremet [30]. The influence of Ra, St, and Ostrogradsky numbers on the speed of melting was analysed. They affirmed that the increase in all the three parameters have positive influence upon heat transmission enhancement and diminishes the time of melting. Arıcı et al. [31] investigated the impact of the volume concentration of the nanoparticles added in the PCM filled in a square cavity with varying wall temperatures. The analysis is performed with Paraffin wax, and Al_2O_3 is employed as nanoparticles in different proportions (1%, 3%, and 5%). The results explained that the increase in volume fraction after 1% has a lower effect after 20 min of time. The orientation of the heater plays a vital role after that time than the nanoparticle concentration. Enhancement of heat transfer using PCM material inside the annular region between two concentric circular, elliptical cylindrical with different orientations inside circular cylinder, and incorporation of fin inside cylinder was studied numerically by Rabienataj Darzi et al. [32]. The analysis is also carried out with the inclusion of Cu nanoparticles in the PCM. They reported higher melting rate at the upper part of the annular segment than the lower, and the usage of upright elliptical tube orientation reduces melting time. Also, blending Cu nanoparticles improves the heat transmission, and fins positioned on the higher and lower temperature walls enhance the melting rate. Evaluation of the heat transmission process in latent thermal energy storage units filled with nano-PCM is performed by Tasnim et al. [33]. The impact of dimensionless parameters is studied using scaled analysis for complete melting of PCM. They observed that heat transmission by both conductive and convective modes was degraded by addition of nanoparticles in PCM. Experimental analysis of the enhancement of the heat transmission in a PCM-filled enclosure using different inclination angles is carried out by Kamkari et al. [34]. The PCM used in this work is lauric acid with the Ra ranging from 3.6 to 8.3 E8, and the inclination angles of 0, 45, and 90° are performed. The photographs taken are image processed in order to differentiate the solid and liquid regions, and temperatures are recorded with the

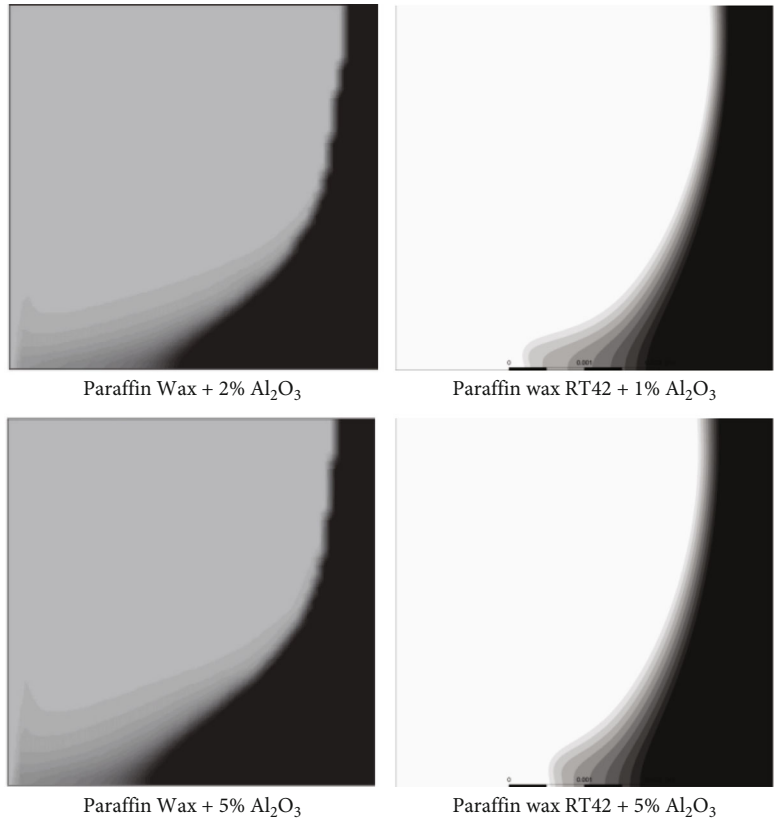

Figure 4: Comparison of the present work with reference work.

help of thermocouples. They noted that changing the orientation from vertical 90° to 0° will create the Benard which will affect the natural convection. Also, the rate of melting enhanced 35% and 53% for 45° and 0° compared to perpendicular orientation. The analysis of the melting rate of n-octadecane PCM using suspended CuO nanoparticles in a cavity with uniform thermal heat flux supplied to one of the edges was performed by Dhaidan et al. [35]. The influence of Ra, nanoparticle volume concentrations, and the subcooling was investigated. The PCM melting is dominated with the conduction represented as straight line shapes in the beginning, later as time marches it is shifted to natural convection curved shapes, they noted. Also, the heat transmission enhancement and rate of melting are improved upon optimum addition of nanoparticles and with increase in Ra. Bashirpour-Bonab et al. [36] numerically investigated the melting fraction of CuO-blended nano-PCM filled in a multitube heat exchanger. The impact of nanoparticle volume fraction, number of tubes, and spacing between the tubes on rate of melting is studied. They reported that the melting fraction is improved to 33.87% with 7% volume concentration and 4 number of tubes and 20.54% by increasing the distance between the tubes. The analysis of heat transfer characteristics of PCM filled in a combined fractal fin-based heat exchanger is carried out by Luo et al. [37]. The influence of combined fractal fins, fin's area, spacing, and partition between the fins is studied. The time to liquify the PCM is reduced with the fractal fins by 68%. They concluded that the decrement of width takes a long time to raise the fin's temperature and increase the heat transfer area results in reduction of thermal resistance. However, the mean liquid fraction of PCM does not continuously rise with the area of heat transfer. Zhang et al. performed the numerical study on the thermal management of the buildings using encapsulated PCM. They focused on the effect of geometry of the encapsulation on the melting behaviour of the PCM and validated the numerical outcomes with the experimental results. Also, the variation of shell orientation, size, and temperature difference is studied. They affirmed that the pyramidal-shaped shell attains the minimum time of melting and recommended the medium size capsule with low initial temperature differences. Experimental heat transfer analysis of composite PCM prepared with lauric and palmitic acid distributed in mesoporous graphite (MG) is conducted by Nirwan et al. [38]. The impact of variation of weight fraction is studied using differential scanning calorimeters. The weight fraction of 1 : 5 MG-PCM composite takes away the maximum heat by reducing the temperature of the heating source by 20°C. They recommended this ratio of the composite rather than the pure form of PCM for maximum heat transfer in electronic devices. Li et al. [39] worked on the microencapsulation of aluminium and zinc for high-temperature thermal energy storage applications. The preparation and characterization of microencapsulated PCMs are explained. They observed that the latent heat of MEPCMs after boehmite, thermal oxidation, and copper

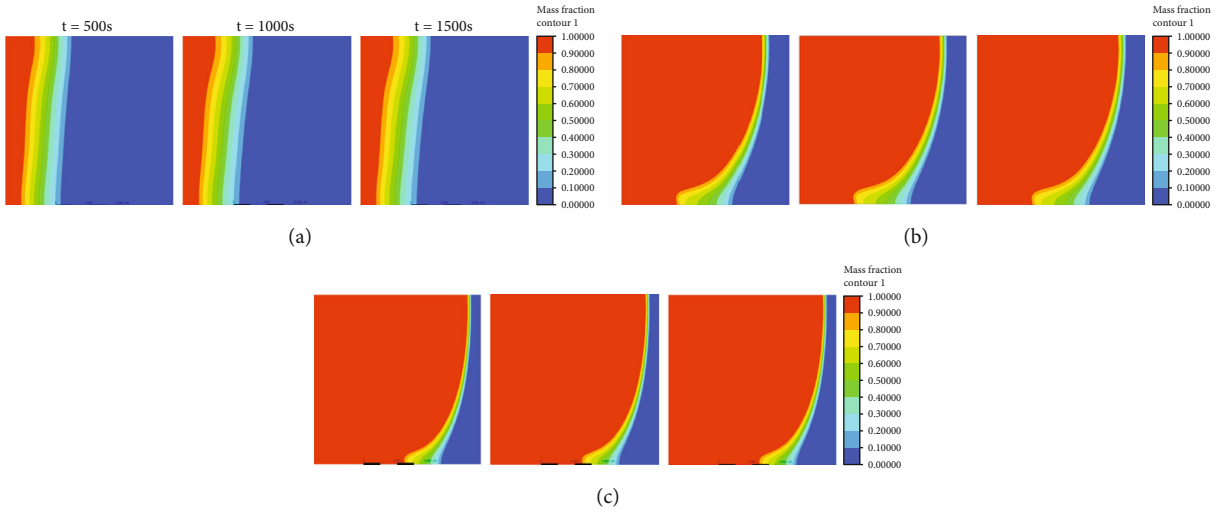

Figure 5: Melt-fraction contours of PCM melting for (a) Gr = 5000, (b) Gr = 13000, and (c) Gr = 20000.

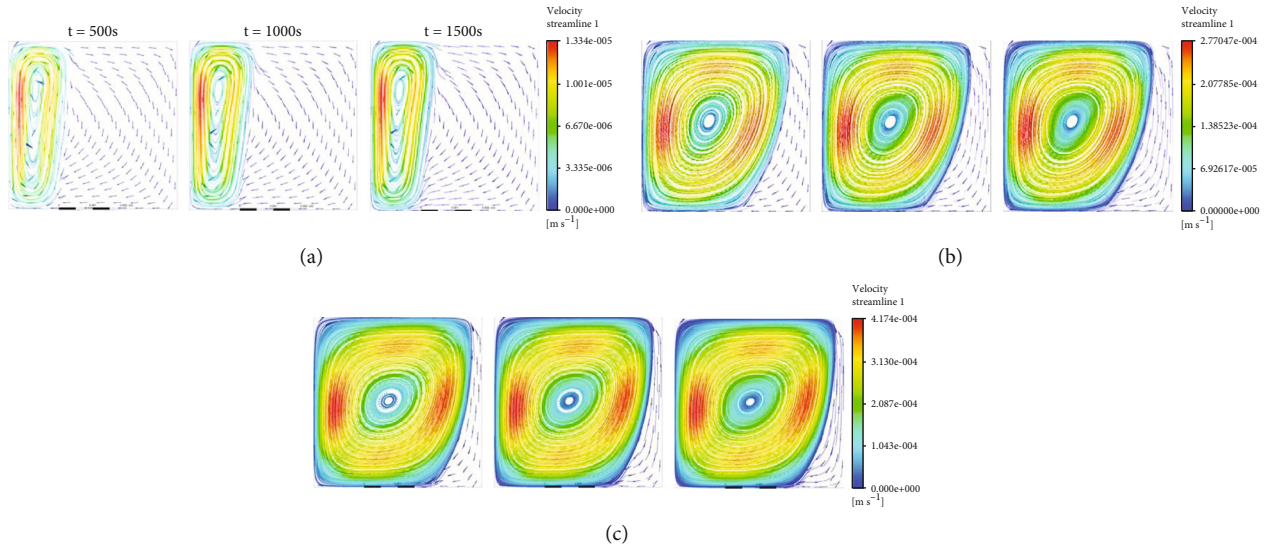

Figure 6: Velocity streamlines of pure PCM for Gr (a) 5000, (b) 13000, and (c) 20000.

plating treatment reduced to 160.7 J/g, 126.4 J/g, and 89 J/g from 176 J/g of pure Al-Zn MEPCM. However, they noted the life of the MEPCM has improved after the copper plating treatment. The experimental investigation of microencapsulation of $C_{10}H_{20}O_2$ (CA) and $C_6H_{32}O_2$ (PA) eutectic mixture in polyvinyl chloride (PVC) is carried out by Xing et al. [40]. From the characterization of the encapsulated PCM, they found that the optimum ratio of shell and core is 1 : 2 with the liquefaction temperature of 17.1°C and pure solvent melting heat of 92.1 J/g. A 500 : 300 nm thickness microencapsulation of $ZnO : Al_2O_3$ composite material for medium temperature applications is prepared by Kawaguchi et al. [41]. It exhibits a melting temperature of 510°C with a pure solvent melting heat of 117 J/g and noted that 75% of encapsulations maintained the same spherical form after 100 cycles. Also, they sintered the MEPCM with glass frit and observed almost 100% of shape retainment after 100 cycles. Jevnikar and Siddiqui [42] performed the experimental and numerical flow and thermal analysis of PCM. The influence of heating location on the flow field and heat transfer of PCM is studied. They noted that the melting and thermal performance of PCM is influenced by the fluid flow regulated by natural convection. Numerical analysis of the effect of vertical aluminium fins on the heat transfer enhancement of PCM is carried out by Abdi et al. [43]. They affirmed that with the usage of five numbers of long fins, a 200% of power improvement, 6% of energy storage reduction, and 12% of depletion in PCM content are observed. Kamkari and Amlashi [44] numerically investigated the impact of orientation of the enclosure on the melting performance of PCM. A reduction of 52% and 37% of melting time is observed for 0° and 45° orientations. They also presented the correlations to predict the melting rate, energy stored, and Nu at any instant. The design of PCM container with double pipe helical coiled tube for thermal energy storage application is examined numerically by Mahdi et al. [45]. They concluded that the

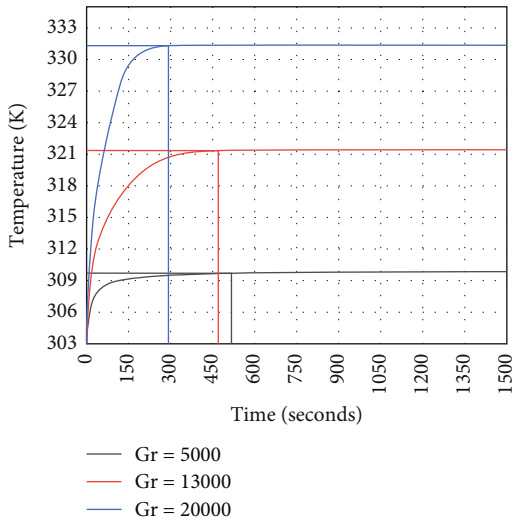

Figure 7: The effect of Gr on temperature of PCM with time.

proposed design reduces the melting rate by 25% and 59% compared to parallel and perpendicular double pipe energy storage systems. Also, the pitch of the coil effects incredible phase change transformation; however, they selected the optimum pitch of outer diameter as 2. The design and optimization of a multilayer shell and tube unit incorporated with longitudinal and radial metal fins are carried out by Xu et al. [46]. The amount of melting time reduced is 56%, 65%, and 71% with the addition of fins than no fin condition. The maximum reduction in time is observed for radial type of fin, and this is selected as the best arrangement. The optimum configuration increases the comprehensive storage density evaluation to 36%.

The detailed review of many researches apprises the various techniques involved in PCM-based thermal storage systems. However, only few discussed the combined effect of nanoparticle incorporation and angular orientation of the container. The main objective of this work is to study the effect of Grashof number (5000, 13000, and 20000), nanomaterial type (Al_2O_3, CuO, and MWCNT), volume concentration (0%, 1%, 3%, and 5%), and orientation angle (30, 45, and 60°) on the melting rate of the PCM in a square container. The analysis is carried out with RT42 PCM up to 1500 sec.

1.1. Problem Description and Methodology. A two-dimensional transient numerical analysis of the PCM filled in a square enclosure inclined in different orientations is performed. Figures 1(a) and 1(b) show the geometry description of the enclosure studied.

In this work, a square enclosure with 5 mm × 5 mm is modelled in ANSYS design modeler. This cavity is embedded by phase change material (RT-42) and consolidated with different nanoparticles (Al_2O_3, CuO, and MWCNT) by varying concentration (1%, 3%, and 5%). The top and lower walls are kept adiabatic, the left side wall is subjected to higher temperature(T_h), and the right side wall is subjected to room temperature (T_c) so that $T_h > T_c$. Transient numerical study is carried out for the time steps of 500, 1000, and 1500 seconds. Also, the same analysis is executed by changing the orientation of the base side of the cavity with different inclinations (30, 45, and 60°) as shown in Figure 1(b). The governing equations for numerical computation are listed below from equations (1) to (3):

Continuity equation:

$$\frac{\partial \rho}{\partial t} + \nabla . \left(\rho \vec{U} \right) = 0. \tag{1}$$

Momentum equation:

$$\frac{\partial}{\partial t} \left(\rho \vec{U} \right) + \nabla . \left(\rho \vec{U} \vec{U} \right) = -\nabla P + \rho \vec{g} + \nabla . \vec{\tau} + \vec{F}, \tag{2}$$

where $\rho \vec{g}$ and $\vec{F}$ are gravitational and external body forces, respectively. P is static pressure, and $\vec{\tau}$ is a stress tensor.

Energy equation:

$$\frac{\partial (\rho H)}{\partial t} + \nabla . \left(\rho \vec{U} H \right) = \nabla . (K \nabla T) + S. \tag{3}$$

Here, H, T, ρ, and K are enthalpy, temperature, density, and conductivity of nanoparticle enhanced-phase change material (NEPCM), respectively. $\vec{U}$ is velocity and S, and volumetric heat generation term is assumed zero in present analysis. The gross enthalpy of PCM H is aggregate of sensible heat (h) and latent heat (ΔH), respectively. Latent heat is expressed as

$$\Delta H = \beta L, \tag{4}$$

where $L$is the latent heat of PCM, and β is the liquid fraction given by the following equation,

$$\left.\begin{aligned} &\beta = 0 \quad \text{if} \quad T < T_{solidus} \\ &\beta = 1 \quad \text{if} \quad T > T_{solidus} \text{ and,} \\ &\beta = \frac{T - T_{solidus}}{T_{Liquidus} - T_{solidus}} \quad \text{if} \quad T_{solidus} < T < T_{liquidus} \end{aligned}\right\}. \tag{5}$$

Now thermophysical properties of nano-PCM such as density, heat capacity, latent heat, and viscosity are calculated using the Arasu and Mujumdar [47], Ebrahimi and Dadvand [48], and Teja et al. [49] presented from equations (6) to (9), and the variation of these properties with volume concentration is shown in Figure 2.

$$\rho_{npcm} = \varphi \rho_{np} + (1 - \varphi) \rho_{pcm}, \tag{6}$$

$$c_{p,npcm} = \frac{\varphi \left(\rho c_p \right)_{np} + (1 - \varphi) \left(\rho c_p \right)_{pcm}}{\rho_{npcm}}, \tag{7}$$

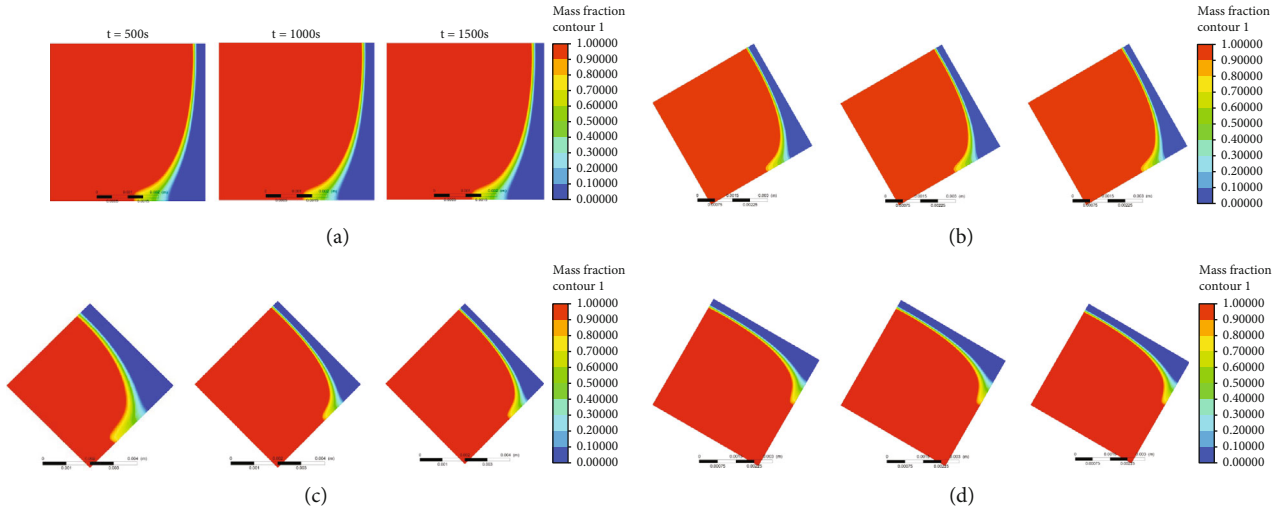

Figure 8: Melt-fraction contours of pure PCM in a container oriented in (a) 0°, (b) 30°, (c) 45°, and (d) 60°.

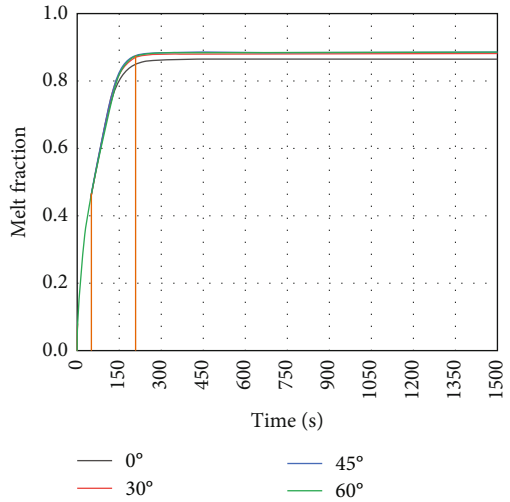

Figure 9: Effect of orientation on melt-fraction with time.

$$L_{npcm} = \frac{(1-\varphi)(\rho L)_{pcm}}{\rho_{npcm}}, \tag{8}$$

$$\mu_{npcm} = 0.983 e^{(12.959\varphi)} \mu_{pcm}. \tag{9}$$

While the effective thermal conductivity is expressed as

$$K_{npcm} = \frac{K_{np} + 2K_{pcm} - 2(K_{pcm} - K_{np})\varphi}{K_{np} + 2K_{pcm} + (K_{pcm} - K_{np})\varphi} K_{pcm} + 5 \times 10^4 \beta_k \zeta \varphi \rho_{pcm} C_{p,pcm} \sqrt{\frac{BT}{\rho_{np} d_{np}}} f(T, \varphi), \tag{10}$$

where B is Boltzmann constant, and its value is 1.381×10^{-23} J/K and,

$$\beta_k = 8.4407 (100\varphi)^{-1.07304}, \tag{11}$$

$$f(T, \varphi) = \left(2.8217 \times 10^{-2}\varphi + 3.917 \times 10^{-3}\right) \frac{T}{T_{ref}} + \left(-3.0669 \times 10^{-2}\varphi - 3.91123 \times 10^{-3}\right). \tag{12}$$

Here, T_{ref} is assumed to be 303 K. The properties of NEPCM for different volume fractions (1%, 3%, and 5%) of nanoparticles (Al_2O_3, CuO, and MWCNT) are calculated using the equations (6) to (10). The thermophysical properties of the base materials are listed in Table 1. Also, the dimensionless Grashoff number and Nusselt number used are expressed as

$$Gr = \frac{g\beta_f (T_h - T_c) H^3}{\nu_f^2}, \tag{13}$$

$$Nu = \frac{hL}{K}. \tag{14}$$

The boundary conditions applied to the model in the study is mathematically given by:

$T = T_h$ for $X = 0$ and $0 < Y < 5$ on left vertical wall.

$T = T_c$ for $X = 5$ and $0 < Y < 5$ on right vertical wall.

$dQ = 0$ for $0 < X < 5$ and $Y = 0$ on bottom horizontal wall.

$dQ = 0$ for $0 < X < 5$ and $Y = 5$ on top horizontal wall.

1.2. Numerical Procedure. In the present study, numerical analysis is carried out with ANSYS FLUENT software. The governing equations based on boundary conditions are numerically solved by fluent using FVM. Construction of geometry is done in a design modeler from the fluid flow (fluent) geometry component. Meshing of the model is done by taking an adaptive size function with a fine relevance center. The skewness for mesh is maintained minimum while the orthogonal quality is kept closer to 1 by incorporating quadrilateral mesh cells by setting quadrilaterals as the meshing method.

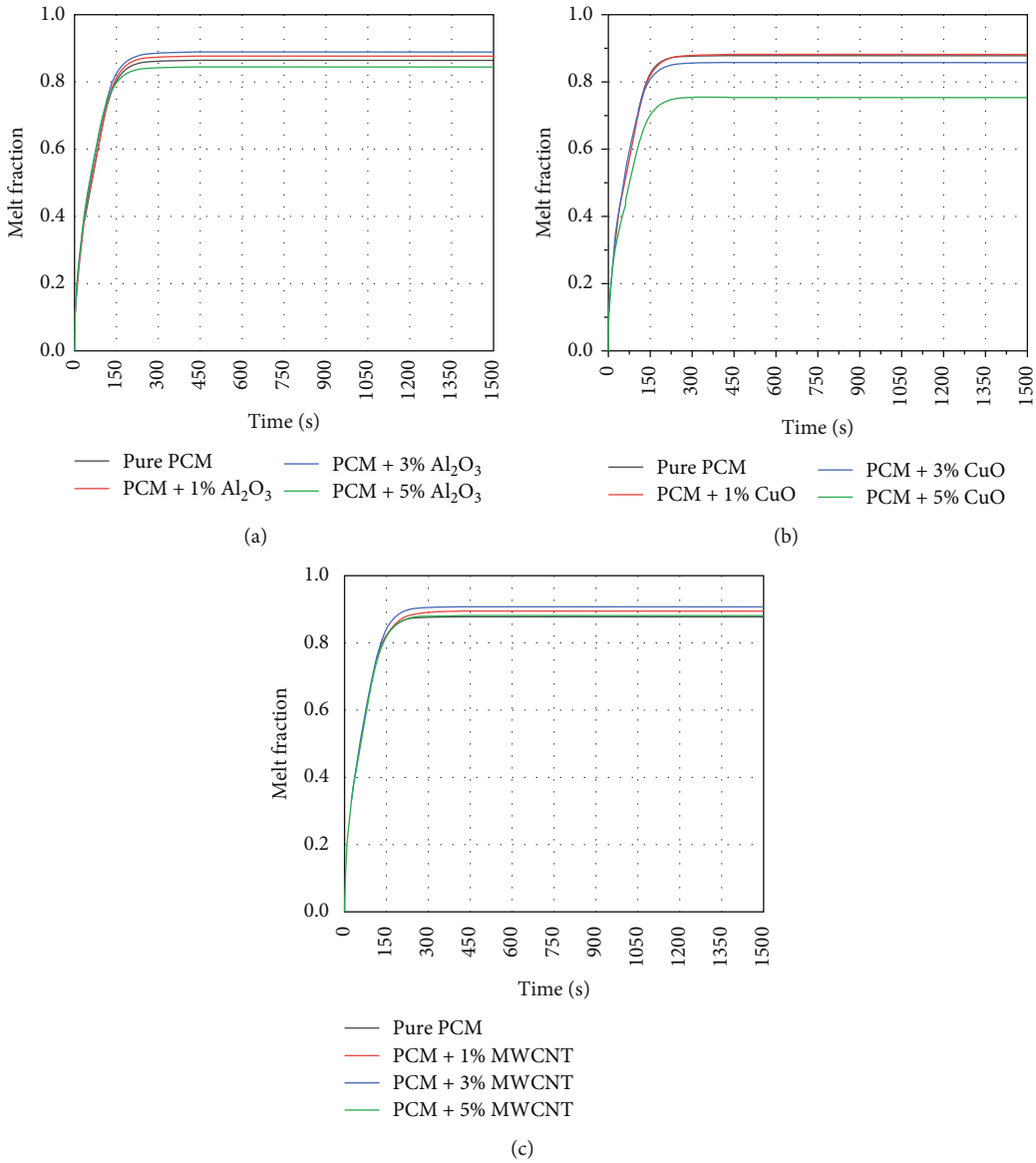

Figure 10: Effect of nanoparticles (a) Al_2O_3, (b) CuO, and (c) MWCNT with different volume concentrations (1%, 3%, and 5%) on melt fraction at Gr = 20000.

Pressure-based solver along with its velocity coupling and adjustment equation is utilized with simple algorithms and PRESTO! Scheme, respectively. While the equations of momentum and energy are evaluated using an upwind scheme of second order. Transient analysis is performed by taking the time step size as 0.2 s, and the maximum number of iterations is fixed as 20 for every time step. The convergence limit for residuals is fixed as 10^{-3} for continuity, momentum equations, and it is 10^{-6} for an energy equation.

1.3. Grid Independence Study and Validation. To select the appropriate grid size, the numerical model is verified with different element sizes. The mesh consists of uniform quadrilaterals distribution throughout the enclosure. Five different mesh sizes were examined with the number of cells varying from 61×61, 100×100, 143×143, 179×179, and 200×200, respectively, as shown in Table 2. As shown in Figure 3, the difference in the Nusselt numbers for 179×179 (32041 elements) and 200×200 (40000 elements) is very small. Hence, the number of cells in the mesh is selected as 32041 with element size as 0.028 mm for further study.

The validation of the present work is conducted qualitatively by comparing the melt-fraction contours of the present study with Arasu and Mujumdar [47] study. Comparison is done for melting of PCM (Paraffin wax) with 2%, 5% Al_2O_3 addition and melting of PCM (RT-42) with 1%, 5% Al_2O_3 addition of present study. The contours of the melt fraction for both the current work and reference work are matching very nearer as shown in Figure 4.

2. Results and Discussion

Computational thermal analysis of heat transfer and melting of pure PCM/nano-PCM (PCM + nanoparticles) is carried

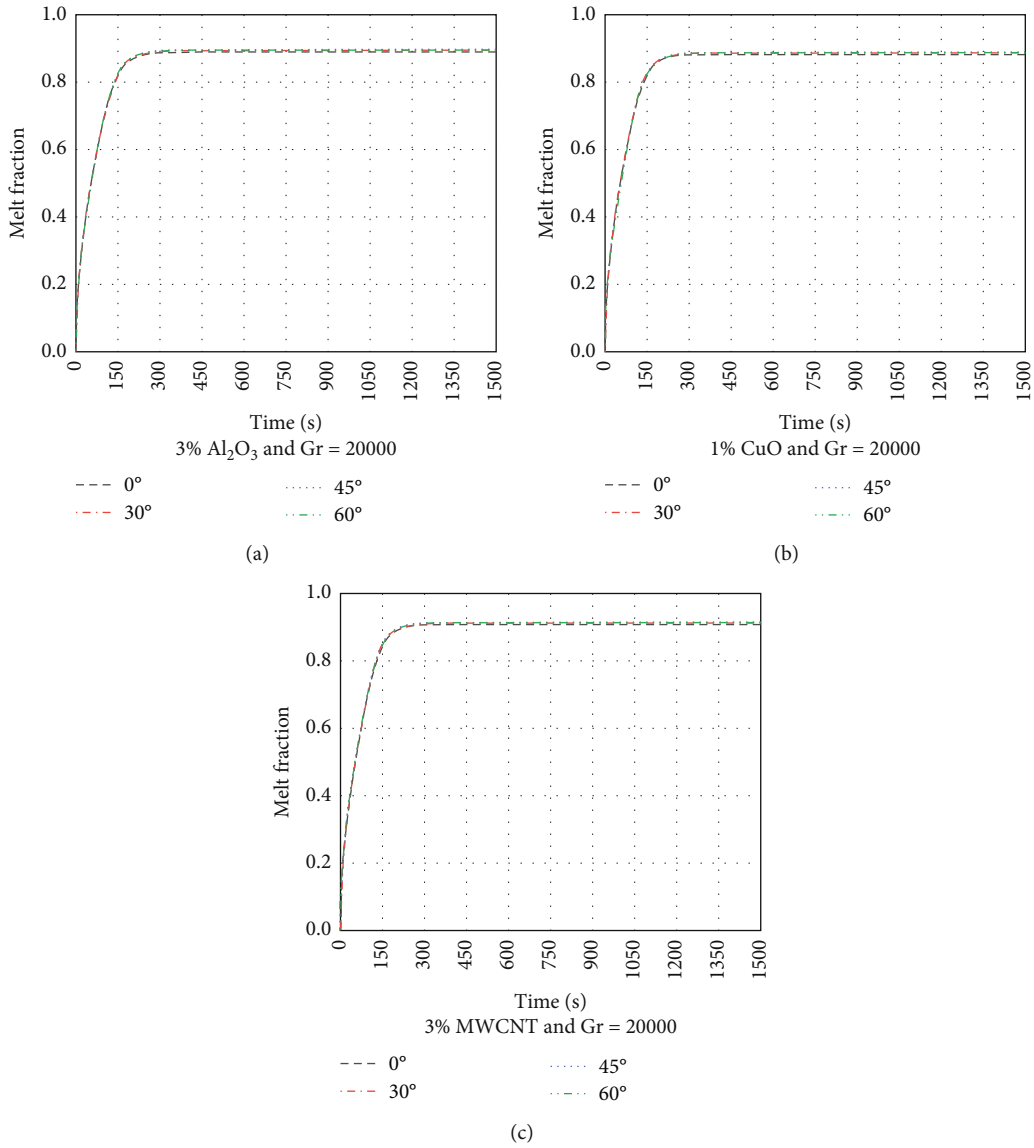

Figure 11: Effect of orientation in (a) PCM + 3% Al_2O_3, (b) PCM + 1% CuO, and (c) PCM + 3% MWCNT based nanofluids on melt fraction at Gr = 20000.

out for three different Grashoff numbers (5000, 13000, and 20000) given to left side wall with the bottom edge oriented in different inclinations (0°, 30°, 45°, and 60°). The effect of nanoparticle type (Al_2O_3, CuO, and MWCNT), concentration (1%, 3%, and 5%), Grashoff number, and inclination is presented.

2.1. Melting of Pure PCM. Figures 5(a)–5(c) show the melt fraction contours of the PCM at three different Grashoff numbers up to 1500 sec with an interval of 500 sec. Red portion in the contour represents the liquefied part of the PCM with a melt fraction as 1.0, and the solid part is described as the blue portion with a melt fraction as 0.0. In between, the different colours of the contours represent the mushy region. It is observed that during the initial stages of melting, the liquid-fraction region is almost vertical as shown in Figure 5(a). This clearly shows that the initial mode of heat transfer was by conduction. After some time, the conduction dominant zone is converted into mixed conduction and convection zone by transforming the solid PCM into liquid. The density difference between the solid and liquid makes the material move by natural convection as shown in Figures 6(a)–6(c) for different Gr.

The movement of the liquid will form upward and downward rotations with small velocities due to the buoyancy forces formed by the temperature difference between hot and cold wall. Also, due to the boundary layer effect by viscosity, the velocity adjacent to the wall is zero, and it gradually increases away from the wall up to the solid portion of the PCM.

With the increase in Gr, the rise in hot wall temperature is evident, and the availability of melted PCM will be more;

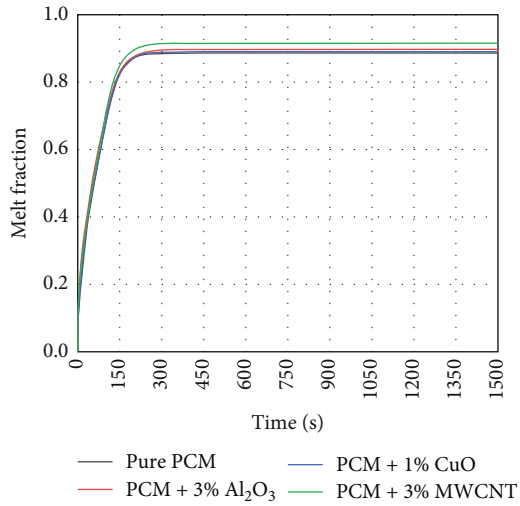

Figure 12: Comparison of melt fraction for 45° oriented enclosure for different nano-PCM at Gr = 20000.

therefore, more velocity has been observed. For Gr = 20000, the highest velocity noted is 4.174e-4 m/s which is 51.23% and 32.97% higher than Gr = 5000 and 13000 case.

Figure 7 depicts the effect of Gr on the temperature of the PCM with respect to time. It is noted that the temperature has been increased with Gr for a period of time; afterward, it comes to a steady state. It is also identified that the slope of the temperature lines are reducing with respect to Gr, indicating that the rate of attaining steady state is less with increase in Gr. The amount of heat transferred to the PCM is stored in the form of phase change. With the increase in temperature, the amount of melting rate also improved from 24.16% to 25.44%, 76% to 76.35%, and 86.4% to 86.417% for Gr = 5000, 13000, and 20000, respectively. For the same time period, the melted region is more for Gr = 20000.

2.2. Melting of PCM in an Enclosure with Angular Orientations. Transient thermal analysis of a square enclosure filled with the PCM, oriented in different angles (0°, 30°, 45°, and 60°), as shown in Figure 1 is performed. Figure 8 shows the melt-fraction contours for different Gr (5000, 13000, and 20000) and varying time intervals (500 s, 1000 s, and 1500 s).

Figure 9 represents the graph plotted for the variation of melt-fraction of PCM with different orientations (0°, 30°, 45°, and 60°) for a time of 1500 seconds and Gr of 20,000. In the beginning, at around 50 seconds, the PCM in all the containers is in the same stage, the PCM is slowly melting into fluid up to 200 seconds, and later, the material in all the containers attains the steady state. It is observed that the amount of melt is more as the inclination angle increases. The percentage increase of melt fraction is less for different orientations and pure PCM. Using 60° orientation, the melt fraction improved is 2.43%, 0.5%, and 0.08% more than the 0°, 30°, and 45° inclinations.

2.3. Effect of Nanoparticle Concentration in PCM. The computational analysis on the melting performance of phase change material blended with different nanoparticles (Al_2O_3/CuO/MWCNT) in various proportions (1%, 3%, and 5%) filled in a square enclosure is carried out. Figures 10(a)–10(c) show the comparison of the melt fraction of nano PCM (PCM + Al_2O_3/CuO/MWCNT) with different concentrations (1%, 3%, and 5%), respectively. It is clearly visible that the amount of melt fraction is not varied linearly with the volume concentration of the nanomaterial. In the first case with Al_2O_3, the maximum melt fraction is observed for PCM + 3% followed by 1%, pure PCM (0%), and 5%. The melting performance is improved with addition of Al_2O_3 up to 3%; afterward, it is reduced. This is because of increased density and viscosity. Also, in the beginning of heating PCM, the transfer of energy is predominantly by conduction succeeded by convection. By adding more amounts of high conductive nanomaterials, the heat transfer will again convert into a conductive zone. Therefore, the melting performance reduces.

With 3% Al_2O_3, the increase in fluid fraction is 2.9%, 1.38%, and 5.27% more than the melt fraction of 1%, pure PCM, and 5% added nanofluid, respectively. In the second case, in Figure 10(b), though the conductivity of the CuO is more than Al_2O_3, the enhancement of effective thermal conductivity is very less compared to effective density. Hence, 1% CuO nanomaterial addition has more amount of liquid fraction than 3 and 5% nanofluid. Figure 2 shows the variation of thermophysical properties of nanofluids for different nanoparticle concentration. With 1% CuO, increase in fluid fraction is 2%, 2.924%, and 11% higher than the melt fraction of 3%, pure PCM, and 5% added nano-PCM. With the incorporation of MWCNT nanoparticles (1%, 3%, and 5%) shown in Figure 10(c), the heat transfer is enhanced due to high effective conductivity of the nanofluid, and also the percentage of change in density is less compared to other two nanoparticles. Similar to Al_2O_3-based nano-PCM, the liquid fraction is more in 3% followed by 1% addition. However, the melt fraction is less in 5% MWCNT due to the effect of thermophysical properties. The increase in fluid fraction of nanofluid blended with 3% MWCNT is 5%, 1.46%, and 2.94% more than pure PCM, 1%, and 5% blended nano-PCM.

2.4. Effect of Orientation and Nanoparticles on Melt Fraction of Nano-PCM. Combining the effect of angular orientation of the enclosure and nanomaterial added to the fluid on the melt-fraction of NEPCM is studied. Figures 11(a)–11(c) represent the graph plotted between time and melt fraction for different inclinations (0°, 30°, 45°, and 60°) of enclosure filled with 3% Al_2O_3, 1% CuO, and 3% MWCNT blended nano-PCM, respectively.

The volume concentration compared is chosen on the basis of the maximum melt fraction with each nanomaterial. It is observed that the utmost amount of melt is occurring in a container with an orientation of 45° for all the nanofluids, despite having marginal change in liquid fraction. Therefore, it is concluded that the effect of enclosure orientation is

negligible compared with the effect of volume fraction of the nanoparticles.

From Figure 12, it is noted that among Al_2O_3, CuO, and MWCNT with different concentrations (pure PCM (0%), 1%, 3%, and 5%) blended with the PCM of RT 42 and orientations (0°, 30°, 45°, and 60°), the maximum amount of heat transfer and liquid fraction is attained for (PCM + 3% MWCNT) nano-PCM oriented with 45°. With the incorporation of 3% MWCNT/PCM in 45° orientated enclosure, an improvement of 3.4%, 2.04%, and 2.94% melt performance than pure PCM, (PCM/3% Al_2O_3), (PCM/1% CuO), respectively, is noted.

This is because the changes in the thermophysical properties of the MWCNT blended PCM are more substantial than the other nanoparticle concentrated PCM. Also, due to symmetry and less buoyancy effects compared to other orientations, the liquid fraction in 45° orientation is more.

3. Conclusions

Numerical analysis on the effect of nanoparticle type (Al_2O_3, CuO, MWCNT), volume concentration (0%, 1%, 3%, and 5%), and angular orientation of the enclosure (0°, 30°, 45°, and 60°) on the melting of phase change material RT 42 is carried out.

It is observed that

(i) For the melting of the pure PCM, it is affirmed that the temperature of the heat source is increased with increase in Gr (5000, 13000, and 20000). Due to this, the heat transfer and melting rate have been enhanced

(ii) The maximum melting fraction is identified for Gr = 20000. Also, the shape of the melted portion is changed from vertical to parabolic curvature profile indicating that the mode of heat transfer is changed to convection from conduction

(iii) The material properties of phase change material consolidated with nanoparticles (Al_2O_3, CuO, and MWCNT) into RT 42 PCM are presented. With increase in volume concentration (1%, 3%, and 5%) of the nanoparticles, the effective density, thermal conductivity, and viscosity are increased, while specific heat and latent heat are reduced. The rise in thermal conductivity is very less compared to all other properties

(iv) The liquid fraction content is not varied linearly with respect to volume concentration of the nanoparticles. Comparing pure PCM, greater rate of melting is achieved in 3% Al_2O_3 and MWCNT, 1% CuO. With 3% Al_2O_3, the increase in fluid fraction is 2.9%, 1.38%, and 5.27% more than the melt fraction of 1%, pure PCM, and 5% added nanofluid, respectively. With 1% CuO, increase in fluid fraction is 2%, 2.924%, and 11% higher than the melt fraction of 3%, pure phase change material, and 5% added NEPCM. The enhancement in the fluid fraction of nanofluid blended with 3% MWCNT is 5%, 1.46%, and 2.94% more than pure PCM, 1%, and 5% blended nano-PCM

(v) Increasing volume fraction beyond the optimum level reduces the melting performance. This is because of the relative escalation of viscous forces than the buoyancy forces with increase in volume fraction. Also, the convection dominant heat transfer will be shifted to conduction state again

(vi) The enclosure orientation has very negligible effects on the advancement of the melt for both phase change material and NEPCM fluids. In case of pure phase change material, the maximum liquid fraction is seen for a 60° oriented container, while it is a 45° orientation for a nano-PCM case

(vii) Among all the nanoparticles, MWCNT-based nanofluids have a high melting rate. This is mainly because of the substantial development of thermophysical properties of MWCNT than all other nanoparticles blended PCM

(viii) Considering all the effects, the 3% MWCNT nano-PCM oriented in 45° is achieving a larger fraction of melting portion. With the 3% MWCNT/PCM filled enclosure oriented in 45°, an improvement of 3.4%, 2.04%, and 2.94% melt performance than pure PCM, (PCM/3% Al_2O_3), (PCM/1% CuO), respectively, is noted

Nomenclature

NEPCM: Nanoparticle-enhanced PCM
TES: Thermal energy storage system
HTF: Heat transfer fluid
RT42: Rubitherm 42
ρ: Density
ϕ: Volume concentration
C_p: Specific heat capacity
L: Latent heat
μ: Coefficient of viscosity
K: Thermal conductivity
β: Volume expansion coefficient
Al_2O_3: Aluminium oxide
CuO: Copper oxide
MWCNT: Multiwalled carbon nanotube
$T_{solidus}$: Solidus temperature
$T_{liquidus}$: Liquidus temperature
T_{ref}: Reference temperature
Gr: Grashof number.

Data Availability

No data were used to support this study.

Conflicts of Interest

The authors declare that they have no conflicts of interest.

References

[1] A. K. Gupta, G. Mishra, and S. Singh, "Numerical study of MWCNT enhanced PCM melting through a heated undulated wall in the latent heat storage unit," *Thermal Science and Engineering Progress*, vol. 27, article 101172, 2022.

[2] C. Xu, M. Liu, S. Jiao, H. Tang, and J. Yan, "Experimental study and analytical modeling on the thermocline hot water storage tank with radial plate-type diffuser," *International Journal of Heat and Mass Transfer*, vol. 186, 2022.

[3] K. Jiao, L. Lu, T. Wen, and Q. Wang, "A modified mixture theory for one-dimensional melting of pure PCM and PCM/metal foam composite: numerical analysis and experiment validation," *International Journal of Heat and Mass Transfer*, vol. 186, p. 122461, 2022.

[4] J. S. Baruah, V. Athawale, P. Rath, and A. Bhattacharya, "Melting and energy storage characteristics of macro-encapsulated PCM-metal foam system," *International Journal of Heat and Mass Transfer*, vol. 182, p. 121993, 2022.

[5] Y. Zhang, M. Vahabzadeh, J. F. Torres, Y. Zhao, and X. Wang, "Dynamic melting of encapsulated PCM in various geometries driven by natural convection of surrounding air: a modelling-based parametric study," *Journal of Energy Storage*, vol. 48, article 103975, 2022.

[6] P. Huang, G. Wei, L. Cui, C. Xu, and X. Du, "Numerical investigation of a dual-PCM heat sink using low melting point alloy and paraffin," *Applied Thermal Engineering*, vol. 189, article 116702, 2021.

[7] J. Guo, Z. Liu, Z. Du, J. Yu, X. Yang, and J. Yan, "Effect of fin-metal foam structure on thermal energy storage: an experimental study," *Renewable Energy*, vol. 172, pp. 57–70, 2021.

[8] C. Nie, J. Liu, and S. Deng, "Effect of geometry modification on the thermal response of composite metal foam/phase change material for thermal energy storage," *International Journal of Heat and Mass Transfer*, vol. 165, article 120652, 2021.

[9] M. Li, Q. Cao, H. Pan, X. Wang, and Z. Lin, "Effect of melting point on thermodynamics of thin PCM reinforced residential frame walls in different climate zones," *Applied Thermal Engineering*, vol. 188, article 116615, 2021.

[10] X. Huang, C. Sun, Z. Chen, and Y. Han, "Experimental and numerical studies on melting process of phase change materials (PCMs) embedded in open-cells metal foams," *International Journal of Thermal Sciences*, vol. 170, article 107151, 2021.

[11] A. R. Abdulmunem, P. Mohd Samin, H. Abdul Rahman, H. A. Hussien, I. Izmi Mazali, and H. Ghazali, "Numerical and experimental analysis of the tilt angle's effects on the characteristics of the melting process of PCM-based as PV cell's backside heat sink," *Renewable Energy*, vol. 173, pp. 520–530, 2021.

[12] M. S. Mahdi, H. B. Mahood, A. N. Campbell, and A. A. Khadom, "Natural convection improvement of PCM melting in partition latent heat energy storage: numerical study with experimental validation," *International Communications in Heat and Mass Transfer*, vol. 126, article 105463, 2021.

[13] G. S. Sodhi and P. Muthukumar, "Compound charging and discharging enhancement in multi-PCM system using non-uniform fin distribution," *Renewable Energy*, vol. 171, pp. 299–314, 2021.

[14] M. T. Chaichan, H. A. Kazem, A. H. A. Al-Waeli, and K. Sopian, "Controlling the melting and solidification points temperature of PCMs on the performance and economic return of the water-cooled photovoltaic thermal system," *Solar Energy*, vol. 224, pp. 1344–1357, 2021.

[15] E. Ozbas, S. Selimli, M. Ozkaymak, and A. S. S. Frej, "Evaluation of internal structure modifications effect of two-phase closed thermosyphon on performance: an experimental study," *Solar Energy*, vol. 224, pp. 1326–1332, 2021.

[16] H. Qin, Z. Wang, W. Heng, Z. Liu, and P. Li, "Numerical study of melting and heat transfer of PCM in a rectangular cavity with bilateral flow boundary conditions," *Case Studies in Thermal Engineering*, vol. 27, article 101183, 2021.

[17] H. Bashirpour-Bonab, "Investigation and optimization of PCM melting with nanoparticle in a multi-tube thermal energy storage system," *Case Studies in Thermal Engineering*, vol. 28, article 101643, 2021.

[18] L. N. Gollapudi, R. Senanayake, C. Georgantopoulou, and A. K. Singh, "Numerical heat transfer analysis of a thermal energy storage system enclosure with horizontal fin for sustainable energy storage," *Case Studies in Thermal Engineering*, vol. 28, article 101670, 2021.

[19] R. De Césaro Oliveski, F. Becker, L. A. O. Rocha, C. Biserni, and G. E. S. Eberhardt, "Design of fin structures for phase change material (PCM) melting process in rectangular cavities," *Journal of Energy Storage*, vol. 35, article 102337, 2021.

[20] A. Abidi, M. Rawa, Y. Khetib, H. F. A. Sindi, M. Sharifpur, and G. Cheraghian, "Simulation of melting and solidification of graphene nanoparticles-PCM inside a dual tube heat exchanger with extended surface," *Journal of Energy Storage*, vol. 44, article 103265, 2021.

[21] K. Hosseinzadeh, M. A. Erfani Moghaddam, A. Asadi et al., "Effect of two different fins (longitudinal-tree like) and hybrid nano- particles (MoS2-TiO2) on solidification process in triplex latent heat thermal energy storage system," *Alexandria Engineering Journal*, vol. 60, no. 1, pp. 1967–1979, 2021.

[22] B. Kok, "Examining effects of special heat transfer fins designed for the melting process of PCM and nano-PCM," *Applied Thermal Engineering*, vol. 170, 2020.

[23] N. Dora, A. R. Mohammad, and R. Chigurupati, "Numerical model development for the prediction of thermal energy storage system performance: CFD study," *International Journal of Energy and Environmental Engineering*, vol. 12, no. 1, pp. 87–100, 2020.

[24] S. Jevnikar and K. Siddiqui, "Investigation of the in fl uence of heat source orientation on the transient fl ow behavior during PCM melting using particle image velocimetry," *Journal of Energy Storage*, vol. 25, article 100825, 2019.

[25] F. Mehdaoui, M. Hazami, H. Taghouti, M. Noro, R. Lazzarin, and A. A. Guizani, "An experimental and a numerical analysis of the dynamic behavior of PCM-27 included inside a vertical enclosure: application in space heating purposes," *International Journal of Thermal Sciences*, vol. 133, pp. 252–265, 2018.

[26] S. Ebadi, S. H. Tasnim, A. A. Aliabadi, and S. Mahmud, "Melting of nano-PCM inside a cylindrical thermal energy storage system: numerical study with experimental veri fi cation," *Energy Conversion and Management*, vol. 166, pp. 241–259, 2018.

[27] M. Bashar and K. Siddiqui, "Experimental investigation of transient melting and heat transfer behavior of nanoparticle-enriched PCM in a rectangular enclosure," *Journal of Energy Storage*, vol. 18, pp. 485–497, 2018.

[28] Y. B. Tao, Y. K. Liu, and Y. L. He, "Effects of PCM arrangement and natural convection on charging and discharging

performance of shell-and-tube LHS unit," *International Journal of Heat and Mass Transfer*, vol. 115, pp. 99–107, 2017.

[29] M. H. Joneidi, M. J. Hosseini, A. A. Ranjbar, and R. Bahrampoury, "Experimental investigation of phase change in a cavity for varying heat flux and inclination angles," *Experimental Thermal and Fluid Science*, vol. 88, pp. 594–607, 2017.

[30] N. S. Bondareva and M. A. Sheremet, "Flow and heat transfer evolution of PCM due to natural convection melting in a square cavity with a local heater," *International Journal of Mechanical Sciences*, vol. 134, pp. 610–619, 2017.

[31] M. Arıcı, E. Tütüncü, M. Kan, and H. Karabay, "Melting of nanoparticle-enhanced paraffin wax in a rectangular enclosure with partially active walls," *International Journal of Heat and Mass Transfer*, vol. 104, pp. 7–17, 2017.

[32] A. A. Rabienataj Darzi, M. Jourabian, and M. Farhadi, "Melting and solidification of PCM enhanced by radial conductive fins and nanoparticles in cylindrical annulus," *Energy Conversion and Management*, vol. 118, pp. 253–263, 2016.

[33] S. H. Tasnim, R. Hossain, S. Mahmud, and A. Dutta, "Convection effect on the melting process of nano-PCM inside porous enclosure," *International Journal of Heat and Mass Transfer*, vol. 85, pp. 206–220, 2015.

[34] B. Kamkari, H. Shokouhmand, and F. Bruno, "Experimental investigation of the effect of inclination angle on convection-driven melting of phase change material in a rectangular enclosure," *International Journal of Heat and Mass Transfer*, vol. 72, pp. 186–200, 2014.

[35] N. S. Dhaidan, J. M. Khodadadi, T. A. Al-Hattab, and S. M. Al-Mashat, "Experimental and numerical investigation of melting of phase change material/nanoparticle suspensions in a square container subjected to a constant heat flux," *International Journal of Heat and Mass Transfer*, vol. 66, pp. 672–683, 2013.

[36] H. Bashirpour-Bonab, "Investigation and optimization of PCM melting with nanoparticle in a multi- tube thermal energy storage system," *Case Studies in Thermal Engineering*, vol. 28, p. 101643, 2021.

[37] X. Luo, J. Gu, H. Ma et al., "Numerical study on enhanced melting heat transfer of PCM by the combined fractal fins," *Journal of Energy Storage*, vol. 45, p. 103780, 2022.

[38] A. Nirwan, D. Gupta, R. Matta, R. Kumar, and B. Mondal, "Evaluation of heat transfer performance of PCM based composites for thermal management of electronics," *Materials Today: Proceedings*, vol. 57, pp. 954–957, 2022.

[39] Q. Li, X. Ma, X. Zhang, J. Ma, X. Hu, and Y. Lan, "Microencapsulation of Al-Zn alloy as phase change materials for high-temperature thermal storage application," *Materials Letters*, vol. 308, p. 131208, 2022.

[40] J. Xing, Y. Zhou, K. Yang et al., "Microencapsulation of fatty acid eutectic with polyvinyl chloride shell used for thermal energy storage," *Journal of Energy Storage*, vol. 34, p. 101998, 2021.

[41] T. Kawaguchi, H. Sakai, N. Sheng, A. Kurniawan, and T. Nomura, "Microencapsulation of Zn-Al alloy as a new phase change material for middle- high-temperature thermal energy storage applications," *Applied Energy*, vol. 276, p. 115487, 2020.

[42] S. Jevnikar and K. Siddiqui, "Investigation of the influence of heat source orientation on the transient flow behavior during PCM melting using particle image velocimetry," *Journal of Energy Storage*, vol. 25, article 100825, 2019.

[43] A. Abdi, V. Martin, and J. N. Chiu, "Numerical investigation of melting in a cavity with vertically oriented fins," *Applied Energy*, vol. 235, pp. 1027–1040, 2019.

[44] B. Kamkari and H. J. Amlashi, "Numerical simulation and experimental verification of constrained melting of phase change material in inclined rectangular enclosures," *International Communications in Heat and Mass Transfer*, vol. 88, pp. 211–219, 2017.

[45] M. S. Mahdi, H. B. Mahood, J. M. Mahdi, A. A. Khadom, and A. N. Campbell, "Improved PCM melting in a thermal energy storage system of double-pipe helical-coil tube," *Energy Conversion and Management*, vol. 203, article 112238, 2020.

[46] H. Xu, N. Wang, C. Zhang, Z. Qu, and M. Cao, "Optimization on the melting performance of triplex-layer PCMs in a horizontal finned shell and tube thermal energy storage unit," *Applied Thermal Engineering*, vol. 176, article 115409, 2020.

[47] A. V. Arasu and A. S. Mujumdar, "Numerical study on melting of paraffin wax with Al_2O_3 in a square enclosure," *International Communications in Heat and Mass Transfer*, vol. 39, no. 1, pp. 8–16, 2012.

[48] A. Ebrahimi and A. Dadvand, "Simulation of melting of a nano-enhanced phase change material (NePCM) in a square cavity with two heat source-sink pairs," *Alexandria Engineering Journal*, vol. 54, no. 4, pp. 1003–1017, 2015.

[49] P. N. S. Teja, S. K. Gugulothu, G. R. Sastry, B. Burra, and S. S. Bhurat, "Numerical analysis of nanomaterial-based sustainable latent heat thermal energy storage system by improving thermal characteristics of phase change material," *Environmental Science and Pollution Research*, vol. 18, pp. 1–14, 2021.